THERMOPHYSICS 2008

Proceedings

Editors: Jozef Leja & Slávka Prváková

Kočovce, October 16–17, 2008

SCOPE OF THE CONFERENCE

The international seminar Thermophysics is a traditional meeting of scientists and experts working in the field of thermophysics and heat transfer. The seminar is focused on thermal energy transfer and storage in gases, liquids, and solids or combinations thereof, including conductive, convective, and radiative modes alone or in combination and the effects of the environment. Topics range from basic research to advanced applications, including theoretical, experimental and computational methods. The aim of the seminar is to bring together people working in this field and provide them a forum for the exchange of their ideas and experiences. The intention of organizers is also to provide the opportunity for young scientists to present their work and discuss their results with experienced researchers. The meeting of Thermophysics Society makes an integral part of the seminar schedule.

ORGANIZERS

- Department of Physics, Faculty of Civil Engineering, Slovak University of Technology
- Slovak Physical Society

ORGANIZING COMMITTEE

- Doc. RNDr. Jozefa Lukovičová, PhD.
- Mgr. Jozef Leja
- Mgr. Slávka Prváková, PhD.

TERMOPHYSICS 2008

Edited by Jozef Leja & Slávka Prváková
Issued by Vydavateľstvo STU
1. issue
Impression: 50 copies
Bratislava 2008

ISBN 978-80-227-2968-0

CONTENTS

PREFACE

It is pleasure for research group at the Department of Physics of Faculty of Civil Engineering at Slovak University of Technology in Bratislava to host the twelfth meeting of the Thermophysical Society – Working Group of the Slovak Physical Society. The meeting was held on October 16 and 17, 2008 in the Kočovce chateau, Western Slovakia. The seminar Thermophysics is meeting of scientists working in the field of investigation of heat transfer and measurement of thermophysical and other transport properties of materials. Nearly 30 participants of the seminar delivered over 20 lectures in which their authors presented current research progress. The aim of the seminar was to attract not only prominent scientists but also young physicists.

Organize committee would like to express thanks to all participants for their interesting contribution.

Jozefa Lukovičová

Application of the Hot Ball Method on Curing Process of an Epoxy Resin

Carlos Calvo Anibarro, Ľudovít Kubičár
Institute of Physics SAV, Dúbravská cesta 9, SK-845 11 Bratislava, Slovakia

Ivan Chodak, Igor Novak
Polymer Institute SAV, Dúbravská cesta 9, SK-845 11 Bratislava, Slovakia

1. Introduction

The paper deals with application of the Hot Ball method on curing process of an epoxy resin. With this method we are able to test the curing stage of the epoxy resin by measuring of the thermal conductivity. Thermal conductivity is a material property that depends on the degree of curing of the polymer. The epoxy resin sample hardens during the curing and the physical properties of the material are changed. We can use this change of the physical properties for identification of the curing process.

Testing of the material property is performed by cycles. In each cycle the thermal conductivity is measured and stored. With the repetition of the cycles a picture on long time material property change is obtained. The curing process has been tested to several temperatures.

2. Description of the Hot Ball method

The Hot Ball method belongs to transient measuring techniques. This method is based on the generation of a constant heat flux by a spherical heat source inside the material to be tested, measuring the temperature response with a thermometer placed in the center of the heat source.

Fig.1. Photo of the hot ball sensor

The constant heat flux is generated by the passage of an electrical current through a resistance assembled to the spherical heat source (r_b). The heat flux penetrates inside the hot ball sensor surrounding (R).

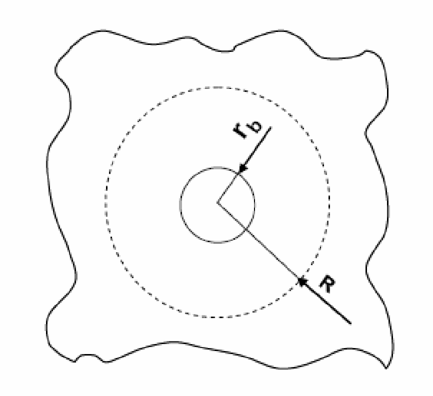

Fig.2. Ideal model

A thermometer placed in the center of the heat source measures a temperature response. While the heat transfer to the surrounding medium is being produced, the temperature of the sample is increased up to a maximal value (T_m), in which the temperature is stabilized.

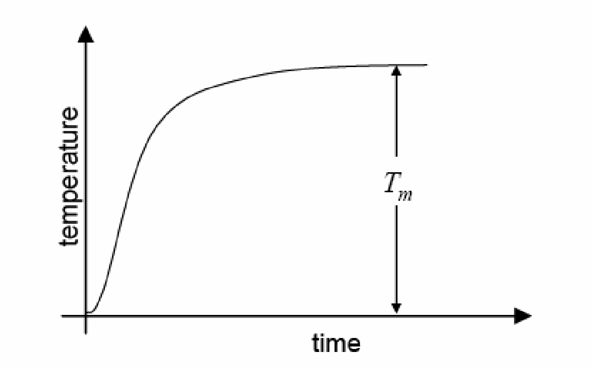

Fig.3. Ideal temperature response

This maximal value of the temperature response is used to calculate the thermal conductivity of the material by the relation

$$\lambda = \frac{q}{4\pi r_b T_m (t \to \infty)}$$

where λ *[Wm^{-1}K^{-1}]* is the thermal conductivity, q *[W]* is the heat flux, r_b *[m]* is the heat source radius and T_m *[K]* is the stabilized temperature value.

In order to obtain a picture on long time thermal conductivity change, testing of the material property is performed by cycles. Each cycle consists on the measuring of the ball temperature (obtaining the base line), the generation of a constant heat until obtaining the stabilized temperature value after some time, and a stabilization stage produced when the heat generation is interrupted.

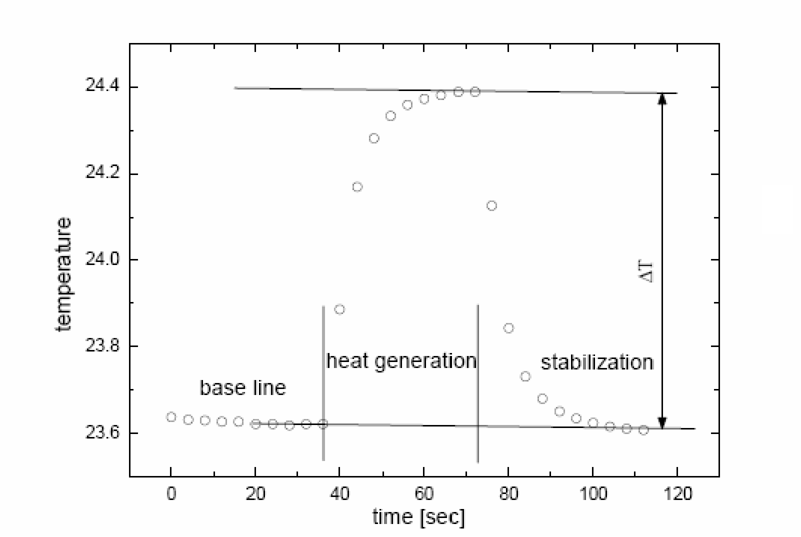

Fig.4.Measuring cycle

Results of each cycle are stored in the data logger and transferred into computer, obtaining automatically the thermal conductivity for each measuring cycle.

3. System

An epoxy oligomer named *ChS Epoxy 513* was used. It is a low-molecular weight epoxyacrylate resin. Its molecular weight is 800 and its viscosity is 400 mPa. A catalyst based on a boric fluoride compound was used as hardener. The sample was prepared by the Polymer Institute of the Slovak Academy of Sciences.

A polymerization following a cationic mechanism is observed. In this kind of polymerization, the catalyst activates an epoxy monomer by forming an oxonium active center.

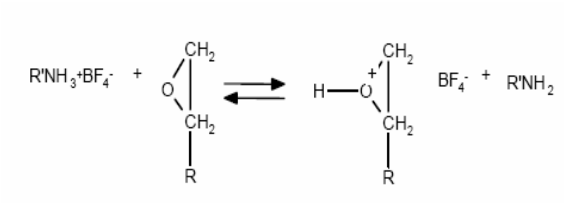

Fig.5.Cationic polymerization initiation

These protonated epoxy molecules can then reacted with other epoxy monomers and proceed in cationic chain propagation by the activated chain end or activated monomer mechanisms.

In the activated chain end mechanism, tertiary oxonium ions are formed and the chain propagates by repeated addition of monomer molecules.

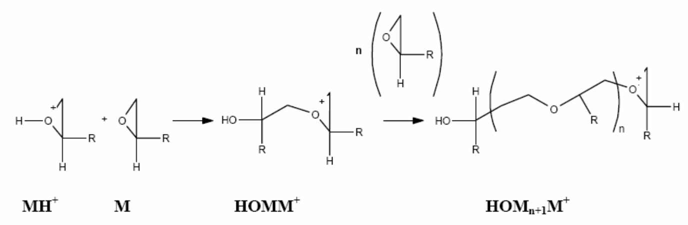

Fig.6.Activated chain end mechanism

Another possibility is the activated monomer mechanism. As the oxiranium ring opens, hydroxyl groups are formed, and with a high formation of active centers, more hydroxyl ions will form. Reaction with these hydroxyls containing species followed a transfer of charge with a monomer to generate the activated monomer, which is again added to a hydroxyl containing species. Thus this path becomes more important as the hydroxyl concentration increases with increasing initiation.

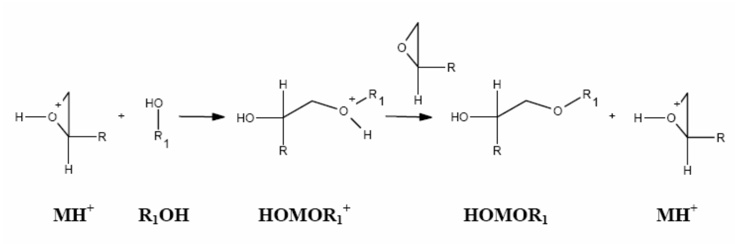

Fig.7.Activated monomer mechanism

A system was prepared in order to realize the measurements. The sample was put inside a metallic recipient, and the hot ball sensor was placed in the middle of this recipient.

A first chamber is placed over the recipient and a second chamber is placed over the first one to have an isothermal process. The temperature inside the chamber is controlled by a thermostat.

The hot ball sensor is connected to an electronic unit that realizes the required functionalities to obtain data on thermal conductivity and to store the corresponding data. Those data are transferred to a computer.

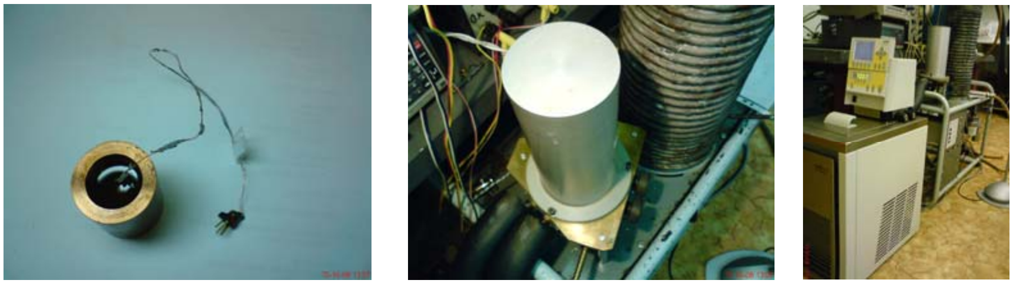

Fig.8.Picture of the hot ball sensor inside the sample

4. Experiment

The calibration of the hot ball sensor is based on the relation

$$q / T_m = 4\pi r_b \lambda = A\lambda$$

The ratio q/T_m is a linear function of thermal conductivity that will be tested using certified materials, namely porofen, calcium, PMMA and glycerol. A calibration function was obtained.

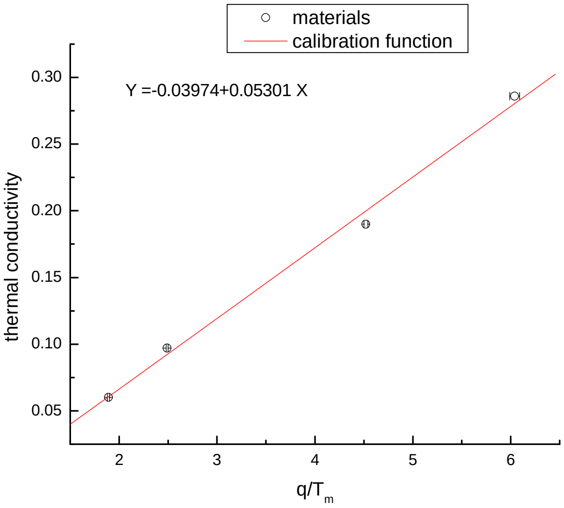

Fig.10.Calibration function

In order to start the monitoring of the curing process, the temperature was set at 30°C. When this temperature was stabilized, the mixture of the epoxy resin was put in the recipient and the hot ball sensor was introduced in the middle of the mixture. The recipient was put into the chamber.

After five days, it was observed that the process was running very slowly. The decision taken was set the temperature at 50°C, in order to accelerate the process.

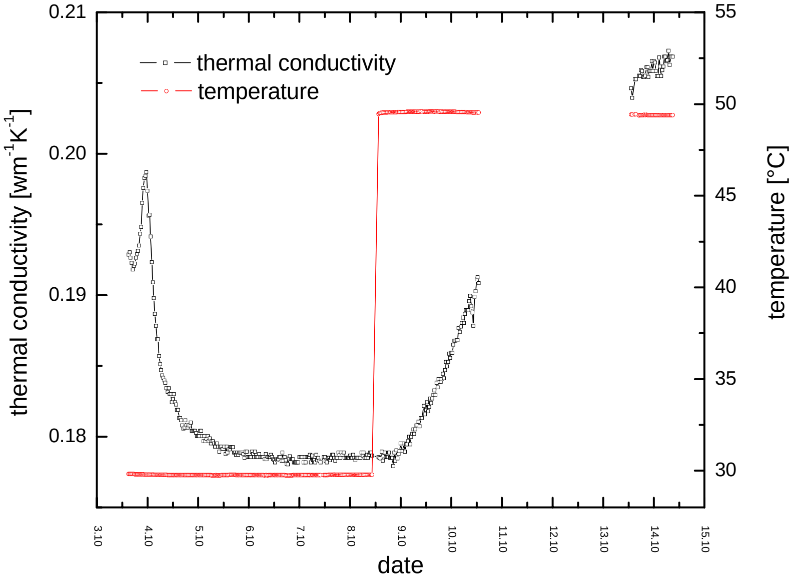

Fig.11.Variation of the thermal conductivity during curing process of the epoxy resin

Fig.11 shows changes of the thermal conductivity and temperature during the experiment. The experiment started at 30°C. Firstly we could observe how the thermal conductivity was going to lower values. It was due to a homogenization of the initial mixture of the two components. When this homogenization had been get, a constant value of the thermal conductivity was obtained. After five days, this constant value was still obtained. We decided to increase the temperature up to 50°C. An increasing in the thermal conductivity was observed, due to the stiffening of the sample. After one week from the beginning of the experiment and due to a problem with the battery of the RTM device, a wide range of measurements were lost. When this problem was solved, the increasing of the thermal conductivity was still running.

5. Conclusion

The application of the Hot Ball method to monitoring curing process of an epoxy resin has been presented.

An epoxy resin based on boric compound has been used for the experiment.

Initially, a lowering of the thermal conductivity was produced, due to a homogenization of the mixture formed by the epoxy resin and the hardener.

The thermal conductivity is increased during the curing process due to the stiffening of the sample.

6. Acknowledgements

This work was supported by project APVV/0497/07.

Authors would like to express thanks to Mr. Markovič for technical assistance and to Mr. Bohač, Mr. Stofanik and Mr. Vretenár for fruitful discussions.

THE ELECTRO-THERMAL MODEL OF SWITCH EFFECT IN THE CHALCOGENIDE GLASSES

Ivan Baník, Jozefa Lukovičová

Abstract
The paper presents modelling of a volt-ampere characteristic of semiconductor chalcogenide glasses, which demonstrates so-called switch effect showing hysteresis behaviour during increasing and subsequent decreasing of current or voltage in the sample. Conductivity of the material is temperature depend. In this model, the cylindrical sample is divided into two parts and the Joule heat is created in both of them. The model assumes that the heat transfers between these parts can be described Newton's law of cooling.

INTRODUCTION

Switch effect

Chalcogenide glasses present an important subgroup of non-crystalline materials with several possibilities of technical applications in the area of electronics and optoelectronics [1-3]. Their electrical properties were explored first time by Kolomijec with colleagues around 1960 [4]. Switch effect as the memory effect in these materials discovered Owshinski in 1968 [5]. Another perspective application of these materials is the photo (current) induced phase structural change [6], which can bring the use in data (incl. holographic) record.

The paper presents electro-thermal model of the switch effect. The aim is to show that the switch effect (by which the volt-ampere characteristic shows strong hysteresis) may be induced also by the electro-thermal mechanism.

SINGLE-LAYER MODEL

Electrical conductivity

The volt-ampere characteristic I(U) of chalcogenide glasses is linear for very small currents. The influence of temperature T on its characteristic is given by

$$I = const\,.\,U\exp(-\frac{W}{kT})$$

where W is the activation energy of the corresponding chalcogenide glass and k is the Boltzman constant. In our case, the temperature of sample T is equal to room temperature T_o.

The higher currents may develop self-heating of the sample, which can be incorporated into the volt-ampere relation through the temperature change induced by current. At the same time a simplified assumption is applied that the sample is isothermal (temperature is equal in whole volume) and the heat release out of the sample is govern by the Newton law for the thermal release. For the mentioned assumptions, the temperature correction is continual proportional to the electric power of the sample UI, so the $T = T_o + \beta UI$, where β is constant. The volt-ampere characteristic of the single-layer sample may be written as follows

$$I = const\,.U.\exp(-\frac{W}{k(T_0 + \beta\, UI)})$$

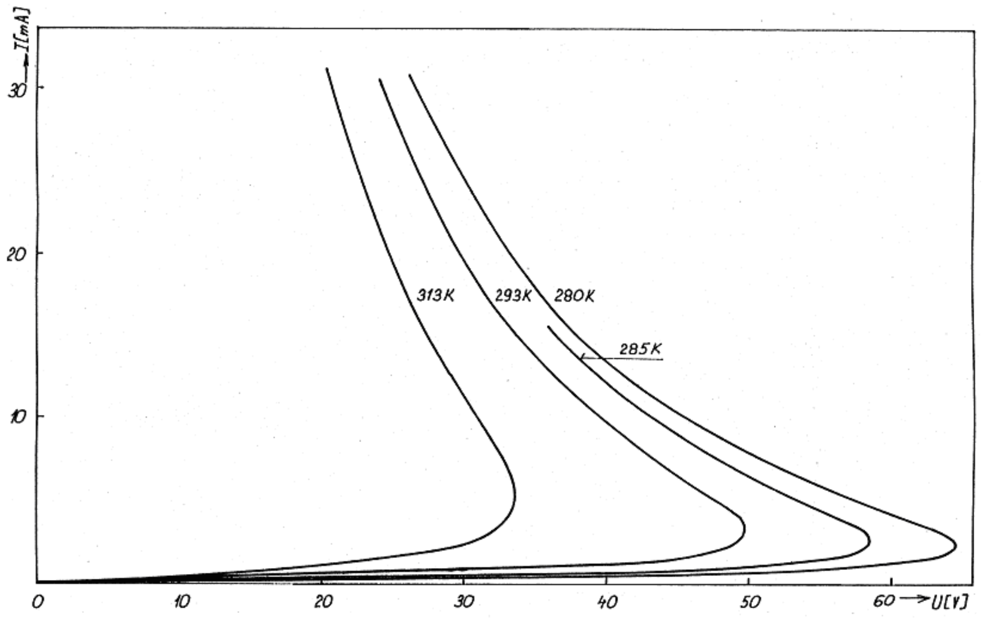

Figure 1

For higher currents are the corresponding volt-ampere characteristics markedly non-linear. The situation with several volt-ampere characteristics at different temperatures of surrounding environment is shown on Figure 1. The characteristics show also the field with negative differential resistance. One has to note, that the whole process is reversible by the rise and decline of the current. The volt-ampere characteristic of single-layer model does not show any hysteresis behaviour.

TWO-LAYER MODEL

This part describes the two-layer model and proves that the corresponding volt-ampere characteristics show hysteresis behaviour, so called switch effect. The entire geometry of the two-layer sample together with an appropriate thermal profile is given on the Figures 2 and 3.

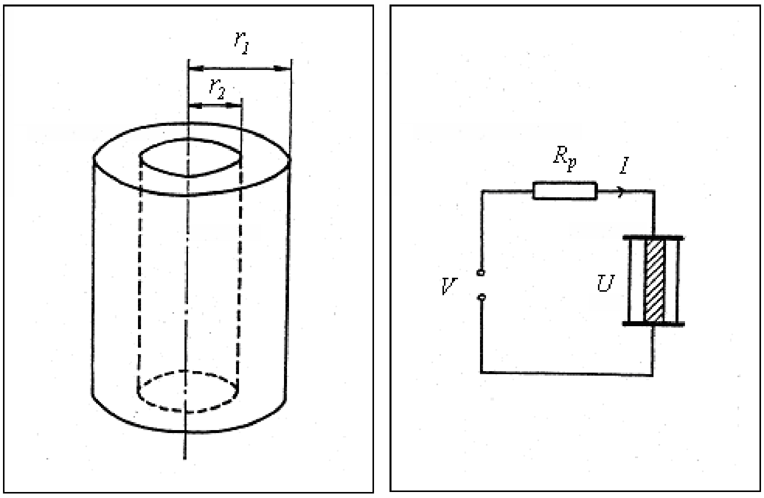

Figure 2.

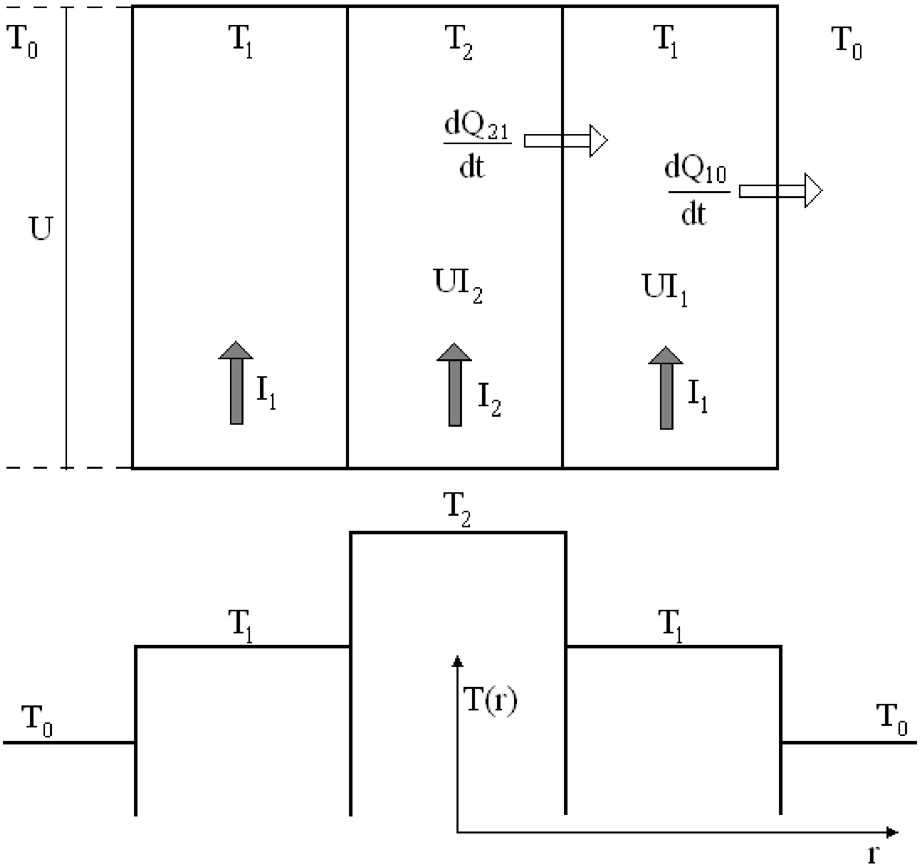

Figure 3.

At the first stage we will investigate the thermal balance in particular sample layers.

In stationary state, the heat rate UI_2 induced by the current I_2 is in the middle (the second) part of the sample in equilibrium with the heat outlet dQ_{21}/dt from the layer 2 to layer 1 per unit of time, and so

$$\frac{dQ_{21}}{dt} = UI_2$$

In respect with the assumption of validity of the Newton's relation, the heat outlet will be given by the equation

$$\frac{dQ_{21}}{dt} = \gamma_{21}(T_2 - T_1)$$

where γ_{12} is a constant.

The thermal balance of the outside layer in equilibrium is given by equation

$$\frac{dQ_{01}}{dt} = \frac{dQ_{21}}{dt} + UI_1 = UI_2 + UI_1 = UI$$

where

$$I = I_1 + I_2$$

is the total current passing through the sample (the both layers). The heat released into the surrounding environment is described by the equation

$$\frac{dQ_{10}}{dt} = \gamma_{10}(T_1 - T_0)$$

From the mentioned follows that

$$\gamma_{10}(T_1 - T_0) = UI$$

$$\gamma_{21}(T_2 - T_1) = UI_1$$

All these relations serve to express the temperatures T_1 and T_2 in particular layers of the sample for the stationary state

$$T_1 = T_0 + \beta_{10}UI$$

$$T_2 = T_0 + \beta_{10}\,UI + \beta_{21}\,UI_2$$

where

$$\beta_{21} = \frac{1}{\gamma_{21}}$$

$$\beta_{10} = \frac{1}{\gamma_{10}}$$

are the corresponding constants. The currents, which are passed through particular layers are described by the analogous relations like in the case of single-layer sample, so

$$I_1 = const\,.\,U\exp\left(-\frac{W}{k(T_0 + \beta_{10}UI)}\right)$$

$$I_2 = const\,.\,U\exp\left(-\frac{W}{k(T_0 + \beta_{10}UI + \beta_{21}UI_2)}\right)$$

$$I_1 + I_2 = I$$

By the numerical solving of the above mentioned equations is possible to obtain a graph of corresponding volt-ampere characteristics of the two-layer's sample. The characteristics show hysteresis behaviour already during the corresponding rundown.

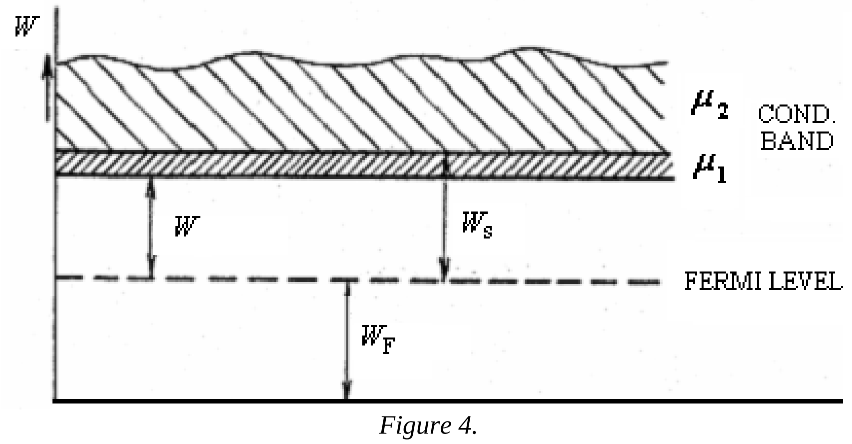

Figure 4.

Another improvement of the volt-ampere characteristics model of the chalcogenide glass can be achieved by the implementing of two sub-bands of carrier mobility (Figure 4).

TWO SUB-BANDS OF MOBILITY IN NON-CRYSTALLIC SEMICONDUCTORS

Electronic spectrum of the chalcogenide glasses features with an existence of low mobility sub-band situated on the bottom of conduction band (like on the top of valence band). The sub-band of high mobility is situated above it (see Figure 4).

The explanation is following: an occurrence of the low mobility sub-band may be conditional to the existence of potential barriers which make the transport of unbound electrons with low energy harder (see Figure 5). The mobility of unbound electrons with sufficiently high energy (situated at the layers above the top of potential barriers) will be much higher.

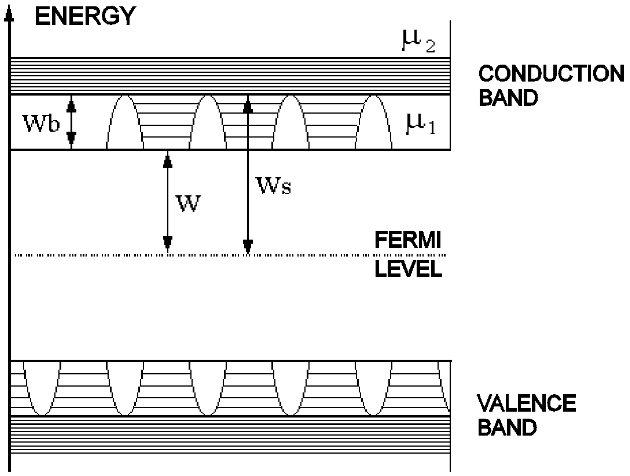

Figure 5

Single- and two-layer sample with two sub-bands of mobility

If the initiated two sub-bands are assigned simply to two different values of mobility μ_1 and μ_2 (see Figures 4, 5), the entire transport in the glass (considering the two-layer sample) can be described by the following three relations

$$I_1 = const\,.U\left[\mu_1 \exp(-\frac{W}{k(T_0+\beta_{10}UI)}) + (\mu_2-\mu_1)\exp(-\frac{W_{O1}(1-cU)}{k(T_0+\beta_{10}UI)})\right]$$

$$I_2 = const\,.U\left[\mu_1 \exp(-\frac{W}{k(T_0+\beta_{10}UI+\beta_{21}UI_2)}) + (\mu_2-\mu_1)\exp(-\frac{W_{O1}(1-cU)}{k(T_0+\beta_{10}UI+\beta_{21}UI_2)})\right]$$

$$I_1 + I_2 = I$$

In addition, the mentioned equations involve a fact that the electric field decreases the mobility gap width W_s, and so $W_s = W_{so} - cU$, where U is the electric tension on the sample and c is constant.

Numerical solution of the three above relations can produces a graph of particular volt-ampere characteristics of the two-layers sample. Illustrative examples are shown on Figures 6 and 7. The characteristics show hysteresis behaviour. Sample is changing its state from the high- to low-resistance and vice versa what is just the principle of the switch effect.

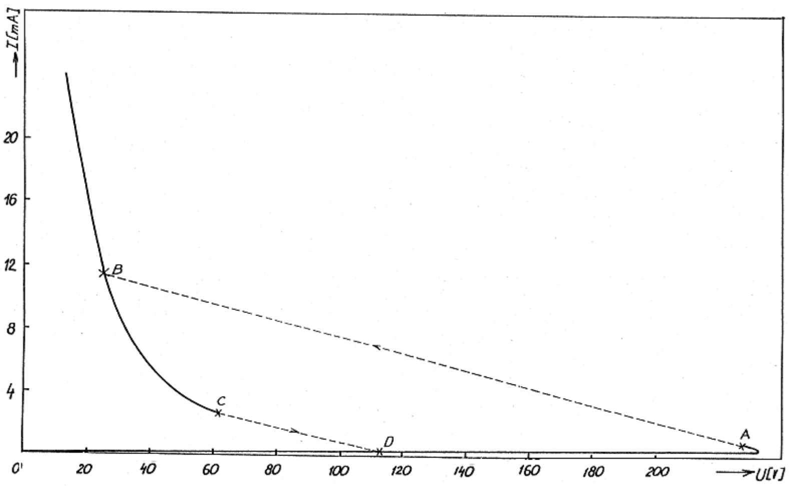

Figure. 6

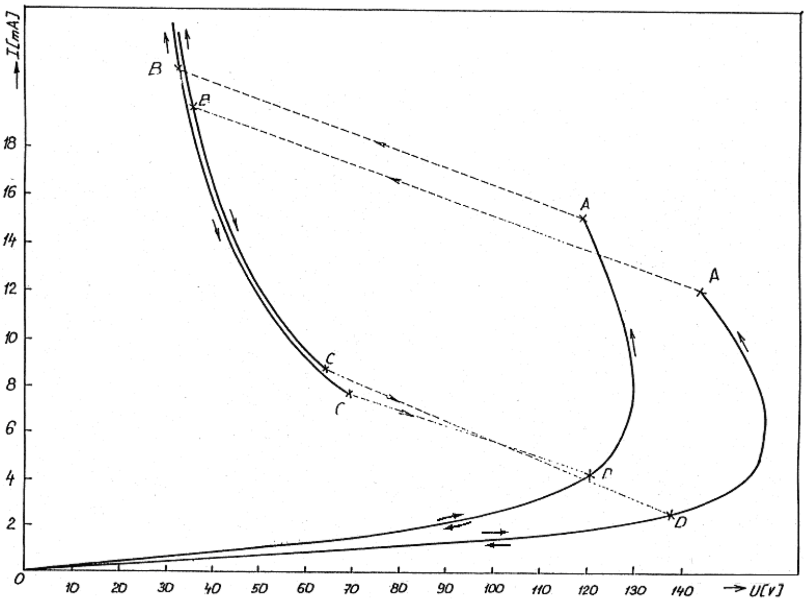

Figure 7

ACKNOWLEDGEMENT:

This paper has been supported by Slovak Grant Agency VEGA (grant No.1/4204/07).

REFERENCES

[1] Mott N. F., Davis E. A.: Electron processes in non-crystalline materials, Clarendon Press, Oxford, (1979). (Elektronnyje processy v nekristaličeskich veščestvach, Mir, Moskva 1982).
[2] Brodsky M. H.: Amorphous semiconductors, Springer Verlag Berlin, Heidelberg, New York, (1979). (Amorfnyje poluprovodniky, Mir, Moskva, 1982).
[3] Banik I.: Electrical and optical properties of non-crystalline semiconductors under normal and high pressure, SUT Bratislava (2002).
[4] Kolomijets B. T.: Glassy semiconductors, (Stekloobraznyje poluprovodniky), Vestnik AN SSSR, 6, p.54, (1969).
[5] Ovshinski S.R.: Phys Rev. Letters 21, 1968, 1450
[6] Popescu M.: J. Optoelectron. Adv. Mater. 6(4), 1147 (2004).

PROPERTIES OF CEMENTITIOUS COMPOSITES AT HIGH TEMPERATURES

Robert Černý

Czech Technical University in Prague, Faculty of Civil Engineering, Department of Materials Engineering and Chemistry, Thákurova 7, 166 29 Prague 6, Czech Republic, email: cernyr@fsv.cvut.cz

Abstract:

Cementitious composites subjected to high temperatures undergo chemical reactions which result in decomposition of some of the original compounds of the cement gel. The reliable knowledge of these reactions and their consequences for both the cement matrix and pore space is of crucial importance for understanding the behavior of this type of composites at high temperatures. In this paper, properties of several characteristic cement-based composites are analyzed both after and during high-temperature exposure and their relation to the thermal decomposition processes is analyzed.

Keywords:

Cement-based composites, high temperatures, properties

INTRODUCTION

Thermal and hygric properties of cementitious composites such as concrete, cement mortar and cement paste are measured at room temperature in standard conditions, in most cases. For many applications of concrete in building structures is it quite sufficient as usual environmental exposure is within the range from about -20°C to +50°C. However, some concrete structures can be exposed to elevated or high temperatures during their lifetime. Fire resistance problems of concrete structures can be considered probably as the most important example in this respect, but special industrial applications of concrete such as in blast furnaces, nuclear safety related structures or heat pipes also become of great significance. In such conditions, high temperature values of thermal parameters are to be determined to analyze the behavior of the particular structures already in the design phase in a proper way.

Concrete is a material that can survive severe thermal conditions. There are examples of concrete structures that were exposed to a major fire but after reconstruction they were quite serviceable (for instance the Great Exhibition Palace in Prague). Therefore, it may also be useful to know its hygric and thermal properties after high-temperature exposure, in order to assess its serviceability after a fire.

In this paper, properties of several characteristic types of cement-based composites are analyzed both during and after high-temperature exposure.

EFFECT OF HIGH TEMPERATURES ON STRUCTURE AND COMPOSITION OF CEMENT-BASED COMPOSITES

There are numerous methods for investigation of concrete structure and composition which can be utilized in the analysis of the effect of high temperatures on the cement matrix and pore space. Thermal analysis and mercury intrusion porosimetry belong to the simplest but very effective methods of this type. Therefore, we will use them for the demonstration of basic processes taking place in concrete subjected to high temperatures.

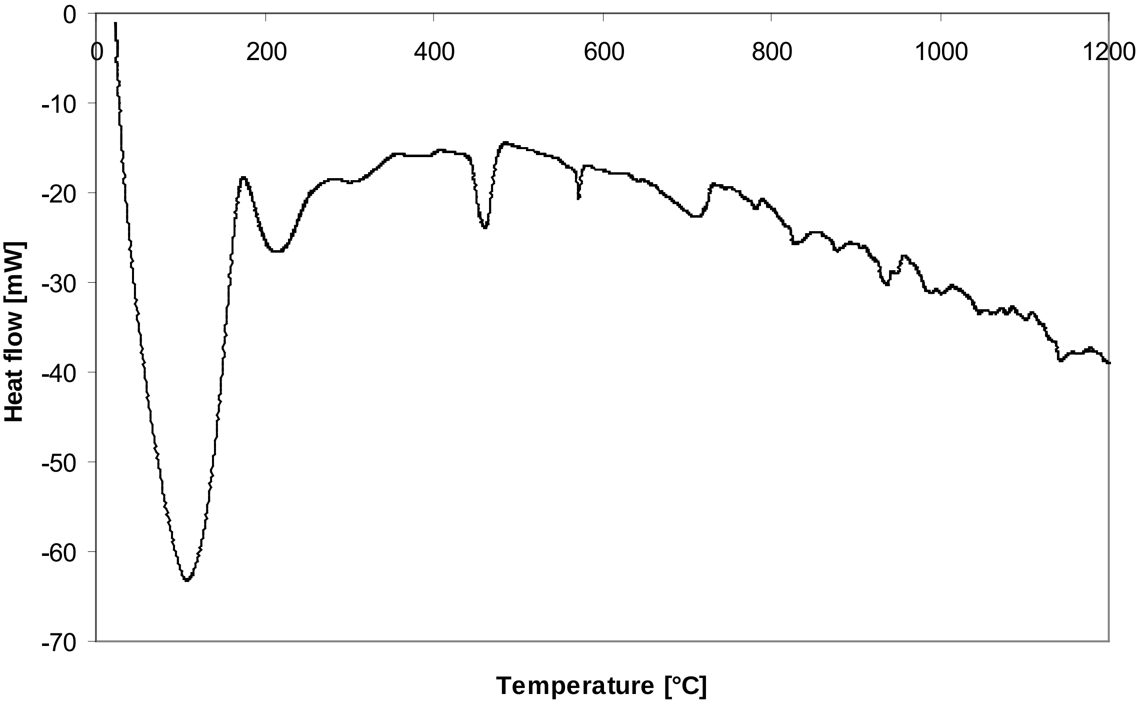

Figure 1 DTA of Portland cement mortar

Fig. 1 shows a typical differential thermal analysis (DTA) curve of Portland cement mortar. The first very pronounced endothermic peak (a minimum) at 107°C represents the evaporation of pore water. This peak probably also includes the decomposition of CSH gels that should take place between 120°C and 140°C [1] and the decomposition of ettringite around 120°C [1]. The second endothermic peak at 212°C corresponds to the decomposition of the aluminate phase $4CaO·Al_2O_3·13H2O$ and sulfoaluminate phases $3CaO·Al_2O_3·CaSO_4·12H_2O$ and $3CaO·Al_2O_3·3CaSO_4·31H_2O$ [1]. The third significant endothermic peak at 460°C represents the decomposition of $Ca(OH)_2$ [1]. The sharp endothermic peak at 573°C is apparently not related to the processes in cement. It shows the α→β phase transition of aggregate SiO_2. The wide endothermic peak with a minimum at 710°C can be assigned to the decomposition of calcium carbonate $CaCO_3$ which appeared in the material due to the carbonation of calcium hydroxide. The other small peaks in the range of 800–1200°C are difficult to identify because their explanation was not reported yet — as far as the author knows — in the literature.

Fig. 2 shows a typical thermogravimetric (TG) curve of Portland cement mortar which was dried before the TG analysis. The total mass loss observed was 16.25%. The first remarkable mass loss below 200°C is approximately 1 mg (i.e., 2.5% of the mass of the sample) and corresponds to the loss of nearly free water from the pore space and water released from CSH gels and ettringite. Further slower mass decreases on the TG curve up to approximately 400°C can be attributed to the decomposition of aluminate and sulfoaluminate phases. It amounts to 0.93 mg (2.33% of mass) and corresponds to the loss of water from these phases. The fast mass decrease between 450 and 470°C is due to the decomposition of calcium hydroxide. The amount of water released during this decomposition was 0.786 mg (1.97% of mass), which corresponds to 3.23 mg of $Ca(OH)_2$ in the sample (i.e., 8.07%). The remarkable mass loss between 600 and 710°C (3.13 mg; i.e., 7.83% of mass) can be assigned to the decomposition of calcium carbonate. The amount of released CO_2 corresponds to 5.26 mg of originally present $CaCO_3$. The slow mass loss at temperatures higher than 710°C cannot be exactly identified; it is not discussed in detail in the literature.

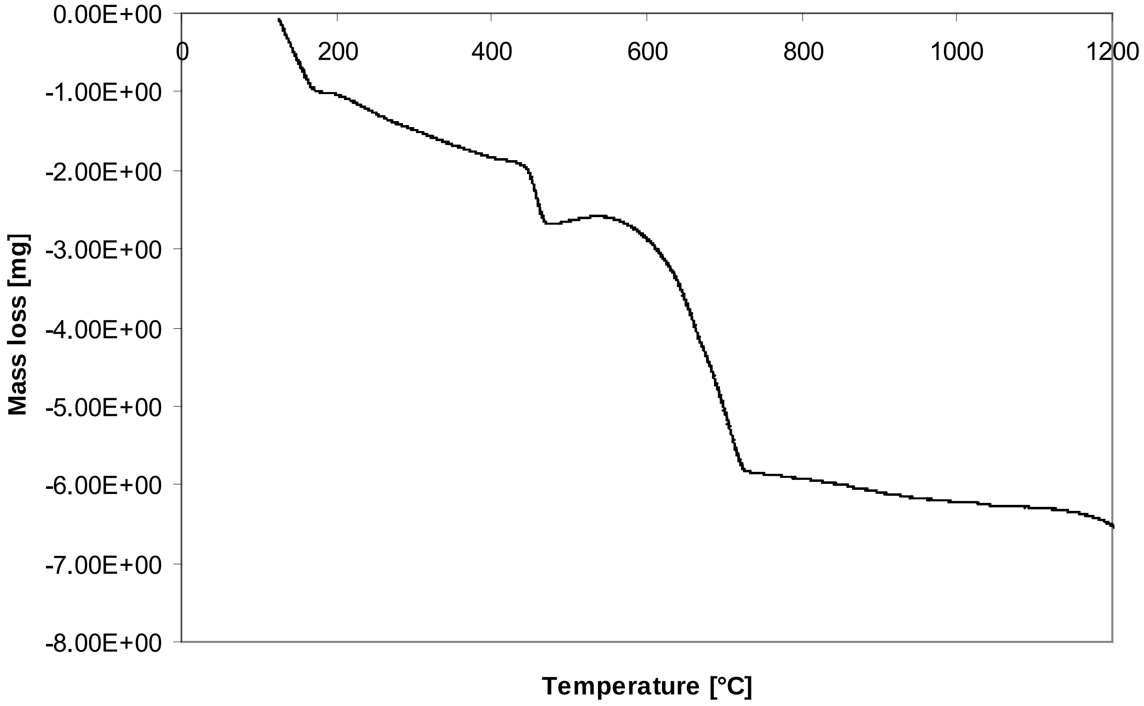

Figure 2 TG of Portland cement mortar

The effect of high temperatures on the pore structure of Portland cement mortar is illustrated in Table 1 and Fig. 3. Table 1 shows global characteristics of the porous space of reference Portland cement mortar and the same mortar which was pre-heated to 800°C for two hours before the measurement; V_p is the total intrusion volume, A_p the total pore area, r_V the median pore radius by volume, ρ the bulk density. Apparently, the effect of thermal load was very pronounced. The median pore radius increased about 15 times compared to the reference specimen, V_p increased by almost 70% and even ρ decreased by 8%.

Table 1 Global characteristics of the pore space of Portland cement mortar

Material	V_p [cm^3/g]	A_p [m^2/g]	r_V [μm]	ρ [kg/m^3]
Reference mortar	0.073	13.62	0.038	2200
Pre-heated to 800°C	0.122	5.46	0.565	2020

Fig. 3 shows a comparison of pore distribution functions of the reference- and 800°C pre-heated Portland cement mortar specimens. The thermally loaded specimen exhibited a very significant increase of pore volume in the region 0.1 μm - 5 μm compared to the reference mortar but a remarkable decrease was observed in the region of smaller pores, r < 0.1 μm.

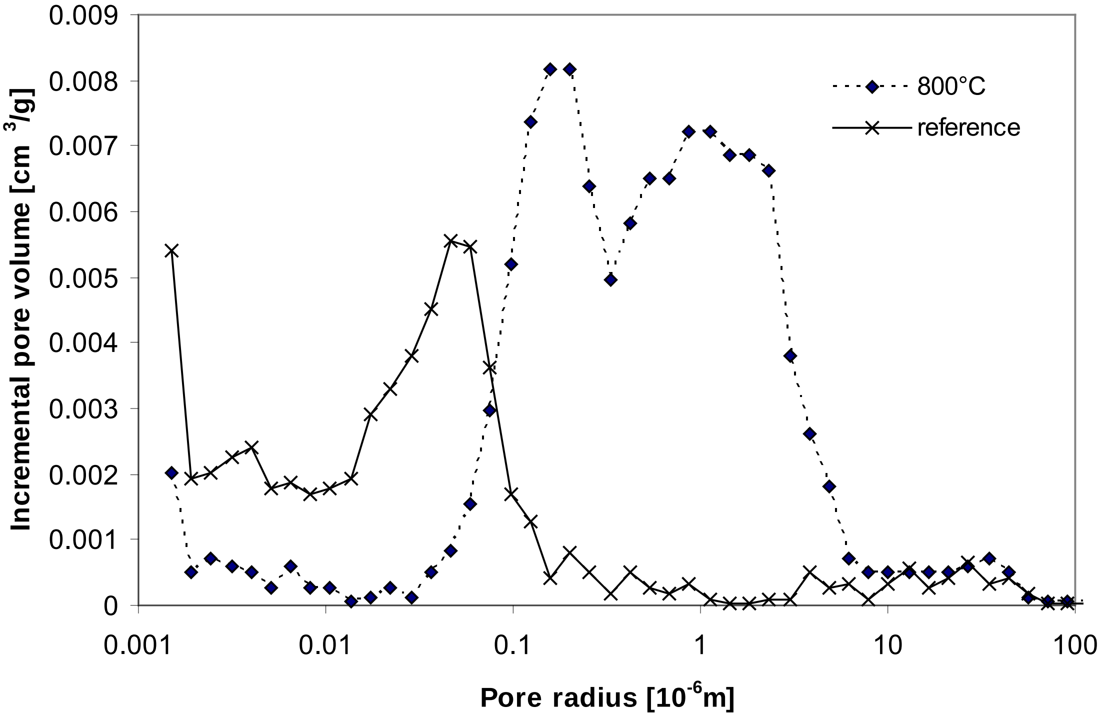

Figure 3 Incremental pore volume of Portland cement mortar

The characteristic example of thermally induced changes in the composition and porous structure of cement mortar presented above gives evidence that the damage of both the matrix and pore space can be quite serious. The rather significant mass loss together with the increase of pore volume and the shift of the major peak of pore distribution curve to the μm range are certainly supposed to result in major changes in principal material parameters. As for the composition and pore structure the material subjected to high temperatures reminds the original Portland cement-based composite only marginally. We will illustrate the effect of high temperatures on hygric and thermal properties of selected Portland cement-based composites, namely cement mortar, high-performance concrete, three types of glass fiber reinforced composites and a carbon fiber reinforced composite material, in what follows.

MATERIALS

The samples of cement mortar (CM) had the following composition (i.e. the mixture for one charge): Portland cement ENV 197 - 1 CEM I 42.5 R (Králův Dvůr, CZ) – 450 g, natural quartz sand with continuous granulometry I, II, III (the total screen residue on 1.6 mm 2%, on 1.0 mm 35%, on 0.50 mm 66%, on 0.16 mm 85%, on 0.08 mm 99.3%) - 1350 g, water – 225 g.

The composition of the high performance concrete (HPC) was as follows: Cement 42.5 R (Mokrá, CZ) - 499 kg/m^3, sand 0/4 size fraction - 705 kg/m^3, gravel sand 8/16 size fraction - 460 kg/m^3, gravel sand 16/22 size fraction - 527 kg/m^3, water - 215 kg/m^3, plasticizer - 4.5 l/m^3.

The samples of glass fiber reinforced cement composites denoted as GC I, GC II, GC III were plate materials with Portland cement matrix (cement CEM I 52.5 Mokrá), which was reinforced by alkali-resistant glass fibers (CEM-FIL 2 250/5B Tex 2450 30 mm for GC I, CEM-FIL 70/30 6 mm for GC II and GC III), the materials GC II and III contained vermiculite and wollastonite. The basic composition of GC I, II, III is shown in Table 2 (the percentage was calculated among the dry substances, water corresponding to the water to cement ratio of 0.8 was added to the mixture).

Table 2 Composition of glass fiber reinforced cement composites in %.

	Cement	Sand	Plasticizer	Glass fiber	Wollastonite	Vermiculite	Microsilica
GC I	47.99	47.99	0.62	3.40			
GC II	47.60		0.45	3.84	38.50	9.61	
GC III	56.88		0.92	7.66	8.68	21.51	4.35

The carbon fiber reinforced cement composite (denoted as CC) had the composition shown in Table 3 (again calculated among the dry substances only). Portland cement CEM I 52.5 Mokrá was used for CC, carbon fiber was pitch based with 10 mm length. Water in the amount corresponding to the w/c ratio of 0.8 was added to the mixture.

Table 3 Composition of carbon fiber reinforced cement composite in %.

Cement	Micro-dorsilite	Plasti-cizer	Carbon fiber	Wolla-stonite	Methyl-cellulose	Defoamer	Microsilica
39.71	16.50	0.98	0.98	39.6	0.11	0.16	1.96

EXPERIMENTAL DETAILS

Moisture diffusivity, thermal conductivity and specific heat capacity were chosen as hygric and thermal parameters most characteristic for the demonstration of the effect of high temperatures on cementitious composites after thermal load. The specimens were heated to either 600°C or 800°C in a furnace, left for two hours at the final temperature and then slowly cooled. The measurements were then done at room temperature on dry specimens.

Thermal conductivity λ and specific heat capacity c in room temperature conditions were determined using the commercial device ISOMET 2104 (Applied Precision, Ltd.). ISOMET 2104 is a multifunctional instrument for measuring thermal conductivity, thermal diffusivity, and volume heat capacity. It is equipped with various types of optional probes, needle probes are for porous, fibrous or soft materials, and surface probes are suitable for hard materials. The measurement is based on analysis of the temperature response of the analyzed material to heat flow impulses. The heat flow is induced by electrical heating using a resistor heater having a direct thermal contact with the surface of the sample.

Moisture diffusivity κ was determined using a simple gravimetric method [2] based on the common sorptivity experiment and the assumption that κ can be considered as piecewise constant with respect to the moisture content. Contrary to the most frequently used methods for κ determination, the method from [2] is very fast even for materials with low κ, and in addition it exhibits a reasonable precision. Therefore, its application for cement based materials is very suitable. The saturated moisture content by mass u_{max} was measured by the capillary saturation method. The specimen was dried at 110°C and weighed, then left for 24 hours in water, weighed again and its moisture content by mass calculated. Water vapor diffusion permeability δ was measured by the common dry cup method [3].

Specific heat capacity, thermal diffusivity and linear thermal expansion coefficient were measured in the temperature range up to 1000°C. As the adiabatic methods are not very suitable for measuring high-temperature specific heat capacity of building materials, mainly because of the necessity to use relatively large samples, a nonadiabatic method [4] was employed for the determination of temperature-dependent specific heat capacity. The measurements of high-temperature thermal diffusivity were done using the double integration method [5]. The thermal diffusivity was determined using the results of experimental measurements of temperature fields in the sample at one-sided heating in the solution of the inverse heat conduction problem. The measurements of linear thermal expansion coefficient were performed by the method described in [6]. This method consists in using a comparative treatment with a known material. A set of strain values corresponding to the given temperatures is determined and the linear thermal expansion coefficient calculated as the first derivative of the strain vs. temperature function with respect to temperature.

RESULTS AND DISCUSSION

Tables 4-9 show the thermal and hygric parameters of studied cement based composites after thermal load. The decrease of room temperature thermal conductivity after exposure to high temperatures that was observed for all materials (except for the high performance concrete where these measurements were not performed) is a consequence of decomposition processes in the Portland cement matrix described before. The decomposition of calcium hydroxide was apparently the most important process from this point of view because the decrease of thermal conductivity was faster between 25°C and 600°C than between 600°C and 800°C. The decrease of thermal conductivity after thermal load was much higher for cement mortar (about 4-5 times) than for fiber reinforced composites (less than 50% in all cases) although the density decrease was quite comparable. This is clearly a positive effect of fiber reinforcement that was able to keep the cement matrix together even after significant decomposition processes and prevent it from the formation of wide cracks, which play the most important role in the decrease of thermal conductivity. This effect was even more pronounced in the moisture diffusivity measurements. While 3 orders of magnitude increase of moisture diffusivity was observed for cement mortar after exposure to 800°C, for GC II, GC III and CC this increase was only about one order of magnitude. High performance concrete exhibited two orders of magnitude increase in moisture diffusivity which was comparable to GC I. The adhesion of fibers to the cement matrix was for GC I probably worse than for the other studied fiber reinforced composites. Water vapor permeability was affected by the high-temperature exposure in a less significant way then moisture diffusivity for all analyzed materials but the changes were important yet; δ increased up to three times compared to the reference specimens. The effect of fibers was not clearly distinguished in this case. The relative increase of water vapor permeability was similar for high performance concrete and fiber reinforced concretes. Apparently, these findings were related to the lower sensitivity of water vapor diffusion to large crack appearance compared to moisture diffusivity and thermal conductivity. While water vapor transport in porous media is more or less related to the volume of open pores, the liquid moisture transport is very sensitive to opening of preferential paths and thermal conductivity of porous materials is highly dependent on the topological characteristics of the porous space.

Table 4 Thermal and hygric parameters of cement mortar after thermal load

Temperature exposure [°C]	ρ_s [kg m^{-3}]	c [J kg^{-1} K^{-1}]	λ [W m^{-1} K^{-1}]	u_{max} [%]	κ [m^2 s^{-1}]	δ [s]
25	2130	850	1.16	8.0	9.70E-9	3.34E-12
800	2020	-	0.27	13.4	1.00E-5	4.03E-12

Table 5 Thermal and hygric parameters of high performance concrete after thermal load

Temperature exposure [°C]	ρ_s [kg m^{-3}]	c [J kg^{-1} K^{-1}]	λ [W m^{-1} K^{-1}]	u_{max} [%]	κ [m^2 s^{-1}]	δ [s]
25	2206	800	1.58	7.0	1.77E-8	3.07E-12
600	2172	-	-	8.8	8.53E-7	1.18E-11
800	2156	-	-	9.8	2.74E-6	-

Table 6 Thermal and hygric parameters of GC I after thermal load

Temperature exposure [°C]	ρ_s [kg m^{-3}]	c [J kg^{-1} K^{-1}]	λ [W m^{-1} K^{-1}]	u_{max} [%]	κ [m^2 s^{-1}]	δ [s]
25	1960	920	1.124	10.6	1.28E-09	4.09E-12
600	1865	920	0.706	15.6	9.57E-08	8.53E-12
800	1820	900	0.666	16.2	1.79E-07	1.35E-11

Table 7 Thermal and hygric parameters of GC II after thermal load

Temperature exposure [°C]	ρ_s [kg m^{-3}]	c [J kg^{-1} K^{-1}]	λ [W m^{-1} K^{-1}]	u_{max} [%]	κ [m^2 s^{-1}]
25	1090	1090	0.275	47.5	2.52E-08
600	1030	1050	0.198	56.8	1.27E-07
800	990	960	0.160	56.8	3.18E-07

Table 8 Thermal and hygric parameters of GC III after thermal load

Temperature exposure [°C]	ρ_s [kg m^{-3}]	c [J kg^{-1} K^{-1}]	λ [W m^{-1} K^{-1}]	u_{max} [%]	κ [m^2 s^{-1}]
25	970	1285	0.274	58.1	3.36E-08
600	900	947	0.198	68.4	1.92E-07
800	900	837	0.159	68.4	3.36E-07

Table 9 Thermal and hygric parameters of CC after thermal load

Temperature exposure [°C]	ρ_s [kg m^{-3}]	c [J kg^{-1} K^{-1}]	λ [W m^{-1} K^{-1}]	u_{max} [%]	κ [m^2 s^{-1}]	δ [s]
25	1610	1020	0.511	25	5.63E-09	1.71E-11
600	1480	930	0.382	28	2.08E-08	2.49E-11
800	1430	870	0.366	28.5	7.67E-08	4.01E-11

The results of specific heat capacity measurements are shown in Fig. 4. Two basic types of *c(T)* functional relationships could be identified. The first was characteristic for cement mortar, high performance concrete and GC I. Here *c(T)* was an increasing function up to about 600°C, and then it began to decrease. For GC II, GC III and CC *c(T)* was a decreasing function in the whole studied temperature range.

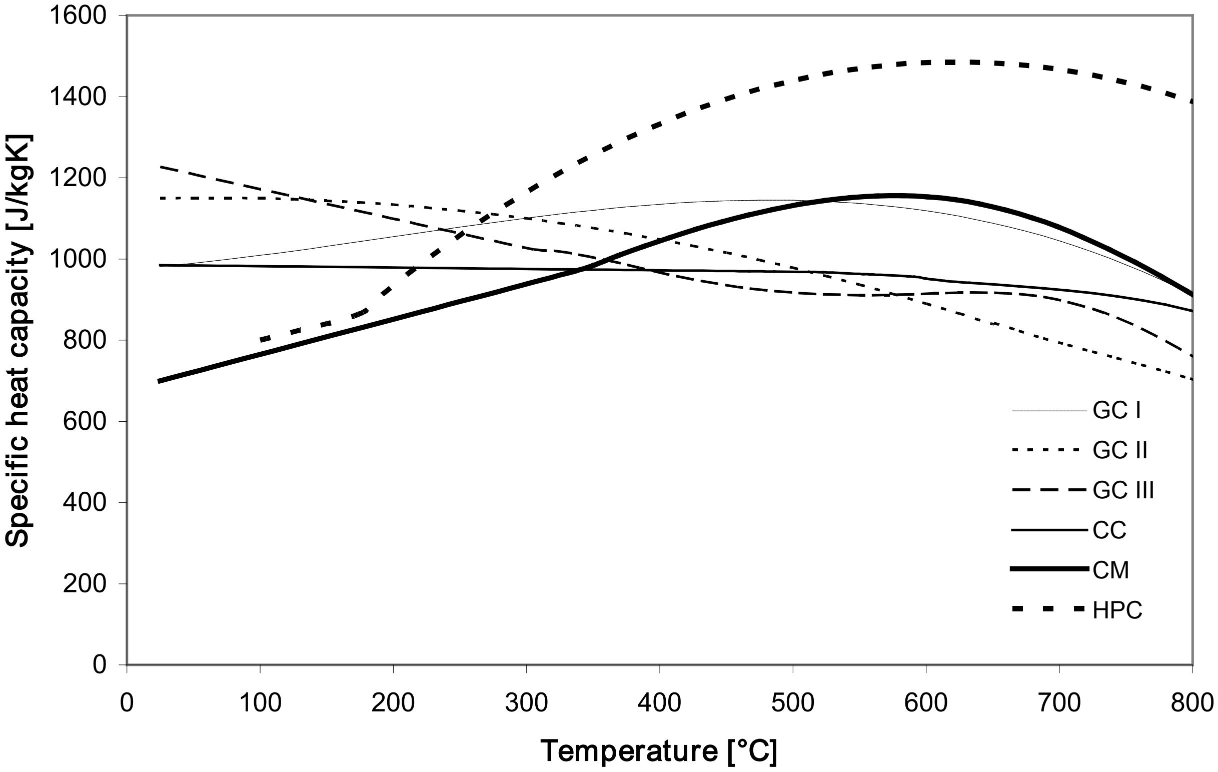

Figure 4 Specific heat capacity of cement based composites

The relatively fast increase of specific heat capacity of cement mortar in the temperature range of 25-600°C can be attributed probably to the effect of siliceous aggregates. Silicon dioxide has at 25°C the specific heat capacity of 730 J/kgK while at 575°C it is 1380 J/kgK [7]. This is in basic accordance with our results because the cement to sand ratio for the cement mortar was 1:3, for high performance concrete 1:3.4, so that the effect of aggregates on the specific heat capacity (which is an additive quantity in the sense of the theory of mixtures) was very pronounced. Similarly we can explain the decrease of the specific heat capacity of cement mortar above 600°C. Silicon dioxide undergoes at 573°C the $\alpha \rightarrow \beta$ transition [7], and the newly formed β form has the specific heat capacity of only 1125 J/kgK [7].

Similar effects to those of cement mortar and high performance concrete could be observed on GC I which had similar composition except for the cement to sand ratio that is 1:1. This might be the reason of the slower increase of the *c(T)* function in the temperature range of 25-600°C.

As for the remaining materials, their *c(T)* function behavior could not be explained even in a similar rough and simple way like with cement mortar and GC I because of the lack of reliable data for the specific heat capacities of their particular compounds. Another factor making any statement in this sense even more complicated were the chemical reactions in cement gel after heating that resulted in fact in a determination of specific heat capacity for a set of different materials.

The specific heat capacity of the studied cementitious composites exhibited various temperature dependences for different materials. The increasing character of the *c(T)* functions that is typical for most crystalline solids [7] was observed for the materials with siliceous aggregates, and only up to 600°C. For the other materials the specific heat capacity decreased with temperature. Although this type of *c(T)* function is not very common, it might be explained in general by the complicity of the studied systems where quite a few chemical reactions and phase transitions occur after the temperature increase.

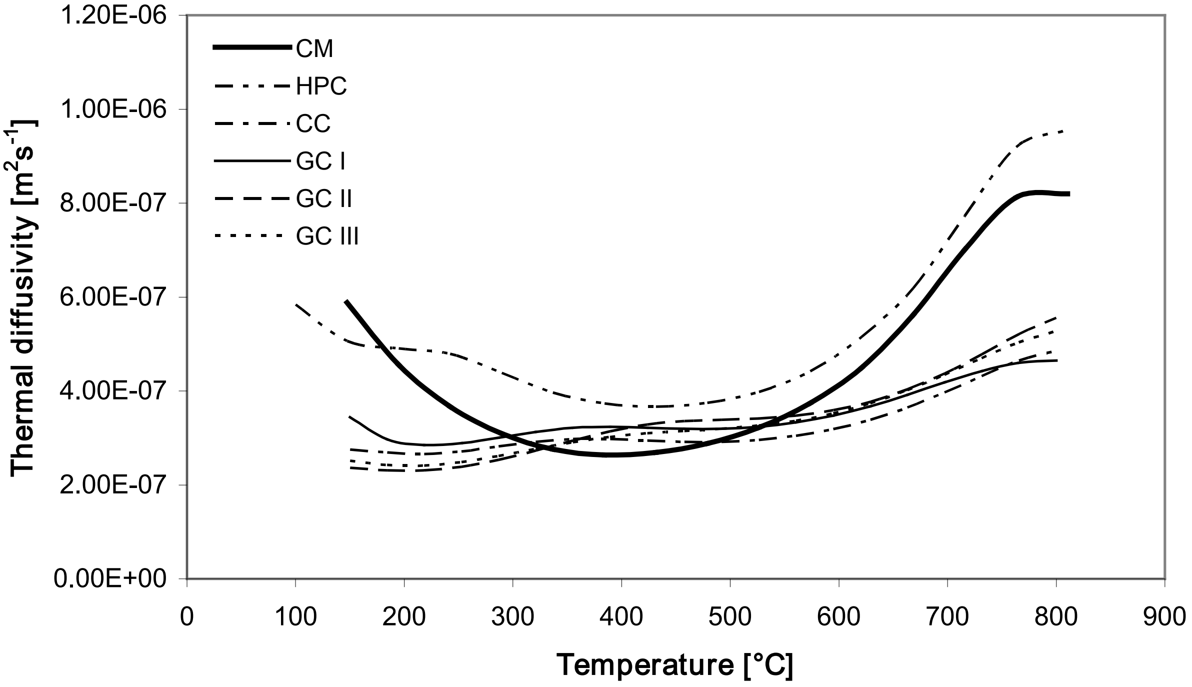

Figure 5 Thermal diffusivity of cement based composites

Fig. 5 shows the results of high-temperature thermal diffusivity measurements. The highest values of thermal diffusivity were achieved in the whole temperature range by high-performance concrete, which is an expected result because it has the highest bulk density (see Tables 4-9). The lighter fiber reinforced composites had significantly lower thermal diffusivity, down to about one half of the values of HPC. The thermal diffusivity of cement mortar was somewhere between these two limits. The character of thermal diffusivity dependence of fiber reinforced composites was different than for HPC and cement mortar without any reinforcement. While the thermal diffusivity of fiber reinforced composites increased in the whole range of temperatures, the thermal diffusivity of HPC and cement mortar first decreased and from 400°C it began to increase. The slower increase of thermal diffusivity of fiber reinforced composites in the range of highest temperatures compared to the cement based materials without any reinforcement can clearly be attributed to the positive effect of the fiber reinforcement that was in certain range able to prevent from opening wide cracks magnifying the convective mode of heat transfer. It should also be noted that the thermal diffusivity of GC I was only slightly higher than of other fiber reinforced cement composites (a higher difference was in the range of lower temperatures up to 400°C) although its density was significantly higher. So, the effect of fiber reinforcement was in the highest temperature range similar for both heavier and lighter fiber reinforced composites. This may be related to the worse mechanical properties of the cement matrix of lighter composites.

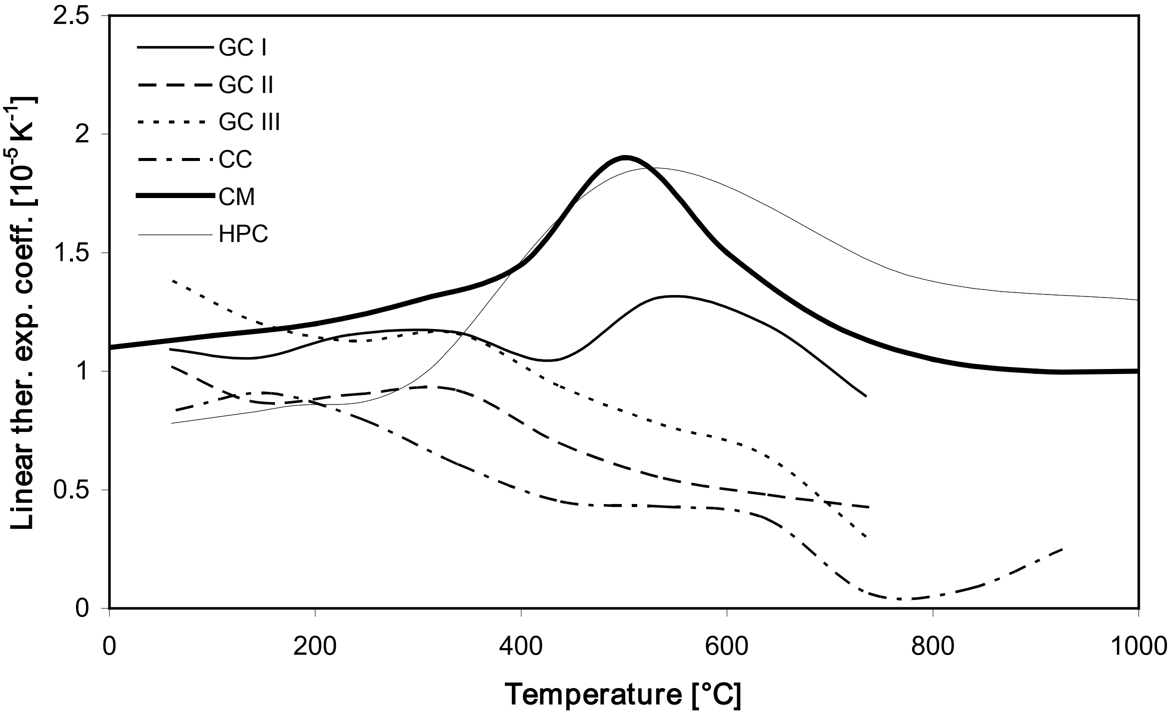

Figure 6 Linear thermal expansion coefficient of cement based composites

The results of measurements of the linear thermal expansion coefficient in the high temperature range (Fig. 6) exhibit once again the positive effect of fiber reinforcement. The linear thermal expansion coefficient of cement mortar and high performance concrete was significantly higher compared to the fiber reinforced composites and markedly increased with temperature up to about 500-600°C. For GC II, GC III and CC the linear thermal expansion coefficient even decreased with temperature in almost whole the temperature range studied. Apparently, the fibers were for these composites able to prevent the matrix from an excessive volume increase due to their good adhesion – contrary to GC I where the linear thermal expansion coefficient was almost constant up to about 600°C. The decrease of linear thermal expansion coefficients in the highest temperature range for most materials is clearly related to the decomposition processes in the cement matrix, where the main role play the decomposition of calcium hydroxide at 460°C and calcium carbonate in the temperature range between 700-800°C.

CONCLUSIONS

Three main factors were shown to affect the hygric and thermal properties of cementitious building materials exposed to high temperatures. The first was the decomposition processes in the cement binder and was clearly negative. The worsening of hygric properties after high-temperature exposure induced by the increase in open porosity and wide crack opening can have fatal consequences for durability of a cement-based material. Presence of fibers as the second factor had in all cases positive consequences; they could partially keep the cement matrix together even after significant decomposition of cement hydration products. However, their positive effects were limited to the moment when glass fibers were melted and carbon fibers exposed to the oxygen from the air after crack opening. The third factor was the composition of the composite. Using vermiculite instead of sand aggregates was clearly positive because of its porous character.

Wollastonite was better choice than sand because of its fibrous character that could partially magnify the effect of fiber reinforcement.

The problem of significant changes in hygric and thermal properties of cementitious composites induced by high temperatures can be regarded with another horizon yet. These changes can serve as sensitive indicators of damage which may not seem apparent in some cases. In particular, the water transport properties may be considered as reliable tool in that respect. Moisture diffusivity is subject of substantial increase if any preferential paths for the transport of liquid water appear; these can be formed even by very small cracks.

ACKNOWLEDGEMENT

This research has been supported by the Czech Science Foundation, under project No 103/06/1474.

REFERENCES

[1] Taylor, H.F.W., Cement Chemistry, Academic Press, London 1992.

[2] Černý, R., Drchalová, J., A Simple Gravimetric Method for Determining the Moisture Diffusivity of Building Materials. Constr. Build. Mat., vol. 17, 2003, pp. 223-228.

[3] Roels, S., Carmeliet, J., Hens, H., Adan, O., Brocken, H., Černý, R., Pavlík, Z., Hall, C., Kumaran, K., Pel, L., Plagge, R., Interlaboratory Comparison of Hygric Properties of Porous Building Materials. J. Therm. Envel. Build. Sci., vol. 27, 2004, pp. 307-325.

[4] Toman J., Černý R., Calorimetry of Building Materials. Journal of Thermal Analysis, vol. 43, 1995, pp. 489-496.

[5] Černý, R., Toman, J., Determination of Temperature- and Moisture-Dependent Thermal Conductivity by Solving the Inverse Problem of Heat Conduction. Proc. of International Symposium on Moisture Problems in Building Walls, V.P. de Freitas, V. Abrantes (eds.), pp. 299-308. Univ. of Porto, Porto 1995.

[6] Toman, J., Koudelová, P., Černý, R., A measuring method for the determination of linear thermal expansion of porous materials at high temperatures. High Temperatures-High Pressures, vol. 31, 1999, pp. 595-600.

[7] CRC Handbook of Chemistry and Physics, edited by D.R. Lide. 72nd Edition, CRC Press, Boca Raton, 1991, pp. 4-83, 5-84.

TEMPERATURE FIELD IN A SOLID BODY RESTRICTED BY TWO PARALEL PLANAR SURFACES

František Čulík, Ivan Baník, Jozefa Lukovičová

Abstract

We present the solution of 1D - heat conduction equation using Laplace transformation for a solid body restricted by two parallel planar surfaces which temperatures are constants. Comparison of that solution with measured values of temperature somewhere inside the solid body permits to determine thermal parameters (like diffusivity a, thermal conductivity λ, specific heat c) of the solid. The formula $a = l^2 \theta_c / t_c$ determining diffusivity is derived.

Key words

Isothermal border plane. Temperature field. Determination of thermal parameters.

1. Introduction

Fig. 1 shows a sample the coordinate system and initial and final distribution of the temperature.

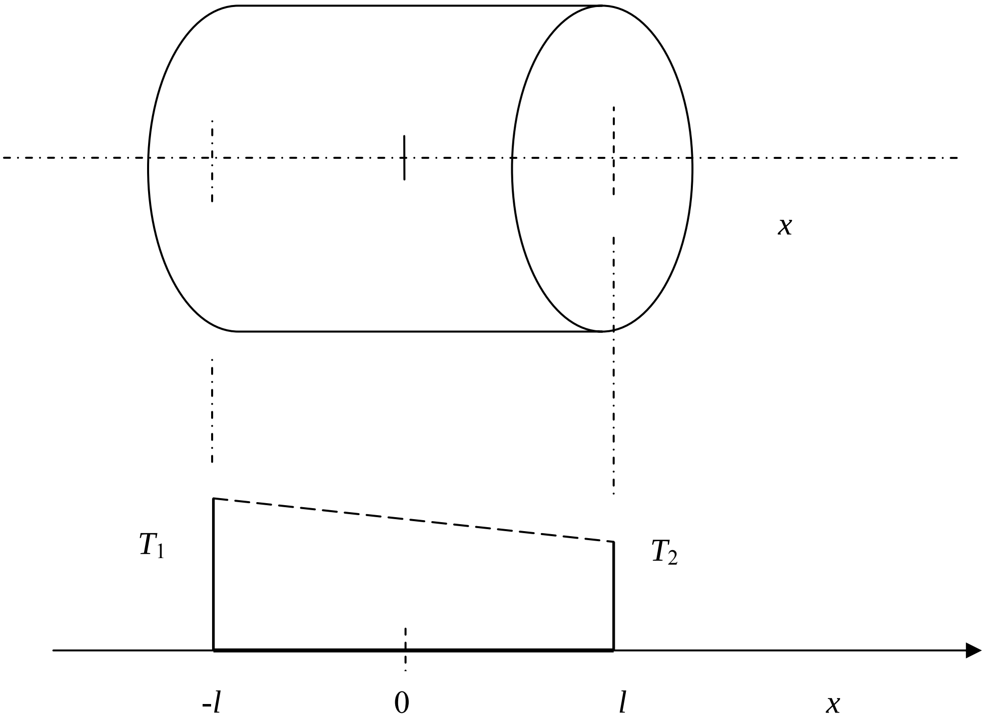

Fig. 1

It is assumed that the temperature at the border surfaces is constant and initial temperature inside a body is zero. After switching on the temperature in time interval $t > 0$ at the border plane $x = -l$ is constant and equals to T_1 as well as at the second border plane $x = l$ where the constant temperature is equal to T_2. In words of mathematics:

$$T\left(x = -l, t\right) = T_1 \qquad t > 0 \tag{1.1}$$

$$T\left(x = l, t\right) = T_2 \qquad t > 0 \tag{1.2}$$

$$T\left(x, t = 0\right) = 0 \qquad -l < x < l, \quad t = 0 \tag{1.3}$$

We are searching for solution $T\left(x,t\right)$ of 1D - heat conduction equation

$$\frac{\partial T}{\partial t} - a\frac{\partial^2 T}{\partial x^2} = 0, \tag{1.4}$$

assuming it obeys boundary (1.1), (1.2) and initial (1.3) conditions. Here $a = \lambda / c\rho$, and ρ is the density of a body.

2. Method of solution

After sufficiently long period of time one can expect that the temperature field inside a body becomes stationary (if $T_1 \neq T_2$). Then

$$\frac{\partial \tau}{\partial t} = 0. \quad \text{In this state} \qquad \frac{d^2\tau}{dx^2} = 0 \tag{2.1}$$

Solution of this equation obeying boundary conditions is

$$\tau\left(x\right) = \frac{T_1\left(l - x\right) + T_2\left(l + x\right)}{2l} \tag{2.2}$$

Solution of non-stationary heat conduction equation we write down as a sum of two functions

$$T\left(x,t\right) = \Theta\left(x,t\right) + \tau\left(x\right) \tag{2.3}$$

Then the boundary conditions for the function.

$$\Theta\left(x,t\right) = T\left(x,t\right) - \tau\left(x\right) \quad \text{are:} \tag{2.4}$$

$$\Theta\left(x = -l, t\right) = T\left(x = -l, t\right) - \tau\left(x = -l\right) = T_1 - T_1 = 0 \tag{2.5}$$

$$\Theta\left(x = l, t\right) = T\left(x = l, t\right) - \tau\left(x = l\right) = T_2 - T_2 = 0 \tag{2.6}$$

and the function Θ fulfils the initial condition

$$\Theta\left(x,t=0\right)=T\left(x,t=0\right)-\tau\left(x\right)=-\tau\left(x\right) \tag{2.7}$$

It is easily to show that the Θ function is also a solution of the heat conduction equation

$$\frac{\partial\Theta}{\partial t}-a\frac{\partial^2\Theta}{\partial x^2}=0 \tag{2.8}$$

(see Appendix).
We have obtained the solution given by the formula (A.16a) in Appendix. Using that solution and introducing new dimensionless variables: time $\theta=\frac{at}{l^2}$ - (this variable gives the time value t in the new time unit characteristic for a given sample - namely $\left[l^2/a\right]$) - and the space coordinate $\xi=\frac{x}{l}$, $-1<\xi<1$. Then considering (A.16a) relative temperature can be expressed as follows

$$\frac{T\left(\xi,t\right)}{\tau\left(\xi\right)}=\frac{1}{\tau\left(\xi\right)}\sum_{n=0}^{\infty}\left(\text{-}1\right)^n\left[T_1\text{erfc}\left(\frac{\left(2n+1\right)+\xi}{2\sqrt{\theta}}\right)+T_2\text{erfc}\left(\frac{\left(2n+1\right)-\xi}{2\sqrt{\theta}}\right)\right]+$$

$$\frac{\left(T_1-T_2\right)}{\tau\left(\xi\right)}\sum_{n=0}^{\infty}\left[\text{erfc}\left(\frac{\left(4n+3\right)+\varsigma}{2\sqrt{\theta}}\right)-\text{erfc}\left(\frac{\left(4n+3\right)-\xi}{2\sqrt{\theta}}\right)\right] \tag{2.9}$$

where

$$\tau\left(\xi\right)=\frac{1}{2}\left(T_1\left(1-\xi\right)+T_2\left(1+\xi\right)\right)\quad\text{is the local (at point } \xi \text{) steady temperature} \tag{2.10}$$

One can draw 3D graph of this relative temperature function in good approximation accounting few first terms from infinite series.
The relation (2.9) shows that one of the simplest cases occurs when temperature at both border planes is the same $T_1=T_2$ and one measures the time development of temperature in the middle of the specimen at $x=0$. In this case dimensionless temperature is

$$\frac{T\left(\xi=0,\theta\right)}{T_1}=2\sum_{n=0}^{\infty}\left(\text{-}1\right)^n\,\text{erfc}\left(\frac{\left(2n+1\right)}{2\sqrt{\theta}}\right) \tag{2.11}$$

In our approach influence of thermal contact at the border plane is neglected and strictly speaking a heat flow exists along x - axis only. Approximately, this flow prevails so that the heat losses trough cylinder jacket (of a cylindrical sample) during time of measurement temperature is negligible.

3. Universal theoretical temperature dependence on dimensionless time

Now, we want to use the local time development of temperature mentioned above to measure diffusivity a of a solid body and measurement to execute in relative short period of time.[1]
If one restricts himself by the first six terms of the series in (3.2) [2]

$$\frac{T(\xi=0,\theta)}{T_1} = 2\sum_{n=0}^{\infty}(-1)^n \operatorname{erfc}\left(\frac{(2n+1)}{2\sqrt{\theta}}\right) \doteq$$
$$f(\theta) = 2\operatorname{erfc}\left(\frac{0.5}{\sqrt{\theta}}\right) - 2\operatorname{erfc}\left(\frac{1.5}{\sqrt{\theta}}\right) + 2\operatorname{erfc}\left(\frac{2.5}{\sqrt{\theta}}\right) - 2\operatorname{erfc}\left(\frac{3.5}{\sqrt{\theta}}\right) + 2\operatorname{erfc}\left(\frac{4.5}{\sqrt{\theta}}\right) - 2\operatorname{erfc}\left(\frac{5.5}{\sqrt{\theta}}\right) \tag{3.1}$$

and draws a graph of $f(\theta)$ function (in program Mathematica 4) then can see that it rises relatively steep in an interval $0 < \theta < 2.5$ and approaches close to the equilibrium value of the temperature T_1. This curve does not depend either on dimension of the sample or on diffusivity *a*.

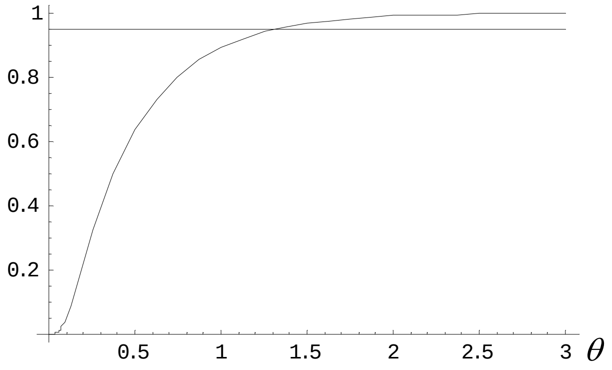

Fig. 2

The dimensionless time variable was introduced as $\theta = at/l^2$. It was already said that quantity l^2/a can be taken for a proper "unit of the tine" of the particular sample. If we would dispose a sample for which this quantity would be $l^2/a = 1$ then θ would be equal to *t*, $\theta = t$.

That quantity l^2/a is characteristic for transition of the particular sample into the equilibrium state with temperature T_1. The order of l^2/a is approximately equal to "the time of transition" $t_r \sim l^2/a$.

---

[1] One can examine behavior of derivative log *T* with respect to diffusivity *a* (like in [3]) which characterizes sensibility of temperature to a change of diffusivity.

[2] Behavior of a member of this infinite series is discussed in [1] and [2].

The temperature T is less then or equal to T_1. If we choose the value of $T\left(\theta\right)$ then the ratio

$$\frac{T\left(\theta\right)}{T_1} \doteq f\left(\theta\right) \tag{3.2}$$

is known.

The eq. (3.2) determines coordinate θ_c of the intersection point which coordinates are

$$\left[\theta_c,\ \frac{T}{T_1}\right] \qquad \text{(see Fig.2)} \tag{3.3}$$

For example coordinates of the intersection point of that line $T/T_1 = 0.95$ with the curve (3.1) are $\left[\theta_c, T/T_1\right] = \left[\ 1.314,\ 0.95\right]$. It holds

$$\theta_c = \frac{a}{l^2}t = \frac{\lambda}{c\rho l^2}t \tag{3.4}$$

In the relation (3.4) the values of θ_c and l are known but the diffusivity a and corresponding time t are unknown. So we need to have one more formula connecting these four quantities. It follows; we shall be searching for this formula.

4. Determination of diffusivity using experimental local time development of temperature

Let us assume that temperature dependence on time t at $x = 0$ is known from experiment

$$\frac{T\left(x=0,t\right)}{T_1} = f_{\text{exp}}\left(t\right) \tag{4.1}$$

Parameters a and l do not appear in the function $f_{\text{exp}}\left(t\right)$ explicitly. If this experimental curve will coincide nearly with theoretical (3.1) (after substitution $\theta = at/l^2$ in it), in an interval of time <0, t_m> then one can find from experiment the value t_c and using the formula (3.4) calculate the diffusivity a (or thermal conductivity λ assuming $\rho c l^2$ is known). Then - with respect to (3.4) – it holds

$$a = l^2 \frac{\theta_r}{t_r} \tag{4.2}$$

From Vretenar`s measurement [3] on SiC sample which length was $2l$ = 2.84 mm, we take values of $a = 21.2\times10^{-6}\,\text{m}^2 s^{-1}$ and thermal conductivity $\lambda = ac\rho = 46.187$ Wm^{-1}K^{-1} (where the values $\rho = 3242$ kg.m^{-3} and $c = 672$ J.m^{-1}.K^{-1} were accounted). We do not dispose of this experimental curve $f_{\text{exp}}\left(t\right)$. Nevertheless; we try to show that above presented method of determination diffusivity really works in this case.

Using some of these data we are going *to test* our approach to determine *a*. We put again $T/T_1 = f_{\exp}(t) = 0.95$. Then that eq. determines the time coordinate t_c.

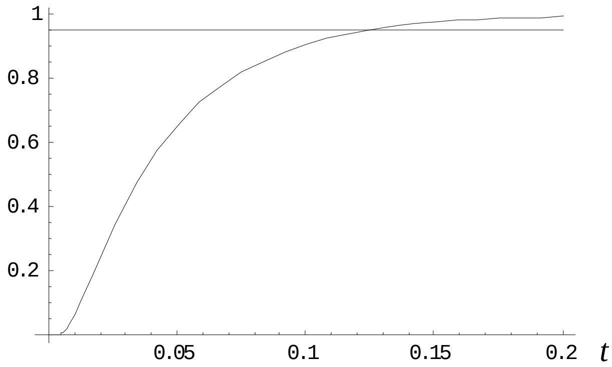

Fig.3

Fig. 4 depicts dependence of $T(x=0,t)/T_1$ given by (3.1) on the time (in seconds). This curve we have obtained by inserting $\theta = \frac{at}{l^2} = \frac{21.2}{1.42^2}t$ in (3.1). That curve supplies experimental one $f_{\exp}(t)$. We are looking for such value of the time *t* for which value of "experimental function" is equal to 0.95 and that value equals to $t_c = 0.125\ \mathrm{s}$. (It is very short time to gain experimental data needed for determination of temperature development in time.). Then we have obtained the value of diffusivity

$$a = l^2 \frac{\theta_r}{t_r} = (1.42)^2 \times 10^{-6} \frac{1.314}{0.125}\ \mathrm{m^2 s^{-1}} = 21.196 \times 10^{-6}\,\mathrm{m^2 s^{-1}}$$

This is in excellent agreement with Vretenar`s result
It seems to us that more suitable should be a longer sample. For ten times longer sample 2.84 cm the time t_c should be hundred times bigger. In such a case it would be 12.5 s.

Now, we shall discuss shortly the case when $T_2 = 0$ and $\xi = 0$ then

$$\frac{T(\xi=0,\theta)}{\tau(\xi=0)} = \frac{T(\xi=0,\theta)}{T_1/2} = 2\sum_{n=0}^{\infty}(-1)^n \operatorname{erfc}\left(\frac{(2n+1)}{2\sqrt{\theta}}\right) \tag{5.3}$$

This formula shows that temperature approaches its stationary (maximal) value $T_1/2$ in the plane at $x=0$ in the same time interval as before (in the case when T_1 was equal to T_2). But at that time the maximal value at $x=0$ was T_1 - twice as big as now.)

The more detailed analysis of the temperature field given by (2.9) offers further possibilities for determining thermal parameters (see [3]).

5. Conclusions

It is assumed that the time development of the temperature at the center plane at $x = 0$ of a specimen is measured and consequently known. Then it is possible to draw a graph of temperature dependency on the time $T\left(x=0,t\right)=T_1 f_{\exp}\left(t\right)$ in a short time interval $\left\langle 0,t_m\right\rangle$ (t_m represents a few ten seconds). t_c represents the time lying in an interval $\left\langle 0,t_m\right\rangle$.

On the other hand the theoretical time dependence of the temperature is given by (3.1) (in the same time interval). Then it is possible to find the value of θ_c at which $T/T_1 = f\left(\theta_c\right) = f_{\exp}\left(t_c\right)$ holds. The diffusivity value of the sample is expressed by the relation (4.2). We expect that by insertion this value of a as well as l in theoretical temperature dependence (3.1) on time t it will coincide with experimental dependence $f_{\exp}\left(t\right)$.

APPENDIX

Indeed $\dfrac{\partial\left(\Theta+\tau\right)}{\partial t}-a\dfrac{\partial^2\left(\Theta+\tau\right)}{\partial x^2}=0$, and $\dfrac{\partial\tau}{\partial t}=\dfrac{\partial^2\tau}{\partial x^2}=0$

Laplace transformation of the Θ function $\vartheta\left(x,s\right)=L\left[\Theta\left(x,t\right)\right]$ fulfils the eq.

$$L\left\{\frac{\partial\Theta}{\partial t}\right\}-a\frac{\partial^2 L\{\Theta\}}{\partial x^2}=s\vartheta-\left(-\tau\left(x\right)\right)-a\frac{\partial^2\vartheta}{\partial x^2}=0$$

This is ordinary nonhomogeneous differential eq. of second order

$$\frac{d^2\vartheta}{dx^2}-\frac{s}{a}\vartheta=\frac{\tau\left(x\right)}{a} \qquad \text{(A.1)}$$

Further we shall denote $\sqrt{s/a}=k$. Then, the general solution of this eq. is equal to the sum of the general solution

$$\vartheta_0 = A_0\exp\left(kx\right)+B_0\exp\left(-kx\right) \qquad \text{(A.2)}$$

of the corresponding homogeneous eq. $\vartheta''-k^2\vartheta=0$ and of some particular solution $\tilde{\vartheta}$ of the nonhomogeneous eq. $\tilde{\vartheta}''-k^2\tilde{\vartheta}=\tau/a$.

To find particular solution $\tilde{\vartheta}$ the method of variation of parameters A, *B* was used

$$\tilde{\vartheta}=A\left(x\right)\exp\left(kx\right)+B\left(x\right)\exp\left(-kx\right) \qquad \text{(A.3)}$$

This leads to expressions

$$A(x) = -\frac{1}{2ak^3}\exp(-kx)\left(k\tau + \frac{T_2 - T_1}{2l}\right)$$

$$B(x) = -\frac{1}{2ak^3}\exp(kx)\left(\left(k\tau - \frac{T_2 - T_1}{2l}\right)\right)$$

Then

$$\tilde{\vartheta} = -\frac{\tau(x)}{ak^2} \tag{A.4}$$

We have obtained the general solution of the nonhomogeneous eq. in form

$$\vartheta(x,s) = A_0 \exp(kx) + B_0 \exp(-kx) - \frac{T_1(l-x) + T_2(l+x)}{2alk^2}, \quad k = \sqrt{s/a} \tag{A.5}$$

This solution should satisfy transformed boundary conditions

$$\vartheta(x = -l, s) = 0 \tag{A.6}$$

$$\vartheta(x = l, s) = 0 \tag{A.7}$$

Thus, we obtain two eqs. for determination A_0, B_0

$$A_0 \exp(-kl) + B_0 \exp(kl) - \frac{T_1}{ak^2} = 0 \tag{A.8}$$

$$A_0 \exp(kl) + B_0 \exp(-kl) - \frac{T_2}{ak^2} = 0 \tag{A.9}$$

witch solution is

$$A_0 = \frac{\exp(-3kl)\left[T_2 \exp(2kl) - T_1\right]}{ak^2\left[1 - \exp(-4kl)\right]}, \tag{A.10}$$

$$B_0 = \frac{\exp(-3kl)\left[T_1 \exp(2kl) - T_2\right]}{ak^2\left[1 - \exp(-4kl)\right]} \tag{A.11}$$

Thus, the transformed solution satisfying transformed boundary conditions is

$$\vartheta(x,s) = A_0 \exp(kx) + B_0 \exp(-kx) - \left[T_1(l-x) + T_2(l+x)\right]\big/2alk^2 =$$

$$\frac{\left[T_2 - T_1 \exp(-2kl)\right]\exp\left(-k(l-x)\right) + \left[T_1 - T_2 \exp(2kl)\right]\exp\left(-k(l+x)\right)}{ak^2\left[1 - \exp(-4kl)\right]}$$

$$-\left[T_1(l-x) + T_2(l+x)\right]\big/2alk^2 \tag{A.12}$$

Using the expansion

$$\frac{1}{\left[1-\exp\left(-4kl\right)\right]}=\sum_{0}^{\infty}\exp\left(-4nkl\right)\quad \text{valid for } 1>\exp\left(-4kl\right) \tag{A.13}$$

We can rewrite $\vartheta\left(x,s\right)$ as

$$\begin{aligned}\vartheta\left(x,s\right)=&\frac{1}{s}\sum_{0}^{\infty}\left[T_2\exp\left(-\left(4nl+l-x\right)\right)\sqrt{s/a}-T_1\exp\left(-\left(4nl+3l-x\right)\right)\sqrt{s/a}\right]+\\ &\frac{1}{s}\sum_{0}^{\infty}\left[T_1\exp\left(-\left(4nl+l+x\right)\right)\sqrt{s/a}-T_2\exp\left(-\left(4nl+3l+x\right)\right)\sqrt{s/a}\right]-\\ &\frac{1}{2ls}\left[T_1\left(l-x\right)+T_2\left(l+x\right)\right],\end{aligned} \tag{A.14}$$

One can obtain the inverse Laplace transformation using following formulae $L^{-1}\left[\vartheta\right]=\Theta\left(x,t\right)$

$$L^{-1}\left[\frac{\exp\left(-u\sqrt{s/a}\right)}{s}\right]=\text{erfc}\left(\frac{u}{2\sqrt{at}}\right),\quad \text{holding for}\quad \kappa=\frac{u}{\sqrt{a}}\geq 0 \tag{A.15}$$

(see [1]) and

$$L^{-1}\left[\frac{1}{s}\right]=1,\quad L^{-1}\left[\frac{1}{2ls}\left[T_1\left(l-x\right)+T_2\left(l+x\right)\right]\right]=\frac{1}{2l}\left[T_1\left(l-x\right)+T_2\left(l+x\right)\right]=\tau\left(x\right)$$

it follows

$$\begin{aligned}T\left(x,t\right)=&\sum_{0}^{\infty}\left[T_1\text{erfc}\left(\frac{\left(4n+1\right)l+x}{2\sqrt{at}}\right)+T_2\text{erfc}\left(\frac{\left(4n+1\right)l-x}{2\sqrt{at}}\right)\right]\\ &-\sum_{0}^{\infty}\left[T_1\text{erfc}\left(\frac{\left(4n+3\right)l-x}{2\sqrt{at}}\right)+T_2\text{erfc}\left(\frac{\left(4n+3\right)l+x}{2\sqrt{at}}\right)\right]\end{aligned} \tag{A.16}$$

One can see that by the function $T\left(x,t\right)$ the boundary conditions as well as the initial condition are both fulfilled.

The last expression can be rewritten into the form

$$T\left(x,t\right)=\sum_{n=0}^{\infty}(-1)^{n}\left[T_1\text{erfc}\left(\frac{\left(2n+1\right)l+x}{2\sqrt{at}}\right)+T_2\text{erfc}\left(\frac{\left(2n+1\right)l-x}{2\sqrt{at}}\right)\right]+$$

$$\left(T_1-T_2\right)\sum_{n=0}^{\infty}\left[\operatorname{erfc}\left(\frac{(4n+3)l+x}{2\sqrt{at}}\right)-\operatorname{erfc}\left(\frac{(4n+3)l-x}{2\sqrt{at}}\right)\right] \qquad \text{(A.16a)}$$

Notice

In [2] p.101, formula (3.9) is introduced (without derivations) which gives the temperature distribution in a slab $-l < x < l$ with constant initial temperature $V_0 \neq 0$ and temperature at border planes maintain zero (Fig. 4)

$$v=V_0-V_0\sum_{n=0}^{\infty}(-1)^n\left[\operatorname{erfc}\left(\frac{(2n+1)l-x}{2\sqrt{at}}\right)+\operatorname{erfc}\left(\frac{(2n+1)l+x}{2\sqrt{at}}\right)\right] \qquad \text{[2] p.101, f (3.9)}$$

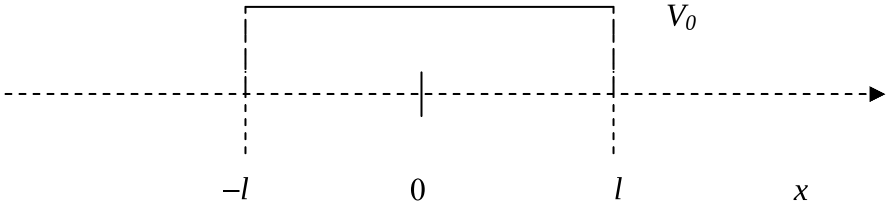

Fig. 4

We show that this is one special case of our formula derived above when $T_1 = T_2$.
If we change V_0 for $\rightarrow -T_1 < 0$ we obtain initial temperature well instead of initial temperature barrier and then we shift the zero temperature down at $-T_1$ we finally obtain

$$T(x,t)=v+T_1=T_1\sum_{n=0}^{\infty}(-1)^n\left[\operatorname{erfc}\left(\frac{(2n+1)l-x}{2\sqrt{at}}\right)+\operatorname{erfc}\left(\frac{(2n+1)l+x}{2\sqrt{at}}\right)\right] \qquad \text{(A.17)}$$

References

[1] Lykov A.V., Teorija teploprovodnosti p.. 585, formula 50 – in Russian (Heat conduction theory))
[2] Carslaw H. S., Jaeger J. C.: Conduction of Heat in Solids, 2nd ed, Oxford University Press, reprinted 1980
[3] Vretenár V.: Extended version of Pulse transient method, Proceedings of Thermo physics, 2005, Contents, pp. 92-103, October 2005, Meeting of the Thermo physical Society.

HYDRATION OF PORTLAND CEMENT PASTE

Pavel Demo[1,2], Petra Tichá[1,2], Petr Semerák[1] and Alexej Sveshnikov[1,2]

1Czech Technical University in Prague, Faculty of Civil Engineering, Thákurova 7, 166 29 Praha 6, Czech Republic
2Institute of Physics, Academy of Sciences of the Czech Republic, Cukrovarnická 10, 162 53 Praha 6, Czech Republic

Abstrakt:
During hydration and hardening, the concrete is gaining mechanical strength, resistibility and chemical stability, while physical and chemical reactions are in progress. Workability of concrete belongs to the crucial parameters. Concrete should be workable, but not segregate or bleed excessively. Knowledge of the rate of reaction between cementing materials and water (hydration) is important to determine setting time and hardening. An electrical measurement technique has been used to measure the electrical resistivity of cement paste at various temperatures. The different hydration periods were identified from the electrical resistivity curve, where inflex points mark the beginning and the end of a certain period.

INTRODUCTION

Application of cement-based materials is extremely wide, ranging from stomatology to civil engineering. Incubation time represents one of major parts of the so-called workability corresponding to a time when hardening cement-based materials is formable and transportable to required locations. Recent effort is oriented to prolongation of the incubation time (and, thus, also of the workability) in terms of various types of additives retarding process of hardening. The study of early stages of hardening of cement-based materials may give a clue.

As a typical example, an indispensable material in civil engineering - Portland cement - can be considered. Portland cement is the most used and best known type of cement, it is a mixture of calcium silicates (mainly tricalciumsilicates → 3CaO.SiO2 →C3S). If water is added to the cement, the process of silicate hydration is triggered and the products are calcium-silicate-hydrate gel (the so called CSH gel) and dihydroxide calcite are produced.

The process of hydration (see Fig. 1) starts with the addition of water. In the very beginning liquid and cement grains are present, shortly after addition of water the so-called chemical stage is in process. Ions from Portland cement are released into the solution and the coating gel appears around the grains.

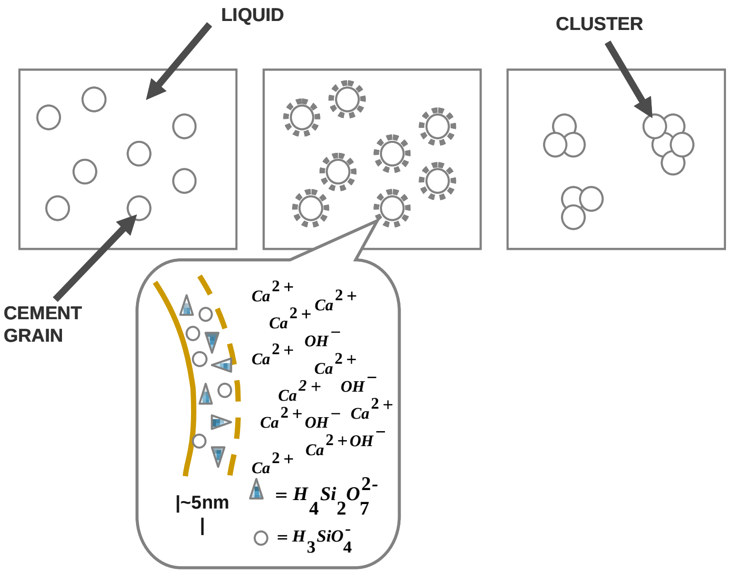

Figure 1.
Hydration of Portland cement.

Next stage is the so-called induction period, the value of pH is increasing steadily and the concentration of calcium ions together with CSH gel on the surface of grains is responsible for decrease in the solubility of phases of Portland cement. The formation of ettringit is developed and the hardening of cement is initiated. Finally, the fibrils of hydrated calcium silicate grow into a cluster (for details, see, e.g. [3]).

HEAT EVOLUTION

Heat evolution of the hydration of cement may be divided into three stages – chemical stage, nucleation and growth.

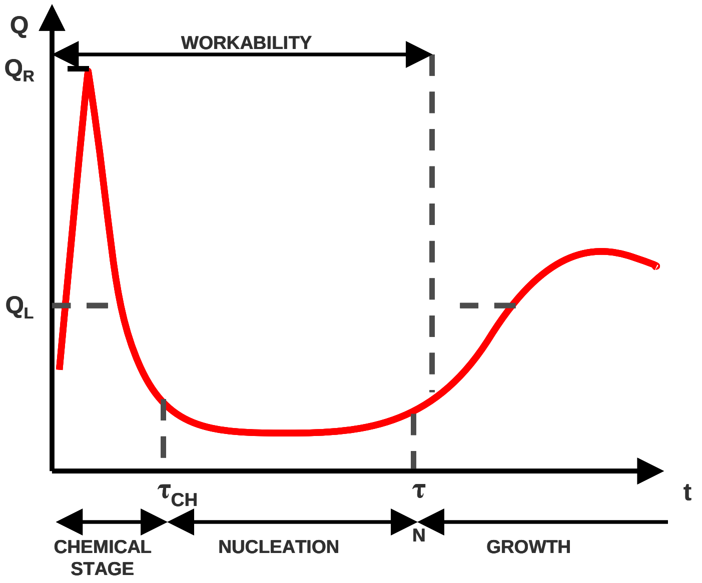

Figure 2.
Heat evolution of hydration of cement paste (schematically).

When the starting cementitious material is mixed with water (but also other kinds of liquids may be used, for example in stomatology) a set of chemical reactions produces a significant amount of heat released due to exothermal reactions and this amount of heat can be measured (for example, using various modifications of calorimetric methods – see, e.g. [5]). Duration of these chemically based reactions may be affected by different types of retarders (e.g. [6]). Beside of heat released also a number of various charged objects (dominantly calcium ions, resp. hydroxyl groups [3]) are intensively produced during this reaction kinetics. These ions play essential role in subsequent, nucleation stage of evolution and form the so-called monomers – the building units from which the product, solid phase is successively built up.

Indeed, the chemical stage of evolution is followed by the so-called incubation (or dormancy) period when the pure chemical processes are slowly terminated and the first-order phase transformation (solidification) starts within the metastable system. At a very first stage of cementitious paste hardening, the sub-nanosized domains of a new, solid phase are formed via sufficiently large fluctuations (the monomers are already present as a consequence the chemical stage).

Number density of these newly-forming clusters is too low in order to influence the magnitude of practically negligible total heat release within hardening system, which is clearly visible in the heat evolution – no observable peaks or increases in Q. Thus, the calorimetry methods are, in fact, inapplicable to obtain useful information on processes occurring in the cement paste during incubation period. Nevertheless, the fact that the building units are charged with various levels of mobility can be usefully utilized. Hence, time-change of electrical conductivity may be straightforwardly related to the immediate stage of system evolution.

The beginning of macroscopic growth (and, thus, termination of incubation period) can be characterized by dramatical change in the time-dependency of electrical resistance because of appearing of the massive clusters with relatively low mobilities. This process is accompanied by increasing release of the latent heat Q_L.

MODEL

Duration of incubation period, τ_N, can be estimated using following path. Due to chemically based process of solvation of the cementitious material in water, various types of charge carriers (monomers Ca^{2+}, OH^-, etc.) are released and free to move within the system. Due to chemical reaction and physical processes occurring within hardening cementitious paste, a number density of ions changes with time logically followed also by the change of electric properties of the system. In particular, temporal dependency of electrical resistance (resp. conductivity) may be closely related to τ_N.

For this purpose, we have measured electrical resistance of hardening cement paste. We used the cement CEM type II 32,5 produced by HeidelbergCement Group (chemical composition of cement paste is collected in Tab. 1). There exist many methods how to measure electrical resistance in cement-based materials (e.g. [7] - [10]).

Tab. 1. Chemical composition of cement paste

Chemical	weight
SiO_2	2.27
Fe_2O_3	0.62
Al_2O_3	25.36
CaO	4.12
MgO	6.90
SO_3	55.40

We used a relatively simple set-up for measuring electrical resistance (see Fig. 3). Typical data obtained by the set-up are shown in Fig. 4, where time-dependency of resistance was measured for cement paste with water to cement ratio 0.5 at temperature 21.8 °C (water to cement ratio is amount of water related to the amount of cement).

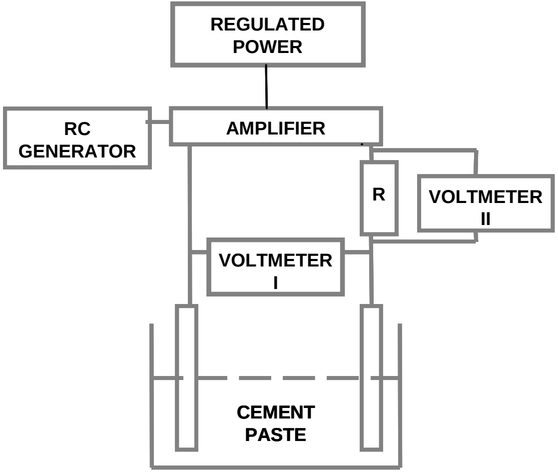

Figure 3.
Scheme of applied electric set-up.

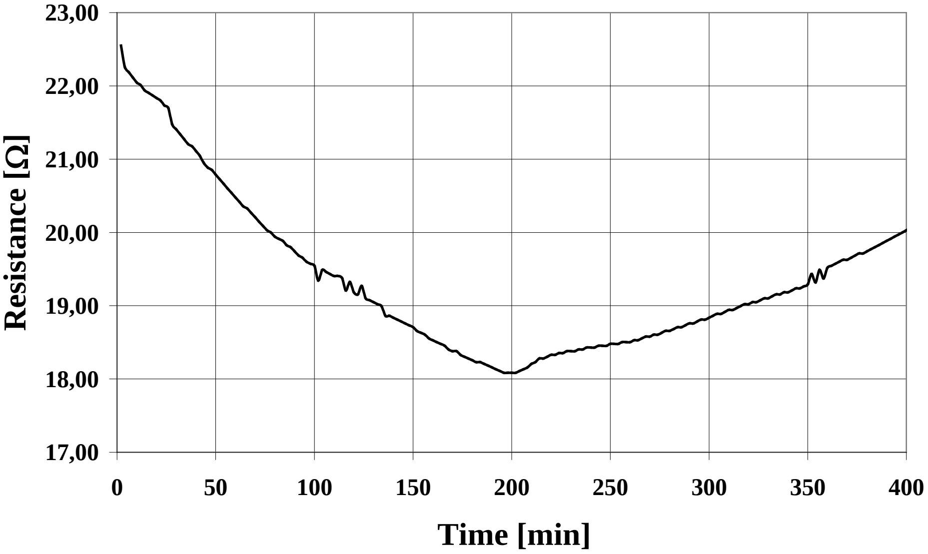

Figure 4.
Typical temporal dependency of electrical resistance of cement paste (w/c = 0.5; T= 23.8°C).

Formation of clusters in material is a consequence of fluctuations. If the classical Boltzmann theory from statistical physics is applied to the process of cluster formation, it can be found out that the probability of appearing of a cluster consisting of n-building units can be expressed as follows:

$$\Pr(n) \approx \exp\left[-\frac{\Delta G(n)}{kT}\right], \qquad (1)$$

where k is Boltzmann constant, T is the temperature, and the ΔG is the change of Gibbs potential given by (see, e.g. [4])

$$\Delta G = -n \cdot \ln \mathscr{S} + \gamma \cdot \sigma \cdot n^{2/3}, \qquad (2)$$

where n is number of monomers in the newly-forming cluster, $\mathscr{S}$ is given supersaturation of the system (water + cement), σ represents surface energy between cluster and its environment and γ expresses geometrical shape of the cluster (plot of ΔG versus n is on Fig. 5). ΔG reaches maximum at the moment when the newly forming clusters have the critical size n_C. When the cluster consists of n particles and n is less than n_C, then dissolution takes place; otherwise, the cluster tends to grow.

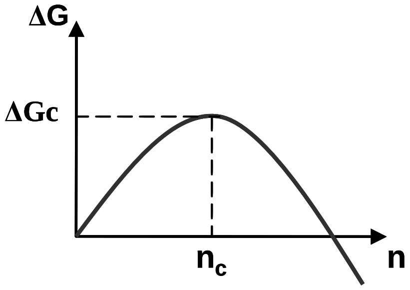

Figure 5.
Plot of ΔG versus n.

The critical size of cluster can be derived from extremum condition for ΔG to be:

$$n_c = \left[\frac{2\gamma\sigma(T)}{3\ln \mathscr{S}}\right]^3 . \qquad (3)$$

RESULTS AND DISCUSSION

Crucial quantity entering above relationship, dividing the unstable (undercritical) and stable (supercritical, growing) regimes of evolution via nC is temperature dependent surface energy *σ(T)* between solid cluster and original liquid phase. It can be found in standard books on physical chemistry [3] that surface energy σ usually decreases with increasing temperature and vanishes at equilibrium temperature TM. Dependency of nC versus temperature can be derived from formula for the critical size of cluster. Since σ decreases with increasing temperature, taking into account eq. (3), following behavior of nC (as a function of T) may be assumed for given supersaturation:

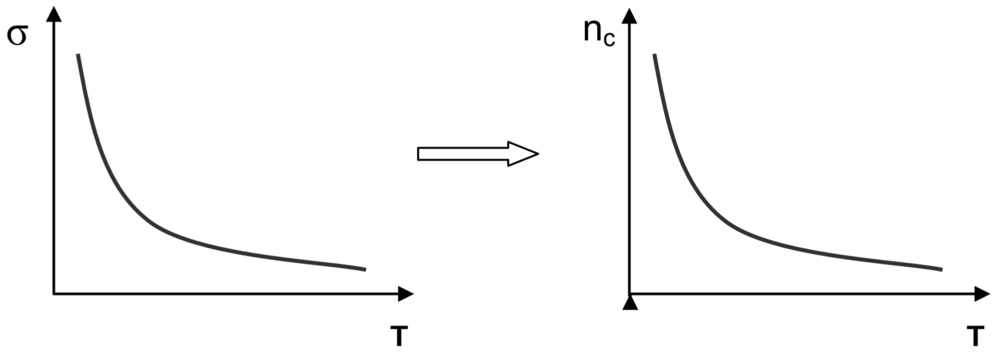

Figure 6.
Dependencies of σ , resp. n_C on temperature T.

The newly-forming cluster becomes stable and growable when overcross the so-called nucleation barrier ΔG_C (corresponding to ΔG_C at critical size n_c) that can be determined from relationships (2), resp. (3) to be:

$$\Delta G_C = \frac{4\gamma^3}{27(\ln \mathscr{S})^2}\sigma^3(T)\,, \qquad (4)$$

Or, with given supersaturation

$$\Delta G_C = const.\,\sigma^3(T)\,. \qquad (5)$$

Consequently, with increasing temperature T the nucleation barrier decreases (as it follows from the Fig.6 and formula (4)). Thus, the boltzmannian probability (1) defining, in fact, a boundary separating unstable and growable states strongly depends on temperature dependent surface energy of cluster.

$$\Pr(n) \approx \exp\left[-\frac{const.\,\sigma^3(T)}{kT}\right]. \qquad (6)$$

In other words, the higher temperature T, the higher probability of formation of a new, growable cluster (usually called nucleus [11]).

In standard nucleation theory, the number density of supercritical nuclei formed within unit volume per unit time corresponds to nucleation rate (see, e.g. [12]-[15]), while time-integral of this quantity (integral flux) expresses “intensity” of early stage of the phase transformation and becomes time-independent from a certain time defining incubation time of nucleation [15]. From this moment, intensive growth of a new phase begins and critical (resp. supercritical) clusters present in system dramatically increase their sizes. Moreover, due to change of viscosity (as a consequence of increasing density of solid phase within liquid one!) the mobility of charge careers (Ca^{2+}, reps. OH^- ions) markedly decreases resulting in dramatical increasing of electrical resistivity of hardening cement paste. We relate this moment to incubation time of nucleation. Then, utilizing our measurements of temporal dependency of electrical resistance at various temperatures (but for fixed w/c ratio) we obtain from inflex points of these curves the following influence of temperature on induction period τ_N of nucleation:

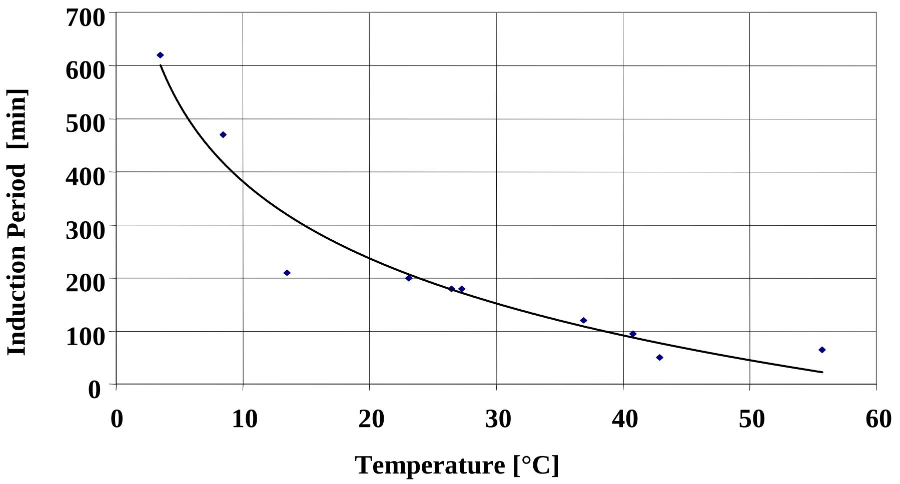

Figure 7.
Temperature dependency of induction period (w/c=0,5).

Summarizing, in terms of temporal behavior of electrical resistance the rate of evolution of a very first stage of solidification (i.e., nucleation) within cementitious materials can be indirectly estimated. The crucial role is played by surface energy of newly-forming cluster which modulates the height of nucleation barrier and separates the unstable and growable regimes of system.

ACKNOWLEDGMENT. This work was supported by the Ministry of Education of the Czech Republic under project No. CEZ MSM 6840770003. One of us, A.S., also gratefully acknowledges the support of the Grant Agency of the Czech Republic, Project No. 101/05/2214.

REFERENCES

[1] Bakker R.: Application and advantages of blended cement concrete, QCL Group Technical Note, March 1999
[2] Bakker R.: The hardening of Portland cement, QCL Group Technical Note, March 1999
[3] Taylor H.F.W.: Cement Chemistry, London, Thomas Telford 1997
[4] Demo P., Kožíšek Z.: Thermochimica Acta 280/281(1996)101-126
[5] Princigallo A., Lura P., Breugel K. van: Early development of properties in a cement paste :A numerical and experimental study, Cement and Concrete Research, December 2002
[6] Taylor H. : Cement Chemistry, second edition, Academic Press 1997, p.309,323-328
[7] Princigallo A., Breugel K. van, Levita G.:Influence of the aggregate on the electrical conductivity of Portland cement concretes, Cement and Concrete Research, April 2003
[8] Levita G., Marchetti A., et al. : Electrical properties of fluidified Portland cement mixes in the early stage of hydration, Cement and Concrete Research, April 2000
[9] Morsy M. S.: Effect of temperature on electrical conductivity of blended cement pastes, Cement and Concrete Research, October 1998

[10] McCarter W. J., Starrs G., Chrisp T. M.: Electrical conductivity, diffusion, and permeability of Portland cement-based mortars, Cement and Concrete Research, April 2000
[11] Demo P., Kožíšek Z.: Philosophical Magazine B70(1994)49-57
[12] Demo P., Kožíšek Z.: Phys.Rev.B48(1993)3620-3625
[13] Demo P., Kožíšek Z.: Materials Sci. and Eng.A173(1993)41-44
[14] Demo P., Kožíšek Z., Šášik R.: Phys.Rev.E59(1999)5124-5127

Models for measurement of thermophysical parameters

P. Dieška

Department of Physics, STU FEI

Ilkovičova 3, 812 19 Bratislava, Slovakia

October 16, 2008

P.Dieška 2008/10/16

Model as a image of real experiment

Heat equation:

$$c\rho\frac{\partial T}{\partial t} = \nabla \cdot \lambda \nabla T \tag{1}$$

Initial and boundary conditions:

$$adequate\ to\ the\ experimental\ setup \tag{2}$$

Solution:

$$T(t, \mathbf{r}) \sim T_{EXP}(t, \mathbf{r})$$

c ... Specific heat capacity

ρ ... Density

λ ... Thermal conductivity

P.Dieška 2008/10/16

Specification of the problem

- The parameters are temperature independent ⇒Linearisation of the problem
- The sample have certain symmetry ⇒Possibility of spatial dimension reduction
- The heat source is external ⇒Time dependent boundary conditions

Used methods

- Laplace transform for time dependence
- Specific integral transform for spatial dependence
- Superposition method

P.Dieška 2008/10/16

Solved models - 1D

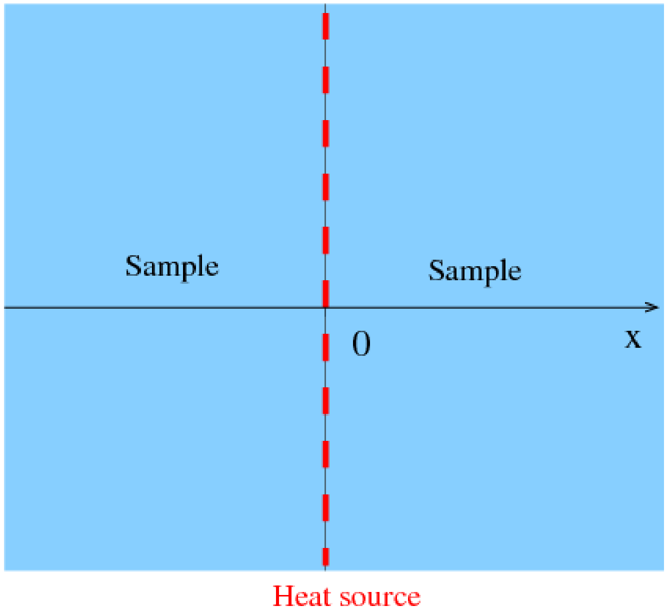

1. Ideal model. Instantaneous planar heat source placed between two semiinfinit samples. The thermal contact of heat source and samples is ideal . Heat equation:

$$\frac{1}{k}\frac{\partial T}{\partial t} = \frac{\partial^2 T}{\partial x^2} \tag{3}$$

Initial condition:

$$T(0,x) = 0 \tag{4}$$

Boundary conditions:

$$-\lambda \frac{\partial T}{\partial x}\bigg|_{x=0} = q1(t) \tag{5}$$

P.Dieška 2008/10/16

$$T(t,\infty) = 0 \tag{6}$$

Solution

$$\boxed{T(t,x) = T_0\left[\frac{e^{-u^2}}{\sqrt{\pi}u} - \Phi^*(u)\right]}$$

$$u = \frac{x}{2\sqrt{kt}} \qquad T_0 = \frac{qx}{\lambda}$$

T ... temperature
t ... time
x ... Cartesian coordinate
q ... heat flow density at source
$1(t)$ ... Heaviside unit step function
λ ... thermal conductivity
k ... thermal diffusivity
C ... heat capacity per unit area of source
α_s ... heat trasfer coefficient for sample - heat source interface
$\Phi^*(u)$ is the complementary error function .

2. Slabs - symmetric disposition

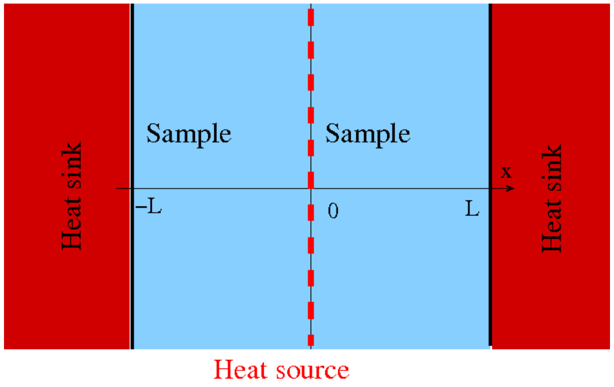

Boundary conditions:

$$-\lambda \frac{\partial T}{\partial x}\bigg|_{x=0} = \alpha_s (T_s - T\Big|_{x=0}) \qquad (7)$$

$$q1(t) = C\frac{\partial T_s}{\partial t} + \alpha_s (T_s - T\Big|_{x=0}) \qquad (8)$$

$$T(t, L) = 0 \qquad (9)$$

Solution

$$\boxed{T(t,x) = T_0 \left\{ (1 - \tfrac{x}{L}) + 2a \sum_{\nu} e^{-\frac{kt}{L^2}\nu^2} \times \frac{\nu \sin(\nu \frac{x}{L}) - (a - b\nu^2)\cos(\nu \frac{x}{L})}{\nu^2 [b^2\nu^4 - (2ab - b - 1)\nu^2 + a(a+1)]} \right\}}$$

P.Dieška 2008/10/16

$$T_0 = \frac{qL}{\lambda} \qquad a = \frac{\lambda L}{Ck} \qquad b = \frac{\lambda}{L\alpha_s}$$

T_s ... temperature of heat source
L ... thickness of sample
C ... heat capacity per unit area of source
α_s ... heat transfer coefficient of source - sample interface
ν is a root of equation

$$(a - b\nu^2)\cos\nu - \nu\sin\nu = 0$$

3. Slabs - asymmetric disposition

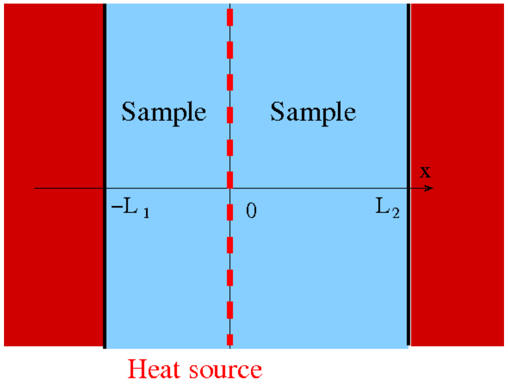

Boundary conditions:

$$-\lambda \frac{\partial T}{\partial x}\bigg|_{x=0+} + \lambda \frac{\partial T}{\partial x}\bigg|_{x=0-} = 2q1(t) \tag{10}$$

$$T|_{x=0+} - T|_{x=0-} = 0 \tag{11}$$

$$T|_{x=-L_1} = T|_{x=L_2} = 0 \tag{12}$$

Solution

$$\boxed{T(t,x) = \frac{2q\sqrt{kt}}{\lambda} \sum_{j=-\infty}^{\infty} (-1)^j \left[\frac{e^{-u_j^2}}{\sqrt{\pi}} - u_j \Phi^*(u_j) \right]}$$

$$u_j = \frac{\left||x| + 2Lj + \frac{1}{2}(L_1 - L_2)[1-(-1)^j]\right|}{2\sqrt{kt}}$$

L_1, L_2 ... thicknesses of samples
$L = \frac{1}{2}(L_1 + L_2)$
$2q$ ... sum of heat flow densities at source

4. Sandwich disposition

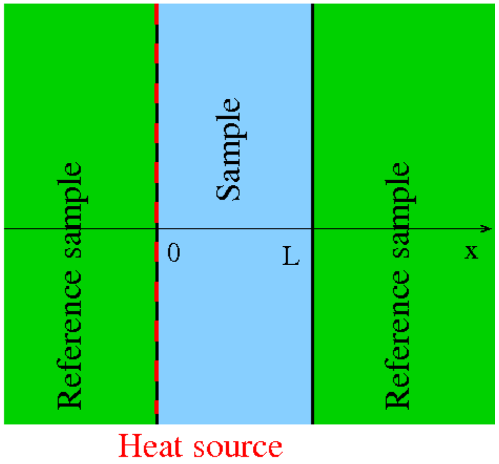

Boundary conditions:

$$T(t, -\infty) = 0 \tag{13}$$
$$T(t, \infty) = 0 \tag{14}$$

$$-\lambda \frac{\partial T}{\partial x}\bigg|_{x=0^+} + \lambda_0 \frac{\partial T}{\partial x}\bigg|_{x=0^-} = 2q1(t) \tag{15}$$

$$T|_{x=0^+} - T|_{x=0^-} = 0 \tag{16}$$

$$-\lambda \frac{\partial T}{\partial x}\bigg|_{x=h^-} + \lambda_0 \frac{\partial T}{\partial x}\bigg|_{x=h^+} = 0 \tag{17}$$

$$T|_{x=h^-} - T|_{x=h^+} = 0 \tag{18}$$

Solution

$$\boxed{T_{13}(t,x) = T_0 \frac{\gamma}{u_0} \sum_{j=0}^{\infty} \delta^j \left[\frac{e^{-u_j^2}}{\sqrt{\pi}} - u_j \Phi^*(u_j) \right]}$$

$$T_0 = \frac{qh}{\lambda} \quad u_j = \frac{(n+\frac{1}{2})h}{\sqrt{kt}}, \quad \gamma = \left(\frac{2}{1 + \frac{\lambda_0}{\lambda}\sqrt{\frac{k}{k_0}}} \right)^2, \quad \delta = \left(\frac{1 - \frac{\lambda_0}{\lambda}\sqrt{\frac{k}{k_0}}}{1 + \frac{\lambda_0}{\lambda}\sqrt{\frac{k}{k_0}}} \right)^2$$

h ... thickness of the sample
λ_0 ... reference thermal conductivity
k_0 ... reference thermal diffusivity

P.Dieška 2008/10/16

Solved models - 2D

5. Semi-infinite cylinder

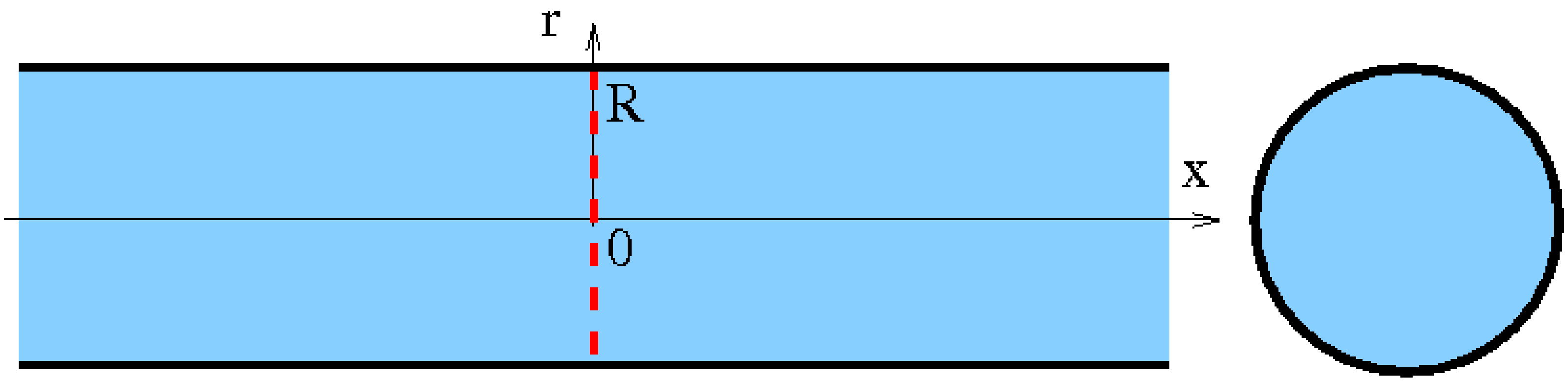

Heat equation:

$$\frac{1}{k}\frac{\partial T}{\partial t} = \frac{\partial^2 T}{\partial x^2} + \frac{1}{r}\frac{\partial}{\partial r} r \frac{\partial T}{\partial r} \tag{19}$$

Initial condition:

$$T(0,x) = 0 \tag{20}$$

Boundary conditions:

$$-\lambda \frac{\partial T}{\partial r}\bigg|_{r=R} = \alpha T\bigg|_{r=R} \tag{21}$$

$$-\lambda \frac{\partial T}{\partial x}\bigg|_{x=0} = q1(t) \tag{22}$$

$$T\bigg|_{x=\infty} = 0 \tag{23}$$

Solution

$$\boxed{T(t,x,r) = T_0 \frac{R}{x} \sum_{\xi} \frac{\beta}{\xi(\xi^2+\beta^2)} \frac{J_0(\xi\frac{r}{R})}{J_0(\xi)} F(u,v)}$$

$$F(u,v) = e^{-2uv}\Phi^*(u-v) - e^{2uv}\Phi^*(u+v)$$

$$T_0 = \frac{qx}{\lambda} \qquad \beta = \frac{R\alpha}{\lambda} \qquad u = \frac{x}{2\sqrt{kt}} \qquad v = \xi\frac{\sqrt{kt}}{R}$$

x ... axial space coordinate

r ... radial space coordinate

R ... radius of the sample

q ... heat flow density at source

α ... heat trasfer coefficient for sample - ambient interface

ξ is the root of the equation

$$\beta J_0(\xi) - \xi J_1(\xi) = 0$$

P.Dieška 2008/10/16

Solved models - 3D

5. Finite cuboid

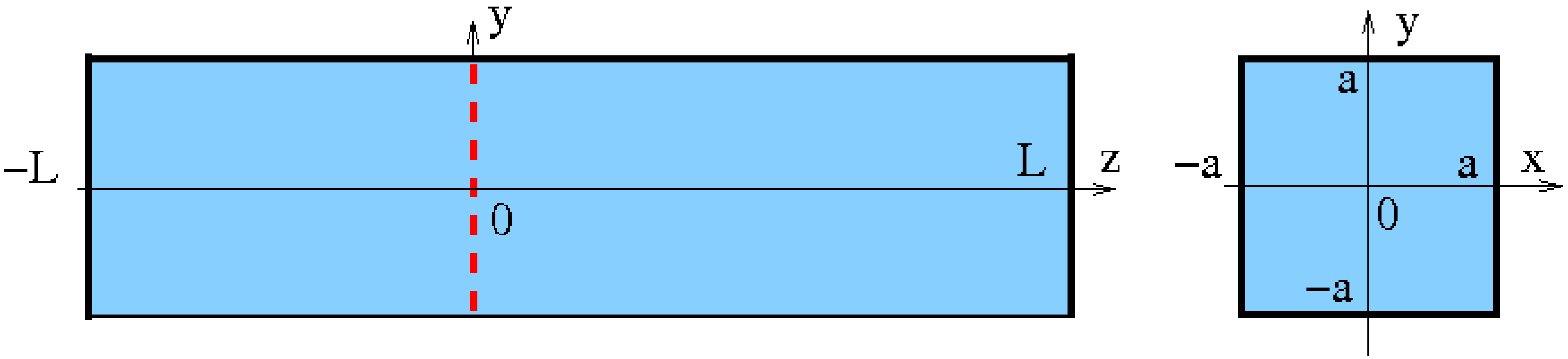

Heat equation:

$$\frac{1}{k}\frac{\partial T}{\partial t} = \frac{\partial^2 T}{\partial x^2} + \frac{\partial^2 T}{\partial y^2} + \frac{\partial^2 T}{\partial z^2} \tag{24}$$

Initial condition:

$$T(0, x, y, z) = 0 \tag{25}$$

P.Dieška 2008/10/16

Boundary conditions:

$$\left.\frac{\partial T}{\partial x}\right|_{x=0} = 0 \tag{26}$$

$$-\lambda\left.\frac{\partial T}{\partial x}\right|_{x=a} = \alpha T\Big|_{x=a} \tag{27}$$

$$\left.\frac{\partial T}{\partial y}\right|_{y=0} = 0 \tag{28}$$

$$-\lambda\left.\frac{\partial T}{\partial y}\right|_{y=a} = \alpha T\Big|_{y=a} \tag{29}$$

$$T\Big|_{z=-L_1} = T\Big|_{z=L_2} = 0 \tag{30}$$

$$T\Big|_{z=0^+} = T\Big|_{z=0^+} \tag{31}$$

$$-\lambda\left.\frac{\partial T}{\partial z}\right|_{z=0^+} + \lambda\left.\frac{\partial T}{\partial z}\right|_{z=0^-} = 2q\,1(t) \tag{32}$$

P.Dieška 2008/10/16

Solution:

$$T(t,x,y,z) = T_0 \tfrac{w}{2} \sum_{n=1}^{\infty} \sum_{m=1}^{\infty} \tfrac{b_n b_m}{v_{nm}} \varphi_n\left(\tfrac{x}{a}\right) \varphi_m\left(\tfrac{y}{a}\right) \sum_{j=-\infty}^{\infty} \Big[F(u_{1j}, v_{nm}) - F(u_{2j}, v_{nm}) \Big]$$

$$\varphi_n(s) = \sqrt{\frac{2\beta}{\beta + \sin^2 \mu_n}} \cos(\mu_n s)$$

$$F(u,v) = e^{-2uv} \Phi^*(u - v) - e^{2uv} \Phi^*(u + v)$$

$$T_0 = \frac{qa}{\lambda}, \quad \beta = \frac{a\alpha}{\lambda}, \quad w = \frac{\sqrt{kt}}{a}, \quad v_{nm} = w\sqrt{\mu_n^2 + \mu_m^2}, \quad b_n = \varphi_n(0)\frac{\sin(\mu_n)}{\mu_n}$$

$$u_{1j} = \frac{|z + 4Lj|}{2\sqrt{kt}} \qquad u_{2j} = \frac{||z| + 4Lj + 2L_1|}{2\sqrt{kt}}$$

z ... axial space coordinate
L_1 ... length of left sample
L_2 ... length of right sample

$L = (L_1 + L_2)/2$

x, y ... transversal space coordinates

$2a$ ... transversal size of the sample

q ... heat flow density at source

α ... heat trasfer coefficient for sample - ambient interface

$\Phi^*(u)$ is the complementary error function

μ_n are the roots of equation

$$\beta \cos \mu - \mu \sin \mu = 0$$

END

Thermal decomposition of waste polymers

J. Haydary, Z. Koreňová, Ľ. Jelemenský, J. Markoš
Institute of Chemical and Environmental Engineering, Faculty of Chemical and Food Technology, Slovak University of Technology, Radlinského 9, 812 37 Bratislava, Tel.: ++421 2 59325265, E. mail: juma.haydary@stuba.sk

ABSTRACT

In this work the thermal decomposition of elastomeric polymers was studied. The pyrolysis of scrap rubber samples was carried out under nitrogen atmosphere over a temperature range of 20-800 ^{o}C using a heating rate of 5 ^{o}C/min. Thermogravimetric (TG) and Differential Scanning Calorimetric (DSC) curves of rubber samples are discussed. The DTG curves show two different peaks corresponding with the decomposition of different components presented in the rubber blends. Using thermogravimetric data the kinetic parameters of thermal decomposition were estimated.

Key words
Thermal decomposition, pyrolysis, kinetic of pyrolysis, scrap tyre, waste rubber

1. INTRODUCTION

The excellent properties of polymeric materials let them penetrate in all spheres of human life; now they are completely irreplaceable and absolutely necessary for people. However, these excellent properties represent at the same time a disadvantage of these materials: they are not quickly decomposed under the influence of the environment aggressive factors as light, heat, atmosphere gases, microorganisms and continue to exist in the form of a long-living waste, inflicting an irreparable damage to the nature.

As though namely people manufacture polymeric materials to satisfy their needs, they also have to protect the nature from a negative influence of synthetic materials. Therefore, to continue using of polymeric material growing volumes, mankind have urgently develop effective methods of polymeric materials utilization and disposal.

In EU the optimum waste management strategies are now becoming key political targets, reflected by the high level of investment in both demonstrating and integrating existing technologies, and the development of fundamental research into new ideas. European legislation and public pressure are furthermore adding weight to the need for a sustainable solution in the very near future.

Thermoplastic such as polyethylene (PE), polypropylene (PP), Polyethylene terephthalate (PET), polyvinyl chloride (PVC), polystyrene etc.) are not croslinked and usually we can they remould by simple thermal treatment. PET bottles, PE and PP coats and bags, PVC carpets, Polystyrene foams and many others are the examples of wastes made from thermoplastics. Wide application of polymers for polyvinylchloride window block construction have set a new target - utilization of these window blocks after 20 years of their operation.

The three main methods of plastic recycling are:

- Mechanical Recycling, the re-processing of the plastic materials into new products.
- Feedstock Recycling, the processing of plastics into basic chemicals.

- Energy Recovery, the recovery of valuable energy from waste plastic through incineration.

Pyrolysis offers an alternative way of polymer recycling and a solution for recycling thermoplastics, for that other recycling methods are not effective. Recycling of polymers by pyrolysis could be an environmentally and economic attractive method. Pyrolysis belongs into feedstock recycling methods. Feedstock recycling is defined as a change in the chemical structure of the material, where the resulting chemicals are used for another purpose than producing the original material.

Used tyres and other elastomer wastes create a considerable part of croslinked thermoset polymeric wastes. Thermoset polymers cannot be simply recycled by heating and remoulding, however, a number of methods for their recycling are known [1]. Generally tyre recycling methods can be divided by the same scheme as plastic recycling:

Due to crosslinked structure of rubber vulcanizates, pyrolysis seems to be the most effective way for tyre recycling. In a pyrolysis reactor the shredded tyres are decomposed into pyrolysis products received in all three phases: solid char (30-40 wt%), liquid residue (50-60 wt%), and gases (3-20 wt%) [1].

Studying thermal decomposition of polymers in laboratory scale apparatuses let us more understand the mechanism of the pyrolysis process leading to the process optimisation.

In this work thermal decomposition of elastomeric polymers is studied. The TG (Thermogravimetric) and DSC (Differential Scanning Calorimetric) curves of different rubber samples are analyzed.

2. EXPERIMENTAL

Materials and samples

Rubber samples prepared from two parts (side wall and tread) of a used MATADOR passenger car tyre for TG and DSC analysis.

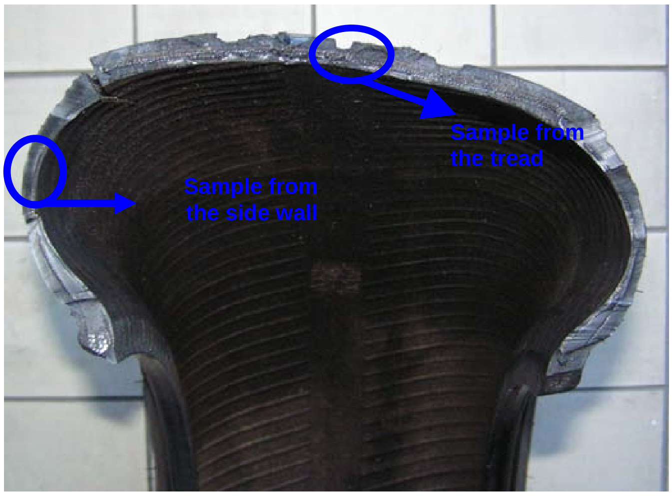

Figure 1: Degradation temperature region during rubber pyrolysis

Experimental method

The simultaneous TG/DSC analyser NETZSCH STA 409PC, was used for both thermogravimetric and differential scanning calorimetric analyses performed simultaneously. The weight of the sample war around 50 mg. As inert atmosphere for thermal decomposition

0.99999 nitrogen with a total flow rate 40 ml/min was used. The behaviour of the thermal decomposition was studied in a temperature range from 20 to 800°C using a heating rate of 5 K/min.

Figure 2: simultaneous TG/DSC analyser

3. RESULTS AND DISCUSSION

The behaviour of the thermal decomposition of rubber is generally studied by thermogravimetric analysis. From the thermogravimetric analysis provided by various authors [2][3] [4] results that more than one degradation temperature region during rubber pyrolysis is recorded. As it is shown in Figure 5, our measurements sustain this fact.

The behavior of the TG and DSC curves of two different scrap tyre samples measured simultaneously is shown in Figures 3 and 4. The TG curve of sidewall sample indicates that its thermal decomposition begins at a temperature of 210°C and practically finishes at 510°C. In the temperature range from 210 to 315°C volatile additives are released. From 315°C probably also decomposition of NR starts, this suggest the derivative thermogravimetric (DTG) curve of this sample (Figure 5). The DTG curve of the sidewall sample shows two peaks one with an extreme at 370°C and one with an extreme at 445°C. By comparing these values with the results of thermal degradation of individual types of rubbers in the literature [5] (for NR 375°C, for SBR 445°C, and for BR 465°C), we see that the first peak corresponds with the decomposition of NR and the second peak with the decomposition of SBR. However, Seidelt et al. [5] reported, that SBR is decomposed in two steps. The first step starts at 360°C and represents the release of styrene, and the second step represents the release of the main butadiene decomposition product, 4-vinylcyclohexane,which starts at 420°C. For this reason the first peak in DTG curve of the tyre sidewall can be caused also by a release of styrene from SBR.

The DTG curve of the sample from the tyre tread (Figure 6) does not show clearly two peaks. This curve, however, reveal the release of volatiles in the temperature range (200-330°C). The only dominant peak with a maximum at 440 °C represents a release of SBR, which is in tyre tread the main type of polymer.

The derivative differential scanning calorimetric (DDSC) curves of both samples (Figure 7) show an endothermic character in general with one main endothermic peak, and also one exothermic peak located before the main endothermic peak. This endothermic character of the thermal decomposition was expected. The exothermic peak can be caused by oxidation of released volatiles by oxygen liberated during the thermal decomposition or by some residual oxygen in the apparatus due to its insufficient remove from the device. The heats of thermal decomposition calculated for the tyre sidewall and the tyre tread sample are 291 J/g and 324J/g, respectively.

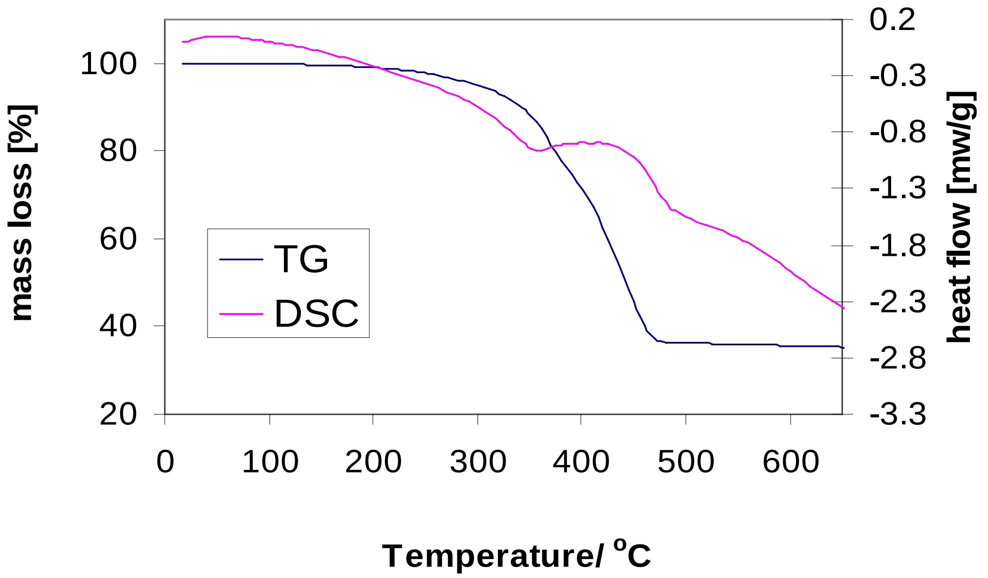

Figure 3: TG and DSC curves of tyre sidewall sample

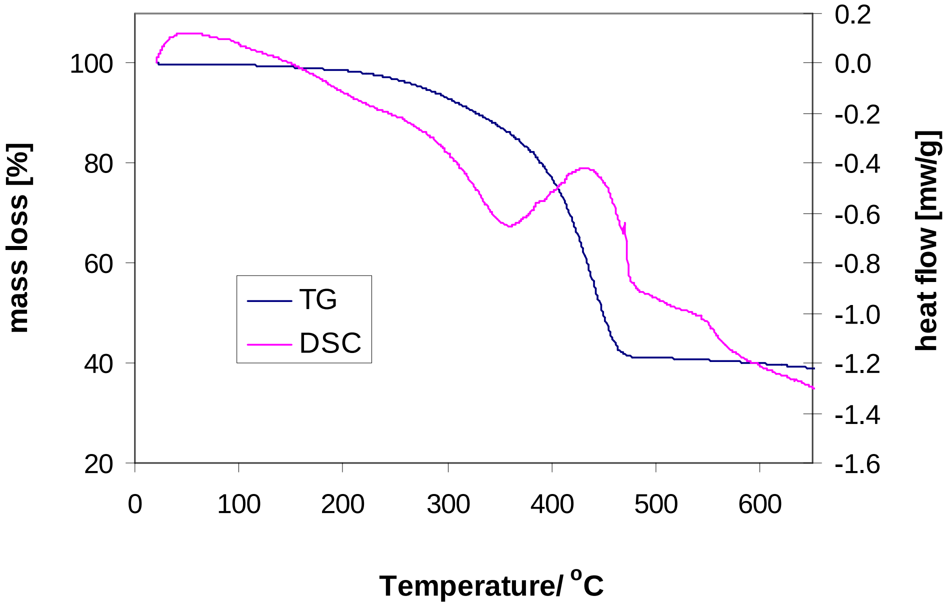

Figure 4: TG and DSC curves of tyre tread sample

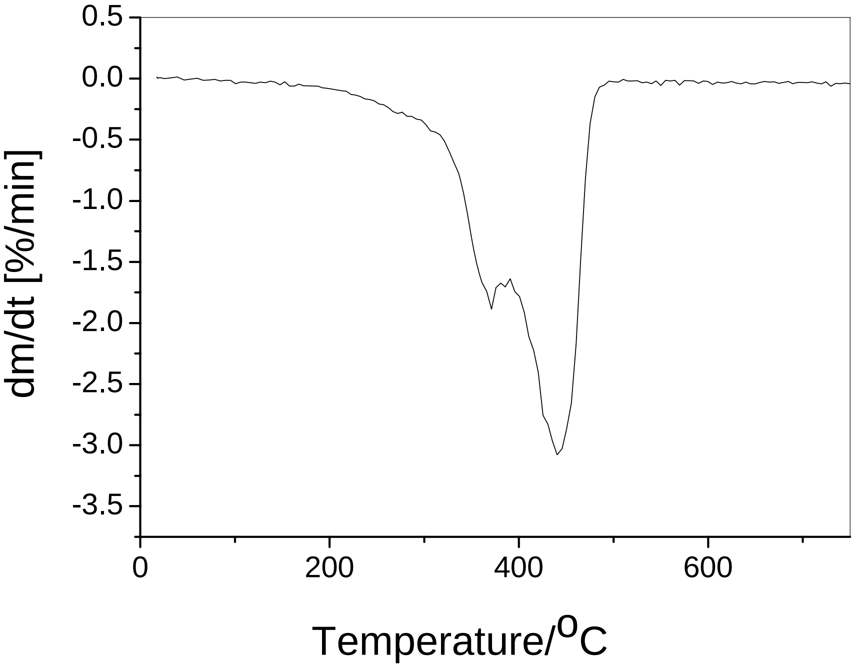

Figure 5: DTG curve of tyre sidewall sample

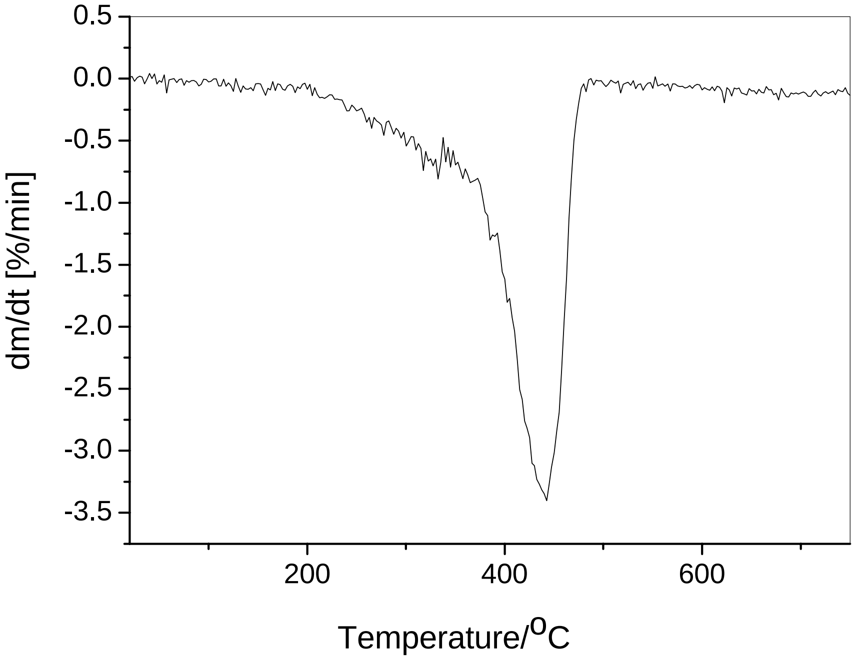

Figure 6: DTG curve of tread sample

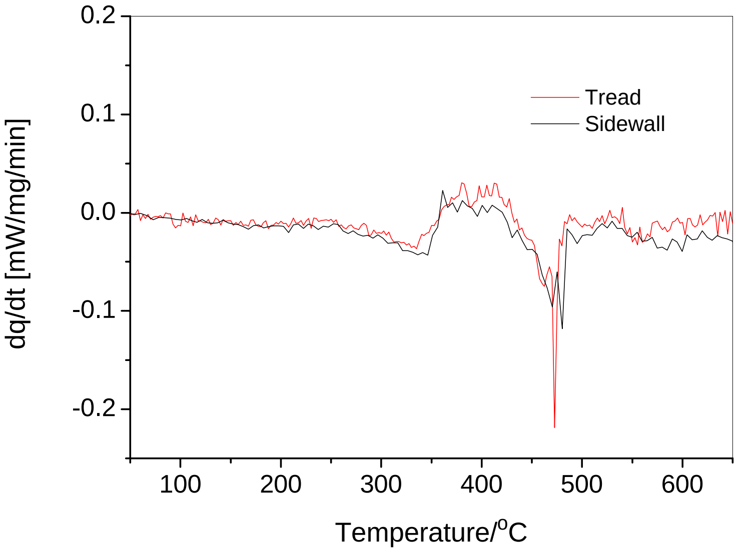

Figure 7: DDSC curves of tyre samples

Kinetic properties of the scrape tyre thermal decomposition

Due to a very complex composition of rubber compounds used in the tyre and also due to multiple unknown chemical reactions during the tyre decomposition, usually the kinetics of this process is described by the use of experimental thermogravimetry data. The first order reaction based on the Arrhenius theory is commonly assumed by researchers in the kinetic analysis of data for tyre decomposition. The rate of decomposition may be expressed by:

$$\frac{dX}{dt} = k.(1-X)^n \tag{1}$$

The rate coefficient is calculated by the Arrhenius equation:

$$k = A.\exp^{\left(-\frac{E}{R.T}\right)} \tag{2}$$

In this equation k is the rate constant; A is the apparent pre-exponential factor, E is the apparent activation energy, n is the reaction order, R and T are the universal gas constant and absolute temperature, respectively. The reaction conversion *(X)* was calculated according to the following equation:

$$X = \frac{m_0 - m_i}{m_0 - m_{final}} \tag{3}$$

where m_0 is the initial sample mass, m_i is the sample mass at arbitrary time and m_{final} is the final mass of the sample.

In the case of multistep decomposition, a multistep rate equation, which is a sum of individual step's rate equations could be used (equation 4). However, estimating kinetic parameters from this equation requires separation of thermogravimetric data into intervals for individual reactions. This kind separation of thermogravimetric data is usually very difficult.

$$\frac{dX}{dt} = \sum_{i=1}^{s} \frac{dX_i}{dt} = \sum_{i=1}^{s} A_i \exp(-\frac{E_i}{RT})(1 - X_i)^n \qquad (4)$$

In equation 4 *s* represents the number of mass loss regions or decomposition steps.
The distance between the first and the second pyrolysis stage depends on the composition of the tyre rubber. Due to a small distance between the first and the second pyrolysis stage of our samples, we modelled the thermal decomposition as a single stage process. The parameters of equation 1 and 2 were obtained using experimental thermogravimetric data and an optimization programme developed in MATLAB.

In Table 1 are shown the estimated kinetic parameters and also for comparison kinetic parameters obtained by other authors. Compared to results of other authors our results show similar values of apparent activation energy and lower values of apparent per-exponential factor.

Table 1: Kinetic parameters of the scrap rubber decomposition

Author	Activation energy *E* (kJ/mol)	Pre-exponential factor, *A* (min-1)	Reaction order, *n*
This paper, sidewall	105.0	$6.84\text{x}10^6$	1
This paper, tread	96.0	$1.52\text{x}10^6$	0.8
Leung and Wang [3]	99.1-218.7	$1.02\text{x}10^7$-$1.13\text{x}10^{17}$	1
Yang et al. [4]	152 - 215	$8.82\text{x}10^9$-$3.89\text{x}10^{16}$	1-2
Kim et al. [6]	42.1 – 203.9	$1.44\text{x}10^3$- $2.04\text{x}10^{14}$	-
Chen et al. [7]	147.6-148.1	$5.02\text{x}10^{10}$-$7.57*10^{10}$	1.63-1.98
Wiliams and Besler [8]	102.8-145.0	$5.58\text{x}10^9$-$1.26\text{x}10^{10}$	-

4. CONCLUSIONS

The TG, DTG, DSC and DDSC analyses of two different types of tyre rubber material were investigated. The DTG curve of the sample from the tyre sidewall can be characterized by two separate peaks with a maximum at 370 and 445°C, which correspond to a release of NR and SBR. The DTG curve of tyre tread sample shows only one dominant peak, but the release of volatiles also caused a deformation of this curve.
By analyzing DSC and DDSC curves the overall reaction heat of thermal decomposition was estimated. Values of 291J/g for sidewall rubber and 324 J/g for tread rubber was calculated. However, for both rubber materials also an exothermic peak was observed.

Acknowledgement***:*** *This work was supported by the Grant VEGA No. 1/4446/07 from the Slovak Scientific grant Agency.*

References

1. Juma M., Koreňová Z., Markoš J., Annus J., Jelemenský Ľ., Pyrolysis and combustion of scrap tire. Petroleum and Coal 48 (1), 2006
2. Conesa J. A., Font R., Fullana A. and Caballero J. A., Fuel, 77, 13, 1998, 1469-147
3. Leung D. Y. C. and Wang C. L., Journal of Analytical and Applied Pyrolysis, 45, 2, 1998, 153-169
4. Yang J., Tanguy P. A. and Roy C., Chemical Engineering Science, 50, 12, 1995, 1909
5. S. Seidelt, M. Müller-Hagedorn, H. Bockhorn, J. Anal. Appl. Pyrolysis 75 (2006), 11-18
6. Kim S., Park J. K., Chun H.D., J. Environg. Eng., 1995, 507- 514.
7. Chen K.S., Yeh R. Z., Chang, Y. R., Combust Flame, 1997, 108, 408-418
8. Williams J P.T and Besler S., Fuel 74,1995,1277–1283

Effect of elevated temperature on texture, composition and properties of fiber reinforced cement composites

Martin Keppert[a], Eva Vejmelková[a], Silvie Švarcová[b],
Petr Bezdička[b], Robert Černý[a]

[a]Department of Materials Engineering and Chemistry,
Faculty of Civil Engineering,
Czech Technical University in Prague,
Thákurova 7, 166 29 Praha 6, Czech Republic

[b]Institute of Inorganic Chemistry,
Academy of Sciences of Czech Republic, v.v.i,
250 68 Řež, Czech Republic

Email: martin.keppert@fsv.cvut.cz

Abstract

Behavior of four types of fiber reinforced cement based composites was studied after thermal load up to 1000° C. As the reinforcement were used glass and PP fibers, PVA fibers, aramid fibers and carbon fibers. The effect of thermal load on the texture and composition of the samples was evaluated; behaviour of the used fibers was compared. The moisture diffusivity of the loaded samples and the reference sample (unloaded) was measured. It was found that three independent degradation process take place when the composites are thermally loaded. The effect of thermally unstable fibers (PVA, aramid) on moisture diffusivity is less important than effect of the cement matrix thermal degradation.

Introduction

Fiber reinforced cement based composites are recently widely studied materials because some better properties of them compared to conventional concrete. The study of effect of elevated temperature on fiber reinforced composites is motivated by possible damage of these materials by fire or other extreme conditions. It is necessary to evaluate and predict behavior of fiber composites under elevated temperature. Such behavior of conventional concrete is well known but here also to fibers play a role. Many types of fibers were applied as concrete reinforcement; four of them were studied within this work. The fibers differ in their ability to resist to elevated temperature. This property joins to other concrete's properties which influence its behaviour under elevated temperatures.

Materials

The effect of elevated temperature was studied on four types of fiber reinforced cement based materials (**Tab. 1**). Two types of matrix were used, cement CEM I 52.5 was used. Samples SC (alkali proof glass + polypropylene fibers) and K (polyvynilacetate fibers) were mixed with low w/c ratio and added superplasticizer, fine quartz sand was used as aggregates. Samples UC (carbon fibers) and T (aramid fibers) were mixed with high w/c ratio and quartz and wollastonite were used as aggregates. Small amount of microsilica was added to all materials.

The measurements were performed by reference sample and by annealed samples. The annealed samples were exposed to gradual temperature increase up to 600, 800 and 1000° C during two hours, then left for next 2 hours at the given temperature and then were slowly cooled down. All the specimens were dried at 110° C before each measurement, hence the reference (unloaded) samples are considered as loaded at 110° C.

Tab. 1 Composition of studied fiber reinforced cement composites (mass %).

		SC	K	UC	T
CEM I 52.5		54	54	40	36
w / c		0.33	0.32	0.85	0.9
Microsilica		3	3	2	4
Aggregates					
	Quartz	40	40	17	17
	Wollastonite	-	-	40	39
Fibers					
	Glass *12 mm*	3			
	PP *30 mm*	0.3			
	PVA *6+12 mm*		1.8		
	Carbon			1	
	Aramid *1.5+6 mm*				4

Experimental

The texture of studied materials was characterized by density ρ, bulk density ρ_b, and pore size distribution. Density was determined by means of helium pycnometer Pycnomatic (Porotec, Germany). Bulk density was calculated from mass of dried sample and its geometrical volume (prismatic specimens were used). These two values provide porosity and total pore volume V_p [1]. The pore size distribution was determined by mercury intrusion porosimetry (MIP) by instruments Pascal 140 and 440 (Thermo, Italy). The surface tension of mercury was assumed to be 480 mN m^{-1} and contact angle 130˚.

The phase composition of SC samples was studied by X-ray diffraction analysis (XRD) performed by means of X´pert PRO (PAnalytical, Netherland) instrument. Data were evaluated by software Highscore 1.0d (PAnalytical, Netherland) using database JCPDS PDF2 (International center for diffraction data, USA).

The apparent coefficient of moisture diffusivity κ_{app} [m^2 s^{-1}] was determined by help of imbibition experiment [2]. The content of water in sample (in kg m^{-2}) was recorded automatically and plotted as function of square root of time. The slope of linear part of the dependence signed A was used to calculation of κ_{app} as follows (Eq. 1) where w_{sat} is the saturated water content.

$$\kappa_{app} = \left(\frac{A}{w_{sat}} \right)^2 \qquad \text{(Eq. 1)}$$

Results

The simplest way of observation of thermal degradation of cement based materials is measurement of porosity upon thermal load (**Fig. 1**). The two types of matrix – with low and high w/c ratio resulting to higher and lower porosity – are clearly distinguished. The higher w/c ratio leads to higher content of gel pores. The thermal load causes increase of porosity of all the tested materials, the slope is roughly the same for each type of matrix, regardless the type of fibers.

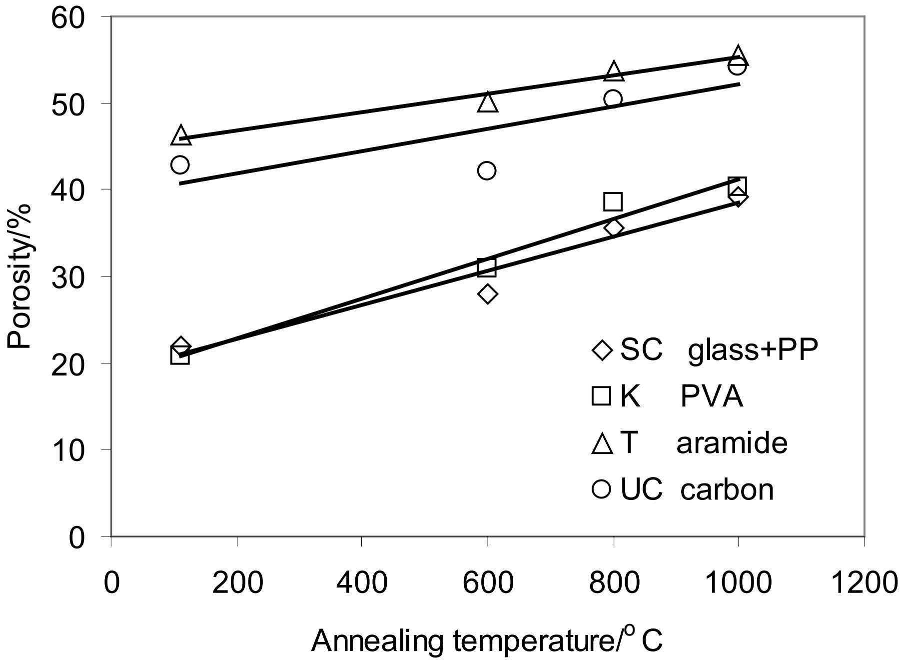

Fig. 1 Porosity of thermally loaded fiber composites.

In order to explain the increase of porosity of fiber reinforced composites, the effect of thermal load on pore size distribution and composition of samples was studied.

The XRD reveals that the thermal load induces two processes taking place in the cement binder. Portlandit $Ca(OH)_2$ decomposes to CaO and water vapor. The equilibrium decomposition temperature of portlandit is 520° C but the process probably starts at somewhat lower temperature. The decomposition of portlandit causes the destabilization of phase equilibrium in hydrated cement binder which leads, together with high temperature, to disintegration of binding CSH and CAH structures and consequently to loss of their binding ability. The diffractograms of loaded samples contain calcite $CaCO_3$ (forms from CaO in air) and clinker minerals (C_2S, C_3A etc.) as products of decomposed CSH and CAH hydrates. This is the reason for the strength reduction of thermally loaded cement based materials.

The results of pore size distribution measurements of loaded materials are presented in **Fig. 2 a** and **b**. The general trends are of pore size distribution evolution are similar in all of the materials. The pore system of cementitious materials is formed by three groups of pores. The smallest are gel pores formed in cement binder. The second group is called capillary pores and the largest are technological pores and voids.

The plots show that the volume of smallest (diameter 0.001 to 0.1 μm) pores – gel pores – is reduced with increasing annealing temperature. It corresponds to the XRD results; the gel structure decomposes to calcite and clinker minerals what is accompanied by the sintering of the gel fine porous texture. At 1000° C are practically all the gel pores gone. The diminishing of gel pores may be observed also by measurement of specific surface area of the samples [3].

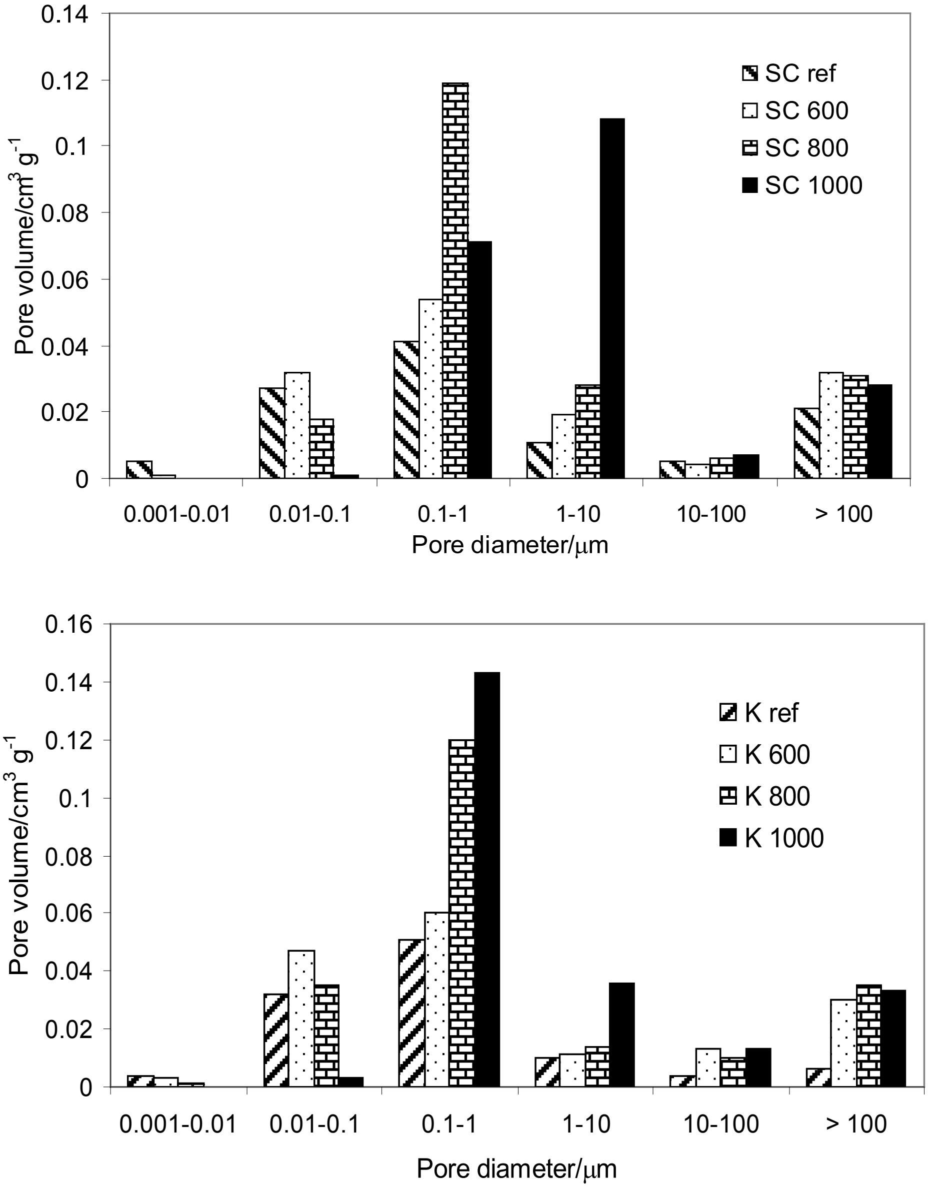

Fig. 2 a Pore size distribution of SC (glass + PP) and K (PVA) composites.

The volume of capillary pores (diameter 0.1 to 100 μm) increases with the thermal load. The explanation has to be searched in thermal dilation of individual components of the materials. The initial (room temperature) quartz modification (α-quartz, specific volume 0,378 cm^3 g^{-1}) converts reversibly at 573° C to β-quartz (0,395 cm^3 g^{-1}). Another reversible modification change takes place at 867 C (β-quartz to β-tridymite; 0,442 $cm^3\ g^{-1}$), thus quartz increases its volume by 17 %. Wollastonite aggregates are less sensitive to temperature changes but at approximately 850˚ C also wollastonite starts to change its volume, β-wollastonite forms [4]. Eventhough these volume changes are reversible, they cause, together with sintering of the binder, the loss of contact between the binder and aggregates which results to formation of new, interconnected to each other, capillary pores between binder and aggregates. The cracks formed between binder and aggregates contribute to the lowering of strength and influences the moisture and heat transport parameters of the material.

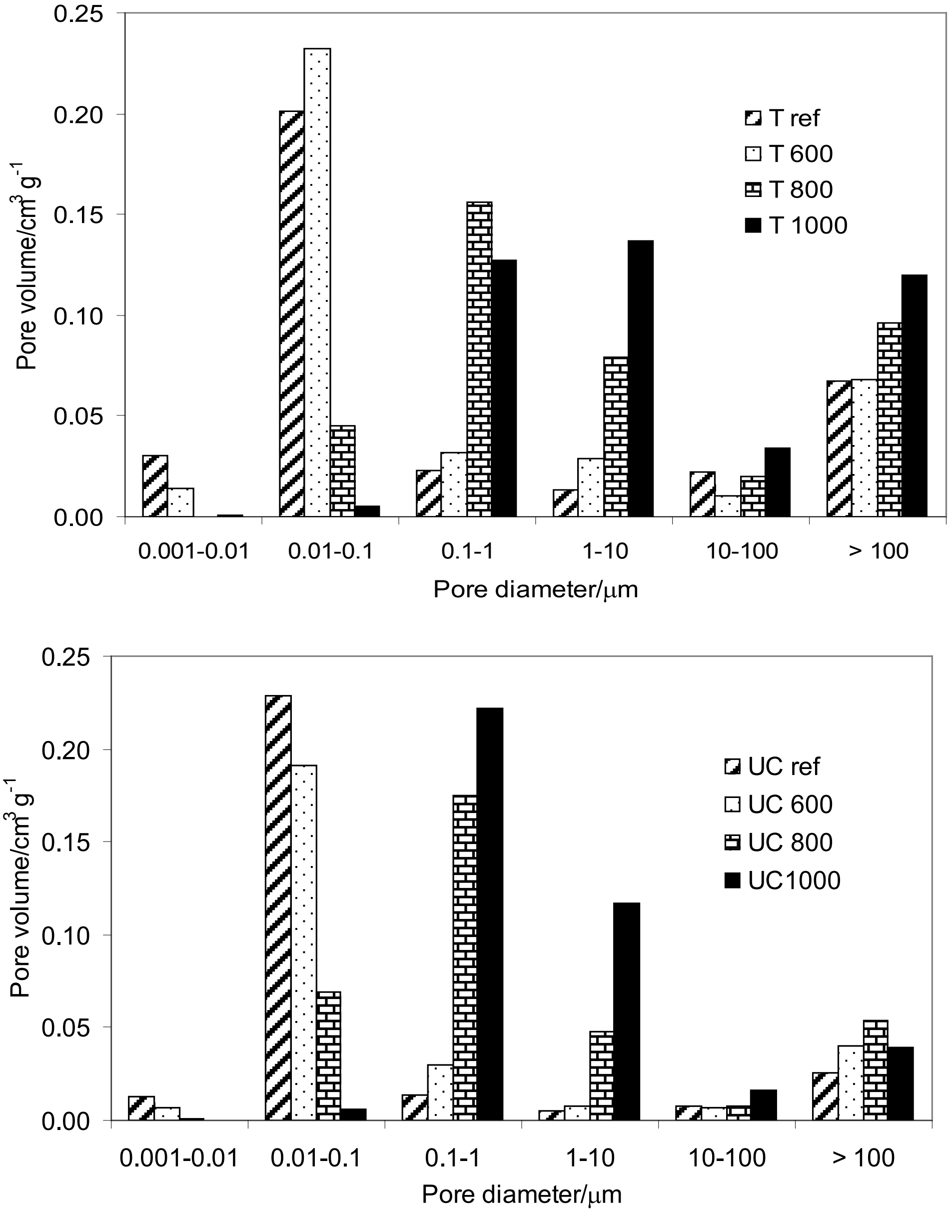

Fig. 2 b Pore size distribution of T (aramid) and UC (carbon) composites.

The volume change of the largest pores in the studied materials may be explained by assuming of different thermal stability of used fibers. Samples SC are reinforced by glass fibers and small amount of PP fibers (0.3 %). The latter obviously burn out at elevated temperature, but the glass fibers should keep their properties. It was indirectly proved by the MIP measurement (**Fig. 2 a**) where any increase of the largest pores was not observed. The PVA fibers do not resist to elevated temperature. This fact influences significantly the pore size distribution of sample K (**Fig. 2 a**) where one observes high increase of volume of the largest pores due to burn out of the PVA fibers. The aramid fibers (material T) are stable up to cca 500° C where aramid decomposes. Again it has certain influence on the increase of volume of the largest pore fraction in samples T (**Fig. 2 b**). At last, the carbon fibers (UC) incorporated in cement matrix feature good thermal stability (at least at the used experimental conditions) as well as the glass fibers.

One of the important properties which are highly influenced by the pore structure of the material is moisture diffusivity. In fact, the moisture diffusion coefficient is function of moisture content in the material. Within this work, the apparent moisture diffusion coefficients κ_{app} of studied materials were determined by means of imbibition experiment [5]. The rate of water suction was found to be positively dependent on volume of capillary pores. The reasonable linear fit provided variation on well known Arrhenius plot; the logarithm of measured κ_{app} was plotted as function of reciprocal volume of pores of diameter 1 to 100 μm (**Fig. 3**). This dependences fall into straight lines which are able to be described by semiempirical Eq. 2. The meaning of constants A and B is not physically clear and correct, but it may be assumed, that slope B depends on properties of the material, such are its surface energy and morphology of the pore system.

$$\kappa_{app} = A \cdot \exp\left\{-\frac{B}{V_{1-100}}\right\} \qquad \text{(Eq. 2)}$$

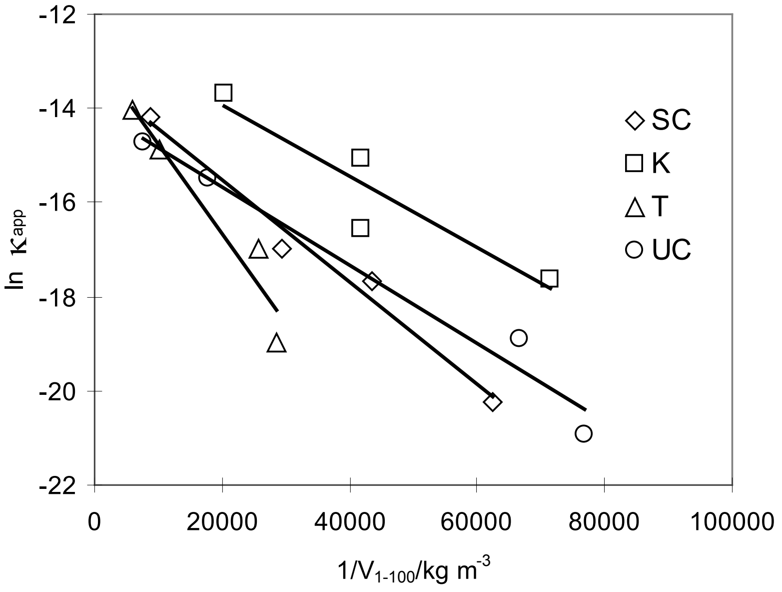

Fig. 3 Measured values of apparent moisture diffusion coefficients plotted as function of capillary pore volume.

Discussion

The characterization of pore system of the studied materials showed that three independent degradation processes are taking place in the materials under thermal load. The binder structure, formed by CSH, CAH and portlandit decomposes thermally and converts to calcite and clinker minerals. The binder also sinters during the thermal load and the gel pores diminish. On the other hand the aggregates expand during the annealing which causes the loss of contact between binder and aggregates. The thermal decomposition of PVA and aramid reinforcing fibers takes place which results to increase of volume of the largest pore fraction. The carbon and glass fibers were found to be sufficiently stable under the thermal load. The pore size distribution analysis revealed that degradation processes of matrix (gel sintering and aggregates expansion) influence the pore system more significantly than the degradation of thermally unstable fibers. Moreover the channels formed after burn out of the fibers are too large to contribute to capillary action. The thermal stability of fiber reinforced composites could be enhanced by applying of principles used in production of refractory cement: employing of aluminate cement and some aggregates with lower thermally induced volume changes than quartz.

The experimentally determined apparent coefficients of moisture diffusivity were correlated by volume of capillary pores found in the materials. Very simple semiempirical equation describing this relationship was proposed. The physical meaning of the constants in this equation has to be clarified in future.

Conclusions

Three independent degradation processes were identified in thermally loaded fiber reinforced cement composites. The decomposition of cement binder was observed by means of chemical changes as well as by parallel sintering of the gel structure. When the samples were loaded at 1000˚ C the gel pores diminished completely. The most important – from the point of view of transport properties – is the second degradation process what is loss of contact between binder and aggregates due to the thermal expansion of aggregates. It leads to formation of high amount of interconnected capillary pores which enable intensive transport of liquid water through the material. The decomposition of thermally unstable fibers (PVA, aramide) is responsible for the formation of large channels in the composites, but their contribution to enhanced transport of liquid water is negligible because of the large diameter of these channels.Their contribution to vapor transport would be more important.

Acknowledgement

This research has been supported by Czech Ministry of Education, Youth and Sports, under Project No. MSM 6840770031.

References

[1] Keppert, M., 2008. Application of Mercury Intrusion Porosimetry in Building Materials Science. In: proceedings of 2nd on Experimental and Computational Methods for Directed Design and Assessment of Functional Properties of Building Materials, 6th October 2008. Ed: Zbyšek Pavlík a Milena Pavlíková. Czech Technical University in Prague, Prague.

[2] Kumaran, M. K., 1994. Moisture Diffusivity of Building Materials from Water Absorption Measurements. IEA Annex 24 Report T3-CA 94/01, Ottawa.

[3] Keppert, M., Vejmelková, E., Konvalinka, P., Toman, J., Černý, R., 2008. Relations between material's texture and its hygric and thermal properties. In: proceedings of 2nd on Experimental and Computational Methods for Directed Design and Assessment of Functional Properties of Building Materials, 6th

October 2008. Ed: Zbyšek Pavlík a Milena Pavlíková. Czech Technical University in Prague, Prague.

[4] Demidenko, N. I., Telnova, G. B., 2004. Microstructure and properties of a Material based on Natural Wollastonite. Glass and Ceramics 61.

[5] Vejmelková, E., Konvalinka, P., Černý, R., 2007. Properties of Glass and Polypropylene Hybrid Fiber Reinforced Cement Composite. In: Contributions to Numerical and Experimental Investigation of Building Materials and Structures. Ed: Petr Konvalinka. Czech Technical University in Prague, Prague.

THICKNESS EFFECT CURVE IN THE ASPECT OF ANALYTICAL AND NUMERICAL EVALUATIONS

Piotr Koniorczyk, Janusz Zmywaczyk

Institute of Aviation Technology, Department of Mechatronics,
Military University of Technology, Kaliskiego 2, 00-908 Warsaw, Poland
email: piotr.koniorczyk@wat.edu.pl, janusz.zmywaczyk@wat.edu.pl

Abstract

This paper concerning the problem of analytical and numerical modelling of ‘thickness effect curve’ under steady-state conditions for interactive optical media, where simultaneous radiation and conduction heat transfer occurs. Considerations are performed for a 1-D steady-state heat transfer model in an absorbing, emitting and anisotropically scattering grey medium confined by grey surfaces. To find dependence of the radiative thermal conductivity $k_r(l)$ on the sample thickness l, a finite difference method (FDM) together with a discrete ordinate method (DOM) and the Henyey-Greenstein phase function were used iteratively.

Key words: radiative-conductive heat transfer, thermal conductivity, absorption, emission and scattering of radiation, thickness effect curve, phase function

1 Introduction

The results of modelling and numerical simulation of the effect of reduction in thermal conductivity $k(l)$ for small thickness samples of semitransparent media in case when enclosing the medium surfaces are grey and diffuse are reported. The subject of an interest is isotropic and homogeneous material with thermal conductivity dependence $k(l)$ on the sample thickness l obtained as a result of measuring it under conditions of a definite value (a few degrees) of the temperature difference ΔT between the heater T_2 and the cooler T_1 of the plate apparatus – Figs. 1÷2. The visible in Fig. 2 two points marked as A and B correspond to the two different sample thicknesses l_A and l_B.

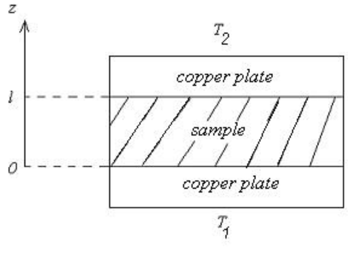	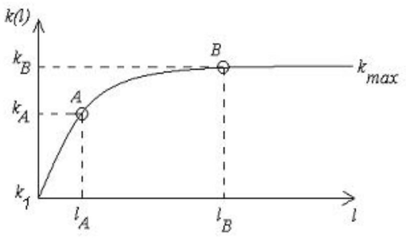
Fig. 1 The sample of thickness l between the heater T_2 and the cooler T_1 of the plate apparatus	Fig. 2 Effect of reduction in thermal conductivity $k(l)$ in small thickness sample: k_1 - conductive component of thermal conductivity, $k_r(l) = k(l) - k_1$

2 Analytical model

Let us assume that the material with different forms of the curve of thermal conductivity $k(l)$ dependence on the sample thickness l having also different values of the limiting sample thickness l_{gr}, above which the reduction of $k(l)$ may be neglected, is considered. The jump-like relation $k(z)$, presented in Figs 3 and 4, shows the model dependence on the thermal conductivity $k(z)$ (for a given sample thickness l) [1] from which it follows that $k = k_1 + k_r$ where, in particular case, at z=0 and T=T_1 we have $k(z=0)=k_1$. Similarly, for the other side of the sample at z=l and T=T_2 we have also $k(z=l)=k_1$ (Figs. 3 and 4). Each curve $k(z)$ can be divided into three parts, the first and the third of which correspond to the region from z=0 to z=l_{gr} where $k = k_1$ and from z=l-l_{gr} to z=l where $k = k_1$, too. The second corresponds to the region from z=l_{gr} to z=l-l_{gr} where $k = k_2$. Now it is possible to determine $k(l)$ dependence for a sample divided into three layers, where the thickness of the particular layer equals l_{gr}, l-$2l_{gr}$, l_{gr}, respectively, by solving the linear 1-D steady-state heat conduction problem for each of the particular region [1]:

$$k(l)=\frac{k_1k_2l}{2l_{gr}k_2+(l-2l_{gr})k_1}=\frac{k_1k_2}{2\frac{l_{gr}}{l}(k_2-k_1)+k_1}, \tag{1}$$

where l_{gr} is a function of absorption coefficient a and sample thickness l. Then the radiative heat flux density $\dot{q}_r(l)$ can be calculated from the following expression [1]:

$$\dot{q}_r(l)=k_r\frac{dT_{II}}{dz_1}\frac{(l-2l_{gr})}{l}=(k_2-k_1)\cdot\frac{T_2-T_1}{(l-2l_{gr})\left(1-\frac{k_2}{k_1}\right)+\frac{k_2}{k_1}l}\cdot\frac{(l-2l_{gr})}{l} \tag{2}$$

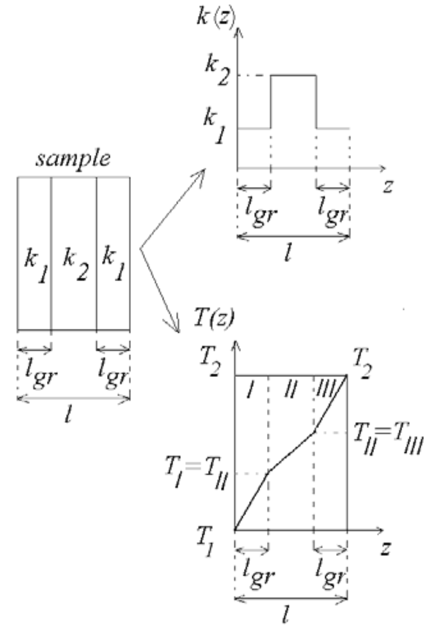

Fig. 3. The model of dependence of $k(z)$ (for the sample thickness l) accepted for analytical considerations [1]

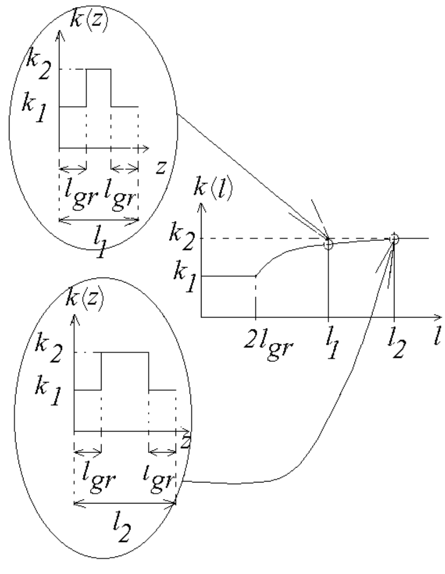

Fig. 4. Plot of $k(l)$ along different sample thickness l with marked two points corresponding to the two different sample thicknesses l_1 and l_2 [1]

When the sample thickness l is getting closer to $l=2l_{gr}$, the mean free path of photons becomes comparable to the space between plates and some of the photons leaving the hot surface manage to reach almost or actually the cold surface before they become absorbed. In our opinion such a situation permits us to replace l_{gr} with expression $l'_{gr} = l_{gr}\left(1-e^{-a\cdot b\cdot l}\right)$, where b is a constant parameter [1]. After doing some algebraic manipulations, one can obtain the following condition for the limiting thickness of the sample l_{gr} as well as for a new form of expressions for $k(l)$ and $\dot{q}_r(l)$ [1]:

$$l_{gr} = \frac{k_1}{3ak_1 + 4\sigma_B n^2 (T_1+T_2)(T_1^2+T_2^2)}, \tag{3}$$

$$k(l) = \frac{k_1(k_1+k_{r\infty})}{2\frac{l_{gr}}{l}\left(1-e^{-\frac{l}{2l_{gr}}}\right)k_{r\infty}+k_1} \tag{4}$$

$$\dot{q}_r(l) = \frac{(T_2-T_1)k(l)\left[k_{r\infty}-k_1\left(\frac{k_1+k_{r\infty}}{k(l)}-1\right)\right]}{l(k_1+k_{r\infty})}, \tag{5}$$

$$\left(k(l)\right)_{l\to\infty} = k_1 + k_{r\infty} = k_2\,, \tag{6}$$

$$k_{r\infty} = \frac{16\sigma_B n^2}{3a}\cdot\frac{1}{4}(T_1+T_2)(T_1^2+T_2^2), \tag{7}$$

where: σ_B is the Stefan-Boltzmann constant ($\sigma_B = 5.67\cdot 10^{-8}\ \mathrm{W\,m^{-2}\,K^{-4}}$), n is the index of refraction, k_1 denotes the conductive component of thermal conductivity [5-8]. Some preliminary calculations of $k(l)$ and $\dot{q}_r(l)$ obtained both from the numerical solution of the Radiative Transfer Equation (RTE – exact formulation) coupled with 1-D heat conduction in an emitting-absorbing medium and from analytical model are shown in Figs. 5 and 6 [1].

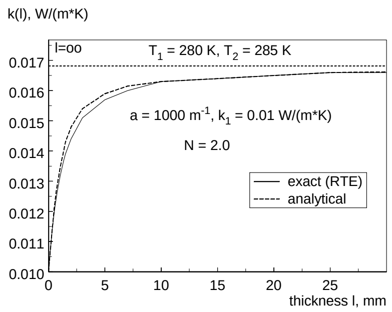	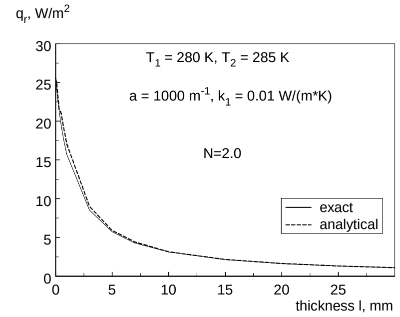
Fig. 5. Thermal conductivity *k(l)* obtained from RTE vs. analytical model [1]	Fig. 6. Radiative heat flux density $\dot{q}_r(l)$ obtained from RTE vs. analytical model [1]

The biggest discrepancy between the precise numerical results and the given model occurs when the conduction to radiation parameter N equals 0.02 [1]. It is not surprising that in that case the biggest non-linearity of temperature distribution $T(z)$ inside the sample occurs along its thickness. It has to be underlined that all calculations and analytical model have been made for emissivity of the walls $\varepsilon_1=\varepsilon_2=\varepsilon=1$. When the surfaces enclosing the medium are grey and are diffuse reflectors, the results of calculations which were made to include the influence of the surface emissivity on the $k(l)$ are illustrated in Fig. 7. In case of very low emissivity of the wall one can observe that curves $k(l)$ reveal characteristic inflexion in the range of small thickness of the samples l corresponding to the maximum of curves $\dot{q}_r(l)$. The analytical model takes into account both inflexion of curves $k(l)$ as well as maximum of $\dot{q}_r(l)$. In the vicinity of the sample surface the energy transferred by conduction is a larger fraction of the total energy flux than in the region located farther from the walls. Thus temperature gradient in the neighborhood of the walls increase with the decreasing emissivity, and therefore the conductive flux in these regions becomes a larger fraction of the total energy flux. In our opinion such situation permits us to replace l by $l' = l + 2l'_{gr}$ and l'_{gr} by the expression $l'_{gr} = l''_{gr}\left(1-e^{-a\cdot l'}\right)$ [2]. Just like before performing some algebraic rearrangements one can obtain the following condition for the limiting thickness of the sample l''_{gr}

$$l''_{gr} = \frac{1-\sqrt{\dfrac{l_{gr}\left[3a+\dfrac{4\sigma_B n^2}{k_1}\left(T_1+T_2\right)\left(T_1^2+T_2^2\right)\right]}{\dfrac{2}{\varepsilon}-1}}}{2a} = \frac{1-\sqrt{\dfrac{\varepsilon}{2-\varepsilon}}}{2a} \qquad (8)$$

and a new form of expressions for $k(l)$ and $\dot{q}_r(l)$ [2]:

$$k(l) = \frac{k_1\left(k_1+k_{r\infty}\right)lG(l)}{2l''_{gr}\left(1-e^{-a\cdot l}\right)\left\{\left(k_1+k_{r\infty}\right)G(l)-H(l)\right\}+lH(l)} \qquad (9)$$

$$G(l) = l - 2l''_{gr}\left(1-e^{-a\cdot l}\right),\ H(l) = 2l_{gr}\left(1-e^{-\frac{G(l)}{2l_{gr}}}\right)k_{r\infty} + k_1 G(l),\ \dot{q}_r(l) = \left(k(l)-k_1\right)\frac{\Delta T}{l} \qquad (10)$$

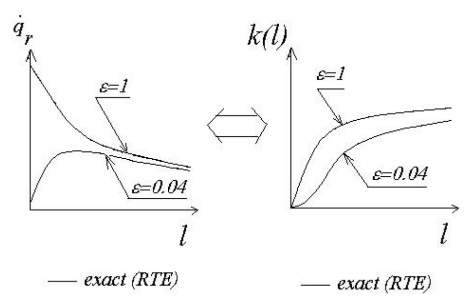

Fig. 7. Plot of thermal conductivity $k(l)$ and radiative heat flux density $\dot{q}_r(l)$ along different sample thickness l according to RTE calculations with surface emissivity less than one [2]

In order to verify the proposed method some preliminary calculations of $k(l)$ and $\dot{q}_r(l)$ were carried out [2]. Dependencies of $k(l)$ and $\dot{q}_r(l)$ on the sample thickness l obtained from RTE and from analytical model are shown in Figs. 8 and 9. With the increase of the parameter N the discrepancies between the analytical functions of $k(l)$, $\dot{q}_r(l)$ and the exact results decrease and for N=2 the errors are acceptable [2].

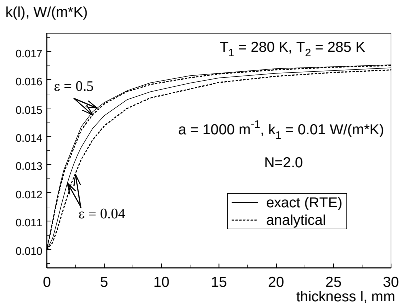

Fig. 8. Dependence of *k(l)* obtained from RTE and analytical model: $\varepsilon_1=\varepsilon_2=\varepsilon$ = 0.5 or 0.04 [2]

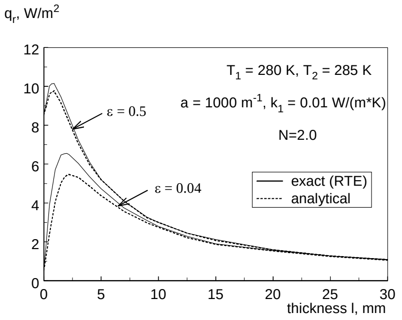

Fig. 9. Dependence of $\dot{q}_r(l)$ obtained from RTE and analytical model: $\varepsilon_1=\varepsilon_2=\varepsilon$ = 0.5 or 0.04 [2]

3 Numerical model

A model of 1-D steady-state combined conductive-radiative heat transfer in the absorbing, emitting and anisotropically scattering medium confined between grey surfaces has been considered. To find the radiative thermal conductivity dependence $k_r(l)$ (for a sample thickness l) and dependence of the radiative heat flux density $\dot{q}_r(l)$ upon the sample thickness l, a finite difference method together with the discrete ordinate method and the Henyey-Greenstein phase function expanded into Legendre polynomials have been used iteratively [3, 4]. The Henyey-Greenstein phase function $P(\cos\Theta)$, where Θ denotes the scattering angle (angle between incident and scattered direction of radiation), allows us to understand the influence of the asymmetry parameter g on the shape of the scattering phase function [4]. When the asymmetry parameter g increases, the anisotropic scattering radiation increases too and, at the same time, the range of influence of scattering extends. Parameter of asymmetry g defines forward scattering for g=1, backward scattering for g=-1 and isotropic scattering for g=0. Other values of the asymmetry parameter g which belong to the interval $g\in[-1; 1]$ are also possible [3, 4]. In our considerations it is assumed that the conductive component of thermal conductivity $k_1 = k_c$ is constant. The radiative properties of the medium such as the absorption coefficient a, extinction coefficient κ and index of refraction n are also constant. The governing equation for a non-grey medium which represents energy conservation in 1-D formulation of the coupled conduction-radiation problem is given by [3, 4, 5-8]:

$$\frac{d}{dz}\left(k_c \frac{dT}{dz}\right) = \frac{d\dot{q}_r(z)}{dz}, 0 < z < l \tag{11}$$

$$T(z=0) = T_1, \tag{12}$$

$$T(z=l) = T_2, \tag{13}$$

$$\dot{q}_r(z) = 2\pi \int\limits_0^{\infty} \int\limits_{\mu=-1}^{\mu=+1} I_\lambda(z,\mu)\,\mu\,\mathrm{d}\mu\,\mathrm{d}\lambda\,, \tag{14}$$

$$\begin{aligned}\mu \frac{dI_\lambda(z,\mu)}{dz} &= a_\lambda(\mu)\; I_{b,\lambda}(T(z)) - (\kappa_\lambda(\mu))\, I_\lambda(z,\mu) + \\ &+ \frac{1}{2}\int_{-1}^{+1} \sigma_{s,\lambda}(\mu')P(\mu' \to \mu) I_\lambda(z,\mu')d\mu'\end{aligned} \tag{15}$$

$$I_\lambda(0,\mu) = \varepsilon_1 I_{b,\lambda}(T_0) + 2(1-\varepsilon_1)\int\limits_{-1}^{0} I_\lambda(0,\mu')\mu' d\mu', \quad 0 < \mu \le 1 \tag{16}$$

$$I_\lambda(l,\mu) = \varepsilon_2 I_{b,\lambda}(T_l) + 2(1-\varepsilon_2)\int\limits_{0}^{+1} I_\lambda(l,\mu')\mu' d\mu', \quad -1 \le \mu < 0 \tag{17}$$

$$I_{b,\lambda} = \frac{C_1}{\lambda^5[\exp(C_2/\lambda T)-1]},\; I_b(T) = \int\limits_{\lambda=0}^{\infty} I_{b,\lambda}(T)d\lambda = \frac{1}{\pi}\sigma_B T^4\,, \tag{18}$$

$$C_1 = 1.19\cdot 10^{-16}\ \mathrm{W\cdot m^2},\; C_2 = 0.014388\ \mathrm{m\cdot K}\,, \tag{19}$$

$$\kappa(\mu) = a(\mu) + \sigma_S(\mu),\; \mu = \cos\theta\,, \tag{20}$$

where: I_λ is the spectral radiation intensity, Wm^{-2}; $I_b = n^2\sigma_B T^4/\pi$ stands for the blackbody intensity, Wm^{-2}; θ is the polar angle and σ_s is the scattering coefficient, m^{-1} [5-8].

In order to elucidate the physics of the analyzed complex phenomenon of simultaneous conduction and radiation in an emitting, absorbing and anisotropically scattering medium confined between grey surfaces some preliminary calculations of $k_r(l)$ and $\dot{q}_r(l)$ were carried out [3, 4]. The initial data for performing numerical calculations are enclosed in Tab. 1. Data used in calculations were chosen in such a way that the impact of albedo ω and the parameter of asymmetry g on $k_r(l)$ and $\dot{q}_r(l)$ thickness dependences are visible. Finally the calculations were performed using 6 fluxes in the conductive-radiative heat transfer model. Six fluxes turned out, in this case, to be quite enough to obtain an engineering accuracy of calculations [4]. The dimensionless conduction to radiation parameter N=8 was taken big enough so as to avoid instability of numerical calculations. The results of calculation are shown in Figs. 10÷13 [3, 4].

Table 1. Data for performing numerical calculations of $k_r(l)$ and $\dot{q}_r(l)$ [3, 4]

$\kappa = 1000\ m^{-1}$, $k_1 = k_c = 0.1\,Wm^{-1}K^{-1}$, $\omega \in [0;1]$, n=1, T_1=280 K, T_2=380 K, N=8	
$\varepsilon_1 = \varepsilon_2 = \varepsilon = 1$	$\varepsilon_1 = \varepsilon_2 = \varepsilon = 0.04$
$\omega = \in \{0.0,\ 0.3,\ 0.5,\ 0.9,\ 1.0\}$, g=-0.8 or g=+0.8	
$P(\cos\Theta) = (1 - g^2)/(1 + g^2 - 2g\cos\Theta)^{3/2}$	
ε - emissivity of the walls, $\omega = \sigma_S / \kappa$ - single scattering albedo, $\kappa = a + \sigma_S$ - extinction coefficient, m^{-1}, σ_S - scattering coefficient, m^{-1}	

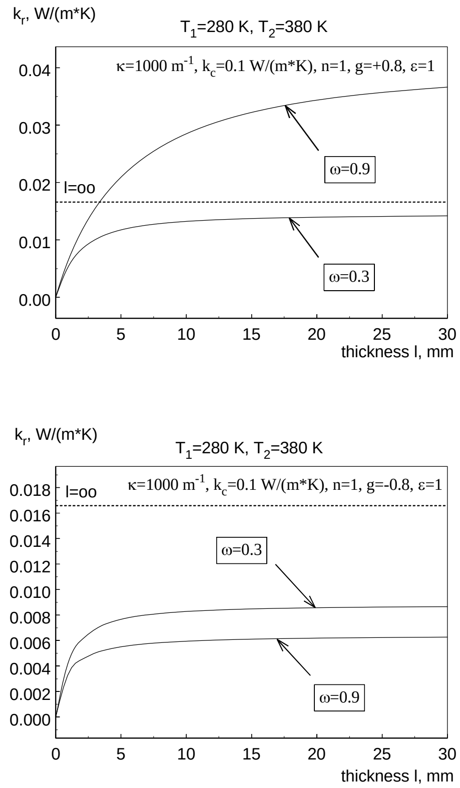

Fig. 10. Dependence of $k_r(l)$ for anisotropic scattering: g=±0.8, $\omega \in \{0.3, 0.9\}$, ε_1=ε_2=ε = 1.0 [4]

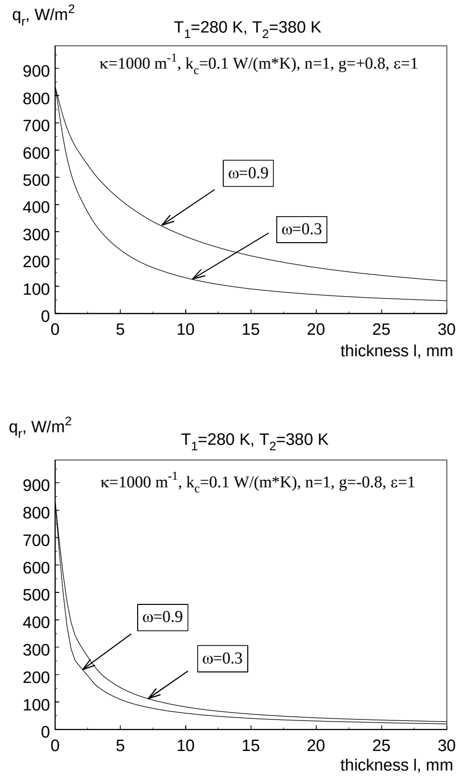

Fig. 11. Dependence of $\dot{q}_r(l)$ for anisotropic scattering: g=±0.8, $\omega \in \{0.3, 0.9\}$, ε_1=ε_2=ε = 1.0 [4]

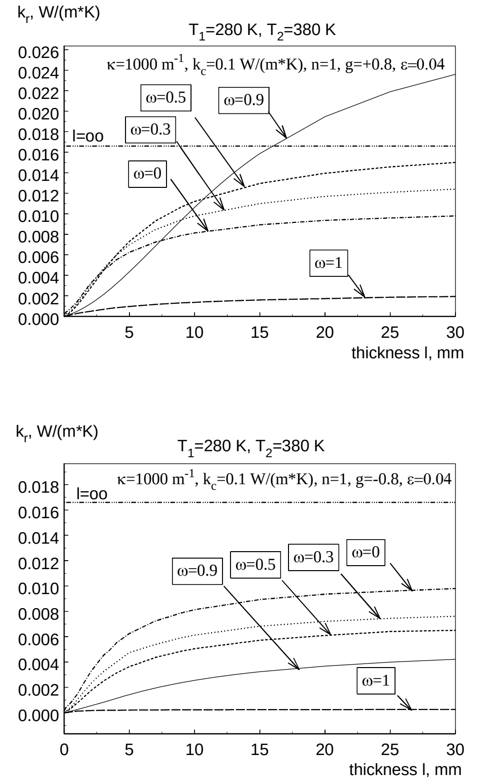

Fig. 12. Dependence of $k_r(l)$ for anisotropic scattering: $g=\pm0.8$, $\omega \in \{0.0, 0.3, 0.5, 0.9, 1.0\}$, $\varepsilon_1=\varepsilon_2=\varepsilon = 0.04$ [4]

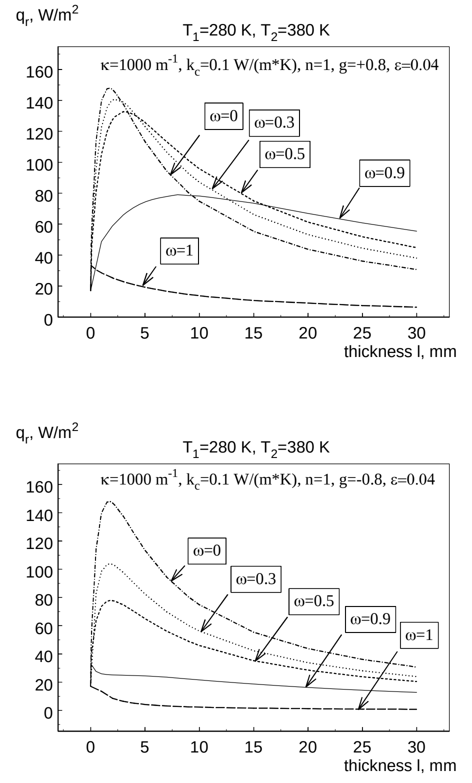

Fig. 13. Dependence of $\dot{q}_r(l)$ for anisotropic scattering: $g=\pm0.8$, $\omega \in \{0.0, 0.3, 0.5, 0.9, 1.0\}$, $\varepsilon_1=\varepsilon_2=\varepsilon = 0.04$ [4]

The most interesting situation occurs when anisotropic scattering is considered [3, 4]. The higher value of albedo ω the more important role plays the parameter of asymmetry g. And so for $\omega = 0.3$ the influence of the coefficient g on the $k_r(l)$ and $\dot{q}_r(l)$ dependencies is relatively small – Figs. 10÷13. The curves $k_r(l)$ are places below line l_∞ - Figs. 10 and 12. For $g = +0.8$ that is for strong scattering the curves $k_r(l)$ are close to the values $k_{\max} = k_{Ross} = \dfrac{16 n^2 \sigma_B T^{*3}}{3\kappa}$ (where: $T^*=T_2$) marked as l_∞ - Figs. 10 and 12 [3, 4]. For $g = -0.8$ curves $k_r(l)$ are significantly below the line l_∞ [3, 4]. The situation changes totally when the albedo is equal to $\omega = 0.9$. For $g = +0.8$ the curves $k_r(l)$ lie significantly above the line l_∞ [3, 4]. This case plays a fundamental role in real experiment. It turns out that the values of radiative component of thermal conductivity $k_r(l)$ may be measurable and the role of heat transfer by radiation, even in relatively low temperatures, might be significant.

4 Conclusions

The results of modelling and numerical simulation of the effect of reduction in thermal conductivity $k(l)$ in small thickness samples of semitransparent media have inspired the authors to develop a possible precise enough analytical and numerical model for the abovementioned effect. It is worth noticing that the analytical model works qualitatively well [1÷4]. In case of numerical evaluation the stress was put on the method of solving the coupled radiative-conductive heat transfer problem using FDM to find temperature fields along the layer thickness of considered material together with DOM to find the radiation intensity which were used to calculate the source term appearing in the governing equation of energy conservation. The analysis of the obtained numerical results enabled to draw practical conclusions concerning the experimental measurements with respect to the effect of reduction in thermal conductivity $k(l)$.

References

[1] P. Koniorczyk, J. Zmywaczyk: *Approximate analysis of combined heat radiation and conduction in aspect of the flat sample thickness effect on heat conduction of semitransparent media,* Archives of Thermodynamics, Vol. 25(2004), No. 2, pp. 81-93

[2] P. Koniorczyk, J. Zmywaczyk: *Approximate analysis of influence of surface emissivity on combined heat radiation and conduction in aspect of the flat sample thickness effect on heat conduction of semitransparent media,* Archives of Thermodynamics, Vol. 26(2005), No. 4, pp. 3-16

[3] P. Koniorczyk, J. Zmywaczyk: *Analysis of thermal conductivity reduction in grey medium using a dfiscrete ordinate method and the Henyey-Greenstein phase function for absorbing, emitting and anisotropically scattering media,* Archives of Thermodynamics, Vol. 29(2008), No. 2, pp. 47-60

[4] P. Koniorczyk, J. Zmywaczyk: *Investigations of radiative-conductive heat transfer,* monograph, Military University of Technology, Warsaw, Poland, 2008 (in Polish)(186 pages)

[5] M.F. Modest: *Radiative Heat Transfer,* McGraw Hill International Edition, 1993

[6] H. Reiss: *Radiative Transfer in Nontransparent, Dispersed Media,* Springer – Verlag, 1988

[7] H.C. Hottel, A.F. Sarofim: *Radiative Transfer,* McGraw Hill IBook Company, New York, 1967

[8] R. Siegel, J.R. Howell: *Thermal radiation heat transfer,* McGraw Hill Book Company, New York, 1972

MOISTURE DEPENDENCY OF THERMAL CONDUCTIVITY OF CERAMIC BRICKS

Olga Koronthalyova

Institute of Construction and Architecture, Slovak Academy of Sciences, Dubravska 9, 845 43 Bratislava, Slovakia. e-mail: usarkoro@savba.sk, usarmat@savba.sk

Abstract:
Measurement of thermal conductivity moisture depencency of commonly manufactured burnt clay bricks was performed using an impulse technique. The relationships between microstructure and moisture dependency of thermal conductivity were analysed. The using formely developed microstructural model for the dry composite materials was disscussed and its modiffication was suggested.

Keywords:
Thermal conductivity, moisture dependency, clay brick, porosity, model

INTRODUCTION

Porous building materials generally consist of solid, gaseous and liquid phase. The effective thermal conductivity of the porous material depends on thermal conductivities of particular phases, their volume portion, their distribution and interconnection.

Burnt clay bricks are common building material manufactured from the clay-sand mixture (the portion of the sand can be from 30 to 50%). The burning takes place at temperatures 900 - 1000°C. Their microstructure is dependent of the particle size distribution, mineralogical and chemical composition, type of burning additives and the way of burning [2, 3]. The thermal conductivity of clay brick body can also vary depending on its factual mineralogical and chemical composition.

In the previous works [5], [6] the relationship between the thermal conductivity and pore structure parameters for dry CSH-based materials and ceramic bricks was analysed. It was found out that in the first approximation the thermal conductivity of tested materials was proportional inversely to the second power of their total porosity. It was also shown that the thermal conductivity of the tested materials could be modeled by serial configuration of the high conductivity fraction (solid phase fraction) and low conductivity fraction (pore volume fraction + interfacial transition zone) weighted by the power function of their volume fractions. The exponents of the power function were determined using the particular components fractal dimensions.

In the paper the moisture dependence of effective thermal conductivity of burnt clay bricks was measured and analysed. In the first step the possibility of using the formely developed microstructural model [5], [6] was investigated. For the more precise modelling of the moisture dependence of thermal conductivity the lattice-type periodic model [9, 10] was used for an expression of thermal conductivity of moist pore volume (including the interfacial transition zone).

THEORY

Macroscopic thermal conductivity of composite material can be expressed using the thermal conductivities of particular components.

Wiener bounds

The lower and upper limits of effective thermal conductivity of moist composite material can be evaluated by Wiener bounds. Their derivation is based on assumption of strictly parallel or serial setting of particular phases [13]. In case the material consists of three phases – solid, air and water the Wiener upper bound is given by relation (1):

$$\lambda_{up} = \lambda_s \cdot (1-\Phi) + \lambda_w \cdot u_v + \lambda_a \cdot (\Phi - u_v) \tag{1}$$

and the Wiener lower bound by relation (2):

$$\lambda_{low} = \frac{1}{\frac{(1-\Phi)}{\lambda_s} + \frac{u_v}{\lambda_w} + \frac{(\Phi - u_v)}{\lambda_a}} \tag{2}$$

Where λ_s, λ_w, λ_a are thermal conductivity of solid, water and air respectively, Φ is total porosity and u_v is volume portion of moisture content.

Microstructural model of effective thermal conductivity

For the continuous high conductivity components fractions with the discrete low continuity components the macroscopic thermal conductivity can be modeled by the summation of particular components:

$$\lambda = \sum_i \lambda_i \cdot (\Phi_i - \Phi_{i,crit})^{n_i} \tag{3}$$

Where λ_i is thermal conductivity of component,
Φ_i is component volume fraction,
$\Phi_{i,crit}$ is the critical volume needed for a connected network to be formed through the material,
$n_i = 1 + FD$,
FD is the fractal dimension of the component or pore volume fraction [5].
In case of parallel configuration of the components, $n_i = 1$.

In case of discrete high conductivity components in the continuous low conductivity or pore volume fractions the following relation can be applied:

$$\lambda = \frac{1}{\sum_i \frac{\left(\Phi_i - \Phi_{i,crit}\right)^{n_i}}{\lambda_i}} \tag{4}$$

Where $n_i = 1$for serial configuration of the components, $n_i > 1$ in case of dispersion of the low conductivity component.

In the previous works [5], [6] the relations between the thermal conductivities of dry composite materials and their total porosity were studied. The following empirical relation between thermal conductivity and total porosity was found out for ceramic bricks and CHS based materials:

$$\lambda = \frac{1}{\dfrac{\Phi^2}{0.064}} \tag{5}$$

It was also shown that the thermal conductivity of the tested composite materials could be modeled by serial configuration of the high conductivity fraction (solid phase fraction) and low conductivity fraction (pore volume fraction + interfacial transition zone) weighted by the power function of their volume fractions. It was supposed that the interfacial zone volume fraction represented 10% of the total porosity in average [14]. As the thermal conductivity of low conductivity zone the value λ_{low} = 0.064 W/mK, corresponding to the value measured for the pure CHS – xonotlite [4], was considered. In this highly porous material the volume portion of solid phase is also about 10%. The resultant thermal conductivities of dry material was given by following relation:

$$\lambda = \frac{1}{\dfrac{(1-1.1\cdot\Phi)^{n1}}{\lambda_{high}} + \dfrac{(1.1\cdot\Phi)^{n2}}{\lambda_{low}}} \tag{6}$$

The exponent of solid phase was estimated as $n_1 \approx 1.0$, the exponent of pore volume fraction was estimated as $n_2 \approx 2.7$ [6].

Lattice-type periodic model

In case of two-phase system created by continuous medium with thermal conductivity λ_0 and dispersed phase with thermal conductivity λ_1 and on condition that dispersed phase is created by spherical particles of the same size and they are dispersed regularly the resultant relation for effective thermal conductivity λ_{ef} can be written as [9, 10]:

$$\lambda_{ef} = \lambda_0 \cdot \left[1 + 3.844 \cdot \left(\frac{\lambda_1 - \lambda_0}{\lambda_1 + 2\lambda_0}\right) \cdot \left(\frac{\Phi_1}{\Phi_0}\right)^{2/3}\right] \tag{7}$$

Where Φ_1 is volume portion of dispersed phase and Φ_0 is volume portion of continuous medium. The equation (7) was derived on condition of simple cubic lattice, taking into account mutual interaction of dispersed phase up to fourth neighbour. It is valid for case of small dispersion, i. e. on condition that $(\Phi_1/\Phi_0)^{2/3}$ lies between 0 and 0.4 [10]. When $(\Phi_1/\Phi_0)^{2/3}$ lies between 0.4 and 1.0, the effective thermal conductivity is given by relation (8) [10]:

$$\lambda_{ef} = \lambda_1 \cdot \left[1 + 3.844 \cdot \left(\frac{\lambda_0 - \lambda_1}{\lambda_1 + 2\lambda_0}\right) \cdot \left(1 - \left(\frac{\Phi_1}{\Phi_0}\right)^{2/3}\right)\right] \tag{8}$$

Practically the same relation with slightly different coefficient (3.74 instead of 3.844) was derived in [11] for case of cylindrical lattice structure. The relations (7) and (8) has been used in [10] for expression of thermal conductivity of moist air in pore system of sand.

EXPERIMENTAL

The measurements were done for four types of burnt clay bricks.

The pore size distribution, the open porosity and the specific surface area of pores were studied using the mercury intrusion porosimetry (MIP): the high-pressure porosimeter mod. 2000 and macro-porosimeter mod. 120 (both Carlo Erba, Milan). This system enables determination of micropores with the radius from 3.7 up to 7500 nm and of larger pores with a radius up to 0.06mm. The porosimetry measurement was carried out by the fraction of broken dried (up to 105°C) samples. Specific surface area of pores was determined using the cylindrical model.

The open porosity was also determined from the suction test.

The thermal conductivity was measured by transient pulse method using the commercial device ISOMET 2104 with the surface probe API 210412. The used surface probe is suitable for thermal conductivities in the range from 0.3 to 2 W/m·K. The measurement is based on the analysis of the temperature response of the practically semi-infinite body to the heat flow impulse. The heat flow is generated by electrical heating using a resistor heater having a direct thermal contact with the surface of the sample. The declared precision of the measurement is about 5%. The mean values from five measurements were taken into account in analysis of results.

The interval of measured moisture contents of samples was form 0 to 9% (by volume). It follows that for the considered materials the maximum volume fraction of moisture in pore space was 0.23 and therefore the condition of small dispersion water in pore air was fulfilled. The samples were moistened and conditioned for at least 24 days to achieve homogeneous moisture content distribution. The moisture content was checked before and after measurement gravimetrically.

RESULTS AND DISCUSSION

The total porosity, specific surface area and pore radius median values, determined by MIP [1] as well as the values of open porosity, bulk and true density are in Tab. 1. Because for the clay bricks the values of open porosity and total porosity are practically identical [3], the values of open porosity were used in the following analysis of the relationships between the thermal conductivity and microstructure.

Table 1. Basic material parameters of tested bricks

Material	Bulk density [kg/m^3]	Total porosity (MIP) [-]	Open porosity (suction test) [-]	True density [kg/m^3]	Specific surface area [m^2/g]	Pore radius median [nm]
Brick D	1724	-	0.3	2460	-	-
Brick L	1710	0.28	0.33	2550	2.39	559.1
Brick P	1377	0.50	0.42	2370	8.07	535.1
Brick S	1426	0.43	0.44	2590	1.44	542.9

In the first step of modelling the tested bricks thermal conductivity moisture dependence the possibility of using formely developed microstructural model for the dry composite materials (relations (5) and (6)) was tested. In case of moist bricks instead the total porosity the free porosity – the difference between the total porosity and volumetric moisture content was used. In Fig. 1 the relationship between the measured thermal conductivity and total / free porosity is compared with the calculated values according relations (5) and (6). The considered thermal conductivity of the solid phase λ_{high} (thermal conductivity of clay brick body with density equal to ca 2500 kg/m^3 - see Tab. 1) was about 1.5 W/m·K [8]. As can be seen from the Fig. 1 the thermal conductivity / free porosity dependence of the tested bricks can be in the first approximation expressed by empirical relation (5) as well as by the serial model (6) similarly like in case of dry materials.

The more detailed representation of the measured thermal conductivities of particular types of moist bricks vs. their modeled values is shown in Fig. 2.

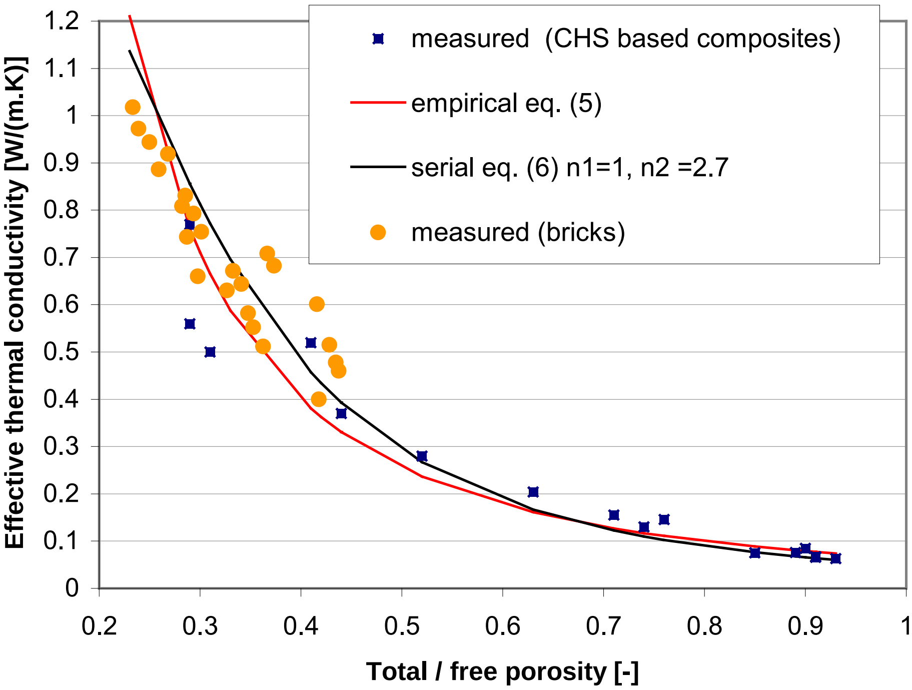

Fig. 1 Thermal conductivities of clay bricks and CHS based materials vs. total / free porosity. Comparison of the measured values with empirical approximation (5) and serial model (6)

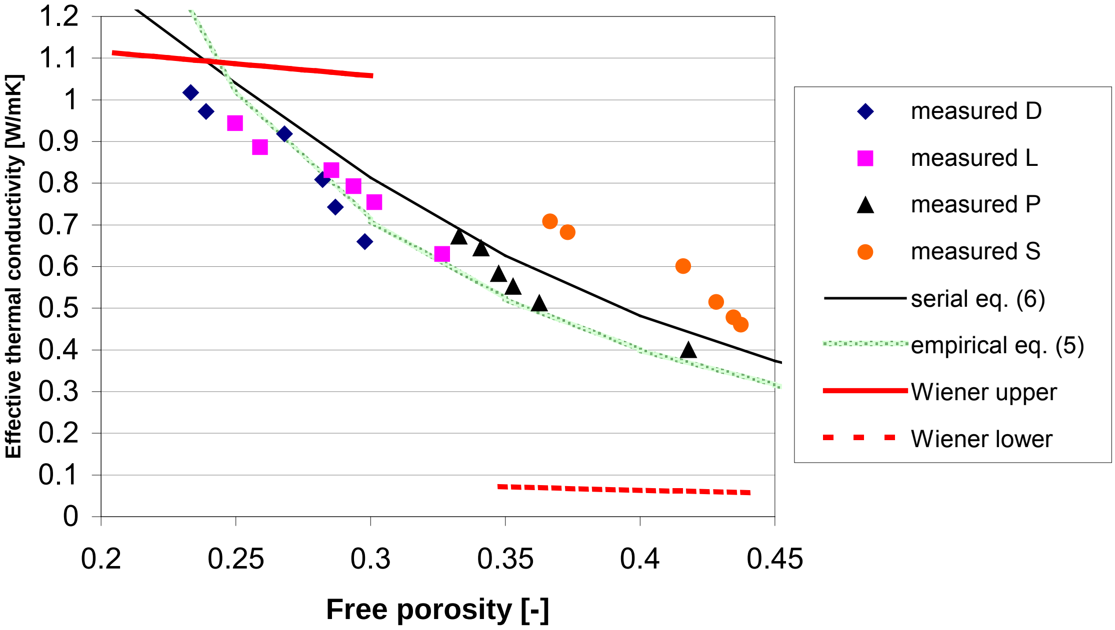

Fig. 2 Thermal conductivities of moist clay bricks vs. free porosity. Comparison of the measured values with empirical approximation (5), serial model (6) and Wiener bounds

As can be seen from the Fig. 2, in case of bricks D, L, P the measured values of clay bricks are in a relative satisfactore agreement with the relations (5) and (6) up to the free porosity value ca 0.26. For the lower values of free porosity the relations (5) and (6) predicted values are in contradiction with the upper Wiener bound (eq. 1). In case of S brick the measured values of thermal conductivity were higher than the modeled. It could be partly caused by different minearology and therefore thermal conductivity of S brick body.

The comparison of the measured and modeled thermal conductivities vs. moisture content are presented in Fig. 3 and Fig. 4. In this comparison the thermal conductivity of solid phase λ_{high} = 1.05 W/m·K for bricks D, P, L and λ_{high} = 2.5 W/m·K for brick S was considered. The serial model (6) coincides roughly with the measured values but it is not able to express the changing slope in the effective thermal conductivity vs. moisture content dependency. Similar changing slopes were noticed also by other authors – for example [10] for moist sands with porosity of 0.42 and 0.52, [12] for moist sand with porosity of 0.3 or [7] for composite material with porosity of 0.32.

With the aim to get more precise description of the moisture influence on thermal conductivity the above described lattice-type periodic model was used for thermal conductivity of moist pore space (including interfacial zone) $\lambda_{m,low}$. Because the considered moisture contents fulfill condition of small dispersion the relation (7) was used:

$$\lambda_{m,low} = \lambda_{low} \cdot \left[1 + 3.844 \cdot \left(\frac{\lambda_w - \lambda_{low}}{\lambda_w + 2\lambda_{low}} \right) \cdot \left(\frac{u_v}{1.1 \cdot \Phi} \right)^{2/3} \right] \tag{8}$$

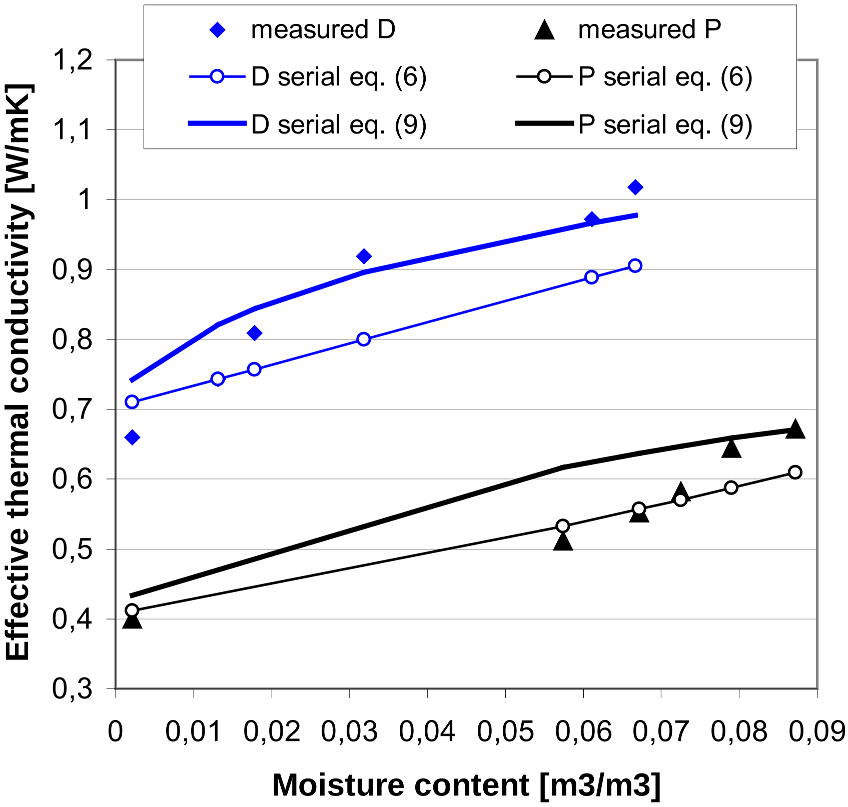

Fig. 3 Thermal conductivities of bricks D and P vs. moisture content. Comparison of the measured values and modeled values by eq. (6) and (9)

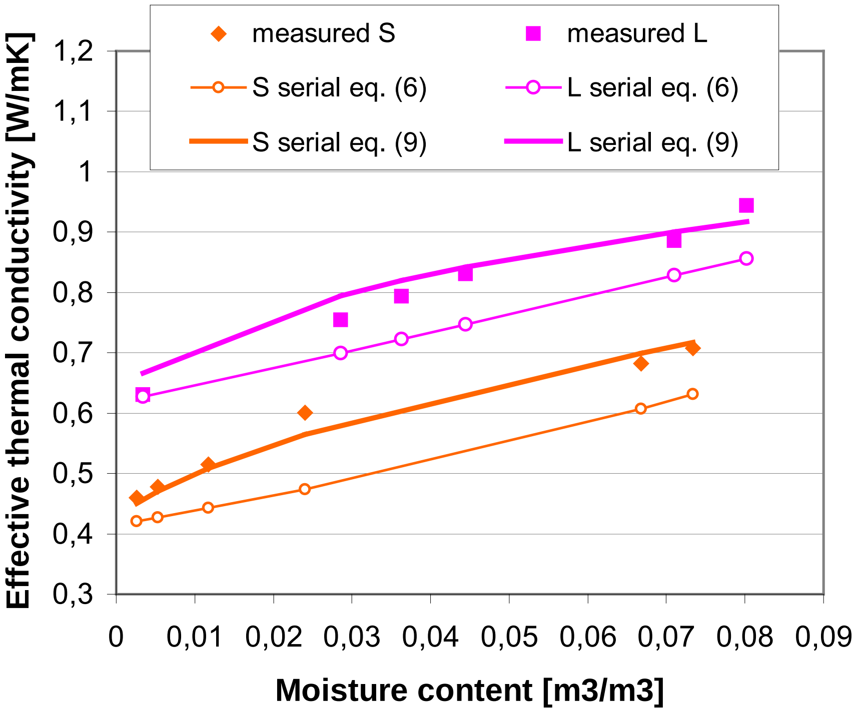

Fig. 4 Thermal conductivities of bricks S and L vs. moisture content. Comparison of the measured values and modeled values by eq. (6) and (9)

The relation (6) then changed into:

$$\lambda = \frac{1}{\dfrac{(1-1.1\cdot\Phi)^{n1}}{\lambda_{high}} + \dfrac{(1.1\cdot\Phi)^{n2}}{\lambda_{m,low}}} \tag{9}$$

The results of modelling are shown in Fig. 3 and Fig. 4. Using of the upgraded model (9) improved significantly the agreement between measured and modeled values in case of bricks D, L, S. As to the brick P, it is a material with relative high non-homogeneity. Therefore the existing discrepancies were probably caused by the higher measurement uncertainty.

CONCLUSIONS

The relation between effective thermal conductivity and moisture content was investigated for four types of burnt clay bricks.

In the range of measured moisture contents (0-9%) the first approximation of effective thermal conductivity of moist clay bricks can be modeled by serial configuration of the high conductivity fraction (solid phase fraction + water) and low conductivity fraction (free pore volume fraction + interfacial transition zone) weighted by the power function of their volume fractions**.**

Incorporating the lattice-type periodic model of moist pore space into the formely developed serial model significantly improved the coincidence between the measured and modeled values.

ACKNOWLEDGEMENTS

This paper has been supported by Slovak Grant Agency VEGA (grant No. 2/7113/27).

REFERENCES

[1] Bagel, L. (2001) Structural parameters of clay bricks. Internal report. Institute of Construction and Architecture, SAS, Bratislava (in Slovak).

[2] Cultrone, G. et al. (2004) Influence of mineralogy and firing temperature on the porosity of bricks. *Journal of the European Ceramic Society.* Vol. 24, pp. 547-564.

[3] Dondi, M. et al. (2005) Water vapour permeability of clay bricks. *Construction and Buillding Materials.* Vol. 17, pp. 253-258.

[4] Koronthályová, O., Matiašovský, P. (2003). Thermal Conductivity of Fibre Reinforced Porous Calcium Silicate Hydrate-based Composites. *Journal of Building Physics*, Vol. 26, No. 4, pp.71- 89.

[5] Matiašovský, P., Koronthályová, O. (2005) Thermal Conductivity of Mortars and Fractal Properties of their Microstructure. In *Proceedings of Thermophysics 2004*, USTARCH SAV, ISBN 80-969371-8-9. Bratislava, 2005, pp. 38-45.

[6] Koronthályová, O., Matiašovský, P. (2007) Pore structure and thermal conductivity of burnt clay bricks. In *Proceedings of Thermophysics 2007*, Vydavatelstvo STU, ISBN 978-80-227-2746-4. Bratislava, 2007, pp. 100-106.

[7] Pavlik, Z., Fiala, L., Cerny, R. (2007) Application of Maxwell mixing role in the measurement of thermal conductivity of porous building materials. In *Proceedings of Thermophysics 2007*, Vydavatelstvo STU, ISBN 978-80-227-2746-4. Bratislava, 2007, pp. 34-38.

[8] Raznjević, K. (1984) Thermophysical Tables, ALFA Bratislava, (in Slovak).

[9] Singh, R., Beniwal, R., S. and Chaudhary, D. R. (1987) Thermal conduction of multi-phase systems at normal and different interstitial air pressures. *J. Phys. D: Appl. Phys.* Vol. 20, pp.917-922.

[10] Singh, A. K., Singh, R. and Chaudhary, D. R. (1990) Prediction of effective thermal conductivity of moist porous materials. *J. Phys. D: Appl. Phys.* Vol. 23, pp.698-702.

[11] Singh, R., Sharma, P. (2008) Effective thermal conductivity of polymer composites. *Advanced Engineering Materials,* Vol. 10, pp. 366-370.

[12] Veselsky, J. (2006) Investigation of thermal properties of soil by impulse method. In *Proceedings of Thermophysics 2006*, Vydavatelstvo STU, Bratislava, 2006, pp. 115-123.

[13] Wiener, O. (1912) Die Theorie des Mischkoerpers fur das Feld des stationaren Stromung. Abh. Math – Phys. K1 Konigl. Saechs. Gesel. Wissen, 32, pp. 509-604.

[14] Winslow, D. N. et al. (1994) Percolation and pore structure in mortars and concrete. *Cement Concrete Research* 24, pp. 25-37

THEORY AND EXPERIMENTS BY HOT BALL METHOD FOR MEASUREMENT OF THERMAL CONDUCTIVITY

Ľudovít Kubičár[1], Vladimír Štofanik[1], Vlastimil Boháč[1], Peter Dieška[2]

[1]Institute of Physics SAV, Dúbravská cesta 9, SK-845 11 Bratislava, Slovakia
[2]Fakulty of Informatic and Electrical Engieneering, STU, Bratislava
Email: kubicar@savba.sk

Abstract

The paper deals with theory and application of a hot ball sensor for measuring thermal conductivity. The sensor, in a form of a small ball, generates heat and simultaneously measures temperature response. A working relation of the sensor has been found on the base of an ideal model. The ideal model represents an empty sphere placed in specimen. Consequently there is a constant heat flow q for $t > 0$ streaming from the empty sphere into surrounding environment. A calibration procedure has been proposed to obtain reliable data. A working range of thermal conductivities of the tested materials has been estimated to be from 0.06 up to 1 W m^{-1} K^{-1}. Ideal model and a model considering heat capacity of the hot ball were tested.

Key words: transient methods, hot ball method, disturbing effects, heat capacity of the hot ball

1 Introduction

Recently a new class of dynamic methods – transient methods for measuring thermophysical properties has started to spread in research laboratories as well as in technology. The technique of transient methods has initiated construction of a range of new innovative laboratory instruments [4-10]. Improvements in methodology of the transient methods and use of recent electronic elements allow construction of some portable instruments and monitoring systems which significantly simplify operation [7, 11]. Construction of such devices has evoked a search for suitable sensors which would provide information on the thermophysical properties of tested objects. Recently a hot ball sensor in a single component configuration, i.e. when a heat source and a thermometer are unified in a single unit, has been presented [13].

The present paper deals with description of basic characteristic of the hot ball technique for the measurement of thermal conductivity. The performance of the sensor has been tested using certified materials. Ideal model and a model considering heat capacity of the hot ball have been tested.

2 Hot Ball Sensor

The working equation of the hot ball sensor is based on an ideal model. The ideal model assumes a constant heat flux F per surface unit from the empty sphere of radius r_b into the infinitive medium starting to be delivered for times $t > 0$. Then the surface of the hot ball is characterized by the function [15]

$$T(r_b,t) = T_0\left\{1-\exp\left(u^2\right)\mathrm{erfc}(u)\right\} \tag{1}$$

where erfc(x) is error function defined by $\mathrm{erfc}(x) = 1 - \frac{2}{\pi}\int_0^x \exp\left(-\zeta^2\right)d\zeta$ and $T_0 = qr_b/\lambda$, $u = \sqrt{at}/\lambda$ and λ, a are thermal conductivity and thermal diffusivity of the surrounding specimen, respectively. The equation (1) is a solution of partial differential equation for heat conduction considering boundary and initial conditions

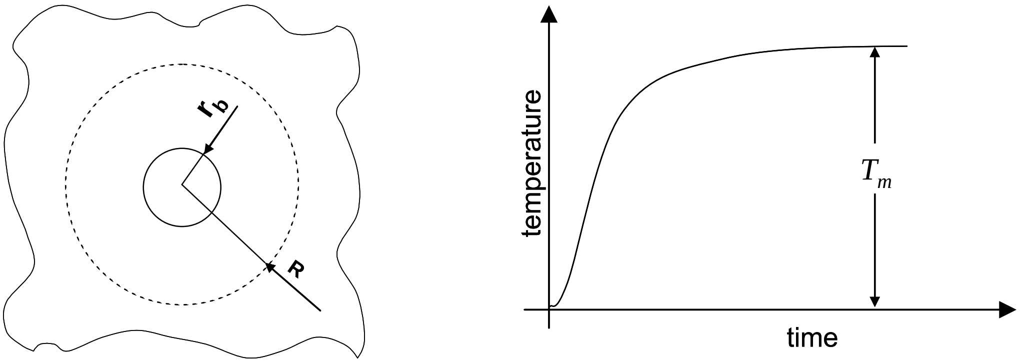

Figure 1. Model of the hot ball (left) and its temperature response for heat output of the ball

$$T(r,0) = 0,$$

$$\lambda\frac{\partial T(r,t)}{\partial r}\bigg|_{r=r_b} = -F\text{ , } F = const,\ t > 0.$$

The measuring method based on function (1) belongs, in fact, among the class of transient ones. Nevertheless, the heat source of the spherical symmetry possesses a special feature i.e. it yields the steady state in long times and this moment is utilized to measure the thermal conductivity. It should be stressed that the steady state regime of the hot ball has nothing to do with the one used in the Guarded Hot Plate technique. The latter is based on the existence of the heat and the cold plates (heater and sink) while the former utilizes physics of the heat spread from the spherical heat source. The heat penetrates to sphere with radius R during the temperature stabilization to T_m. Then the determined thermal conductivity corresponds to material within this sphere. Then an averaged value is to be determined for inhomogenous materials. Function (1) gives a working equation (2) of the measuring method in long time approximation $t \rightarrow \infty$ assuming that temperature is measured at the surface of the empty sphere r_b

$$\lambda = \frac{q}{4\pi r_b T_m(t\rightarrow\infty)} \tag{2}$$

where the heat flux of the empty sphere F is recalculated to the overall ball heat production q according $F = q/4\pi r_b^2$, and T_m is stabilized value of the temperature response. The empty sphere represents an ideal ball of radius r_b characterized by a negligible heat capacity and high thermal conductivity $\lambda_b \to \infty$.

3 Heat capacity of the hot ball

A ball must be constructed of parts generating constant heat on one hand and measuring the temperature response on the other hand. Sensing elements of the hot ball might disturb the measuring process. Therefore an analysis will be performed to estimate the influence of the heat capacity of the hot ball. Then the function that characterises the sensor surface temperature has a form

$$T(R,t) = T_0 \left\{ 1 + \frac{1}{z_1 - z_2} \left[z_2 w\left(= i z_1 \sqrt{t}\right) - z_1 w\left(- i z_2 \sqrt{t}\right) \right] \right\} \tag{3}$$

where

$w(z) = \exp\left(-z^2\right) erfc(-iz)$, $z_{1,2} = A\left(-1 \pm \sqrt{1-B}\right)$, $T_0 - q r_b / \lambda$, $A = \lambda / \left(2\sqrt{a C_s}\right)$, $B = 4 C_s a / \lambda r_b$.

C_s is heat capacity of the unit area of sensor surface and other symbols have been above specified.

4 Calibration of the hot ball

The strategy of the theory verification is based on the calibration of the ball sensors by the Eq. (2) rewritten in a form

$$q / T_m = 4 \pi r_b \lambda = A \lambda \tag{4}$$

where A is a constant $A = 4\pi r_b$. The ratio q/T_m is a linear function of thermal conductivity that will be tested using certified materials. A difference between the experimental data and the theoretical function should indicate the weight of the thermal contact and the temperature gradient within the ball. Materials tested within intercomparison measurements by different measurement methods have been used for calibration. The phenolic foam, calcium silicate and PMMA were used for the verification experiments. Table 1 gives thermophysical data of the tested materials together with the structure characterization. The tested specimen consists of two parts and the sensor is placed in the contact of the two specimen surfaces. A groove was made into one part of the specimen in which the ball was placed. A paste (Middland Silicon Ltd) was used for thermal contact improvements. While testing a porous structure the contact surfaces were covered by epoxy varnish to prevent the paste diffusion into material.The ball sensor consists of a heating element and a thermometer. Both elements are fixed in a ball by epoxy resin (Fig. 2 left) (patent pending). Diameter of the ball is in the range of 2÷2.3 mm.

The RTM 1.01 instrument was used for measurements [7]. The scheme of the instrument is shown in Fig. 2 right. A stabilized voltage was used for driving the heating element. Resistance stability of the heater is ±1.5%. Typical measurement signal is shown in Fig. 3 along with the characteristic points used to calculate the thermal conductivity.

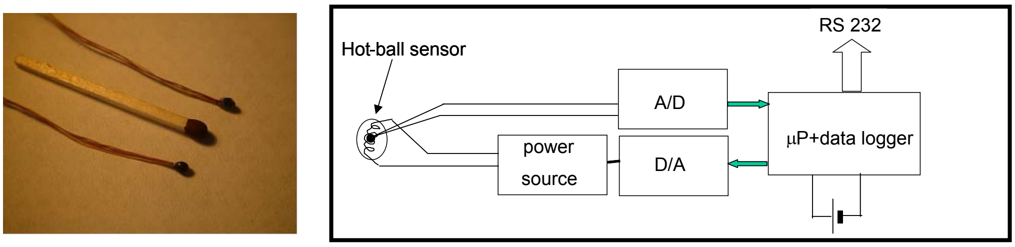

Fig. 2. Photo of the ball sensor (left) and a scheme of the RTM1.01 instrument (right).

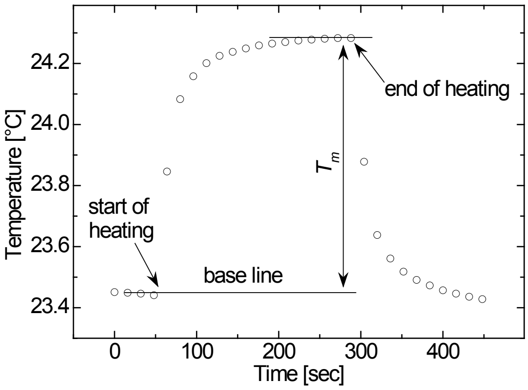

Fig. 3. Measuring cycle. Material: aerated concrete, ball heat output q = 3.5 mW.

The measuring procedure consists of the specimen temperature measurement (base line), switching on the heating and simultaneously scanning the ball temperature. When the ball temperature has stabilized, the heating is interrupted and a period of the temperature equilibration follows. When the temperature in the specimen parts is equilibrated the next measurement may be realized. The repetition rate of the measurements depends on the thermal conductivity and it takes from 10 up to 40 minutes.

5 Results

Evaluation by empty sphere model. A test of the measurement reliability has been performed by measurement of the thermal conductivity of the aerated concrete provided that the ball heat output varies in a broad range. The ball radius r_b = 1.05 mm has been used. Data on thermal conductivity were stable in the range 2.5÷30 mW within $\delta\lambda$ = +/- 0.0007 $W\cdot m^{-1}\cdot K^{-1}$. The measured data are shifted to higher values (λ = 0.265 $W\cdot m^{-1}\cdot K^{-1}$) however the shift is constant within a broad range of ball heat output.

A test of steady-state regime has been performed using the PMMA and measuring parameters q = 0.0025 W, ball radius r_b = 1.05 mm and measuring period (heating time) 3000 s. Equation (2) was used for data evaluation point by point of the scanned temperature response. Data on thermal conductivity started to be stabilized in time window 500 – 3000 s within $\delta\lambda$ = +/- 0.0033 $W\cdot m^{-1}\cdot K^{-1}$. Again data are shifted to higher value λ = 0.265 $W\cdot m^{-1}\cdot K^{-1}$. Data of thermal conductivity obtained on the set of materials specified in Table 1 are shown in Fig. 4. Around 4 measurements of the assembled unit have been performed. At least two reassemblings have been used. A reassembling consists of cleaning the groove, a deposition of the contact paste at the groove point where the hot ball is fixed, fixing the ball into the groove and assembling both parts of the tested materials together into one unit. Analysis of data statistics has shown that the measurement reproducibility of an assembled unit is rather high. Data scatter is well below 1%. Reassembling induces data scattering within 3-5%.

A theoretical curve is plotted in the Fig. 4 using Eq. (5) where the ball radius is assumed to be r_b = 1.05 mm. A difference between the experimental data and the theoretical curve indicates a disharmony with the ideal model.

Table 1.: Characteristics of materials used for calibration

Material	Thermal conductivity [W m^{-1} K^{-1}]	Structure	Block size [mm^3]
Glycerol	1.9	fluid	-
PMMA	0.19	compact	ϕ50, length 25
Calcium silicate	0.097	porous	150x150x50
Phenolic foam	0.06	porous	150x150x50

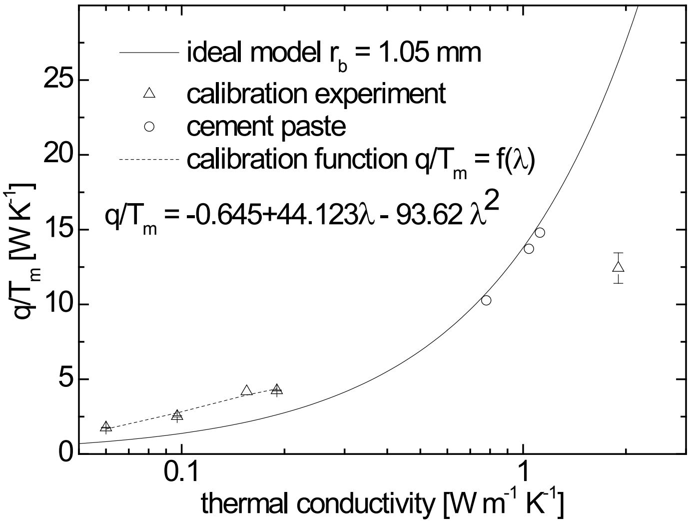

Fig. 4. Calibration of the hot ball sensor.

For given q/T_m, a data shift can be found with the low thermal conductivity range and to lower ones for high thermal conductivity range.

Evaluation by heat capacity model. Fitting procedure of Levenberg-Marquat was used for data evaluation using the function (3). Plots in Table 2 show experimental data together with the fitting functions for 4 different materials specified in Table 1. Experimental data were fitted in both in the heating and the cooling period of the hot ball. Four parameters have been fitted, namely thermal conductivity λ, thermal diffusivity a, surface capacity of the hot ball C_s and radius of the hot ball r_b. As too many parameters have to be fitted, the thermal conductivity of the measured materials as an input parameter was used and the radius of the hot ball was used to test the model validity.

Table 2.: Experimental points and fitted function (3).

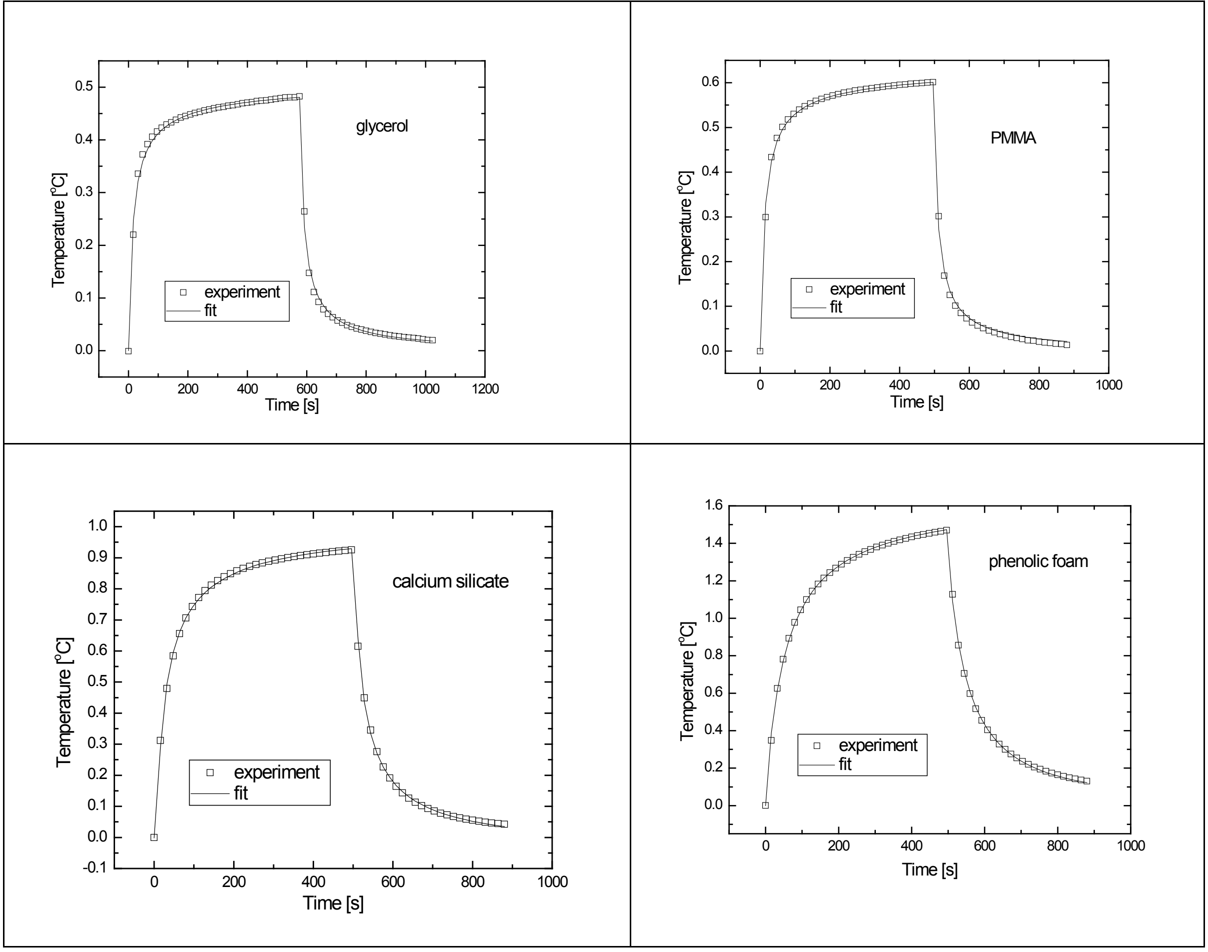

Table 3 gives data on thermal conductivity, thermal diffusivity and the calculated hot ball radius. There is clear discrepancy on hot ball radius considering different materials even fitted function (3) follows close experimental data. This discrepancy indicates that a refined model that includes heat capacity of the hot ball the measuring process is not adequate for characterisation of the measuring process. For a more reliable model an additional disturbing effect has to be included into working relation of the hot ball.

Table 3.: Input and fitted parameters for a range of used materials

Material	Thermal conductivity [W m^{-1} K^{-1}]	Hot ball radius [mm]
Glycerol	0.289	6.49
PMMA	0.19	1.6
Calcium silicate	0.097	2.16
Phenolic foam	0.06	2.3

6 Conclusion

Theory of the hot ball sensor and its experimental verification has been presented. The sensor is based on a ball that generates a constant heat and simultaneously it measures the temperature response for $t > 0$. The ideal model of the empty ball in an infinitive specimen gives a working relation of the hot ball method. The working equation concerns the steady state regime reached after some period of time. The steady state regime could be reached in tens of seconds up to tens of minutes depending on thermal diffusivity of the tested material. Then the thermal conductivity of the specimen is determined by the stabilized value of the temperature response. In addition a revised model considering heat capacity of the hot ball has been presented.
A calibration procedure has based on ideal model been used to analyze the sensor reliability. The experiment has proven that the working range covers the interval from 0.06 up to 0.5 W m^{-1} K^{-1}. A discrepancy has been found considering measured and published data for materials having thermal conductivity in a range from 0.05 up to 0.5 W m K. Data on thermal conductivity are shifted to higher values when real radius of the hot ball was used. A fitting procedure for data evaluation was used using hot ball heat capacity model. A negligible difference between the experimental data and the fitting function was found in both in heating and in cooling period of the hot ball. A radius of the hot ball was extracted from the fitting parameters to intercompare it with the real one. However not realistic data on the hot ball radius were found. This indicates that different disturbing effect is active during measuring process.

Acknowledgements

Authors would like to thank to Marian Markovic for technical support. This work has been supported by the EU project G6RD-CT2000-00266 and by VEGA project 2/0146/08.

References

[1] Krempaský J.: Meranie termofyzikálnych veličín. Vyd. SAV, Bratislava, 1969, 1-288 (in Slovak).
[2] Kubičár Ľ., Boháč V., Kubičár Ľ., Boháč V., Review of several dynamic methods of measuring thermophysical parameters. in “Proc. of 24th Int. Conf. on Thermal Conductivity / 12th Int. Thermal Expansion Symposium”, ed. P.S. Gaal, D.E. Apostolescu, Lancaster: Technomic Publishing Company (1999), pp. 135–149
[3] Kubičár Ľ. Kubičár L., 1990, Pulse Method of Measuring Basic Thermophysical Parameters, in Comprehensive Analytical Chemistry, Vol XII, Thermal Analysis, Part E, Ed Svehla G, (Amsterdam, Oxford, New York, Tokyo: Elsevier)
[4] Hammerschmidt U and Sabuga W, 1995 Int. J on Thermophysics 21 1255 - 1278
[5] Gustafsson S E, 1991 Rev. Sci. Instrum. 62 767 - 804
[6] Lockmuller N, Redgrove J, Kubičár Ľ, Measurement of thermal conductivity with the needle probe, 2003/2004 High Temp High Press, 35/36, 127
[7] www.transientms.com
[8] www.netzsch.de
[9] www.anter.com
[10] www.hotdisc.se

[11] Model, R., Stosch, R., Hammerschmidt, U., Virtual Experiment Design for the Transient Hot-Bridge Sensor, Int. J on Thermophysics, 2007 in print

[12] Haifeng Zhang, Liqun He, Shuxia Cheng, Zaiteng Zhai and Dayong Gao, 2003Meas Sci, 14, 1369

[13] Kubičár L., Vretenár V., Štofanik V., Boháč V., Thermophysical Sensors: Theory and Reliability of the Hot Ball, Proceedings of the Asian Thermophysical Conference, 21-24 August, 2007, Fukuoka, Japan, sent for publication to Int. J of Thermophysics

[14] Ľ. Kubičár, V. Boháč; Application of the Pulse Transient Method for Measuring Thermophysical Properties in Technology, in Proceedings of the 26th International Thermal Conductivity Conference, 14th International Thermal Expansion Conference, 6-8 August, 2001, Cambridge, Massachusetts USA

Determination of thermal properties from simultaneous monotonic cooling and surface heat transfer measuring

Peter Matiasovsky, Peter Mihalka, Milan Drzik

Institute of Construction and Architecture, Slovak Academy of Sciences,
Dubravska cesta 9, Bratislava, Slovakia

Abstract:

The monotonic heating regime method for determination of thermal diffusivity is based on the analysis of an unsteady-state (stabilised) thermal process characterised by an independence of the space-time temperature distribution on initial conditions. At the first kind of the monotonic regime a sample of simple geometry is heated / cooled at constant ambient temperature. The determination of thermal diffusivity requires the determination rate of a temperature change and simultaneous determination of the first eigenvalue. According to a characteristic equation the first eigenvalue is a function of the Biot number defined by a surface heat transfer coefficient and thermal conductivity of an analysed material. Knowing the surface heat transfer coefficient and the first eigenvalue the thermal conductivity can be determined. The surface heat transport coefficient during the monotonic regime can be determined by the continuous measurement of long-wave radiation heat flow and the photoelectric measurement of the air refractive index gradient in a boundary layer. The obtained eigenvalues and corresponding surface heat transfer coefficient values enable to determine thermal conductivity of the analysed specimen together with its thermal diffusivity during a monotonic heating regime.

Keywords:

monotonic heating regime, surface heat transfer, thermal properties

1. INTRODUCTION

The method of monotonic heating regime of the first kind, under the boundary conditions of the 3rd kind is suitable for the determination of thermal difussivity of high-density materials [3]. For the determination of complex thermal properties a complementary measurement of the specific heat is necessary [4]. In order to avoid this complication the monotonic heating regime method was combined with a simultaneous measurement of the surface heat tranfer coefficient, especially its convective component. This paper is a modified version of the original publication [5].

2. MONOTONIC HEATING REGIME METHOD

The determination of thermal properties by the monotonic heating regime method of the first kind includes the determination of thermal diffusivity and specific heat of the specimens with a simple geometry. The principle of the measurements is based on the monitoring of a cooling of the specimens with a defined geometry in a constant temperature environment.

Let us consider an isotropic sample of the cubic shape, with a side of length *d*. The initial temperature of the cube is θ_0. At the starting time the cube is suddenly moved from the environment with a constant temperature θ_0 to the environment with a different constant temeperature θ_e $(\theta_0 > \theta_e)$. The temperature field of the cube is changing in time and the coefficients of the surface heat transfer are also changing and different at particular cube surfaces during this process. The temperature course at an arbitrary cube point is given by the solution of the heat transfer differential equation (1) for the case of constant material parameters and zero heat sources:

$$a \cdot \nabla^2 \theta = \frac{\partial(\theta)}{\partial t} \tag{1}$$

where: *a* is the thermal diffusivity, θ is the temperature, *t* is the time,
under the boundary conditions of the 3rd kind.

The analysis of the cube cooling under a constant ambient temperature shows that the whole process can be divided into three states:

- At the first state, random, non-steady state the initial temperature distribution is dominant.
- At the second state, known as a monotonic regime, the temperature change with a time runs according to an exponential law.
- The third state corresponds to a steady state, when the temperature in all points of the cube is equal to the ambient temperature.

The second state, the monotonic regime appears after the time of the cooling, when the Fourier number *Fo* is higher than 0.4. Then the time course of relative temperatures of the specimen θ_r at all points under constant boundary conditions can be expressed in the form:

$$\theta_r = \frac{\theta(x,y,z,\tau)-\theta_e}{\theta_0-\theta_e} = A + A_{x1}\cdot\left(\cos\frac{x\cdot\mu_{x1}}{d}+\frac{Bi(d,y,z)}{\mu_{x1}}\cdot\sin\frac{x\cdot\mu_{x1}}{d}\right)\cdot A_{y1}\cdot\left(\cos\frac{y\cdot\mu_{y1}}{d}+\frac{Bi(x,d,z)}{\mu_{y1}}\cdot\right.$$

$$\left.\cdot\sin\frac{y\cdot\mu_{y1}}{d}\right)\cdot A_{z1}\cdot\left(\cos\frac{z\cdot\mu_{z1}}{d}+\frac{Bi(x,y,d)}{\mu_{z1}}\cdot\sin\frac{z\cdot\mu_{z1}}{d}\right)\cdot exp\left[-\left(\frac{\mu_{x1}^2+\mu_{y1}^2+\mu_{z1}^2}{d^2}\right)\cdot a\cdot t\right] \tag{2}$$

where: *Bi(d, y, z)* is Biot number for the surface heat transfer coefficient at the plane parallel the coordinate axes *y, z* at the distance *d*; μ_{x1}, μ_{y1} a μ_{z1} are the first eigenvalues in the directions of the coordinate axes *x, y, z.*

From equation (2) it results that $\ln\theta_r = f(\tau)$ is the line, the tangent of which equals:

$$M = \frac{\partial\left[ln\left(\theta_e-\theta(x,y,z,t)\right)\right]}{\partial\tau} = \frac{ln\theta_r(x,y,z,t_1)-ln\theta_r(x,y,z,t_2)}{t_1-t_2} = \frac{a}{d^2}\cdot\left(\mu_{x1}^2+\mu_{y1}^2+\mu_{z1}^2\right) \tag{3}$$

The quantity *M* is usually called the cooling rate and it is constant in the monotonic heating regime. The thermal diffusivity is then given by the following relationship:

$$a = \frac{M\cdot d^2}{\mu_{x1}^2+\mu_{y1}^2+\mu_{z1}^2} \tag{4}$$

The value *M* can be obtained by calculating the logarithm of the temperature course at an arbitrary point of the cube during the monotonic regime.

The values $\mu_{x1}, \mu_{y1}, \mu_{z1}$ for three pairs of opposite surfaces are the functions of the heat transfer coefficient between given surfaces and the environment. At their determination it is possible to issue from the following assumptions. During the cooling process the cube has surfaces oriented parallel with the coordinate axes, so the heat transfer through 4 vertical surfaces is identical, whilst at the top and bottom horizontal surfaces the heat transfer is different. For the determination of thermal diffusivity then it satisfies to determine only two eigenvalues: $\mu_{x1} = \mu_{y1}$ for vertical surfaces and μ_{z1} for horizontal surfaces of the cube.

At the determination for example of μ_{x1} – value, given by the heat transfer at two opposite surfaces in *x*-axis direction it is possible to issue from the two-points method, based on the fact that the ratio of the temperatures at an arbitrary point of the cube in each moment of the monotonic regime is constant and it is the function of μ_{x1}. Then for the ratios of the temperatures at centres of opposite surfaces to the centre of the cube: k_{xo} and k_{xd} the following relationship is valid:

$$\frac{k_{x0} + k_{xd}}{2} = cos \frac{\mu_{x1}}{2} \tag{5}$$

enabling the calculation of μ_{x1}, or μ_{z1} from the known values of k_{x0} and k_{xd}, or k_{z0} and k_{zd}.

From the cooling rate and the temperatures ratios with use of relations (4) and (5) it is possible to calculate the first eigenvalues $\mu_{x1}, \ \mu_{z2}$ and the thermal conductivity of the sample *a*.
The solution of the following transcendent equation enables to obtain the Biot number expressing the relationship between the thermal conductivity of a specimen and the surface heat transfer coefficient:

$$cot\, \mu_{x1} = \frac{\mu_{x1}^2 - Bi_{(0,y,z)} \cdot Bi_{(d,y,z)}}{\mu_{x1} \cdot \left(Bi_{(0,y,z)} + Bi_{(d,y,z)}\right)} \tag{6}$$

As the values of Biot number at opposite vertical surfaces are identical, equation (6) can be simplified.

3. PHOTOELECTRIC MEASUREMENT OF AIR REFRACTIVE INDEX IN BOUNDARY LAYER

The wall surface convective heat transfer coefficient can be defined by the expression combining the empirical Newton law and the steady state Fourier law of heat conduction:

$$h_c = \frac{-\lambda \cdot \left.\dfrac{d\theta}{dy}\right|_{y=0}}{\theta_{si} - \theta_\infty} \tag{7}$$

where: h_c is the convective surface heat transfer coefficient, $d\theta/dy$ is the air temperature gradient along the vertical *y*-axis, λ is the thermal conductivity of air, θ_{si} and θ_∞ are the temperatures at the surface and outside the boundary layer, respectively.

The experimental determination of the temperature gradient is based on the relationship between the air density dependent on temperature and the air refractive index. This relation is described by the Lorenz-Lorentz law (Fomin 1989):

$$\frac{n^2 - 1}{n^2 + 2} \cdot \frac{1}{\rho} = \frac{N}{M} = const. \tag{8}$$

where: n is the air refractive index [-], ρ is the air density [kg/m^3], N is the air molar refraction [m^3/mol], M is the air molar mass [g/mol].

In the range of 300 – 400 K and under the atmospheric pressure the air can be regarded as an ideal gas. Under the assumption of isobaric condition, the air density change is proportional inversely to the temperature change. Then the refractive index variation is proportional to the air temperature change. A basic constant can be found for the relationship between air temperature change and refractive index change for the wavelength of 650 nm at the temperature of 300 K:

$$\frac{dn}{d\theta} = 0.961.10^{-6} \tag{9}$$

Then, the mutual relationship between the refractive index gradients and temperature gradients is as follows:

$$\frac{d\theta}{dy} = \frac{1}{0.961 \cdot 10^{-6}} \cdot \frac{dn}{dy} \tag{10}$$

Considering the constant distribution of refractive index along the path of optical detection by laser beam and the appropriate geometrical relations, a final equation for the beam deviation in the detector place is:

$$\frac{d\theta}{dy} = \frac{2 \cdot n_0 \cdot \Delta y}{L^2 \cdot 0.961 \cdot 10^{-6}} \tag{11}$$

where: L is the laser beam path length [m], n_0 is the initial refractive index $\cong 1.0$ for air, Δy is the laser beam deviation.

With use of equation (11) the gradient near the surface and then the near-surface temperature profile can be evaluated. Applying then equation (7) the convective heat transfer coefficient can be calculated.

4. EXPERIMENT

The experiment was performed for the polymethyl methacrylate cubic specimen, with the side length of 0.1 m. It consisted of the simultaneous measurement of temperatures at the midpoints of two opposite vertical surfaces and the centre of the cube, the measurement of the laser beam deviations near one vertical surface (2 mm distance) and the measurement of the radiative heat flow between the cube vertical surfaces and the surrounding isothermal surfaces during the cooling experiment. In figures 1 and 2 there are a schematic description of the experiment and a thermograph of the cooled sample. The initial temperature of the specimen was 40 °C and the controlled ambient temperature was 20 °C. The cooling process continued approximately for 3 hours. The monotonic regime lasted during the second hour of the experiment. In figures 3 and 4 there are a time courses of the monitored temperatures and of the near-surface temperature gradient in the air boundary layer calculated by equation (11) from the laser beam deviation data. The corresponding time courses of vertical convective and radiative surface heat transfer coefficients are in figure 5.

An analytical solution of the monotonic cooling of the cube expressed by equation (2) supposes constant boundary conditions. In reality the total surface heat transfer coefficient is decreasing during the proces of cooling. Therefore its average value from the analysed period must be taken into consideration. The time courses of the temperatures ratio k, the first eigenvalue, the total surface heat transfer coefficient, the Biot number and the resultant values of thermal conductivity determined from equations (5) and (6) are in table 1. As the heat transfer at all vertical surfaces of the cube was identical only one *k*-ratio and Biot number could be considered. The average thermal conductivity obtained during the monotonic regime is in agreement with the known value of the polymethyl methacrylate thermal conductivity – 0.185 W/(m.K) determined by the quarded hot plate method.

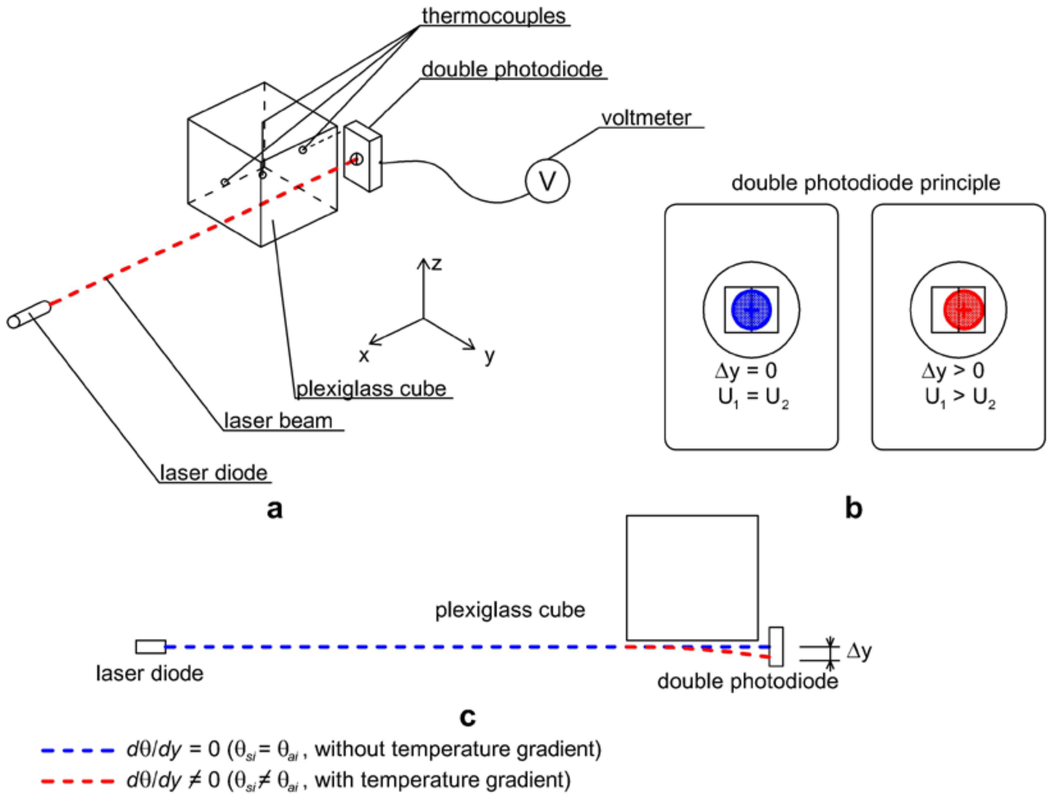

Figure 1 Scheme of experiment

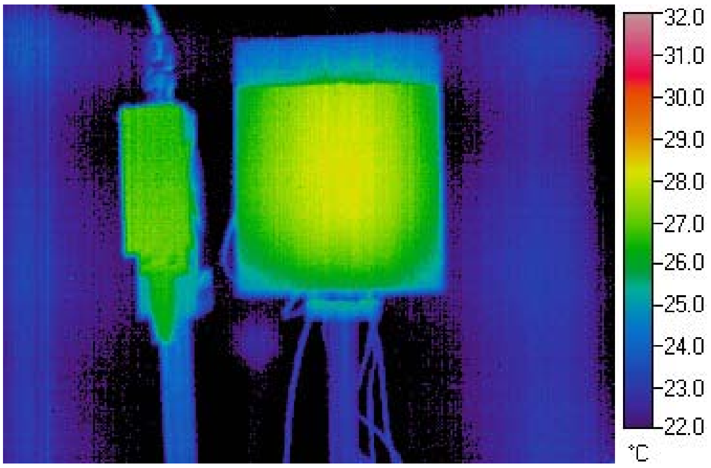

Figure 2 Thermograph of cooled polymethyl methacrylate cube

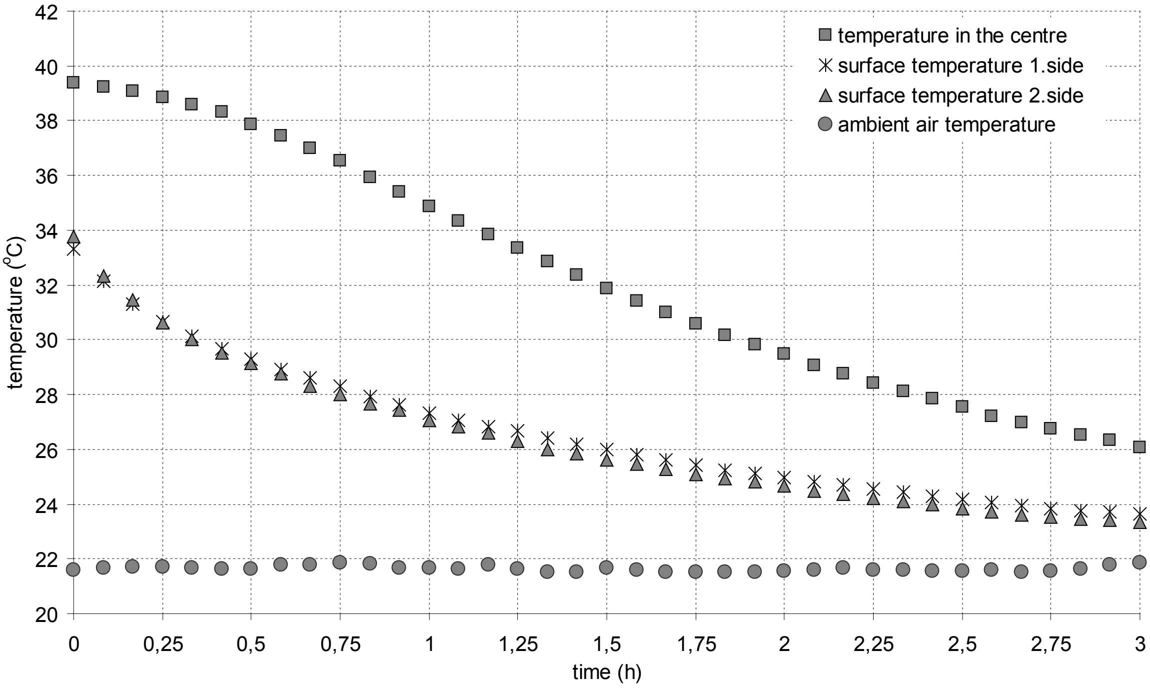

Figure 3 Time course of measured temperatures

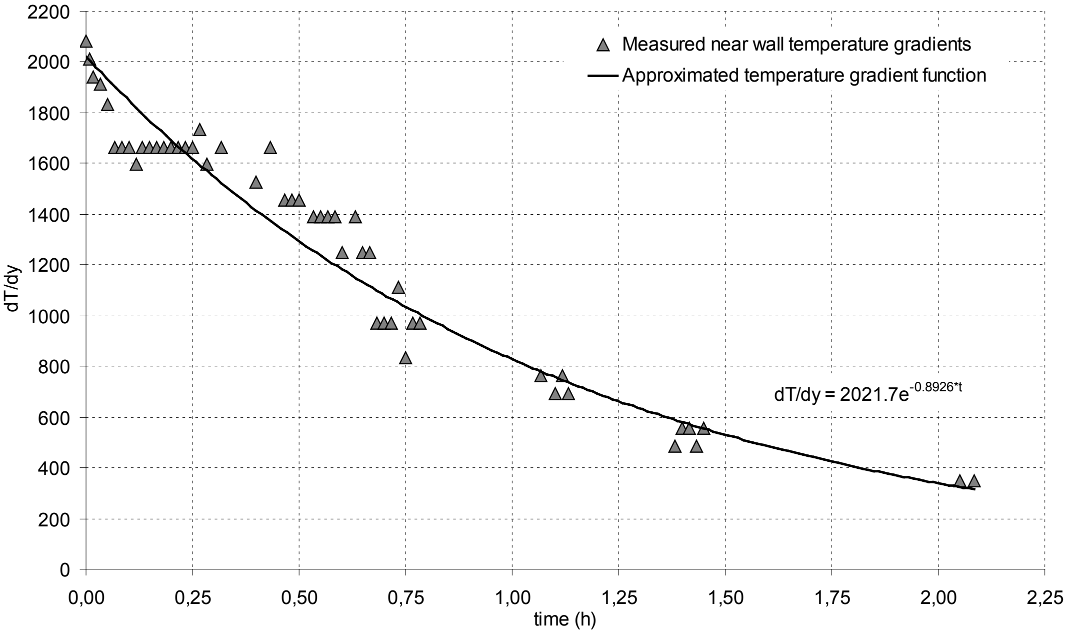

Figure 4 Time course of near-surface temperature gradient

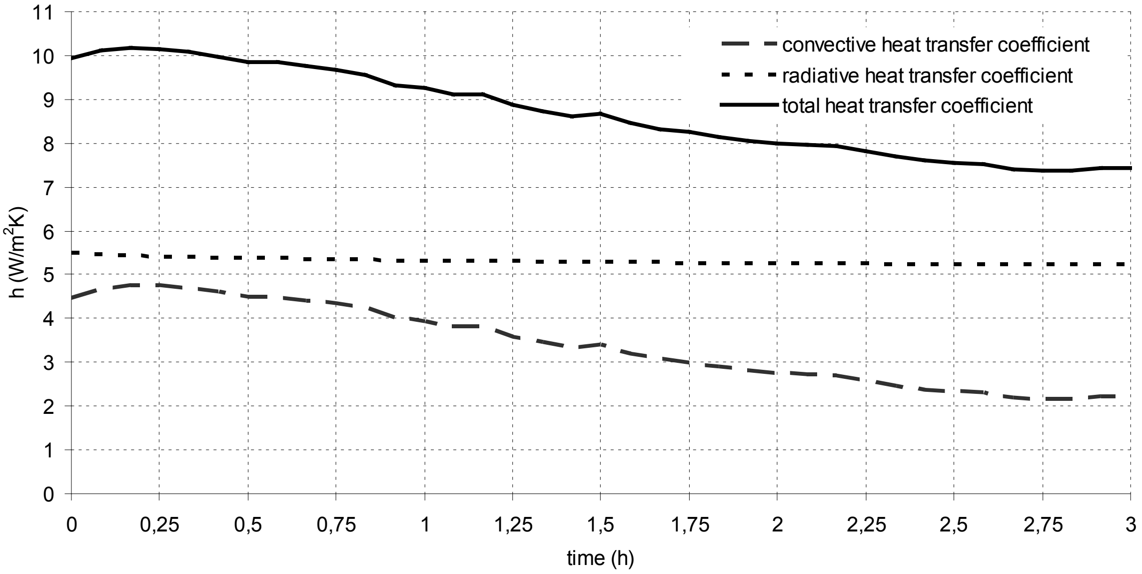

Figure 5 Time course of convective and radiative surface heat transfer coefficients

Table 1 Time courses of measured variables and calculated parameters with resultant thermal conductivities

Time [min]	k [K/K]	μ_1 [1/s$^{1/2}$]	h [W/(m^2.K)]	Bi [-]	λ [W/(m.K)]
60	0.43	2.24	9.25	4.61	0.200
65	0.44	2.24	9.12	4.61	0.198
70	0.44	2.24	9.11	4.66	0.195
75	0.44	2.24	8.87	4.62	0.192
80	0.43	2.25	8.74	4.68	0.187
85	0.43	2.24	8.63	4.67	0.185
90	0.43	2.25	8.66	4.75	0.183
95	0.43	2.24	8.47	4.66	0.182
100	0.44	2.24	8.33	4.63	0.179
105	0.44	2.24	8.24	4.63	0.178
110	0.44	2.24	8.15	4.59	0.177
115	0.44	2.23	8.05	4.57	0.176
120	0.44	2.24	7.99	4.61	0.173
Average	0.44	2.24	8.59	4.64	0.185

5. CONCLUSIONS

An applicability of the simultaneous measurement of the near-surface temperature gradient in air boundary layer during the monotonic heating regime test for the determination of thermal conductivity was proved. The obtained thermal conductivity value was in agreement with the result of independent measurement by the guarded hot plate method.

A combination of the monotonic heating regime method with simultaneous the surface heat transfer measuring enables to determine the thermal diffusivity and the thermal conductivity from one measurement.

Acknowledgement

This work was supported by the Slovak Research and Development Agency under the contract No. APVT-51-030704.

REFERENCES

[1] Fomin N. A. (1989) Speckle interferometrija gazovych potokov. Nauka I technika, Minsk (in Russian).

[2] Chapman A. J. (1960) Heat transfer. The Macmillan Company, New York

[3] Klarsfeld S. (1984) Guarded Hot Plate Method for Thermal Conductivity Measuremenent, in *Compendium of Thermophysical Property Measurement Methods, Vol.1 Survey of Measurement Techniques*, (Maglic K.D, Cezairliyan A., Peletsky V.E., editors), Plenum Press, London p. 169-230.

[4] Matiašovský P., Koronthályová O. (1994) Moisture dependent thermal properties of cellular concrete. *Building Research Journal*, Vol 42, Bratislava, Slovakia, p. 265-273.

[5] Matiašovský P., Mihálka P., Držík M. (2008) Determination of thermal conductivity by a combination of monotonic heating and surface heat transfer measuring. *Proceedings of the 8th Symposium on Building Physiscs in the Nordic Countries,* (Rode C., editor) Report R-189, Dept. of Civil Engineering, Technical University of Denmark, Lyngby, Denmark, p. 33-40.

[6] Mihálka P., Držík M., Matiašovský P. (2007) Measurement of Local Surface Heat Transfer Coefficient by Photoelectric Method. *Proceedings of Thermophysics 2007*, Vydavateľstvo STU, Bratislava, p. 86-92.

[7] Schlichting H. (1979) Boundary-Layer theory. McGraw-Hill.

[8] Vasiljev L. A. (1968) Tenevije metody. Nauka, Moscow (in Russian).

SIMULATION OF HYSTERETIC BEHAVIOR AT DYNAMIC MOISTURE RESPONSE

Peter Mihalka, Ing.*, Olga Koronthalyova, PhD.*, Peter Matiasovsky, PhD.*,
Juraj Veselsky, Assoc. Professor $^+$, Daniel Szabo, MSc. $^+$, Anton Puskar, Professor $^+$

* Institute of Construction and Architecture, Slovak Academy of Sciences, Dubravska 9, 845 43
Bratislava, Slovakia. e-mail: usarmipe@savba.sk, usarkoro@savba.sk, usarmat@savba.sk

$^+$ Slovak Technical University, Faculty of Civil Engineering, Radlinskeho 11, 813 68 Bratislava,
Slovakia

KEYWORDS: simulation, water vapour sorption, hysteresis, scanning curves

SUMMARY:
Simulation tool for solving coupled heat and moisture transfer involving the effect of a hysteresis was developed. A numerical simulation of the dynamic moisture behaviour of autoclaved aerated concrete was compared with the experimental results. Parameters of the used model of hysteresis were determined and applied in the simulation.

INTRODUCTION

For a correct simulation of the dynamic moisture behavior of building structures it is necessary to know not only the basic hygric parameters determined from the measurements under steady state conditions but to determine also a possible differences between the steady and non-steady behaviour.

In most of simulation tools, the process of simultaneous water vapour adsorption and desorption is controlled by unique function, usually main adsorption isotherm. In hysteretic materials, the process of adsorption and desorption is not the same. The equilibrium moisture content during desorption process is higher than the moisture content during adsorption at the same relative humidity.

Simulation tool for solving coupled heat and moisture transfer involving the effect of a hysteresis was developed. The simulation of the dynamic moisture response of a hygroscopic material under different dynamic boundary conditions was performed, results of simulation were confronted with results of laboratory tests.

The tests were done for the autoclaved aerated concrete (AAC) plate, the pore structure of which is characterised by two pore subsystems, consisting of 30 % volume of micropores and 50 % volume of macropores [3]. For this material a hysteretic moisture behaviour is typical [2].

EXPERIMENTS

The main adsorption isotherm of the material was determined by conditioning the samples in desiccators under a constant relative humidity and temperature (23 °C) until the steady equilibrium was achieved [2]. The estimation of main desorption isotherm was done by an analysis of previous measurements of AAC samples [1]. Two primary scanning desorption curves were determined starting from the equilibrium moisture contents corresponding to 94 % and 75 % RH. The water vapour permeability was measured by standard dry-cup (0 – 53 % RH difference maintained by the silica-gel and the climatic chamber) and wet-cup (100 – 53 % RH difference maintained by the water and the climatic chamber) methods.

The dynamic tests were performed in a climatic chamber. The tests were performed under three different regimes of the cyclic RH step changes between 49/79, 45/80, 56/79 % relative humidities, lasting 8/16, 24/48 and 48/96 hours respectively. The temperature during the tests was kept at constant value of 23.0 ± 0.5 °C. The relative humidity changes in the chamber were controlled by the dry and wet air streams. The relative humidity near the sample was monitored by the capacitative RH sensor with ± 1.5% RH precision. The temperature was measured by the electric resistance sensor Pt 100. The specimens were sealed on all but two surfaces by the epoxy resin in order to guarantee 1D water vapour flow. Simultaneously two specimens with the dimensions of 200 x 120 x 39.5 mm were tested (the area of the active surface was 0.096 m^2). A mass of the samples was weighted by the balance with the accuracy of 0.1 g. The mass of the samples, the temperature and the relative humidity in the chamber were registered in hourly intervals. The air flow velocity near the samples varied from 0.05 to 0.15 m/s that corresponded to common interior conditions. A detailed description of the experiments and their results is in [2].

SIMULATION MODEL

The developed simulation model is based on solution of the coupled 1D equations for the heat conduction and the water vapor diffusion through a structure.

1D non-steady heat transfer is described by the Fourier`s equation of heat conduction:

$$\rho \cdot c \cdot \frac{\partial \theta}{\partial t} = \frac{\partial}{\partial x}\left(\lambda \cdot \frac{\partial \theta}{\partial x}\right) \tag{1}$$

Where:
θ – temperature (°C)
ρ – density (kg/m^3)
c – specific heat capacity (J/kg.K)
λ – thermal conductivity (W/m.K)
t – time (s)
x – coordinate (m)

1D non-steady water vapour diffusion is described by the Fick`s equation:

$$\frac{\partial w_c}{\partial \varphi}(\varphi) \cdot \frac{\partial \varphi}{\partial t} = \frac{\partial}{\partial x}\left(\delta_p(\varphi) \cdot \frac{\partial (p_{sat} \cdot \varphi)}{\partial x}\right) \tag{2}$$

Where:
φ – relative humidity (-)
w_c – water content (kg/m^3)
δ_p – water vapour permeability (s)
t – time (s)

x – coordinate (m)
p_{sat} – water vapour saturation pressure (Pa)
$\partial w_c / \partial \varphi$ – moisture capacity

In hysteretic material the moisture capacity is given by scanning curves, which lie always between the main adsorption and desorption isotherms. The description of scanning curves was done by simple empirical model originally used by Pedersen [5]. The moisture capacity in the hysteresis region is represented by slope of the scanning curves:

During adsorption: $$\xi_{hys} = \frac{\gamma_a \cdot (u - u_{adsorption})^2 \cdot \xi_{desorption} + (u - u_{desorption})^2 \cdot \xi_{adsorption}}{(u_{desorption} - u_{adsorption})^2} \tag{3}$$

During desorption: $$\xi_{hys} = \frac{(u - u_{adsorption})^2 \cdot \xi_{desorption} + \gamma_d \cdot (u - u_{desorption})^2 \cdot \xi_{adsorption}}{(u_{desorption} - u_{adsorption})^2} \tag{4}$$

Where:
ξ_{hys} - the moisture capacity (slope of scanning curve) at given relative humidity
u – water content (kg/kg)
$u_{adsorption}$ – the water content calculated from main adsorption isotherm (kg/kg)
$u_{desorption}$ – the water content calculated from main desorption isotherm (kg/kg)
$\xi_{adsorption}$ – the moisture capacity at given relative humidity calculated from main adsorption isotherm
$\xi_{desorption}$ – the moisture capacity at given relative humidity calculated from main desorption isotherm
γ_a, γ_d – the parameters of hysteresis

The numerical solution of equations (1) and (2) using Control Volume Method with 1-D model and implicit time scheme [4] was performed. In the simulation volume elements with constant thickness 1mm were used. The time step was 10 min. The material parameters dependent on moisture content were recalculated during every time step. Every volume element was considered as a material with its own sorption-desorption past.

MATERIAL PROPERTIES

The main adsorption and desorption isotherms of tested AAC were described by the following expression [2]:

$$u_{HANSEN} = u_h \cdot \left(1 - \frac{\ln \varphi}{A}\right)^{-\frac{1}{n}} \tag{5}$$

where: u_{HANSEN} is the moisture content (kg/kg), φ is relative humidity (-), u_h is the hygroscopic moisture content (kg/kg), A and n are approximation parameters.

The used approximation parameters for main adsorption and desorption isotherms are in tab.1. The main storage functions are in Fig.1a.

Table.1: Approximation parameters for main adsorption and desorption isotherms of tested AAC

	Adsorption	Desorption
u_h	0.4	0.4
A	0.000 04	0.001 5
N	3.43	2.4

The moisture capacity in a hygroscopic relative humidity range was expressed by the following formula:

$$\frac{\partial u}{\partial \varphi}(\varphi) = u_h \cdot \frac{\left(1-\frac{\ln(\varphi)}{A}\right)^{-\frac{1}{n}}}{n \cdot \varphi \cdot A \cdot \left(1-\frac{\ln(\varphi)}{A}\right)} \tag{6}$$

In simulation of the moisture uptake and release, the water vapour permeability moisture dependence was approximated by the relation:

$$\mu(\varphi) = \frac{1}{0{,}13 + 0{,}003 \cdot e^{5\cdot\varphi}} \tag{7}$$

The dependence of the vapour diffusion resistance factor on the relative humidity of the AAC is shown in fig.1b.

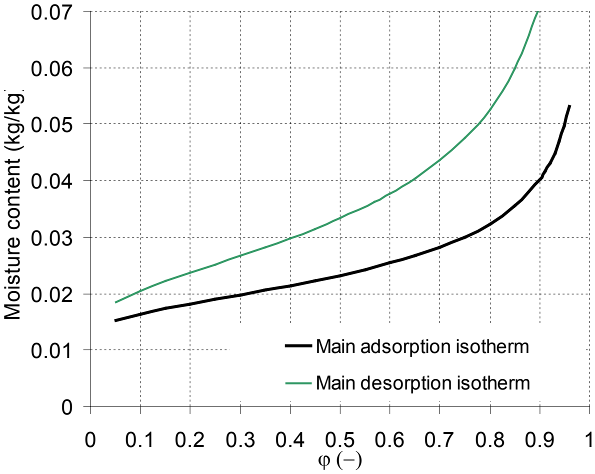

a

b

Fig.1: Approximated material parameters of AAC: a- main moisture storage functions, b – vapour diffusion resistance factor

APPROXIMATION PARAMETERS OF USED HYSTERESIS MODEL

In equations (3) and (4) the coefficients γ_a and γ_d are the parameters of used empirical model. The water vapour content during a scanning between the equilibrium adsorption and desorption can be approximated as [2]:

$$u = u_o + \xi_{hys} \cdot \Delta\varphi \tag{8}$$

or:

during adsorption: $$u = u_o + \Delta\varphi \cdot \left(\frac{\gamma_s \cdot (u - u_{sorption})^2 \cdot \xi_{desorption} + (u - u_{desorption})^2 \cdot \xi_{sorption}}{(u_{desorption} - u_{sorption})^2} \right) \tag{9}$$

during desorption: $$u = u_o + \Delta\varphi \cdot \left(\frac{(u - u_{sorption})^2 \cdot \xi_{desorption} + \gamma_d \cdot (u - u_{desorption})^2 \cdot \xi_{sorption}}{(u_{desorption} - u_{sorption})^2} \right) \tag{10}$$

The measurements of primary scanning desorption from 94 % and 75 % were done [2]. The parameters of hysteresis were approximated by fitting the measured primary scanning desorption curves by equation (4). The best value for the primary scanning desorption process is $\gamma_d = 0.97$ for the desorption started at 94 % relative humidity and $\gamma_d = 0.87$ in case of the desorption started at 75 % relative humidity. Primary scanning adsorption has not been measured. Considering the second parameter of hysteresis the value $\gamma_s = 0.97$ was used. Convenience of the value will be shown in following analyses.

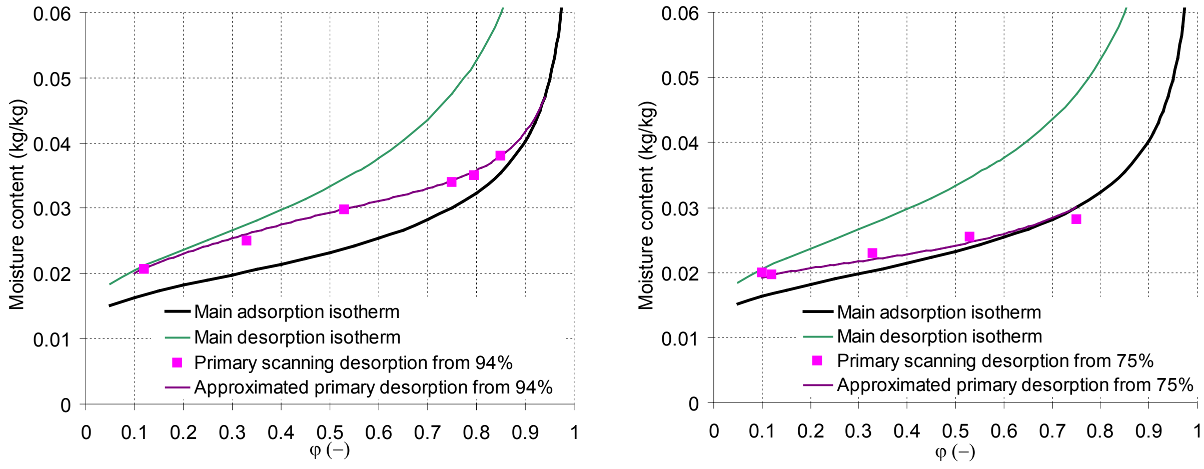

a b

Fig.2: Experimental determination of the hysteresis parameters. a) desorption from 94 % - γ_d =0.97, b) desorption from 75 % - γ_d = 0.87

RESULTS

The tests were performed under three different regimes of the cyclic relative humidity step changes: Test # 1: 8/16 hours - 49/79 % changes (6 steps), Test # 2: 24/48 hours - 45/80 % changes (2 steps), Test # 3: 48/96 hours - 56/79 % (2 steps).

Two independent simulations were done:

- by using the main adsorption isotherm
- by using the described empirical hysteresis model

In all tests an evident gradual moisture uptake step by step occurred.

Test # 1: 8/16 hours intervals with relative humidity changes 49/79 %. During the first moisture uptake the simulations with the main adsorption isotherm and the hysteresis model correspond to the measurements. It is caused by the fact that initial moisture content corresponded to the main adsorption isotherm at the beginning of simulation and measurement, moisture capacity during adsorption was controlled by the main adsorption isotherm.

A significant difference occurred during the first desorption, the water vapour desorption is no more controlled by the main adsorption isotherm. The hysteresis model with the estimated parameters gave results closed to the measured values. After 5th desorption process, a lower water vapour release occurred, with the difference approx. of 0.3 g, thereafter a higher moisture content was calculated after 6th adsorption process. The simulation with main adsorption isotherm reached the quasi-steady state after 3rd step, the measurement and the hysteresis model did not stabilize during measurement.

Test # 2: 24/48 hours intervals with relative humidity changes 45/80 %. Like in the previous test, the first moisture uptake corresponded to the measurement. The hysteresis model fits the desorption process better than than a calculation with the main adsorption isotherm. During 2nd adsorption a significant difference of the mass occurred.

Test # 3: 48/96 hours intervals with relative humidity changes 56/79 %. The simulation with hysteresis fits the measurement also very well. The calculation with main adsorption isotherm shows large deviations during the desorption process.

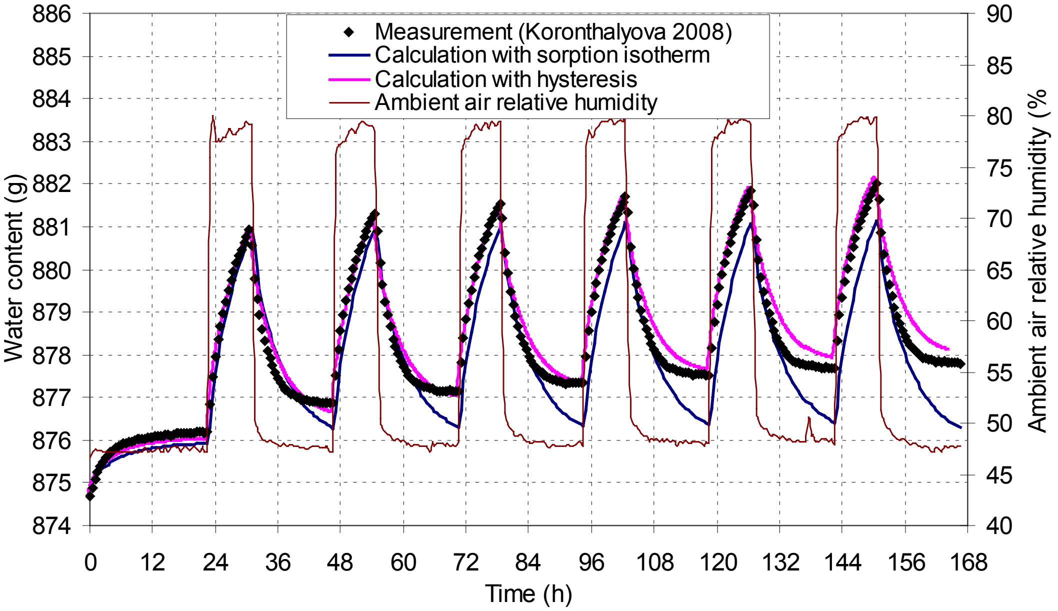

a

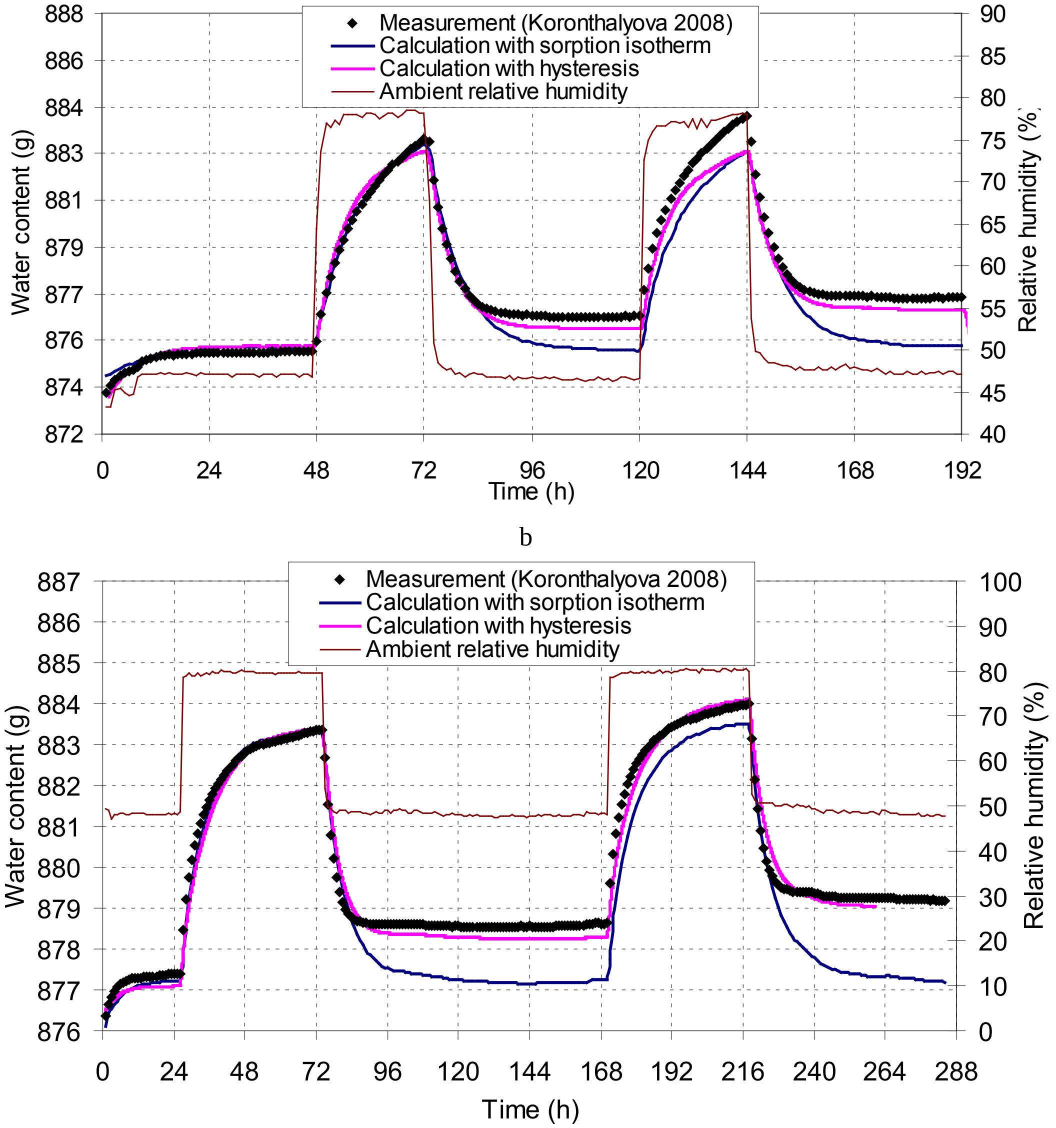

b

c

Fig.3: Measured and simulated mass change during the relative humidity change test, a) Test #1 8/16 - 49/79 %, b) Test #2 24/48 - 45/80 %, c) Test #3 48/96 - 56/79 %.

In fig. 4 there is a visualization of the calculated process of forming the scanning curves for Test # 1 (8/16 h - 49/79 %). The influence of the boundary conditions change delays towards the specimen`s core. After 5th ad/desorption step, a stabilization of the scanning curve on the surface began.

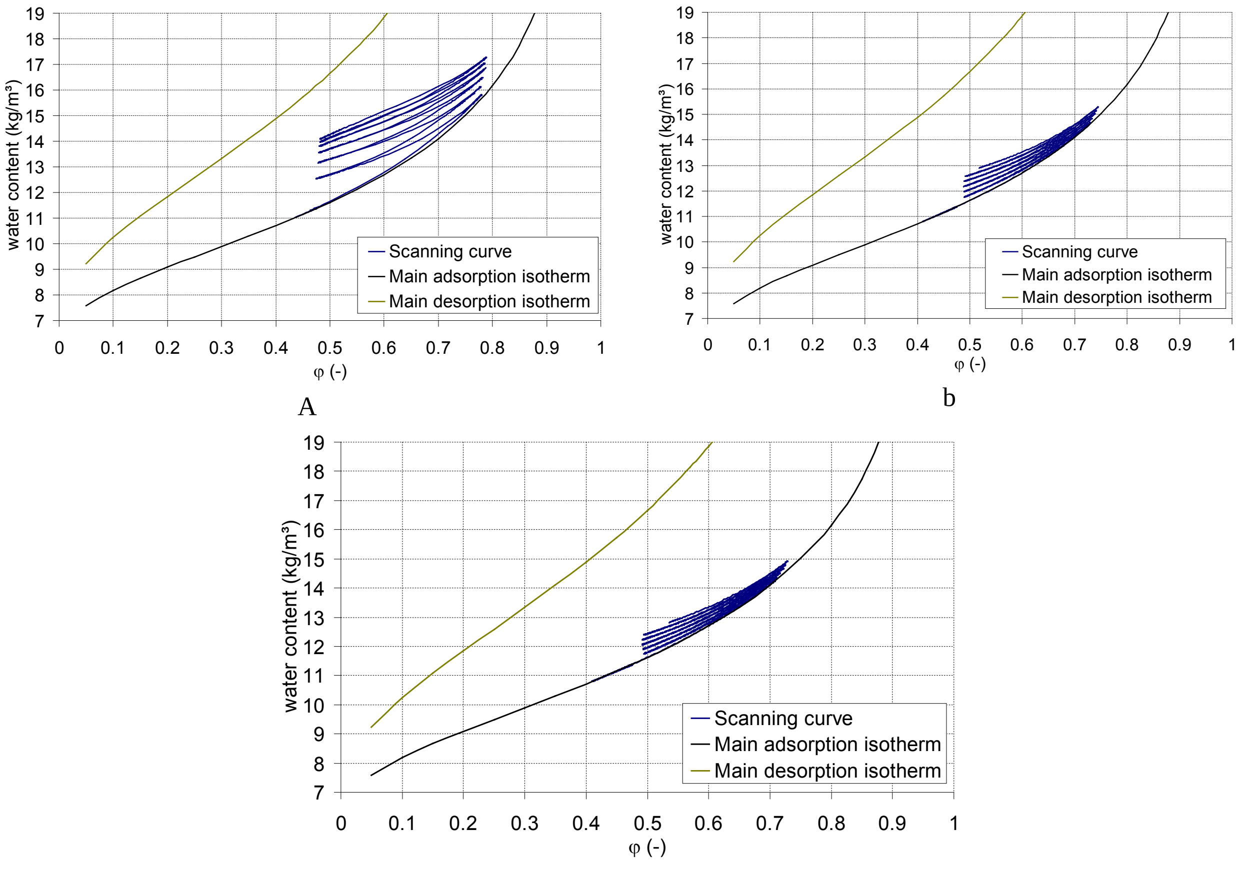

A b

c

Fig.4: Process of forming scanning curves during adsorption and desorption, Test # 1 - 8/16 h - 49/79 %, a) surface element, b) 1 cm under the surface, c) 2 cm under the surface (middle of the specimen)

CONCLUSIONS

The dynamic hygric behaviour of the autoclaved aerated concrete was simulated under three different step cyclic regimes. The simulations analysed previous experimental work. The analysis of a hysteretic behaviour modelling and its comparison with a commonly used assumption of the one-storage function curve was done. In all analysed cases the simulations with the main adsorption isotherm fits the measurements during the first adsorption process, a significant deviation occurred during the desorption process, subsequent adsorption processes never reached the measured moisture content again. The simulation with the considered hysteresis model gives results close to the measurements. In general the analysis was very sensitive to the uncertainty of the measurement.

Acknowledgement

This work was supported by the Slovak Research and Development Agency under the contract No. APVT-51-030704 and of Slovak Grant Agency VEGA (Grant No 2/7113/27).

REFERENCES

[1] Hansen K. K. (1986). Sorption isotherms. A catalogue. Department of Civil Engineering, Technical University of Denmark.

[2] Koronthalyova O. et al. (2008) Simulation of dynamic moisture response of autoclaved aerated concrete *Proceedings of the 8th Symposium on Building Physics in the Nordic Countries,* Copenhagen.

[3] Matiasovsky P., Koronthalyova O. (2002). Modelling of the AAC intrisinic and moisture permeabilities from MIP data. *Proceedings of the 6th Symposium on Building Physics in the Nordic Countries,* Norvegian University of Science and Technology, Trondheim

[4] Patankar, S.V.: Numerical heat transfer and fluid flow, New York: Hemisphere Publishing Corporation, 1980

[5] Pedersen C. R. (1990) Combined Heat and Moisture Transfer in Building Constructions. PhD Thesis. Thermal Insulation Laboratory, Technical University of Denmark.

B-SPLINE PRCESSING OF 90W-7Ni-3Fe WHA DILATOMETRIC DATA

Andrzej J. Panas

Military University of Technology, Kaliskiego 2 Street, 00-908 Warsaw, Poland

Andrzej.Panas@wat.edu.pl

Abstract:

B-spline approximation procedure applied to fitting the high thermal resolution thermophysical data is presented. The procedure has been used for characterisation of a 2-nd order phase transition revealed in dilatometric measurements of 90W-7Ni-3Fe tungsten heavy alloy (WHA). The experiments have been performed applying laser interferometry apparatus. Both the coefficient of linear thermal expansion (CLTE) and the linear expansivity (LE) data from thermal cycling within 20 °C and 1120 °C have been processed. As a result representative characteristics have been obtained. The discussed algorithm has been proved to be efficient in scattered thermophysical data processing.

1. Introduction

Almost every process of thermophysical property characterisation involves the experimental data processing. Usually data are processed for the purpose of introducing the appropriate characteristic into the appropriate database or for its thorough examination. In the first case the problem typically reduces to data averaging. In the second, needs of precise material diagnostics force more thorough examination of the experimental results. A special care is needed when the high thermal resolution data are handled. High thermal resolution means that a certain property is obtained within a very small temperature interval. Such data usually need to be approximated. The problem with approximation is proper selection of the functional basis. In typical cases theoretical indications for a certain functional dependence on the temperature are very weak [1]. In such situation polynomials are usually utilised. However, it was proved that due to many disadvantages single polynomials should be excluded from fitting high resolution thermophysical data [2]. Polynomials are not only badly numerically conditioned [3] but also proved to be inefficient in reconstruction of discontinuities of the investigated functional dependence [4]. On the other hand there is a broad range of possibilities connected with utilisation of splines [5]. Strangely enough, spline functions have rarely been used for that purpose despite the fact that even in a fundamental work of de Boor, titanium specific heat data were applied as an illustrative example of their application [4]. Splines, in that range basis splines (B-splines), exhibit unique features that predestine them to be used for approximation of high resolution thermophysical data. The most important is the possibility of almost unrestricted global and local reconstruction of not only the function but its derivatives as well. This particular feature can be effectively exploited for characterisation of materials exhibiting phase transition [7].

In this work s spline approximation of the high thermal resolution diltometric data (comp. [8]) from investigations of a 90W-7Ni-3Fe tungsten heavy alloy (WHA) is discussed. Tungsten heavy alloys are high–density dispersed composite materials in which quasi-spherical hard tungsten particles are embedded in a ductile matrix [8, 9]. Due to specific combination of mechanical properties, namely high strength and hardness together with good ductility, these alloys have been found increasingly applicable in nuclear and military technologies. The discussed studies of the thermal expansivity are comprised within the frame of a wider research programme on WHSs and related materials. The main purpose of the investigation is characterisation of all thermophysical properties to complement the literature in that domain (comp. eg. [9]). The data will also be exploited in numerical modelling of selected processes of WHA sintering technology.

2. B-spline Approximation

The details concerning the theory of spline functions can be found elsewhere (comp. e.g. [4] and [5]). For the purpose of this work let us just summarise basic facts about splines. A spline function can be defined within a closed interval containing the data [T_a, T_b], where T is the temperature. Let $\{\tau_i\}_1^n$, $T_a \le \tau_i \le T_b$ be a nondecreasing sequence of n points called knots. Let $\{\xi_k\}_1^N$ be a strictly increasing sequence composed of the previous one in such a way that all repetitions of τ_i are excluded. The points ξ_k are called breakpoints. In relation to these two sequences we define another sequence $\{\nu_k\}_1^N$ which counts repetitions of ξ_k in $\{\tau_i\}_1^n$ defining multiplicity of knots.

A spline of order r on [T_a, T_b] with reference to a multiple knot sequence $\{\tau_i\}_1^n$, $\tau_i < \tau_{i+r}$ is the function S_r^τ which [6]:

a) is a polynomial of order r (degree r-1) within every subinterval $\left[\xi_k, \xi_{k+1}\right]$;

b) is a $C^{r-\nu_k-1}$ class function at ξ_k.

In single knot subdivision case the spline is a C^{r-2} class function within the whole interval [a, b] and a C^{r-1} class function within $[a,b]\backslash \{\xi_k\}_1^N$. Multiplication of knots corresponds to lower continuity conditions at breakpoints – if a certain knot is multiplied, then the range of continuity in a corresponding breakpoint is proportionally decreased. For simplicity reasons a knot indication in the notation of splines will be omitted throughout the article.

The spline function S_r can be represented by piecewise polynomial (so called pp-function) of corresponding order r. This representation is equivalent to decomposition of a spline with reference to a base of truncated mononomials [4], [5]:

$$\forall T \in [\xi_k, \xi_{k+1}), k = 1,\dots,N-1 \;\; S_r(T) = \sum_{m=0}^{r-1} c_{km}(T-\xi_k)^m \tag{1}$$

To make this formula complete we take $S(\xi_N) = \lim_{T\to\xi_N} S(T)$. Hence, we conclude that pp-representation for a certain spline consists of: the integers r and N-1 giving order and number of its polynomial pieces, the strictly increasing sequence $\{\xi_k\}_1^N$ of its breakpoints and a matrix [c_{km}] of dimension (N-1) × r which is the matrix of its right derivatives at the breakpoints [5]. The mononomials for piecewise polynomial representation of a spline function is shown at Figure 1.

A spline function can also be referred to another functional basis. This basis consists of special splines every one of which is defined on a closed support. These splines are called basis splines or B-splines. We can introduce B-splines of order r on a knot sequnce $\{\tau_i\}_1^n$ using a recurrence relation:

$$B_{i,1}(T) = \begin{cases} 1 & \tau_i \le x < \tau_{i+1} \\ 0 & \text{otherwise} \end{cases} \qquad B_{i,r}(t) = \frac{T-\tau_i}{\tau_{i+r-1}-\tau_i} B_{i,r-1}(T) + \frac{\tau_{i+r}-T}{\tau_{i+r}-\tau_{i+1}} B_{i+1,r-1}(T) \tag{2}$$

For a strictly increasing knot sequence 1-st order B-spline is a constant, 2-nd order is composed of two pieces of a linear function, 3-rd order of three pieces of a square function, etc.

The formula (2) can also be applied for calculation of B-splines defined on multiple knot sequences. Multiplied knots are utilized whenever discontinuities of any range should be modeled.

B-splines of order r create a basis within an interval $[\tau_{r-1}, \tau_{n+1}]$ for any spline S_r in such a way that:

$$S_r(T) = \sum_{i=1}^{l} \alpha_i B_{i,r}(T) \tag{3}$$

B-representation for S_r consists of [4]: the integers r and l, giving the order r and the number of linear parameters, the vector $\boldsymbol{\tau} = \{\tau_i\}_1^n = \{\tau_i\}_1^{l+r}$ containing the knots and the vector $\boldsymbol{\alpha} = \{\alpha_i\}_1^l$ of the coefficients of the spline S_r with respect to the B-spline basis $\{B_{i,r}\}_1^l$. An example of recurrence creation of such a basis is shown in Figure 2. The B-spline basis, contrary to a basis composed of mononomials, is relatively well conditioned which makes numerical calculations more reliable.

The least square approximation of given data $\{(T_i, y_i)\}_1^M$ resolves itself to search the minimum of

$$\Phi(\alpha, \tau) = \sum_{j=1}^{M} w_i \left[y_j - \sum_{i=1}^{l} \alpha_i B_{i,r,\tau}(T_j) \right]^2 \tag{4}$$

with reference to τ and α as it was described in [5]. The numbers w_i are weights. For a fixed knot sequence τ, the minimisation simplifies to a linear least squares problem. The situation is different when variations of knots are admissible and one is trying to find the best placement of knots that will minimise the least squares error. In this case the problem (the variable knots problem) doesn't usually result in one optimum unequivocal solution.

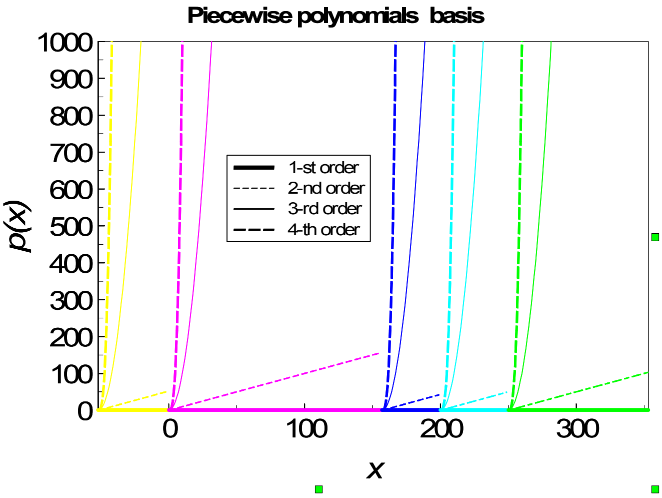

Figure 1. Basis for piecewise polynomial representation of a certain spline within the interval [52; 354] with knots at: -52, 0, 157, 200, 250 and 354

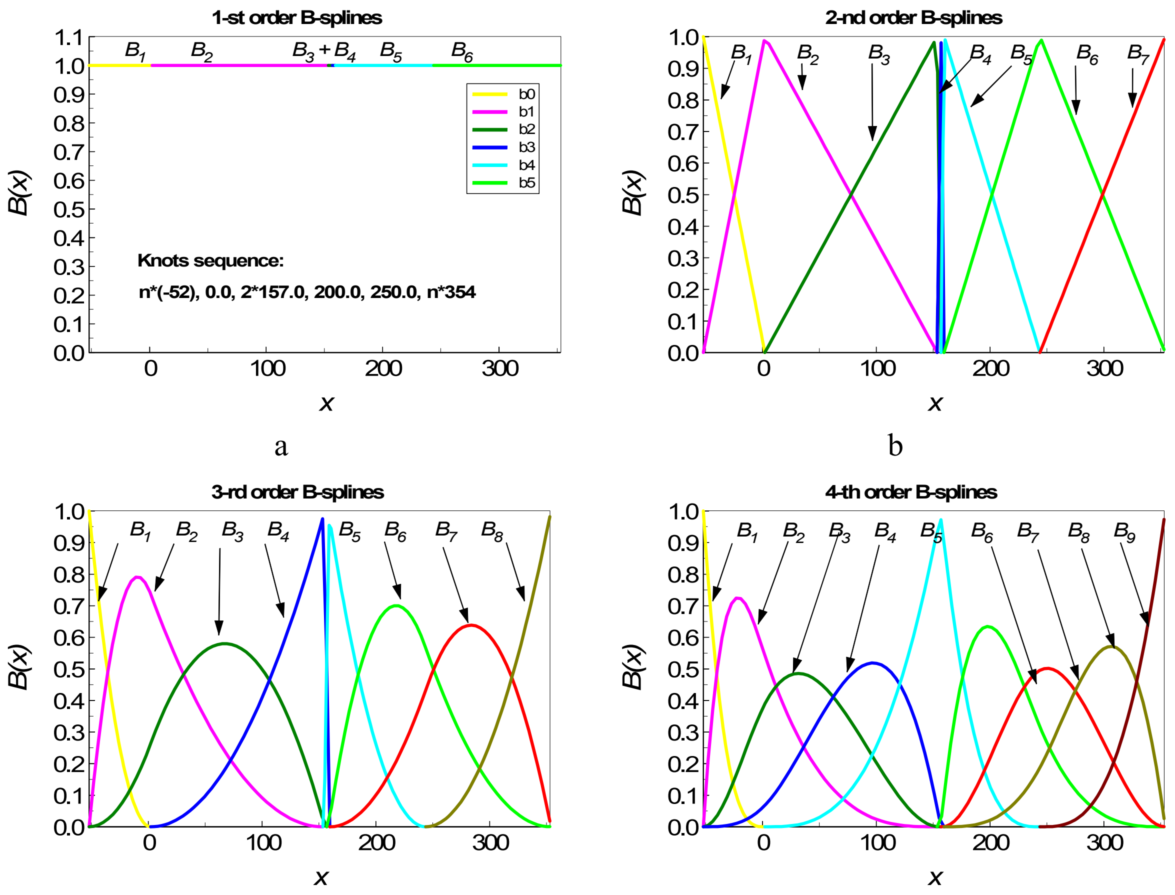

a b

c d

Figure 2. Recurrence construction of a B-spline basis: a - 1st, b – 2nd, c – 3rd and d – 4th order B-splines for the same knot sequence as illustrated in Fig.1

When comparing piecewise polynomial and B-spline representation in solving the approximation problems one can realize that there are strong theoretical and practical indications for preferring the last one. B-splines are better numerically conditioned and easier in recurrence calculations. This makes iterative calculations easier. The B-spline basis is usually composed of not so many functions as in the case of pp-functions. Last but not least it should be underlined that there are both theoretical and practical possibilities of converting splines from B-spline to piecewise polynomial representation.

Determination of the best approximation for a certain experimental data set with utilisation of B-splines resolves itself to the following step by step procedure:

1. Selection of the optimal range r of splines to be applied.
2. Determination of a subdivision of the interval $[T_a, T_b]$ comprising the data with simultaneous analysis (identification) of discontinuity points. This step results in definition of the knot sequence (initial knot sequence in a variable knot procedure).
3. Determination of the sequence of M weights $\{w_i\}_1^M$.
4. Application of fixed or variable knot procedures and evaluation of results.
5. Possible repetition of steps 1-3 with the order r changed or the knot sequence modified. Usually, when variable knot procedures are applied, knots are rearranged according to the obtained results. When certain discontinuities are modeled then fixed knot procedure is preferred in final calculations.
6. Conversion from B-spline to piecewise polynomial representation if necessary.

In numerical calculations described in this paper, both fixed and variable knot procedures were applied. To solve a fixed knot problem, procedures established by the author were used. The variable knot approximation results were obtained with the use of IMSL Fortran procedures that are described in detail in [4].

3. Experimental

Laser Interferometry Dilatometer

Dilatometric measurements were performed using an absolute laser-interferometry apparatus with a microcomputer system for data acquisition and processing (Figure 3). A modified spherical interferometer was utilised. Detailed information of the instrument and the methodology of measurements are given in [7]. The apparatus enables high thermal resolution investigations of CLTE α and linear expansion ε (LE) within a temperature range from –150 K to 1400 K (from about -120 ^{o}C to about 1140 ^{o}C). Specimens of various shapes can be tested. The actual resolution depends on many factors and affects the accuracy of CLTE determination. Both parameters are correlated and should be analyzed together for every individual case. Test measurements performed for a Cu specimen within the range from 300 to 800 had shown that even if the resolution $\Delta T \cong 2$ K was preserved, the uncertainty could be less than 1 % [7]. Usually the resolution ranges from 0.05 K to 2.0 K.

The measured CLTE values are referred to the room temperature specimen length $l_0 = l(t_0 = 20\ ^{o}\text{C})$ giving experimental standard values of $\alpha^*(t)$ (comp. Figure 4.a)

$$\alpha^*(t) = \frac{1}{l(t_0)}\frac{dl(t)}{dt} = \frac{1}{l_0}\frac{dl(t)}{dt} \tag{5}$$

where t stands for the temperature. The LE is referred to l_0 giving the dilatation denoted here as ε. The LE is calculated by integration of the $\alpha^*(T)$ curve (Figure 4.b)

$$\varepsilon(t) = \frac{l(t) - l(t_0)}{l(t_0)} \tag{6}$$

The data processing is completed with “thermal extortion” diagrams, ie diagrams of the temperature change rate as a function of the actual temperature of the specimen (Figure 4.c).

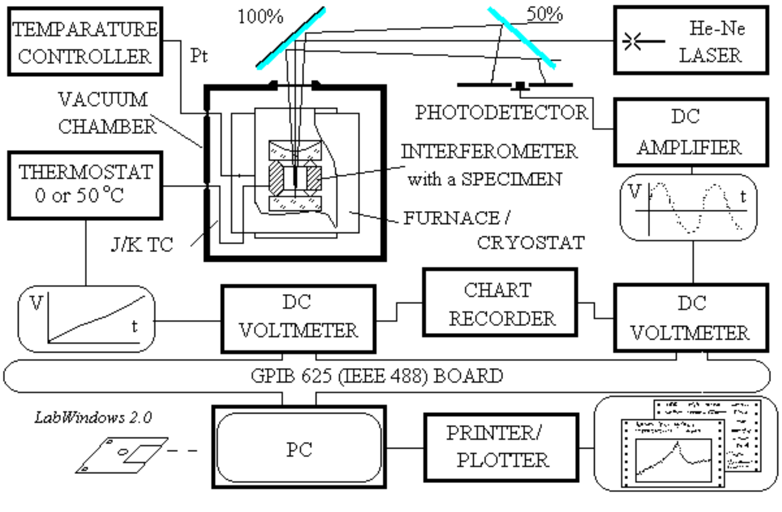

Figure 3. Schematic diagram of the experimental stand

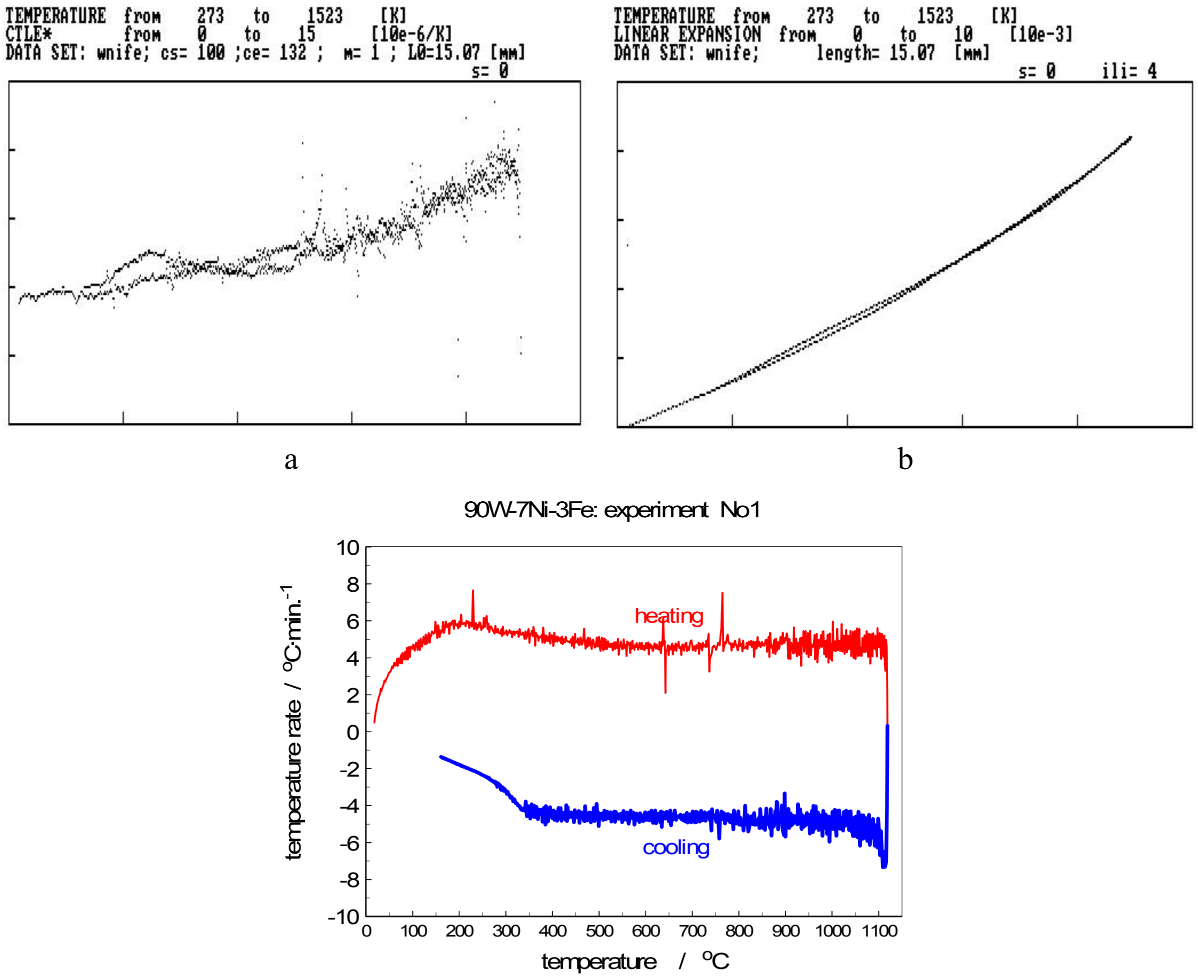

a b

c

Figure 4. Illustration of typical results from dilatometric investigations: a – measured values of the coefficient of linear thermal expansion (CLTE*) in $10 \cdot K^{-1}$, b – linear expansion (LE) i.e. dilatation in $mm \cdot m^{-1}$ and c – temperature rate versus the specimen temperature (thermal programme). The results shown are obtained at 1-st experimental cycle for the 90W-7Ni-3Fe specimen

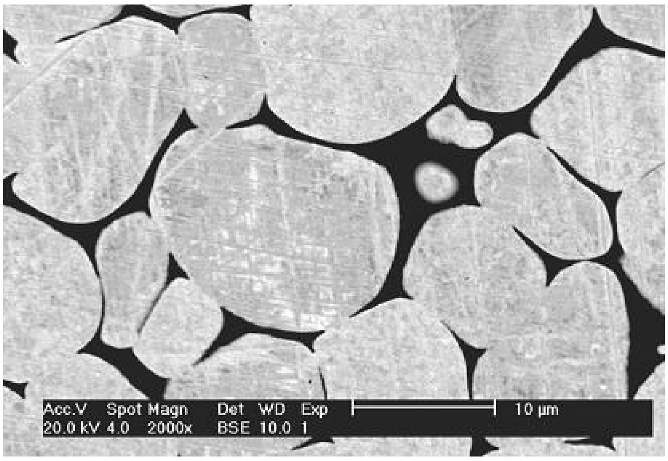

Figure 5. Microstructure of the investigated material: the bright particles are tungsten filler, the dark area is 53Ni-23Fe-24W homogeneous matrix [8]

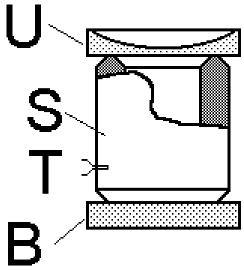

Figure 6. Configuration of the interferometer: U – upper spherical interferometer mirror, B – bottom mirror, T – thermocouple, H – specimen holder, S – cylindrical specimen

Specimen Preparation and Measurement Procedure

The measurements were performed on a 90W-7Ni-3Fe alloy specimen. The numbers in the alloy name stand for the mass composition. The material exhibits typical structure: quasi-spherical hard tungsten particles are embedded in a ductile 53Ni-23Fe-W matrix (Figure 5). The alloy was prepared using standard procedures by sintering its powdered components at about 1650 °C. Cylindrical specimen was prepared from the finally fabricated ingot by machining to the shape of a hollow cylinder (see Figure 6). The outside diameter of the cylinder was about 19.9 mm, the length was equal to 15.07 mm. The upper horizontal surface of the specimen was cut to ensure a tripod support of the upper interferometer mirror. The dilatometric experiments were carried out under vacuum conditions within the range from room temperature to about 1120 °C on both heating and cooling over repeated temperature cycles. The heating/cooling rates were usually about 5 K/min. The investigations included four repeated measurements in total.

Results of Experimental Investigations

Dilatometric measurements established experimental thermal characteristics of CLTE* (α*) and dilatation (LE) of the investigated material. The resolution of the recorded data was better than 2 K. The raw experimental data are shown in Figure 4 (1st run) and in Figure 7 (the next three runs).

Inspection of the obtained results revealed phase transition that appeared roughly about 700 °C. The onset temperature of the transition differ between heating and cooling for about 10÷20 °C. It was also observed magnification of the CLTE* heating and cooling peaks in every consecutive run. The revealed phase transition results in hysteresises observed on LE curves (Figs 4.b, 7.b, 7.d and 7.f). However, these effects were not accompanied by any permanent changes of the basic specimen length l_0.

4. Numerical Processing of the Experimental Data

Basic tasks of approximation analysis were defined in view of processing of high resolution CLTE* data. They are as follows:

1. Smoothing the dispersed CLTE* data.
2. Reconstruction of the analyzed CLTE* thermal characteristic altogether with its discontinuities due to phase transition.
3. Substitution of discrete data with a representative function enabling data tabulation.

All the above also concerns the dilatation ε. However, there is another task constituting a real challenge:

4. Reconstruction of the CLTE* characteristic using only the LE data.

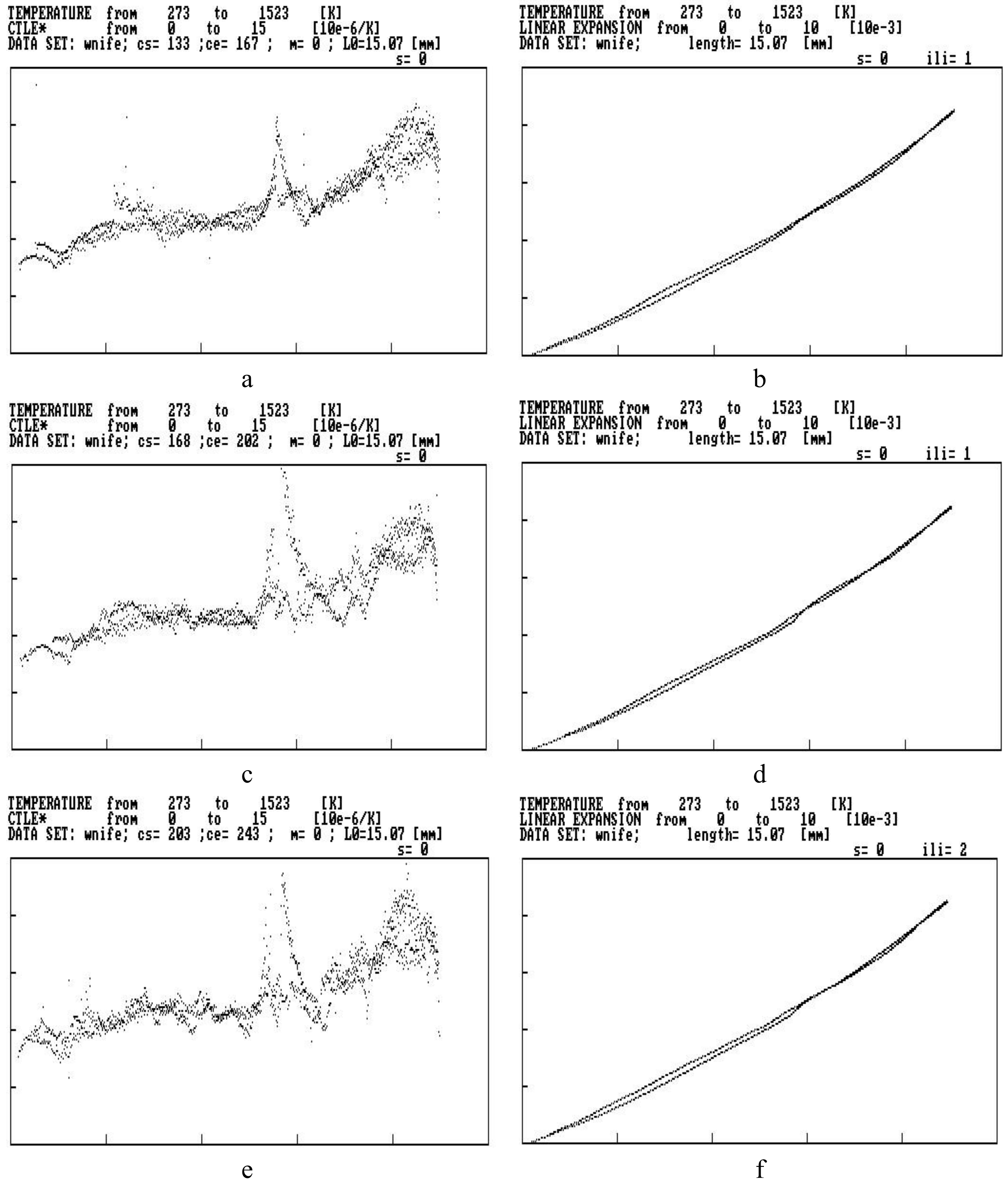

Figure 7. CLTE* and LE results from repeated runs: a, b – 2nd; c, d – 3rd; e, f – 4th

The difficulties in performing the last are mostly due to integral character of dilatation with reference to linear expansivity (comp. eg. [3]).

Basic calculations were performed separately on overlapped heating and overlapped cooling results from all four measurements. Both fixed and variable knot procedures were applied. The uniform weights w_i=1 were taken for the data processing. In calculations 4th order splines were applied. The initial guesses for knots accounted for possible discontinuity of $\alpha^*(T)$ curve at phase transition: corresponding knots at 708 °C for heating and at 695 °C for cooling were multiplied by four. Locations of these crucial knots were established in preliminary calculations – at this stage variable knot procedure was applied once or twice and initial guesses were shifted according to the obtained results. The effects of data processing are shown in Figure 8.

Repeated variable knots calculations applied for compacted CLTE* results made possible more reliable identification of the (averaged) phase transition temperature from sparsely distributed experimental data. Fixed knots algorithm resulted in more reliable representation of the averaged thermal characteristic. Tabulated data and information concerning B-spline representation of the appropriate approximate will not be presented here but it should be mentioned that they are accompanied by a piecewise polynomial representation consisting on 4 and 6 polynomials for heating and cooling respectively (see Tab. 1).

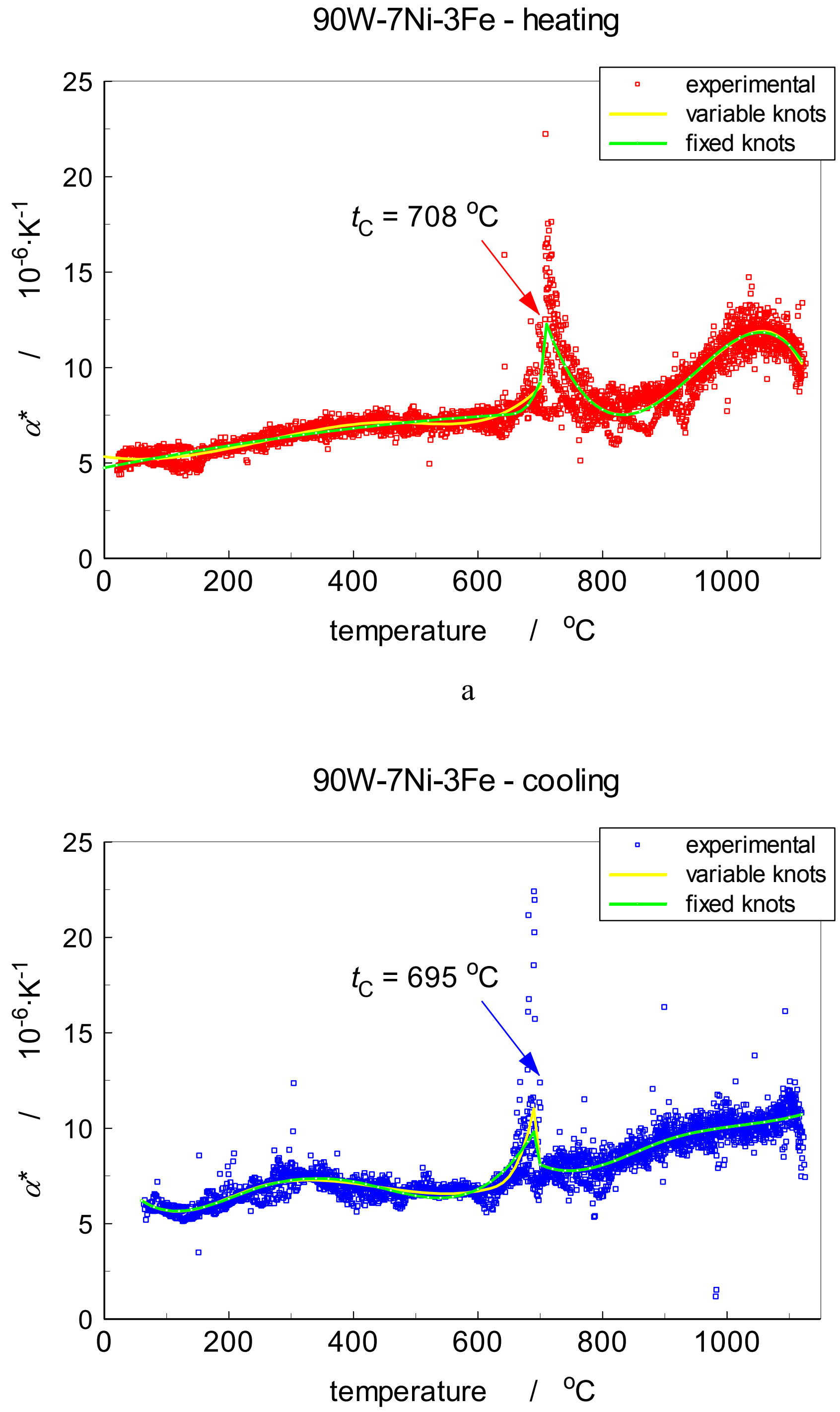

a

b

Figure 8. Results of B-spline approximation of CLTE* experimental data from: a - heating and b – cooling runs with indication of the identified phase transition peak temperatures

Table 1. Knots distributions for spline characteristics obtained for CLTE* results (data in °C)

Heating (Fig. 8.a)		Cooling (Fig. 8.b)	
Fixed / initial guess	Resultant variable	Fixed / initial guess	Resultant variable
-10	-10	40	40
-10	-10	40	40
-10	-10	40	40
-10	-10	40	40
644	461.9863	250	250
708	706.0758	408	617.3073
708	707.6634	690	689.0349
708	708	695	695
708	708	695	695
940	1003.97	695	695
1140	1140	695	695
1140	1140	905	900.92
1140	1140	1140	1140
1140	1140	1140	1140
		1140	1140
		1140	1140

Table 2. Results of B-spline approximation of LE results from 3rd run

Heating (Fig. 9.a – magenta curve)				Cooling (Fig. 9.a – cyan curve)			
t / °C	LE / mm·m	*t* / °C	LE / mm·m	*t* / °C	LE / mm·m	*t* / °C	LE / mm·m
0	-0.1536	600	3.667983			600	3.787316
50	0.156133	650	4.020009			650	4.137864
100	0.409651	700	4.404421	100	0.481182	700	4.60696
150	0.662437	750	5.021262	150	0.716601	750	4.978506
200	0.938911	800	5.489223	200	1.01746	800	5.356592
250	1.23956	850	5.865678	250	1.357883	850	5.767552
300	1.559742	900	6.223205	300	1.717342	900	6.21928
350	1.895078	950	6.623683	350	2.080658	950	6.701695
400	2.241509	1000	7.113113	400	2.438006	1000	7.198724
450	2.595287	1050	7.688818	450	2.784882	1050	7.703204
500	2.952983	1100	8.278246	500	3.12165	1100	8.218685
550	3.311481	1120	8.48811	550	3.452892	1120	8.430792

For illustration of the algorithm performance in reconstruction of a certain thermal data from its integral characteristic results of linear expansion measurements form the 3rd experiment run were arbitrarily selected. The data were processed applying 5th order splines which correspond to 4th order splines applied in CLTE* approximations. The input data as well as the results of calculations are shown in Figure 9. The illustrated results come from variable knot procedure. The data on LE are additionally presented in tabulated form in Table 2.

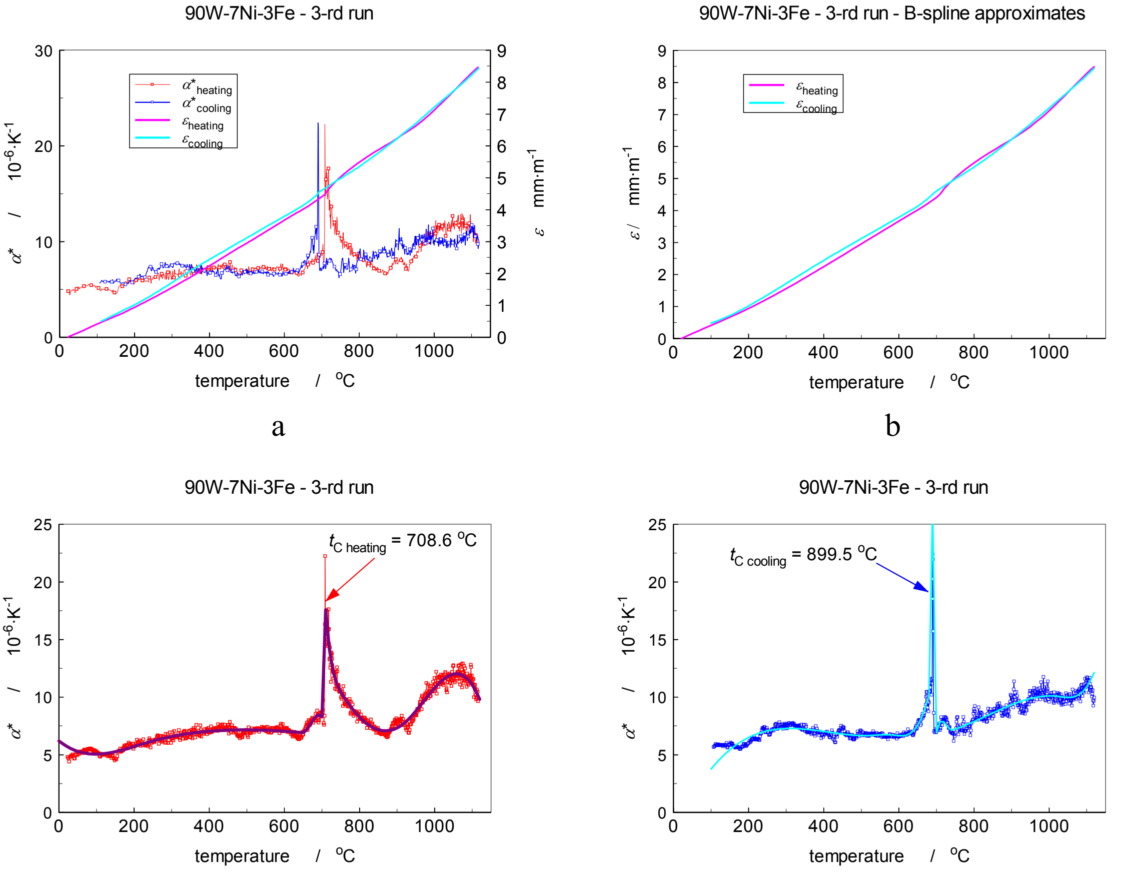

a b

c d

Figure 9. Results of 3rd run of dilatometric measurements (a) and effect of the LE experimental data approximation (b) together with results of CLTE* characteristics identification for heating (c) and cooling (d) from the approximated LE data

Analyzing the results one can notice inconsistency for about 0.7 % at 1120 °C in LE data. This discrepancy reflects initial inconsistency in experimental data and can not be attributed to the approximation procedure. The input data was not corrected for the temperature gradients[1]. However, it should be underlined that like in every approximation problem performance of fitting procedures at both ends of the data range usually is the weakest. Results shown in Figs 9 c and d confirm this observation. As was expected (comp. e.g. [4], [6], [11]) the fixed knot procedures were proved to be more reliable in data representation at the basic interval ends but they need additional information at the input.

5. Summary

The high thermal resolution dilatometric data from 90W-7Ni-3Fe tungsten heavy alloy investigation were numerically processed applying B-spline approximation procedures. The numerical analysis helped in inspection of the raw experimental data and enabled to establish representative thermal characteristics of the investigated property. The results were differentiated between heating and cooling. For the first time (comp. [2], [6] and [11]) the procedure of the spline approximation was applied for combined data from different experiments. There are

---

[1] The problem of the nonuniform temperature distribution within the interferometer system is discussed in [7].

promising outcomes from the performed analysis. The used procedures were proved to be not only well conditioned and effective in reconstruction of differential characteristics, helpful in detection of thermal characteristic singularities but also useful in providing the results averaged between different experimental runs.

The investigations, including numerical analyses results, provided data for further studies. The LE data will be applied in numerical modeling of heat transfer phenomena that occur during material sintering. The results of the phase transition investigation contribute to better understanding of the material under thermal cycling.

Acknowledgement

The research was supported by the State Committee of Scientific Research of Poland grant R 00 024 02 (2006-2010) and MUT project GW-HB 647 (2008).

References

[1] Grimvall, G.: *Thermophysical Properties of Materials*, Elsevier Sc. Publ. B. V., Amsterdam, 1986.

[2] Panas, A. J. and J. Terpiłowski: in *Proc. of the 7th International Symposium on Temperature and Thermal Measurements in Industry and Science TEMPMEKO'99*, May 30 – June 3, Delft 1999, pp. 493-498

[3] Björck, Å. and G. Dahlquist: *Numerical Methods*, Prentice-Hall, London, 1974.

[4] De Boor, C. 1976: *A Practical Guide to Splines*, Appl. Math. Sciences v. 27, Springer Verlag, Berlin, 1976.

[5] Ciesielski, Z.: *Theory of Spline Functions*, University of Gdańsk, Gdańsk, 1976/1977 (in Polish).

[6] Panas A. J.: *Achives of Thermodynamics*, 24 (4), 2003, pp. 47-65.

[7] Panas, A. J.: *The high thermal resolution investigation of the linear expansivity – Dilatometric thermal analysis*, Military University of Technology Monograph, Warsaw 1998, (in Polish).

[8] Panas A. J., Terpiłowsk J., Majewski T.: *Investigation of Thermophysical Properties of 53Ni-23Fe-24W Matrix Phase Component of WHA*, paper presented at the 18th European Conference on Thermophysical Properties, Pau, France, 31st August – 4th September 2008.

[9] Lassner, E., Schubert, D.W.: *Tungsten. Properties, Chemistry, Technology of the Element, Alloys and Chemical Compaunds* KluwerAcademic / Plenum Publishers, New York 1998, p.274.

[10] Taylor, R. E.: *Thermal Expansion of Solids*, CINDAS Data Series on Material Properties, V I-4, C. Y. Ho Editor, ASM International, Materials Park OH, 1998.

[11] Panas, A. J.: *Dilatometric Investigations of Phase Transitions Using B-Spline Data Processing*, in *Thermal Conductivity 27 / Thermal Expansion 15,* Wang H., Porter W. Eds., DEStech Publications, Inc., Lancaster PA, 2005, pp. 584-594.

APPLICATION OF EFFECTIVE MEDIA THEORY IN THE DETERMINATION OF THERMAL CONDUCTIVITY OF WET LIME-POZZOLANA RENDERS

Zbyšek Pavlík, Radka Pernicová, Milena Pavlíková, Lukáš Fiala, Robert Černý

Czech Technical University in Prague, Faculty of Civil Engineering, Department of Materials Engineering and Chemistry, Thákurova 7, 166 29 Prague, Czech Republic,
email: pavlikz@fsv.cvut.cz, radka.pernicova@fsv.cvut.cz,
milena.pavlikova@fsv.cvut.cz, fialal@fsv.cvut.cz, cernyr@fsv.cvut.cz

Abstract:

Moisture dependent thermal conductivity of lime-pozzolana based render is studied in the paper. First, the measurements of thermal conductivity are performed in dependence on moisture content from the dry state to the fully water saturated state using an impulse technique. Then, the obtained data are analyzed using several different homogenization techniques, among them, Lichtenecker, Dobson and Polder and van Santen formulas for various shapes of the pores and inclusions were used. On the basis of this analysis, the most suitable mixing formula giving the best agreement with the experimental data for all studied materials is identified and recommendations for its practical application and possible extensions and limitations to the other types of materials are formulated.

Keywords:

Thermal conductivity, homogenization techniques, lime-pozzolana renders

INTRODUCTION

Thermal conductivity as the main parameter describing the heat transport of building materials appears to be of particular importance for their practical applications. For their use in building structures there is necessary to take into account that their thermal performance is strictly dependent on total pore volume, distribution and cross connections of pores. In materials research, thermal conductivity of dry materials is mainly studied. However, absolutely dry materials never occur in the conditions of building sites. Also the materials already inbuilt in the structures and exposed to the climatic loading exhibit the dependence of their properties on moisture changes. If the material is wet, heat transferred by moisture in the capillaries adds to the density of heat flow rate. The thermal conductivity of water is 0.60 W/mK [1], which is more than 20 times higher than of the air. Therefore, if water is present in the pore space, its effect competes with the effect of air, and the thermal conductivity of a composite material can be considered as a result of this competition, together with the effect of the solid matrix [2]. On this account, there is necessary to have information on the dependence of thermal conductivity on moisture content rising. Experimental measurement of thermal conductivity of several samples having different moisture content is quite time consuming and in consequence expensive, new approaches for the assessment of moisture dependent thermal conductivity have to be explored and tested in materials research.

Homogenization theories working with the concept of an effective medium have proven very useful in a variety of applications in mechanics and in the theory of electricity and magnetism where they already belong to well established treatments (see, e.g., [3]). Within the last couple of years, some references appeared on using the effective media theories for estimation of thermal conductivity of refractory materials, foams, and polymer-based composites. In spite of very promising results, the use of homogenization theory for the assessment of thermal conductivity of lime-based composite materials is still exceptional until now.

In this paper we refer about application of homogenization theory for the assessment of the moisture dependent thermal conductivity of lime-pozzolana composite materials. The measured values of thermal conductivity are analyzed using several types of homogenization formulas originally derived for application in electromagnetic field theory taking into account the limiting bounds of the function of effective thermal conductivity.

EXPERIMENTAL METHODS AND STUDIED MATERIALS

Thermal conductivity as a main parameter describing the heat transport in materials can be experimentally accessed either by steady state methods or by transient methods. For the measurements presented in this work, the commercially produced device ISOMET 2104 (Applied Precision, Ltd.) was used as a typical representative of transient impulse methods. ISOMET 2104 is a multifunctional instrument for measuring thermal conductivity, thermal diffusivity, and volumetric heat capacity. It is equipped with various types of optional probes whereas for our experiments we have chosen surface probe. The measurements in this paper were done in laboratory conditions at average temperature 23 ± 1°C. The material samples were first dried and after that exposed to liquid water for specific time intervals. In this way, the different moisture content of the studied samples was reached. The sample size for thermal conductivity measurement was 70 x 70 x 70 mm.

We have tested newly developed lime-pozzolana based plaster that should find use in restoration and reconstruction of historical buildings (denoted VOM) and reference pure lime plaster (VO). The composition of the studied materials is presented in Table 1.

Table 1. Composition of the studied lime based renders

Type of mixture	Amount in kg			Water
	Lime hydrate	Silica sand 0/2 mm, Bratčice	Metakaoline	
VO	4.80	14.40	-	4.80
VOM	4.80	14.40	0,8	4.80

Plaster mixtures were prepared using laboratory mixing machine with forced rotation for 3 minutes and then compacted using vibrating machine. Each mixture was cast into a cube moulds. After two days were the samples unmoulded and then cured for 28 days in high relative humidity environment.

Both the thermal properties and the moisture content of porous building materials depend mainly on the pore structure of the particular material. Therefore, basic material parameters of the studied materials were measured as well. Nominally, bulk density ρ_b [kg m^{-3}], matrix density ρ_{mat} [kg m^{-3}], and total open porosity ψ [%] were determined. Bulk density was determined on gravimetric principle, matrix density using Pycnomatic ATC. Total open porosity was then calculated from these two quantities. The measured values of basic material parameters are given in Table 2. Since the total porosity of the tested materials is almost the same, the similar thermal performance of the investigated materials can be expected.

Table 2. Basic material parameters of the studied materials

Material	ρ_b [kg m^{-3}]	ρ_{mat} [kg m^{-3}]	ψ [%]
VO	1650	2605	36.7
VOM	1695	2620	35.4

HOMOGENIZATION THEORY

In terms of effective media theory, a porous material can be considered basically as a mixture of three phases, namely solid, liquid and gaseous phase. In the lime based renders studied in this work, the solid phase is represented by the products of joint hydration of lime hydrate, metakaoline and silica sand, the liquid phase by water and the gaseous phase by air. On that account, the homogenization procedure presented in this work was performed in two steps.

The first task was the determination of thermal conductivity of the lime and pozzolana-lime based matrix. This was done on the basis of the known thermal conductivities and amounts of its constituents. In this work, the thermal conductivity of solid matrix was calculated using the Rayleigh [4] mixing rule

$$\frac{\lambda_M - 1}{\lambda_M + 2} = f_c\left(\frac{\lambda_c - 1}{\lambda_c + 2}\right) + f_m\left(\frac{\lambda_m - 1}{\lambda_m + 2}\right) + f_{cf}\left(\frac{\lambda_{cf} - 1}{\lambda_{cf} + 2}\right) + f_w\left(\frac{\lambda_w - 1}{\lambda_w + 2}\right), \tag{1}$$

where λ_M is the thermal conductivity of the whole solid matrix, λ_s thermal conductivity of silica aggregates (3.5 W/mK), λ_c thermal conductivity of hydrated lime – calcium carbonate (5.5 W/mK), f_s volumetric fraction of silica aggregates, f_c volumetric fraction of calcium carbonate. The values of thermal conductivities of particular components of lime-based composites were taken from CRC Handbook of Chemistry and Physics [1]. Because the data on thermal conductivity of metakaoline are not presented in literature, the effect of metaoline addition was involved into the homogenization procedure within the evaluation of the effective thermal conductivity of the whole dry lime based materials on the basis of the comparison of measured and calculated data. Using this backward analysis, the effect of thermal conductivity of metakaoline on the thermal conductivity of pozzolana-lime based composite was identified and considered in homogenization modeling.

The second step within the homogenization procedure represents evaluation of effective thermal conductivity of the whole material, where the mixing is performed for solid matrix, air, and water. As stated in literature, the function of effective thermal conductivity cannot exceed the bounds given by the thermal conductivities and volumetric fractions of its constituents. Several different bounds was already formulated and tested, especially in the theory of electromagnetic field. In this paper, we used for the verification and validation of obtained results Wiener's [5] and Hashin-Shtrikman's [6], [7] bounds.

The upper Wiener's bound is reached in a system consisting of plane-parallel layers of material constituents disposed along the heat flux vector. The lower Wiener's bound is reached in a similar system but with the layers perpendicular to the heat flux. The Wiener's bounds are expressed by the following equations

$$\lambda_{eff} = f_1\lambda_1 + f_2\lambda_2 + f_3\lambda_3, \tag{2}$$

$$\lambda_{eff} = \frac{1}{\frac{f_1}{\lambda_1} + \frac{f_2}{\lambda_2} + \frac{f_3}{\lambda_3}}, \tag{3}$$

where Eq. (2) represents the upper limit and Eq. (3) the lower limit of the effective thermal conductivity (f_j is the volumetric fraction of the particular phase, λ_j its thermal conductivity, and λ_{eff} effective thermal conductivity of the whole porous body).

Hashin-Shtrikman's bounds were originally derived for two-phase systems only. However, we have performed their extension to three- and four- phase systems. The lower limit of the effective thermal conductivity function can be expressed as

$$\lambda_{lower} = \lambda_1 + \frac{3\lambda_1}{\frac{1}{\sum_{i=2}^{n} f_i \frac{\lambda_i - \lambda_1}{2\lambda_1 + \lambda_i}} - 1}, \tag{4}$$

and the upper limit as

$$\lambda_{upper} = \lambda_n + \frac{3\lambda_n}{\frac{1}{\sum_{i=1}^{n-1} f_i \frac{\lambda_i - \lambda_n}{2\lambda_n + \lambda_i}} - 1}. \tag{5}$$

In Eqs. (4)-(5), $f_1 - f_n$ are the volumetric fractions of the particular phase ($f_1 + f_2 + ... + f_n = 1$), and $\lambda_1 - \lambda_n$ are their thermal conductivities, whereas $\lambda_1 < \lambda_2 ... < \lambda_n$.

The second step within the homogenization procedure represents evaluation of effective thermal conductivity of the whole material, where the mixing is performed for solid matrix, air, and water.

For the evaluation of effective thermal conductivity of the whole material several different homogenization techniques can be used. In this paper we have used formulas proposed by Lichtenecker [8], Dobson [9], and Polder and van Santen [10].

The Lichtenecker's formula is expressed by Eq. (6)

$$\lambda_{eff}^{k} = \sum f_j \lambda_j^{k}, \tag{6}$$

and represents straightforward generalization of Wiener's formula whereas the parameter k varies within the [-1, 1] range.

Because of the large difference between the thermal conductivity of free and bound water in porous medium, Dobson et al. extended the Lichtenecker's power-law formula. They arrived at the following relation

$$\theta = \frac{\lambda_{eff}{}^{\beta} - \theta_{bw}(\lambda_{bw}{}^{\beta} - \lambda_{fw}{}^{\beta}) - (1-\psi)\lambda_s{}^{\beta} - \psi\lambda_a{}^{\beta}}{\lambda_{fw}{}^{\beta} - \lambda_a{}^{\beta}} \tag{7}$$

that takes into account the effect of partial water bonding on the pore walls and contribution of thermal conductivity of bound water to the effective thermal conductivity of partially wetted materials. In Eq. (7), θ_{bw} is the amount of water bonded on pore walls [m^3/m^3], λ_{bw} the thermal conductivity of bound water (according to [11], the bound water can be assumed to have the same thermal conductivity as ice, so near -20°C it is equal to 2.4 W/mK), λ_{fw} the thermal conductivity of free water (0.6 W/mK), λ_a the thermal conductivity of air (0.026 W/mK), ψ the total open porosity, and β is an empirical parameter.

Also the effect of the shape of particular constituents can have significant influence on the accuracy and reliability of homogenization formulas for specific groups and types of materials. Polder and van Santen formulated formulas that are valid for spherical inclusions (Eq. (8)) , needle-shape inclusions (Eq. (2)), and board-shape inclusion (Eq (3)). The final formulas can be written in the following way

$$\lambda_{eff} = \lambda_M + \sum f_j (\lambda_j - \lambda_M) \cdot \frac{3\lambda_{eff}}{2\lambda_{eff} + \lambda_j}, \tag{8}$$

$$\lambda_{eff} = \lambda_M + \sum f_j (\lambda_j - \lambda_M) \cdot \frac{5\lambda_{eff} + \lambda_j}{3\lambda_{eff} + 3\lambda_j}, \tag{9}$$

$$\lambda_{eff} = \lambda_M + \sum f_j (\lambda_j - \lambda_M) \cdot \frac{2\lambda_j + \lambda_{eff}}{3\lambda_j}. \tag{10}$$

RESULTS AND DISCCUSION

The results obtained for the reference plaster VO calculated by application of Lichtenecker's formula are presented together with the measured data in Fig. 1. We can see the effect of parameter *k* that was used as empirical fitting parameter for the performed calculations.

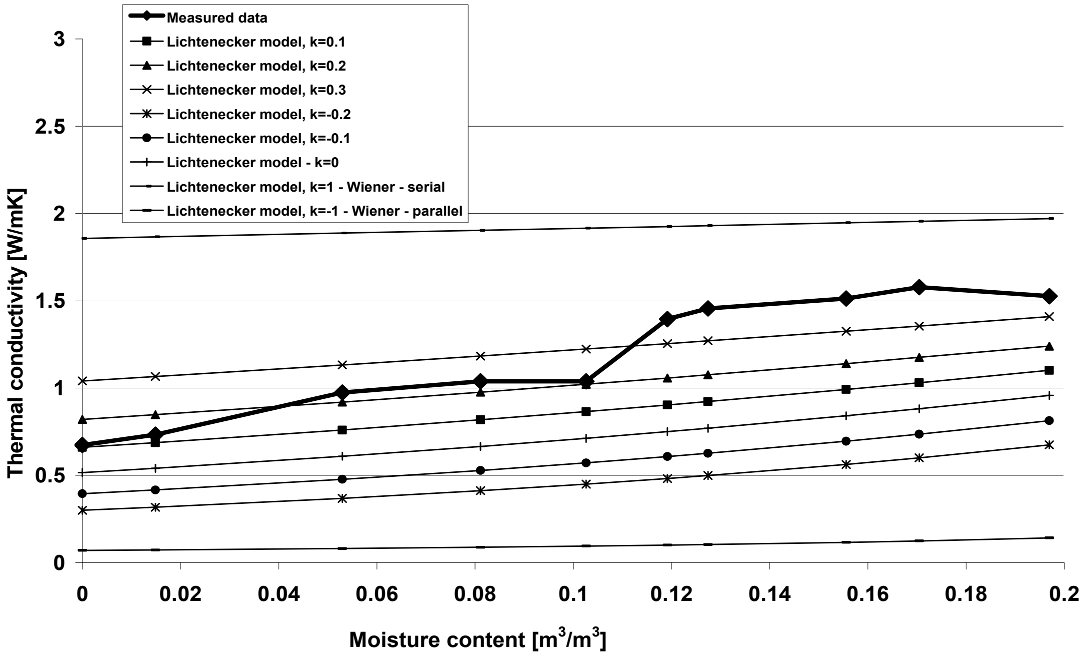

Figure 1 Measured and calculated results for VO, Lichtenecker's formula

Relatively good agreement between calculated results and measured data was obtained in the lower moisture contents, typically up to 10% of volumetric moisture. On the other hand, for the highest moistures, the Lichtenecker's equation completely failed and no reasonable results were obtained. Fig. 2 presents the results obtained by application of Dobson's four phase model for material VO. In this case, based on the parameter β and amount of bound water, the very good agreement between measured and calculated data was obtained in the higher moisture contents.

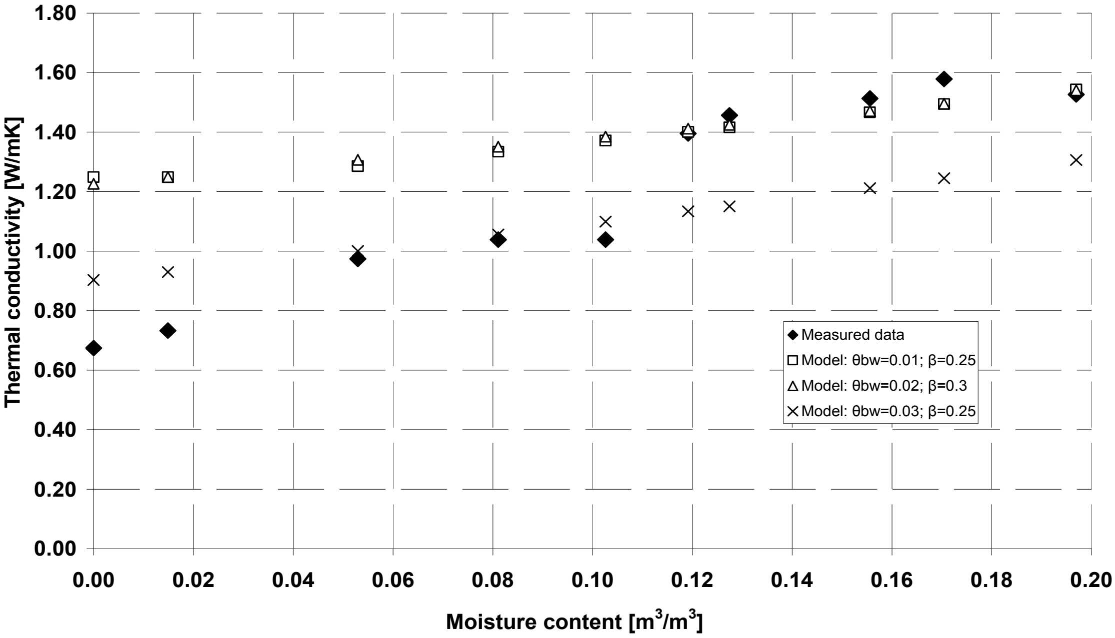

Figure 2 Measured and calculated results for VO, Dobson's formula

Results of application of Polder and van Santen's models for material VO are given in Fig. 3. In this figure, the bounds of effective thermal conductivity function are presented as well.

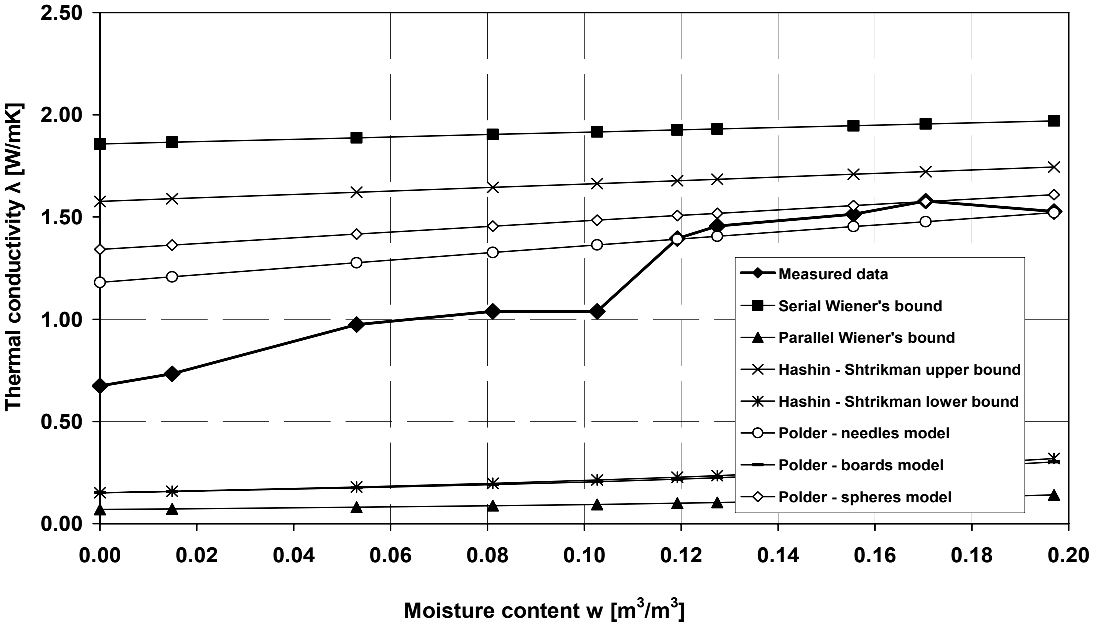

Figure 3 Measured and calculated results for VO, Polder and van Santen's formulas

Very good agreement with measured data was observed again in the range of higher moisture contents but only for model taking into account the needle inclusions in the material. Other tested models completely failed. However, the measured result fulfils the conditions of limiting Wiener's and Hashin-Shtrikman's bounds. This finding can be considered as a certain verification of the performed measurements. The results obtained for material VOM are presented in the following figures.

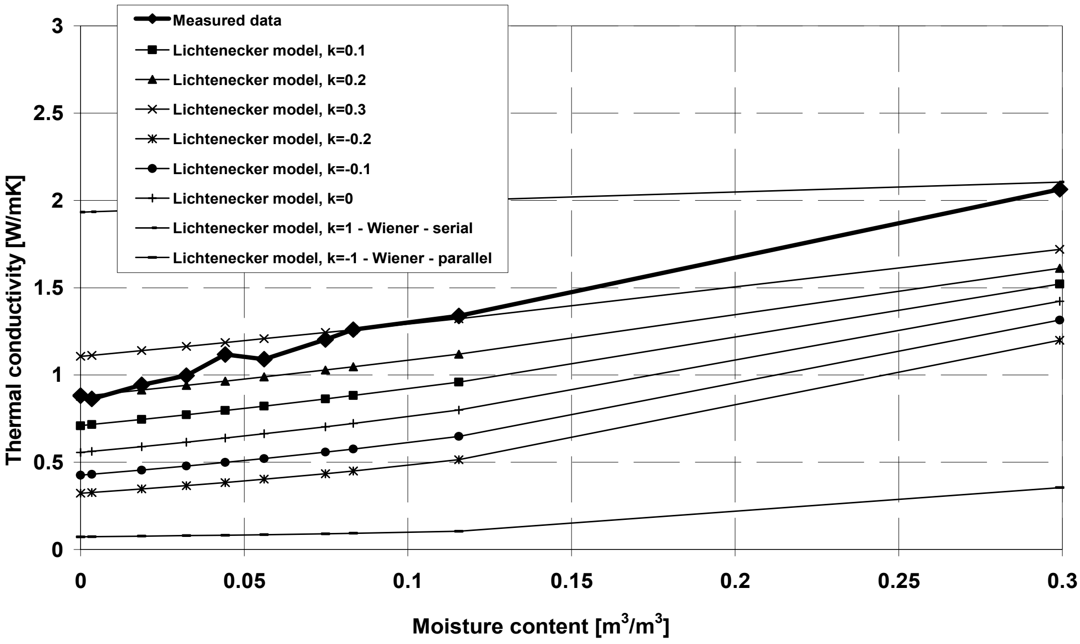

Figure 4 Measured and calculated results for VOM, Lichtenecker's formula

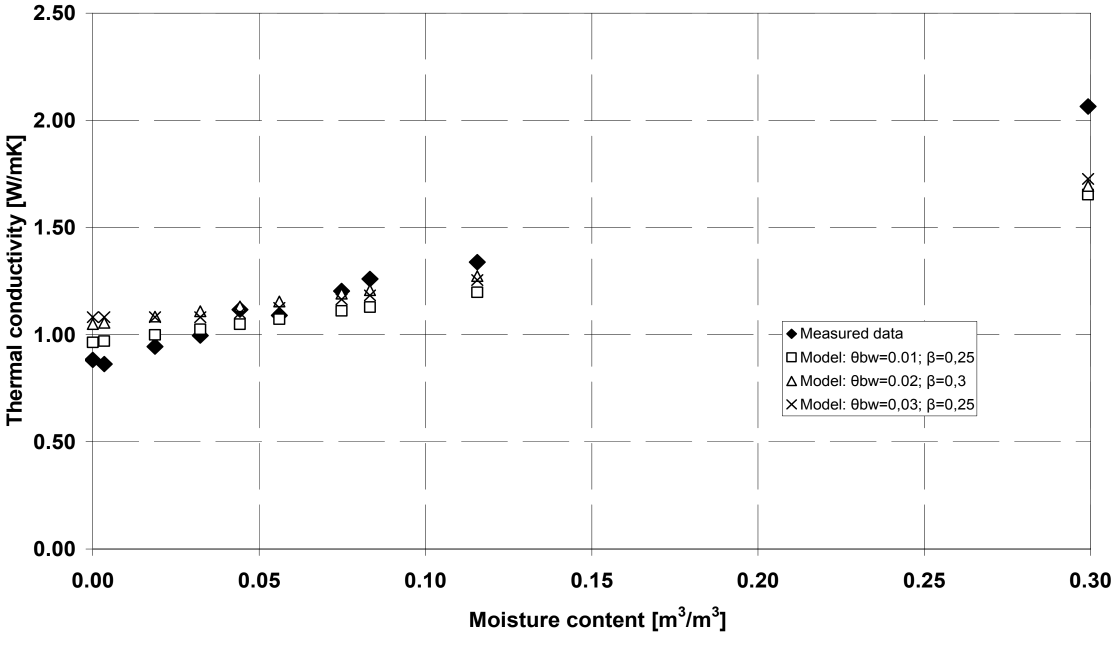

Figure 5 Measured and calculated results for VOM, Dobson's formula

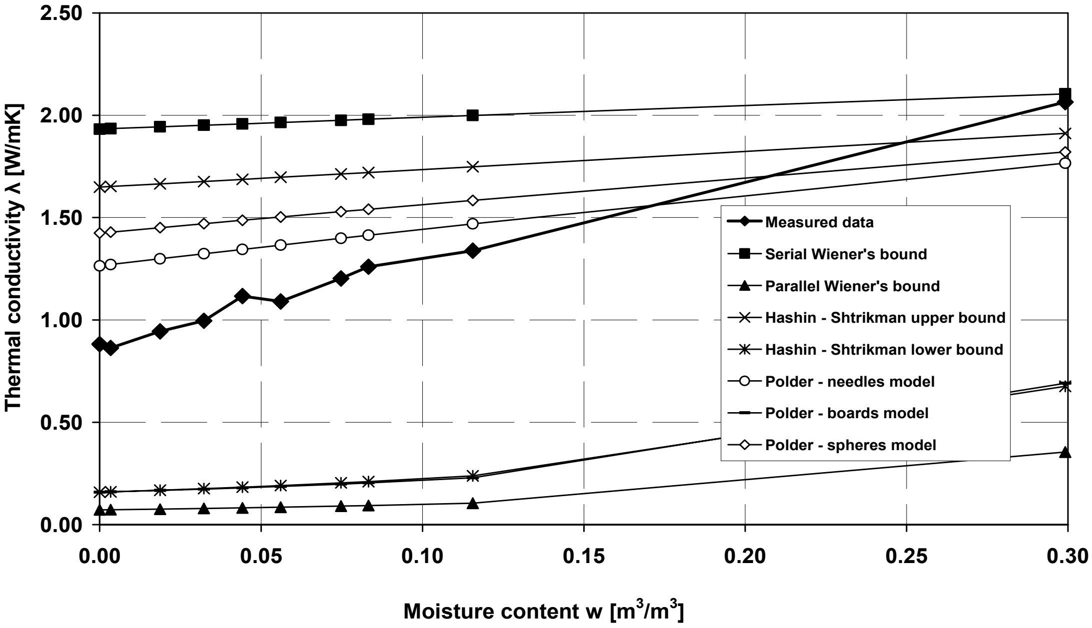

Figure 6 Measured and calculated results for VOM, Polder and van Santen's formulas

In the case of VOM material, the best agreement between measured and calculated data was obtained by application of Dobson's four phase model. However, two fitting parameters were considered in calculations.

CONCLUSIONS

The measured data presented in this paper can find utilization in practical applications of the studied lime based composite renders. The analyzed homogenization techniques were found to be applicable for evaluation of moisture dependent thermal conductivity although the obtained error bar is quit high. Therefore, some other, more detailed analysis will be necessary, with a particular attention to the thermal conductivity values of the components of the lime matrix.

ACKNOWLEDGMENT

This research has been supported by Ministry of Education, Youth and Sports of Czech Republic, under project No MSM: 6840770031.

REFERENCES

[1] Lide D. R. (ed.), CRC Handbook of Chemistry and Physics, 79th Edition, CRC Press, Boca Raton, 1998.

[2] Zuda L., Pavlík Z., Rovnaníková P., Bayer P., Černý R., International Journal of Thermophysics, Vol. 27 (2006), pp. 10765.

[3] IEA-Annex XIV, Condensation and Energy, Volume 3, Material Properties, International Energy Agency, Leuven, 1991.

[4] Lord Rayleigh, On the influence of obstacles arranged in rectangular order upon the properties of the medium. Philos. Mag. 34 (1892), pp. 481–502.

[5] Wiener, O., Die Theorie des Mischkoerpers fuer das Feld der stationaeren Stroemung. Abhandlungen der Mathematischen-Physischen Klasse der Königlichen Sächsischen Gesellschaft der Wissenschaften 32 (1912), pp. 509-604.
[6] Hashin Z., Shtrikman S., Journal of Applied Physics 33(1962), pp. 3125.
[7] Sihvola A., Electromagnetic Mixing Formulas and Applications, The Institution of Electrical Engineers, London, 1999.
[8] Lichtenecker, Physikalische Zeitschrift 27 (1926), pp. 115.
[9] Dobson M. C., Ulaby F. T., Hallikainen M. T., El-Rayes M. A., IEEE Trans. Geosci. Remote Sensing GE 23 (1985), pp. 35.
[10] Polder D., van Santen J. H., Physica 12 (1946), pp. 257.
[11] Moy J. H., Chan King-Cham, Dollar A. M., Journal of Food Science 36 (1971), pp. 498.

THERMAL FIELDS IN LARGE REINFORCED CONCRETE CONSTRUCTIONS DURING THE HYDRATION

Stanislav Šťastník
Brno University of Technology, Faculty of Civil Engineering, 602 00 Brno, Veveří 95,
Czech Republic, e-mail stastnik.s@fce.vutbr.cz

Abstract

Hydration of a silicate binder is a highly exothermic reaction, thus it is possible to characterize the hydration process from the development of temperature of reactive mixtures. The calorimetric isoperibolic method is a very simple and relatively accurate method for the monitoring of hydration heat. The received experimental data are helpful for the formulation of a model of thermal behaviour of a large monolithic reinforced concrete structure.

Key words: Cement, hydration heat, chemical admixtures, calorimeters, reinforced concrete.

1. Hydration of cement

Hydration of cement is a exothermic reaction; the minerals contained in cement react with water and the products are badly soluble compounds, whose fixed connections form the microstructure of the hardening concrete. The intensity of the production of hydration heat depends on the rate of active reactions, conditioned by the mineralogical content of cement, by the presence of active admixtures and also on the environment.

The total amount of the produced hydration heat for a totally hydrated cement specimen is given as a sum of hydration heats corresponding to particular minerals, whose values differ substantially – see Table 1. This fact is able to explain the varying rate of hydration reactions, in the first rough estimate being proportional to the released hydration heat. Namely in the case of the pure Portland cement the dominating part of hydration heat belong to C_3S.

mineral	hydration heat [$J.g^{-1}$]
C_3A	800-1280
C_3S	380-540
C_4AF	120-440
C_2S	90-110
CaO	1116
MgO	812

Table 1: Values of hydration heat for some important minerals.

2. Methods for identification of hydration heat

In general, there are two basic types of methods for identification of hydration heat:

a) *the direct methods*, based on the recording of temperature changes of a test specimen under strictly defined boundary conditions,

b) *the indirect (dissolving) methods*, evaluating the hydration heat from the dissolving heat of the hydrated test specimens (after 7 and 28 days) in certain acid mixture.

The direct methods are rather accurate, but their output is only the total amount of hydration heat just at one selected time of the hydration progress. For the evaluation of hydration heat for a sample which is not hydrated completely, the test specimen has to be washed by the ethyl-alcohol and consequently desiccated.

The indirect methods enable us to record the evolution of quantities proportional to the intensity of production of hydration heat; the total amount of hydration heat can be then obtained from the integration of this intensity in time. Three mostly used types of indirect methods are:

i) *the adiabatic (or semi-adiabatic) methods* with no or negligible heat exchange between a test specimen and the environment during the whole measurement,

ii) *the isothermal methods* where a test specimen is tempered to a certain temperature and the thermal flux between a test specimen and the environment is recorded,

iii) *the isoperibolic methods* where the strictly prescribed conditions for the hydration are designed to simulate (as much as possible) the hydration process in a real building object.

Let us pay more attention to the method iii). This method can be applied both to the characterization of time-dependent production of hydration heat for binder mixtures and to the analysis of the modifying effect of chemical admixtures. Neglecting the thermal accumulation effect, we can consider the intensity of production of hydration heat as proportional to the measured temperature.

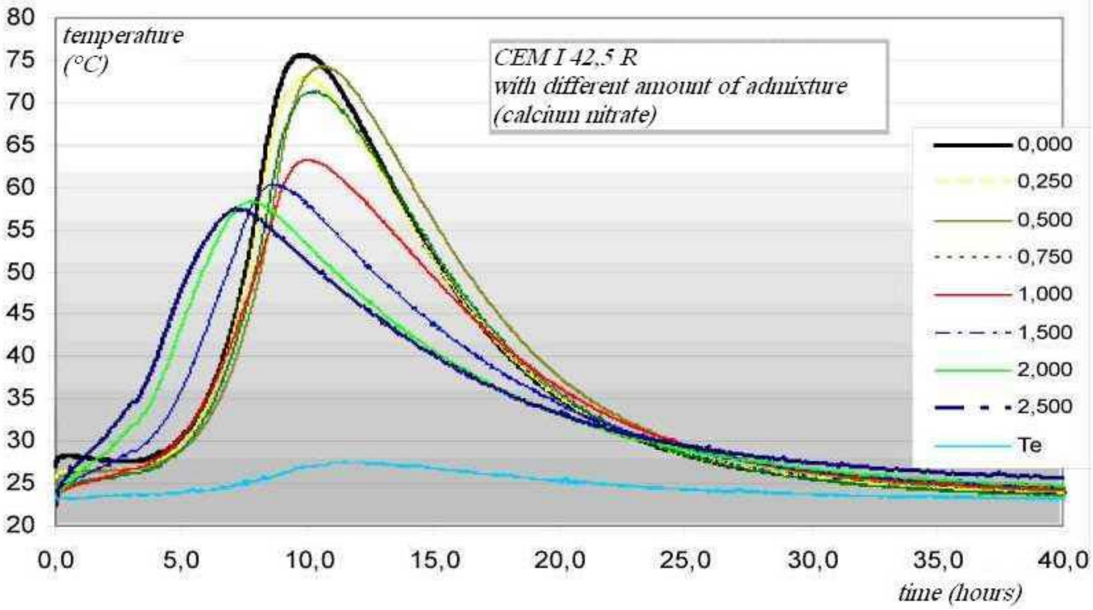

Figure 1: Evolution of hydration temperature in time.

Several colour curves at Figure 1 show the example of the time development of hydration temperature as a function of time. Various colours correspond to the different percentage of the calcium-nitrate-based admixture and (for comparison) to the environment.

3. Three-dimensional computational modelling

From the physical point of view, hydration is a complicated process, driven by a lot of interal thermodynamic relations and equilibrium conditions. The controlled evolution of temperature is needed especially in the case of massive monolithic constructions where a great mass of concrete is concentrated; such structure has a high thermal-accumulation ability and a relatively low amount of thermal losses through its surfaces. For the resulting development of the temperature the following influences seem to belong to the most relevant:

- the quality and amount of the applied cement,
- the geometrical configuration: the shape and the boundary conditions, determined by the foundation and boarding properties,
- the amount and concentrations of all chemical admixtures,
- the initial temperature of a concrete mixture and the time schedule of its depositing,
- climatic conditions.

Further influences, as the effect of cooling of the concrete surface, depend on the regime of the water treatment and with of the removal of boarding of particular fragments. However, the most important seems to be the first influence, whose direct connection with the reaction kinetic is evident; its evaluation, required by the computational modelling, can be performed using the calorimetric measurements.

The distribution of some temperature field t in an arbitrary volume, characterized by the Cartesian coordinates (x, y, z), and also in an arbitrary time τ, can be obtained from one partial differential equation of evolution (of the parabolic type) in the form

$$\frac{\partial}{\partial x}\left(\lambda_x \frac{\partial t}{\partial x}\right)+\frac{\partial}{\partial y}\left(\lambda_y \frac{\partial t}{\partial y}\right)+\frac{\partial}{\partial z}\left(\lambda_z \frac{\partial t}{\partial z}\right)+\frac{\partial Q}{\partial \tau}-\rho .c\frac{\partial t}{\partial \tau}=0 \tag{1}$$

where Q is the energy of internal sources (in general a function of x, y, z and τ), ρ is the material density, c is the heat capacity and λ is the thermal conductivity: in general it can be different in the directions x, y, z, which is distinguished by its index.

If (1) is formulated for certain domain Ω then its boundary Γ can be divided into two non-overlapping parts, Γ_1 and Γ_2, where the mixed boundary conditions are prescribed. The non-homogeneous Dirichlet boundary condition with some prescribed function $\overline{t}$ is

$$t=\overline{t}\left(x,y,z,\tau\right) \text{ on } \Gamma_1 .$$

The remaining boundary condition

$$\lambda_x \frac{\partial t}{\partial x}\nu_x+\lambda_y \frac{\partial t}{\partial y}\nu_y+\lambda_z \frac{\partial t}{\partial z}\nu_z+q\left(x,y,z,\tau\right)+\alpha\left(x,y,z,\tau\right)\left(t-t_\infty\right)=0 \text{ on } \Gamma_2$$

is more complicated, containing the local outward unit normal vector (ν_x,ν_y,ν_z), corresponding to particular points of Γ_2, the prescribed heat flux q and the a priori given thermal convection factor α; t_∞ refers to the temperature of the outer environment. Moreover the initial setting of t (for τ = 0) must be given. The numerical analysis of (1) with the above presented boundary and initial conditions can be seemingly done in the standard way, e.g. using the finite element technique and the Crank-Nicholson time-integration scheme by [3]; however, the reasonable setting of q, Q, etc. requires a lot of (not only) experimental work. The advantage of the original computational model, created at the Institute of Building Materials of the Faculty of Civil Engineering of the Brno University of Technology, is its ability to handle the changes of the domain geometry in time (respecting the fact that the concrete construction is created in several steps), the time-dependent internal generation of hydration heat, due to the age of each concrete element in the massive, and such surface phenomena, as the incorporation of the latent heat of evaporation, the influence of sun shining, the (nearly) periodic development of the climatic temperature in the day cycles, etc.

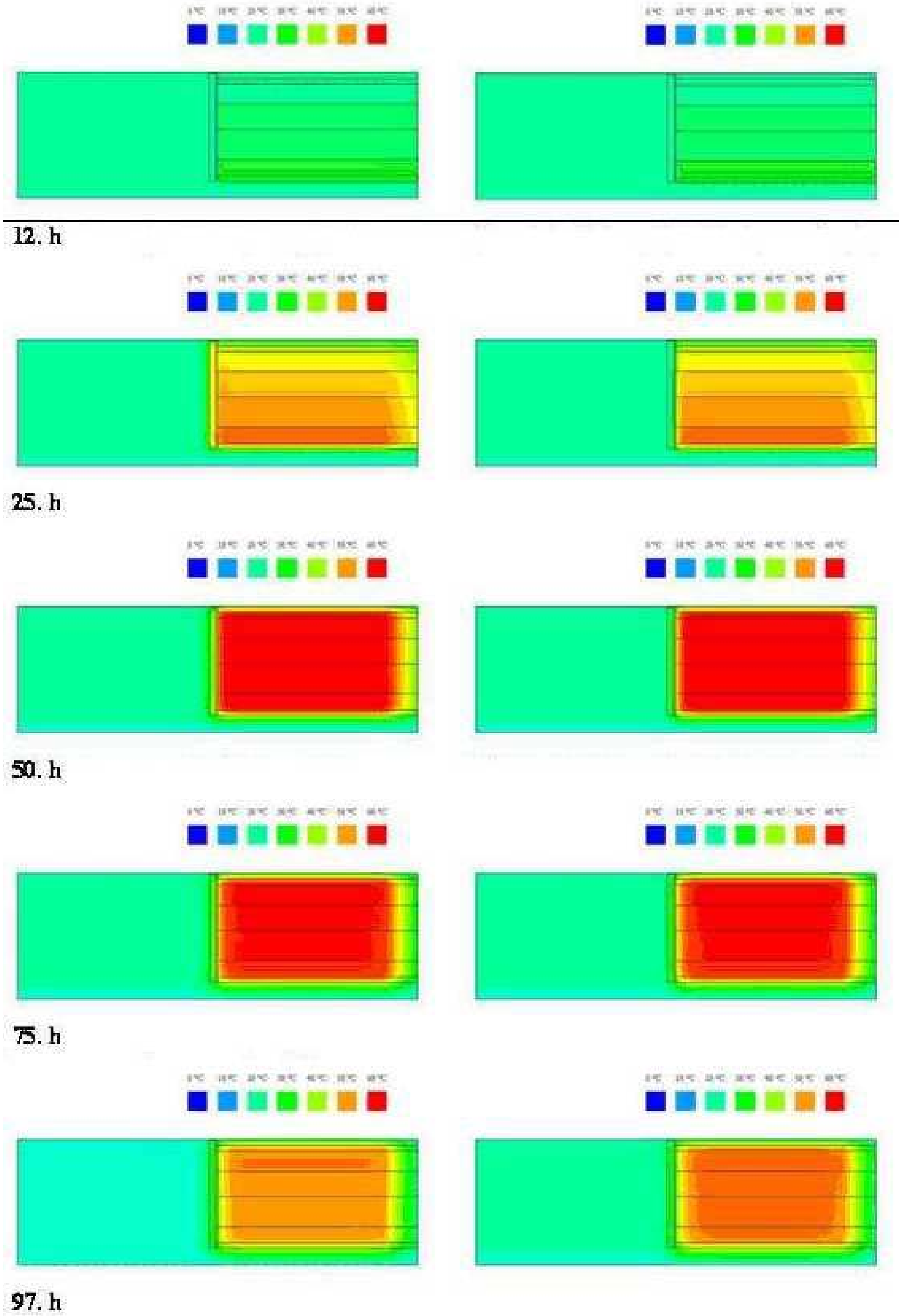

Figure 2: Distributions of temperature in the fragment with and without electrical heating

Figure 2 demonstrates a typical example of the development of temperature in time in one fragment of the large concrete construction, built in more steps – in each step one new fragment was added to the end of the existing one. The risk of undesirable stresses in the massive near the working interface the effect of additional electrical heating was tested and the corresponding changes in the temperature field were simulated during 97 hours. The left-hand pictures show the heating-modified temperature fields (for various times), the right-hand ones the same fields without such arrangement; especially at the last couple of pictures certain effect of additional heating is visible immediately.

4. Risk of cracking

The experimental measurements yield the hypothesis that the probability of crack initiation in concrete is proportional to the highest reached temperature. Since the hydration process has an exothermic character, the early age of concrete is a critical period, namely for the monolithic constructions. The temperature increase can endanger the final status of the whole structure from the point of view of its design properties, especially the inner concrete structure, the porosity, the often required water impermeability, etc. Even the final strength of concrete is usually correlated with the amount of the produced hydration heat.

The tensile stresses during the hydration heat generation in the early-age concrete are very small because of the negligible elasticity modulus. The risk of crack initiation increases with the stiffening of the concrete structure, accelerated in the first phase thanks to the hydration temperature. Therefore in the case of the waterproof concrete the maximum temperature is reduced using special arrangements, limiting the amount of binder and water for the mixture. The expected values of shrinking are shown at Figure 3, coming from [1].

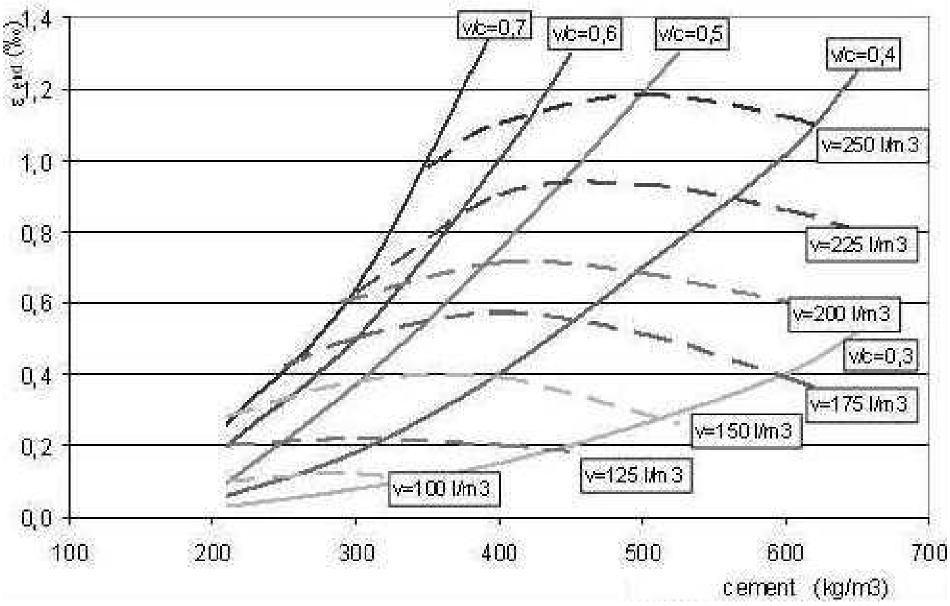

Figure 3: Concrete shrinkage as a function of the amount of cement and water.

4. Conclusion

The analysis of thermal fields in the early-age concrete, sketched in this paper, has been motivated by the practical action of the successive building of a large object. It makes use of some preliminary results, presented in [2], as well as of the experience with some special arrangements, including e.g. the additional reinforcements and the special boarding technology by [1].

However, the results are still far from being satisfactory. The further (both theoretical and experimental) research should come from the scale bridging between the microstructural information and the macroscopic description of material behaviour like (1), extended by some multiphysical considerations, namely by the thermo-mechanical ones with the proper analysis of the moisture influence (cf. [4] where much more references to the relevant literature, including physical principles, mathematical and numerical theory and commercial and research software, can be found, too) to predict the dangerous tensile stresses in the non-reinforced domains in the first step and to control the pre-stressing in the construction with respect of its future use in the second one.

Acknowledgement. This research is supported by the Ministry of Education, Youth and Sports of the Czech Republic, No. MSM 0021630511, DT7.

References

[1] Huber H., Nesitka W. Weisse Wannen – wasserundurchlässige Betonbauwerke, *Z. Östereich. Betonverein*, Heft 43, Wien 2000, 15-24.

[2] Šťastník S. Modelování teplotního pole v železobetonových konstrukcích, *CD Proc. Betonářské dny 2002*, Čes. beton. spol., Pardubice 2002, 6 pp.

[3] Vala, J. Budova jako tepelný systém, *Proc. PRASTAN 2002*, Slov. štatist. spol., Bratislava 2002, 105-120.

[4] Vala J., Šťastník S. On the heat propagation in buildings, *Building Research J.* **52** (2004), 31-56.

IN-SITU MONITORING OF TEMPERATURE AND RELATIVE HUMIDITY FIELDS IN A HISTORICAL BUILDING PROVIDED WITH ADDITIONAL THERMAL INSULATION

Jan Toman, Robert Černý

Czech Technical University in Prague, Faculty of Civil Engineering, Department of Materials Engineering and Chemistry, Thákurova 7, 166 29 Prague 6, Czech Republic, email: toman@fsv.cvut.cz, cernyr@fsv.cvut.cz

Abstract:

Long-term on-site assessment of hygrothermal performance of an interior thermal insulation system on hydrophilic mineral wool basis without water vapour barrier applied on a brick wall is presented in the paper. Experimental results show that the system functioning is flawless during the whole studied time period of four years after reconstruction of the building.

Keywords:

Interior thermal insulation system, hygrothermal performance, long-term on-site assessment

INTRODUCTION

Building envelopes provided with the additional interior thermal insulation systems on the basis of hydrophilic mineral wool without water vapour barrier were subjected to extensive computational analyses during the last few years [1-3]. Several semi-scale tests of their hygrothermal performance in the conditions very close to reality were performed as well [4-6]. The computational and experimental results revealed very good hygrothermal performance of hydrophilic mineral wool in the interior thermal insulation systems applied for several different load bearing structures. However, a convincing proof of the proper hygrothermal function of these systems in on-site conditions was not given yet.

In this paper, long-term on-site assessment of hygrothermal performance of an interior thermal insulation system on hydrophilic mineral wool basis without water vapour barrier applied on a brick wall is presented.

DESCRIPTION OF THE LONG-TERM ON-SITE TEST OF HYGROTHERMAL PERFORMANCE

A kindergarten building in Prague was chosen for the pilot-scale application of the developed interior thermal insulation system. The main reason for this choice was its broken façade, which had to be maintained in its original appearance.

The building was built at the end of the 19th century and corresponds to the urban planning typical for that time. It is a two-storied brick building including a partial cellar. The building has wagon-headed trusses and in the basement there are brick-built wagon-vaults. The truss is wooden with intermediate and apex purlines. The roofing is from Bonn's shingle loaded on the clapboards. The main stairways are two-armed with the stairs on the stair carriages. The walls have stuccos. There are wooden double windows on the eastern, southern and western part of the facade. Wooden windows with double glass in a simple construction are in the yard part. The doors are mainly of a modern design. They have steel pressed doorframes. Most of the floors have vinyl flooring. There is ceramic pavement in some parts of the floors.

The main purpose of the reconstruction work was the increase of the thermal resistance of the building envelope. This increase was achieved mainly by the installation of the hydrophilic mineral wool assemble on the inside surface of a part of the external walls. In order to increase the overall efficiency of the thermal insulation, the ceiling below the roof was thermally insulated using exterior mineral wool insulation.

The preliminary work consisted in careful scaling of all painting coats. Damaged plasters were repaired with lime-cement plaster with stucco surface finish. All damaged places in the plaster due to the inner arrangement and decoration were also repaired. A base coat for the application of the interior thermal insulation system was obtained in this way. The surface where old paint was removed was covered with a universal underlying paint. The inside wooden wall facings were displaced.

The interior thermal insulation was placed on the external walls of all rooms, where the children stay most of the time (playrooms, cabinets, bedrooms) and in the neighboring staff cloak-rooms. The insulation used for this reconstruction was designed in the thickness of 80 mm, due to the space limitations. The value of the thermal resistance of this insulation was determined in laboratory experiments as $R = 1.43\ m^2K/W$ (for 95 % relative humidity). By this account, the total thermal resistance of the construction was higher than the thermal resistance required by the Czech standards with the preservation of the current thickness of the brick-built external walls at 600 mm. The thermal resistance of the construction with additional thermal insulation in the parapet location and with the thickness of the walls of 450 mm achieved the standard requirements.

The DU hydrophilic mineral wool thermal insulation boards consisted of two layers of different density, which were compactly connected. The hard layer had a thickness of 30 mm, and the thickness of the soft layer was 50 mm. The dimensions of the boards were 600 x 1000 mm.

The KAM leveling render was used for gluing of the boards to the wall surface, and played the role of water vapor retarder as well. This render was applied both on the entire surface of the wall and on the entire surface of the boards. The elements sticking out from the basis were padded by the leveling render all around their perimeters.

The mineral wool boards were assembled from the bottom upwards. The vertical board connections were alternating over one half of the board width in order to bond them, and the boards were pinned hard upon the wall. Disk plugs were used for attaching the board. One piece was always used on one board in its center. The holes for these disk plugs broke compactness of the leveling render layer under the thermal insulation. Therefore, the binding assembling foam was put into these holes using an applicator before the disk plugs were inserted and activated. The damaged leveling render layer near the plug shank was sealed in this way.

The internal plaster FFP was applied in the following way. First an FFP layer 3 mm thick was put on the boards, then netting was applied, another layer of FFP covering 1.5 mm thick after that, and finally an FFP layer 1.5 mm thick. The final layer was painted with 2 coats of a common paint. The walls without adaptations were painted with just one coat of the same paint.

The socket outlets on the insulated walls were fixed into the hard layer of the thermal insulation boards. They were anchored with the gypsum mixture. It was necessary to remove the window lining plaster before the application of the thermal insulating system. A curtailed hard layer of hydrophilic mineral wool boards 30 mm thick was used for the thermal insulation of the window heads and window reveals. The adaptation of the window casements and casings, including addition of the external window casements sealing, were carried out to improve the value of the thermal resistance of the envelope. The enlargement of the current wooden window stools over the added hydrophilic thermal insulation was performed at the same time. The constructions of the windows were then painted with two coats of paint. The facing of the wooden walls was fixed on the supporting structure made from lathes. These lathes created the space for ventilation between the thermal insulating surface and the facing of the wooden walls. Gummy foam was used for mounting the frame of the wooden wall facing on the insulating layer. The technology of work and constructive details are demonstrated in Figures 1a, b.

Figures 1a, b Selected constructive details

Common hydrophobic mineral wool boards were laid on the cleansed loft floor. Two layers each 80 mm thick were applied, so that the total thickness of the thermal insulation layer was 160 mm. The building reconstruction was completed between June and August 2002. Since the described reconstruction was considered as a pilot-scale test of the designed insulation system, it was necessary to study the hygrothermal function of the building before and after reconstruction.

The measurements of hygrothermal behavior of the studied structure before building reconstruction were carried out between November 2001 and May 2002. Thermal and hygric parameters were measured in three profiles, on the southern and eastern flank of the ground floor and on the western flank of the second floor. Air temperature at the exterior and at the interior, temperature of the external and the internal surfaces, relative humidity in the exterior and interior and temperature of the radiator surface were measured in every profile.

Combined capacitance probes were used for temperature and relative humidity measurements. In addition, type K thermocouples (NiCr-NiAl) were used for some temperature measurements. The data were recorded in 30-minute intervals and collected in a central unit. The measurements of temperature and relative humidity after reconstruction were carried out since October 2002 until June 2006.

EXPERIMENTAL RESULTS AND DISCUSSION

Figs. 2, 3 show time development of temperatures and relative humidities in the east wall during the last winter before the reconstruction, Figs. 4, 5 during the second winter after reconstruction.

A comparison of temperatures in Figs. 2, 4 shows the positive thermal qualities of the applied interior thermal insulation system. The most substantial temperature changes occurred in the thermal insulation layer.

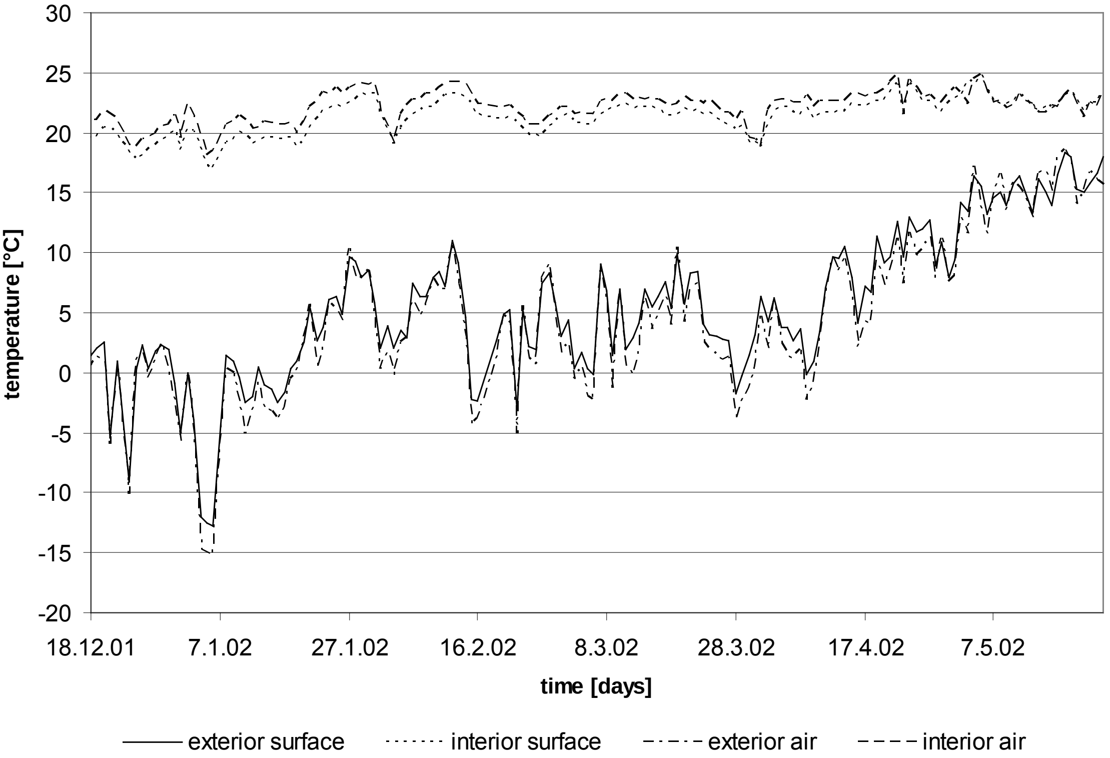

Figure 2 Time development of temperatures in the east wall during the last winter before the reconstruction

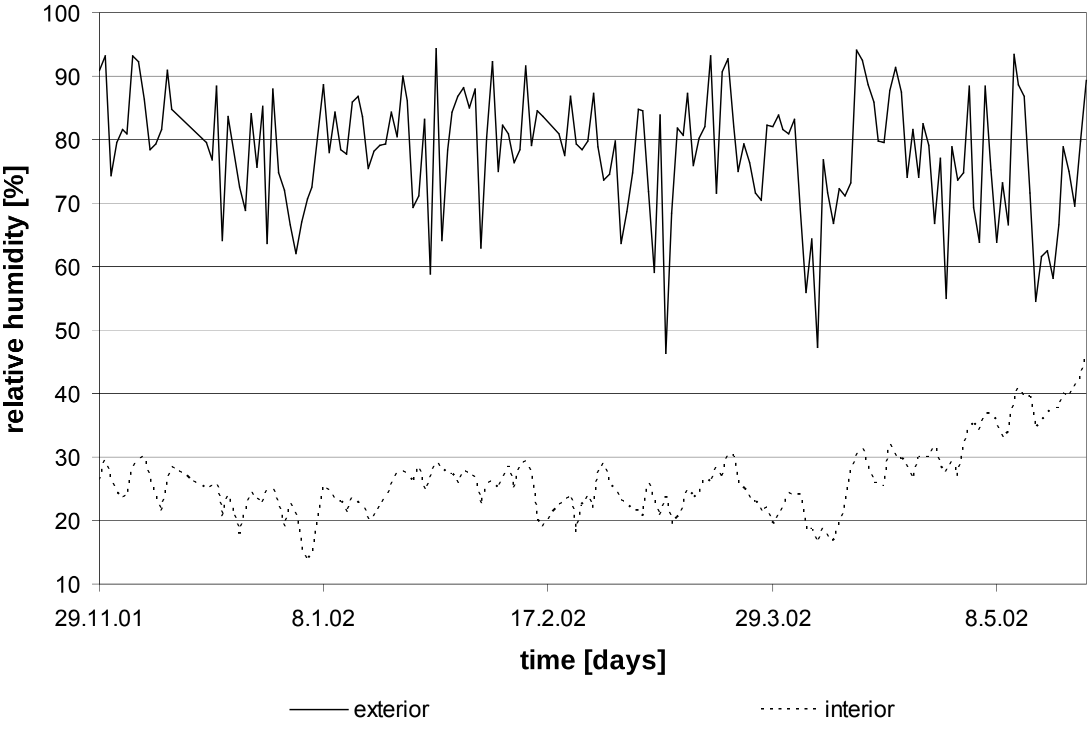

Figure 3 Time development of relative humidity in the east wall during the last winter before the reconstruction

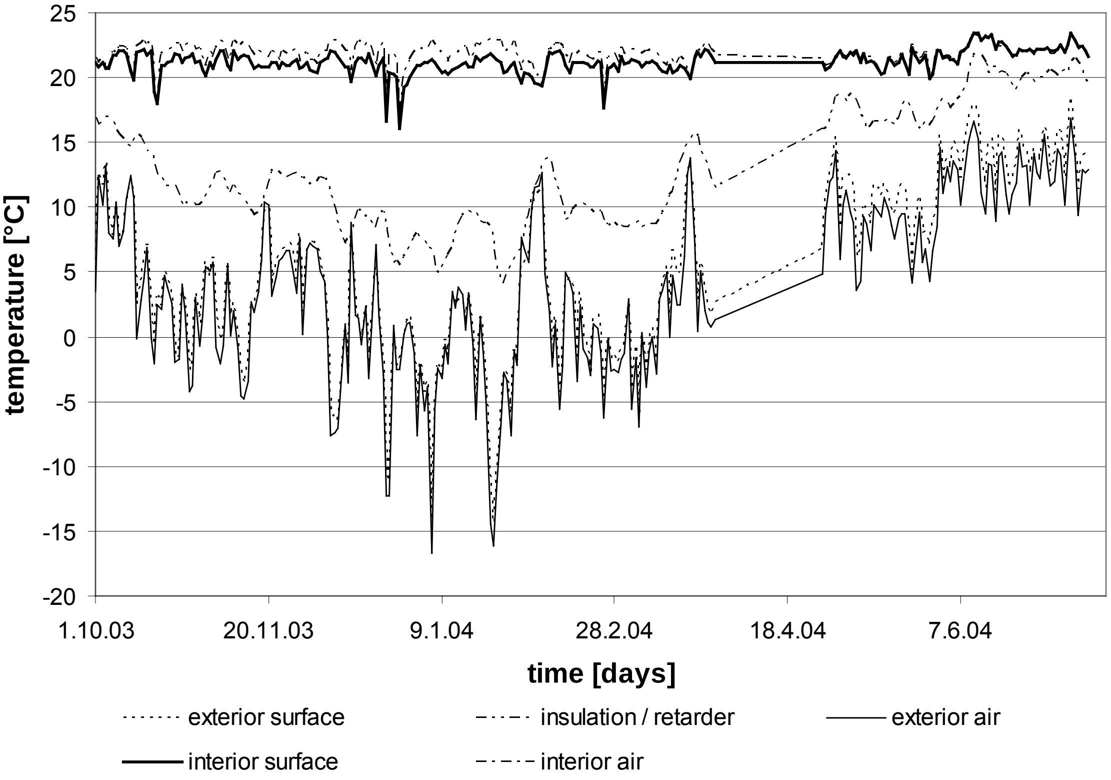

Figure 4 Time development of temperatures in the east wall during the second winter after reconstruction

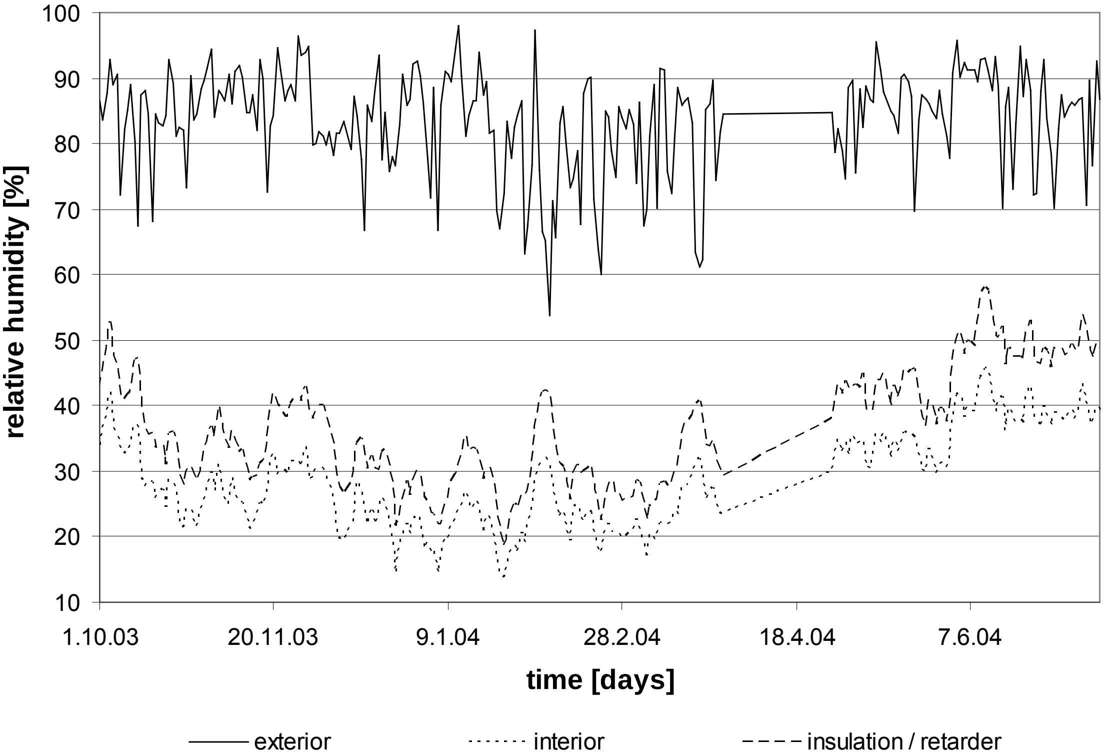

Figure 5 Time development of relative humidities in the east wall during the second winter after reconstruction

The hygric performance of the system was also found to be excellent. Fig. 5 shows that the maximum values of relative humidity on the surface of water vapor retarder, which is the critical point of the designed system, were in the winter period approximately 42%. This is very far from any condensation danger. The higher values of relative humidity in the beginning of the summer period (57%) were caused by a period of rain but the condensation was far from occurring either.

CONCLUSIONS

The on-site experimental analysis presented in this paper gave evidence that the hygrothermal performance of the studied interior thermal insulation system was flawless during the whole time period of four years after building reconstruction. The thermal performance was on the expectedly high level. Water condensation never appeared inside the envelope during the whole four years of testing.

The designed system can find application in practice particularly in the field of reconstruction of historical buildings and contemporary buildings with complicated facades where the application of exterior thermal insulation systems is impracticable. It can also conveniently replace the currently used interior thermal insulation systems with vapor tight layer that are susceptible to easy mechanical damage.

ACKNOWLEDGEMENT

This research has been supported by the Ministry of Education, Youth and Sports of Czech Republic, under grant No MSM: 6840770031.

REFERENCES

[1] J. Maděra, R. Černý, Computational optimization of the composition of building envelopes with interior thermal insulation on the mineral wool basis. Building Research Journal, vol. 50, 2002, pp. 225-240.

[2] R. Černý, J. Maděra, Interior thermal insulation systems in the renovation of historical buildings: a computational analysis. Proceedings of Structural Studies, Repairs, and Maintenance of Historical Buildings VII, C.A. Brebbia (ed.), WIT Press, Southampton, 2001, pp. 405-414.

[3] R. Černý, J. Maděra, J. Grunewald, Numerical simulation of heat and moisture transport in building envelope systems with inside thermal insulation systems on the mineral wool basis. Proceedings of International Conference on Building Envelope Systems and Technologies, B. Baskaran, R. Paroli (eds.). NRC-CNRC, Ottawa 2001, pp. 251-255.

[4] Z. Pavlík, Development of a Semi-scale Technique for the Assessment of Hygro-thermal Performance of Multi-layered Systems of Building Materials. Ph.D. Thesis, Czech Technical University in Prague, Prague, 2004.

[5] Z. Pavlík, J. Pavlík, R. Černý, Experimental analysis of an interior thermal insulation system on the mineral wool basis. Proc. of 11th Symposium of Building Physics, P. Haupl, J. Roloff (eds.), TU Dresden, Dresden 2002, pp. 634-642.

[6] Z. Pavlík, R. Černý, Experimental assessment of hygrothermal performance of an interior thermal insulation system using a laboratory technique simulating on-site conditions. Energy and Buildings, vol. 40, 2008, pp. 673-678.

TWO-SCALE CONVERGENCE IN HEAT TRANSFER

Jiří Vala
Brno University of Technology, Faculty of Civil Engineering, 602 00 Brno, Veveří 95,
Czech Republic, e-mail vala.j@fce.vutbr.cz

Abstract

The reliable analysis of heat transfer in real materials cannot avoid the information about their microstructure. The global computational modelling, covering both the microstructural material properties and the macrostructural behaviour of the whole specimen or even of the complete construction, is usually very expensive or even impossible in practice. This is the principal motivation for the development of the mathematical theory of homogenization, which describes the replacement of a real composite material by a fictious homogeneous one. The approach based on the notion of the two-scale convergence, covering the gap between the weak and the strong convergence in the case of the periodic or quasi-periodic material structure, seems to be useful and physically transparent not only for the pure heat transfer, both for the steady-state and the time-dependent ones, but also for its coupling with other important physical processes. However, most such multiphysical problems contain still a lot of open questions and some microstructural formulations seem not to be able to be homogenized easily.

Key words: Heat transfer, homogenization techniques, two-scale convergence.

1. Mathematical modelling of heat transfer

Advanced materials used in engineering have typically a complicated microstructure, whose simple and intuitive macroscopic representation is not available. On the other side, the distributions of macroscopic quantities, as temperature, strains and stresses, moisture content, concentrations of components or contaminants, etc., are required as final outputs of technical calculations. The simultaneous numerical computations covering the scales from micro- or nanometers (in the case of the microstructural analysis) to meters (for the material specimen or even for the complete construction, typically for some building object in civil engineering) are usually not available: they are very expensive even for the relatively simple model problems and impossible for the realistic computations required by engineering and technological applications. This is the principal motivation for the development of physically transparent computational and numerical techniques of scale bridging, known as the mathematical homogenization (despite the fact that not it all cases the limit description corresponds to quite physically homogeneous material properties).

The history of intensive research in the mathematical homogenization is relatively short, being connected with the technological progress both in the development of advanced materials and in the computer hardware and software. Most authors start with the citation of [3] as the pioneering work in homogenization motivated by engineering problems; however, in the particular cases certain analogous approaches can be found in some old studies from the beginning of the 20th century, namely in [39] for the one-dimensional heat propagation through a layered medium. In this paper, especially at the beginning, we shall pay (for simplicity) attention to the pure heat transfer in a physically isotropic domain Ω located in the three-dimensional Euclidean space R^3 with a (sufficiently smooth, e.g. Lipschitz) boundary $\partial\Omega$; thus the Cartesian coordinate system $x = (x_1, x_2, x_3)$ is available, the classical differential operators (∇, div, $\cdot$ for scalar products, …) can be used and the analysis of the existence and uniqueness of solution, of the convergence of sequences of approximate solutions, etc., can refer to the standard results from the theory of function spaces by [19], namely of the Lebesgue and Sobolev ones, discussed in great details in [23]; the commonly used notation of function spaces will be applied here without further explanation.

We shall consider the boundary $\partial\Omega$ divided into two parts, Γ and Γ_*, where $\partial\Omega = \Gamma \cup \Gamma_*$. The heat transfer is driven by the external heat flow $q(x)$ on Γ and by the internal heat source $r(x)$ in Ω. We are seeking for the distribution of temperature $T(x)$, conditioned by the heat conduction factor $\lambda(x)$ on Ω, with respect to the prescribed temperature $T_*(x)$ on Γ_*, extensible formally to Ω. The differential formulation of the problem can be then written as

$$-\mathrm{div}(\lambda\nabla(\tau + T_*)) = r \tag{1}$$

on Ω and

$$\nabla\lambda \cdot \nu = q \tag{2}$$

on $\partial\Omega$, supplied with the unit normal vector ν; the new variable $\tau = T - T_*$ is introduced to force $\tau = 0$ on Γ_*. Let us remark that in general (1) and (2) (for a non-smooth τ) should be understood only in a distributive sense (not very transparent for the physicists and engineers); nevertheless, this can be removed by the integral formulation, coming from the Green-Ostrogradskiĭ theorem: we have to find such $\tau \in V$ that

$$(\nabla v, \lambda\nabla\tau) = (v, r) + < v, q > -(\nabla v, \lambda\nabla T_*) \tag{3}$$

holds for all $v \in V$; assuming $r \in L^2(\Omega)$, $q \in L^2(\Gamma)$, $T_* \in W^{1,2}(\Omega)$ and some positive bounded λ on Ω and applying the notation of scalar products

$$(\varphi, \psi) = \int_\Omega \varphi(x)\psi(x)\ \mathrm{d}x$$

for all $\varphi, \psi \in L^2(\Omega)$ and

$$(\varphi, \psi) = \int_\Gamma \varphi(x)\psi(x)\ \mathrm{d}\sigma(x)$$

for all $\varphi, \psi \in L^2(\Gamma)$ (σ means the Hausdorff surface measure), we have aa appropriate space of test functions

$$V = \{v \in W^{1,2}(\Omega) : v_1 = v_2 = v_3 = 0 \text{ on } \Gamma_*\}.$$

The solution of (3) is relatively easy and can be performed numerically by probably every software package for the analysis of problems of building physics, continuum mechanics and related fields. The main difficulty is that we do not know how to set λ at the macroscopic scale to incorporate the information from the microscopic one. The naive averaging gives evidently bad results: e.g. the well-known result

$$\frac{2}{\lambda} = \frac{1}{\lambda_1} + \frac{1}{\lambda_2},$$

valid, following [39], for a specimen of the thickness h consisting of a large number n of parallel layers of the same thickness $\varepsilon = h/(2n)$ where the odd and even ones have their heat conduction factors $\lambda_1, \lambda_2, \ldots, \lambda_1, \lambda_2$ with $n \to \infty$ (alternatively: $\varepsilon \to 0$) and the heat transfer is considered only in the direction perpendicular to such system of layers, is quite different from the arithmetical average

$$\lambda = \frac{\lambda_1 + \lambda_2}{2};$$

both results coincide just for $\lambda_1 = \lambda_2$, i.e. for the a priori ideal homogeneous medium.

The assumption on the steady-state heat transfer may be not acceptable in a lot of cases of practical importance. Namely in the analysis of the heat transfer in building the setting of λ reflects only the effect of thermal insulation, not that of (time-dependent) thermal accumulation. Thus (1) has to be extended to the form

$$\kappa(\dot{\tau} + \dot{T}_*) - \mathrm{div}(\lambda \nabla(\tau + T_*)) = r \tag{4}$$

with the dot convention for the partial derivative with respect to the time t increasing from zero to some final time t_*, where at least q, r and consequently also T are allowed to be functions of the time variable t; κ here is introduced as $\kappa(x) = c(x)\rho(x)$ where $c(x)$ is the heat capacity and $\rho(x)$ the material density on Ω. Since (2) stays formally unchanged, (3) converts to

$$(v, \kappa\dot{\tau}) + (\nabla v, \lambda \nabla \tau) = (v, r) + < v, q > -(v, \kappa\dot{T}_*) - (\nabla v, \lambda \nabla T_*) \tag{5}$$

for all $v \in V$; for the time interval $I = [0, t_*]$ and the zero-valued τ in the initial time $t = 0$ we must consider $r \in L^2(I, L^2(\Omega))$, $q \in L^2(I, L^2(\Gamma))$, $T_* \in L^2(I, W^{1,2}(\Omega))$ and some bounded λ and c on Ω and try to find $\tau \in L^2(I, V)$ and consequently $T \in L^2(I, W^{1,2}(\Omega))$. The discussion concerning the identification of λ can be then repeated for κ (or separately for c and ρ), too.

2. Classical homogenization techniques

The first attempt to overcome the difficulty with the identification of some effective value of λ can be done in the following way: we can start from the correct fine ε-scaled configuration where τ^ε is nothing else τ from (3) (or alternatively (1) and (2)) with known λ^ε which refers just to exact λ (often considered as periodic or quasi-periodic on Ω in practice), thus

$$(\nabla v, \lambda^\varepsilon \nabla \tau^\varepsilon) = (v, r) + < v, q > -(\nabla v, \lambda^\varepsilon \nabla T_*) \ , \tag{6}$$

and the aim is to find such λ that the sequence $\lambda^\varepsilon \nabla \tau^\varepsilon$ from (6) converges weakly to $\lambda \nabla \tau$ from (3) in $L^2(\Omega)$. This type of convergence, known as H-convergence in the literature, has found wide acceptance in the composites modelling community, for its ability to incorporate and estimate effective material properties from a representative unit cell, as suggested in [3]. The classical works [4] and [30] are commonly cited to demonstrate that such H-limits λ of corresponding sequences λ^ε where $\varepsilon \to 0$ can be calculated explicitly for periodic systems, although their evaluation is much more complicated than in the one-dimensional case in the historical work [39]. However, in general the derivation of H-limits is not explicit and requires to solve additional non-trivial problems; all details (including the comparison of H-, G- and two-scale limits, the formal mathematical existence and convergence proofs and engineering applications) can be found in [7].

The complicated evaluation of H-limits has motivated the improvements of the concept of H-convergence; here we shall mention only two important directions. For the convergence of λ^ε in the corresponding space of linear operators (or the convergence of the Green operator) the literature (not only for the heat transfer, but in the more general context) refers to G-convergence (cf. [32] and [9])). The convergence of the triples $(\lambda^\varepsilon \nabla \tau^\varepsilon, \nabla \tau^\varepsilon, \tau^\varepsilon)$ is known as Γ-convergence (cf. [24], [10] and [8]). Nevertheless, in such classification the announced two-scale convergence could be interpreted as a specific case of H-convergence, taking usually in account some (quasi-)periodicity of the solution and working with certain rather strange limit functions; in the following text we shall demonstrate a greater significance of the two-scale analysis.

Let us remark that, namely in the last two decades, the above mentioned method have been generalized substantially to handle much more general problems than that formulated by (6) and (3); however, we shall not discuss such generalizations in details to preserve the simplicity and transparency of our notations. Only for the future reference we shall rewrite (5) to the slightly generalized version of (6),

$$(v, \kappa^\varepsilon \dot{\tau}^\varepsilon) + (\nabla v, \lambda^\varepsilon \nabla \tau^\varepsilon) = (v, r) + < v, q > -(v, \kappa^\varepsilon \dot{T}_*) - (\nabla v, \lambda^\varepsilon \nabla T_*) \qquad (7)$$

where not only one sequence λ^ε, but a couple of sequences $(\lambda^\varepsilon, \kappa^\varepsilon)$ of material characteristics, coming from the fine scale, but tending to some effective (λ, κ) for (5), occurs.

3. Two-scale convergence analysis

The two-scale convergence was introduced originally in [26], but this pioneering work (whose form is not very reader-friendly) has not been accepted as an important tool in the homogenization theory immediately. Most authors, using the mathematical two-scale homogenization and the corresponding convergence results to the analysis of physical or technological problems, or even those trying to generalize the formal definition of a (strong or weak) two-scale limit, refer to the later rather extensive overview [1]; its notation will be therefore applied also in this paper. Some useful generalizations will be discussed later.

Let Y be the unit cube in R^3: $Y = [0,1) \times [0,1) \times [0,1)$. This cube should correspond to certain representative volume (small in practice) at the fine scale; thus it would be physically more convenient to take some cube of a realistic volume, but according to $\varepsilon \to 0$ the additional assumption $\mathrm{vol}\, Y = 1$ brings no loss of generality and simplifies most equations. The space of Lebesgue square integrable Y-periodic functions will be denoted by $L^2(Y_\#)$. Its elements are Y-periodic; its restriction to Ω belongs to $L^2(\Omega)$, although its norm is constructed over Y only.

Let us now introduce the two-scale convergence; ε will be a positive real constant (everywhere in this paper). Let S be certain space of admissible functions from $L^2(\Omega \times Y)$. A sequence u^ε is said to *two-scale converge* to a limit $u^0 \in L^2(\Omega \times Y)$ iff

$$\lim_{\varepsilon \to 0} \int_\Omega u^\varepsilon(x) \varphi(x, x/\varepsilon)\ \mathrm{d}x = \int_\Omega \int_Y u^0(x,y) \varphi(x,y)\ \mathrm{d}y\ \mathrm{d}x \qquad (8)$$

for all $\varphi \in S$. The choice of S by various authors is different; for our purpose $S = C(\Omega, L^2(Y_\#))$ will be sufficient. Let us remark that the seemingly simplest setting

$S = L^2(\Omega \times Y)$ is not acceptable, unlike $S = L^2(\Omega, L^2(Y_\#))$ (for the detailed explanation see [13]).

An alternative definition can be rewritten from [2]: Let us consider the system of k-shifted and ε-scaled cells $Y_k^\varepsilon = \varepsilon(Y + k)$ for all triples of integers $k = (k_1, k_2, k_3)$; this system covers the whole space R^3, containing Ω. Let a^ε be a measure preserving mapping of $\Omega \times Y$ onto Ω defined by $a^\varepsilon = \varepsilon(y + k)$ for $x \in Y_k^\varepsilon$ if Y_k^ε is included in Ω (i.e. contained in inner cells) and as $a^\varepsilon = x$ for $x \in Y_k^\varepsilon \cap \Omega$ (i.e. contained in boundary cells). Let A^ε be a transform of $L^2(\Omega, L^2(Y_\#))$ into $L^2(\Omega \times Y)$ defined by

$$(A^\varepsilon v^\varepsilon)(x, y) = v^\varepsilon(a^\varepsilon(x, y))$$

for any sequence v^ε in $L^2(\Omega)$. A sequence u^ε is said to *weakly two-scale converge* to a limit $u^0 \in L^2(\Omega \times Y)$ iff $A^\varepsilon u^\varepsilon$ weakly converges to $L^2(\Omega \times Y)$. A sequence u^ε is said to *strongly two-scale converge* to a limit $u^0 \in L^2(\Omega \times Y)$ iff $A^\varepsilon u^\varepsilon$ strongly converges to $L^2(\Omega \times Y)$.

As verified in [25], the weak two-scale convergence can be identified with the two-scale convergence by (8). The strong two-scale convergence can be characterized as the (weak) two-scale convergence with the additional requirement

$$\lim_{\varepsilon \to 0} \|u^\varepsilon\|_{L^2(\Omega)} = \|u^0\|_{L^2(\Omega \times Y)} .$$

The most useful lemmas working with the two-scale convergence with $\varepsilon \to 0$ are:

On the compactness: If u^ε is a bounded sequence in $L^2(\Omega)$ then, up to a subsequence, u^ε two-scale converges to some u^0 in $L^2(\Omega \times Y)$

On the function products: If u^ε is a strongly two-scale converging sequence to some $u^0 \in L^2(\Omega \times Y)$ and v^ε is a two-scale converging sequence to some $v^0 \in L^2(\Omega \times Y)$ then

$$\int_\Omega u^\varepsilon(x) v^\varepsilon(x)\, \mathrm{d}x = \int_\Omega \int_Y u^0(x, y) v^0(x, y)\, \mathrm{d}y\, \mathrm{d}x .$$

On the weak and strong convergence: If u^ε is a strongly converging sequence to some u in $L^2(\Omega)$ then also u^ε strongly two-scale converges to u^* in $L^2(\Omega \times Y)$ where $u^*(x, y) = u(x)$ for every $x \in \Omega$ and $y \in Y$ If at least u^ε is a two-scale converging sequence to some u^0 in $L^2(\Omega \times Y)$ then u^ε weakly converges to u in $L^2(\Omega)$ where

$$u(x) = \int_Y u_0(x, y)\, \mathrm{d}y$$

for each $x \in \Omega$.

On the gradients: If u^ε is a bounded sequence in $L^2(\Omega)$ and moreover ∇u^ε is bounded in $L^2(\Omega, R^3)$ then, up to subsequences, u^ε has certain two-scale limit in u^* in $L^2(\Omega \times Y)$, whose restriction u to $L^2(\Omega \times Y)$ comes from the preceding lemma, and also ∇u^ε has a (vector-valued) two-scale limit $\nabla u^* + \nabla_y u^1$ where the gradient ∇_y is computed with respect to the second variable $y \in Y$ and u^1 is certain element of $L^2(\Omega, W_\#^{1,2}(Y))$.

The careful application of these lemmas enables us to understand (3) as the two-scale limit version of (6) and verify the existence of an effective λ on Ω for a sequence of quasi-periodic heat conduction factors λ^ε defined by

$$\lambda^\varepsilon(x) = \lambda(x, x/\varepsilon)$$

for all $x \in \Omega$. Moreover, the strong convergence in $L^2(\Omega \times Y)$ can be helpful, too (especially later in the numerical analysis). However, the guaranteed solution of (3) τ contains its oscillatory part τ^1 (cf. the lemma on the gradients), periodic on Y. The meaning of τ^1 is often explained using the formal asymptotic expansion (see [1])

$$\tau^\varepsilon(x)(x) = \tau^0(x, x/\varepsilon) + \varepsilon\tau^1(x, x/\varepsilon) + \varepsilon^2\tau^2(x, x/\varepsilon) + \dots,$$

taking only first two right-hand-side additive terms with τ^0 and τ^1 into account. This leads naturally to the suggestion to include more terms into consideration; such approach, known as reiterated homogenization, has its good support inside the two-scale analysis.

4. Useful generalizations

The generalization of the above introduced two-scale analysis is available in several directions. Some small improvements are clear and simple: e.g. the isotropy assumption can be easily removed, replacing the scalar factor λ by certain symmetrical matrix from $R^{3\times 3}$, q can contain a τ-variable term, incorporating the heat convection from the environment (or from the adjacent layer), etc. It is also possible to admit that λ is a function of T or even to replace $\lambda\nabla\tau$ totally by some function

$$l(x, \tau(x), \nabla\tau(x)),$$

respecting some additional requirements, e.g. of the Carathéodory type, and replace also the spaces $L^2(\Omega)$, $L^2(\Gamma)$, $W^{1,2}(\Omega)$, etc., by the slightly generalized spaces $L^p(\Omega)$, $L^p(\Gamma)$, $W^{1,p}(\Omega)$, etc., with $1 < p < \infty$. More serious complications can be connected with the perforated domains (let us remind that most building materials have a non-negligible pore space) and with the materials containing stiffening thin plates or long fibers located in the matrix: the analysis of such problems requires to substitute the standard Lebesgue and Sobolev spaces by some more general spaces working with the generalized Borel, Young, etc. measures; for more information see [13], [5] and [20]. However, the strong and relatively simple results like [6] cannot be then expected. This is caused by the loss of (quasi-)linearity of the problem and by the absence of the standard compactness arguments from the theory of Hilbert (or at least reflexive Banach) spaces; for more details and references see [37].

Another very useful generalization is the passage from the steady-state heat transfer to the analysis of the time-variable redistribution of temperature, from the mathematical point of view from an elliptic to a parabolic problem. The theoretical two-scale convergence results are available from [16] (even admitting the time-scaled changes of material characteristics); this enables us the passage from (6) and (3) to (7) and (5). The construction of the solution of a parabolic problem from a sequence of approximate solutions of corresponding elliptic problems, based on the method of discretization time and applying the properties of sequences of Rothe, is demonstrated in [35].

Unfortunately, also the periodicity assumption may be far from realistic ones; that the regular location of particles in the material can predict quite other outputs than their stochastic distributions. This is an important motivation for the development of the two-scale analysis without the deterministic periodicity. We have seen the incorrect results of the naive avaraging just in the very simple case of one-dimensional heat propagation; the more complicated anisotropic configurations then need the support of advanced correlation analysis (see [18]). The approach of [17] and [31] tries to solve the sketched problem in the compatible way with the standard notations in the Lebesgue and Sobolev spaces, replacing the Lebesgue, Hausdorff, etc. measures by the probabilistic ones, applying the arguments from the theory of stochastic processes. Another method is presented in [27]: using the basic concept, called homogenization structure, and the deep results from the theory of Banach algebras, the so-called Σ-convergence promises to handle all known non-periodic formulations, including the probabilistic one (via the Radon measures and the Gelfand representations of special algebras). This concept evidently involves the two-scale convergence as a very special case; however, its application to most non-periodic engineering problems is not quite transparent and the whole text expects the very experienced reader, familiar with the methods and results from various branches of pure and applied mathematics; this may be the reason why e.g. the latest monograph on multiscale methods [28] ignores these results at all.

Moreover, the coupling of the heat transfer with other physical processes brings still new problems. Especially the complex analysis of heat, air and moisture propagation (the so-called HAM modelling, possibly accompanied with some contaminant) in buildings, based on the classical thermodynamical principles, namely on the conservation of mass, inertia and energy, leads, even in the case of a priori known macroscopic material characteristics, to some mathematical problems, whose solvability is not clear; for the more proper overview see [38]. The same is true e.g. for the hygro-thermo-mechanical modelling of the early-age concrete, conditioning all later mechanical properties and the durability of the whole structure, discussed in [14]. Typically the treatment of such complicated problems uses various semi-empirical ad hoc simplifications beyond the scope of this paper.

5. Numerical treatment

The number of papers presenting the computational algorithms and the results from the software applications performing the modelling and simulation of engineering problems is much higher than the proper mathematical and physical studies, referenced in this paper. The very frequent engineering approach consists of some experimental computations at various scales, applying rather artificial boundary conditions to commercial software packages, composed by the classical least squares method. Their (more or less strange) result generate good arguments for the minority of critical opinions like [12]: “it begins with naive euphoria” and consequently there is an “overreaction to ideas that are not fully developed, and this inevitably leads to a crash”.

Omitting the ad hoc computations with no or weak theoretical support, we must notice some studies of the two- or more-scale techniques, namely in the finite element method (but also e.g. in the finite volume or finite difference methods or their various combinations). Some of them do not apply any proper homogenization, being concentrated to the analysis of the (possibly parallelized) computations on two or more not necessarily nested grids. A very useful iterative algorithm, based on the improved Schwarz-Cauchy inequality, has been suggested in [15]; as shown in [36], it can be adopted also to the finite element analysis of linear problems incorporating the two-scale approach, i.e. to the formulations like (6) and (3). The four crucial steps of this algorithm (in the very simplified version) after the setting of the first estimate τ_*^0 of τ are:

1. find such $\tau^\varepsilon \in V^\varepsilon$ that

$$(\nabla v^{\varepsilon}, \lambda^{\varepsilon}\nabla\tau^{\varepsilon}) = (v^{\varepsilon}, f) + < v^{\varepsilon}, q > -(\nabla v^{\varepsilon}, \lambda^{\varepsilon}\nabla T_*) - (\nabla v^{\varepsilon}, \kappa^{\varepsilon}, \nabla\tau_*^0)$$

for all $v^{\varepsilon} \in V^{\varepsilon}$,

2. set $\tau_*^{1/2} = \tau_*^0 + \omega\tau^{\varepsilon}$,
3. find such $\tau^h \in V^h$ that

$$(\nabla v^h, \lambda\nabla\tau^h) = (v^h, f) + < v^h, q > -(\nabla v^h, \kappa\nabla T_*) - (\nabla v^h, \lambda\nabla\tau_*^{1/2})$$

for all $v^h \in V^h$,

4. set $\tau_*^1 = \tau_*^{1/2} + \omega\tau^h$,

etc. (obtaining $\tau_*^{3/2}, \tau_*^2, \ldots$, until the error is significant); here $\omega \in (0,2)$ is an appropriate relaxation parameter, V^{ε} and V^h are the finite-dimensional subspaces of V corresponding to the fine scale and to the rough scale, respectively (ε and h can be identified with the norm of decomposition of Ω to finite elements, ε being much lesser than h, but the convergence analysis works with simultaneous $\varepsilon \to 0$ and $h \to 0$ theoretically), and the a priori knowledge of the effective value λ is assumed for simplicity. If the last statement is not true then the construction of the approximate solution of certain non-trivial additional problem should to be incorporated into the algorithm; for more details see [21] and [22].

The convergence analysis of the algorithms of the above sketched type enables us, at least for the linear problems, to derive convergence results comparable with those known from the classical finite element analysis. Some results beyond the linear formulations, both for the steady-state and for the time-dependent formulations, can be found in [11]; nevertheless, the formal verification of the existence of two-scale limits is available for a much larger class of problems than the convergence for such fully discretized schemes.

6. Still open problems

We have mentioned several complex problems, whose theoretical analysis seems to contain still more open questions than complete answers. Other typical problems of this type are those containing some non-local phenomena, occurring often in the simulation of the initiation and development of fracture, of the high-temperature phase transformation, etc. Even seemingly simple one-dimensional problems can lead to the results where any reasonable two-scale analysis is not available.

As an example we shall present the modelling of diffusive and massive phase transformation, whose physical fundamentals are introduced in [33]. The evolution of q substitutional and r interstitial, totally $q-1+r$, molar fractions c in one dimension is characterized in a Cartesian coordinate x and in time t. The coordinate x moves from the left to the right together with the interface of constant thickness h (from $x=0$ to $x=h$); the total size of the specimen is H (in practice much greater than h), the system is assumed to be closed (with zero boundary fluxes) on the interval between $x^L(t)$ and $x^R(t)$. One missing molar fraction comes from the additional condition $c_1 + \ldots c_q = 1$. The resulting system of equations, starting from some a priori known initial values of c, reads

$$Bc' + (K + vN)c - N\frac{C}{\tau} = vNc^{\Diamond} - N\Omega j^{\Diamond} - N\frac{C^{\times}}{\tau} \tag{9}$$

where all variables are evaluated in time t, except $C^{\times} = C(t-\tau)$, τ denotes the time interval, referring (for simplicity here) to the implicit Euler method (the system of differential equations can be derived from such difference ones using the limit passage $\tau \to 0$); B, K and N are square matrices of order $q-1+r$, B full, K and N diagonal, B and K depending on c, N dependent on x only, Ω is the constant molar volume and

$$C(x,t) = \int_0^x c(\xi,t)\mathrm{d}\xi \, , \tag{10}$$

$c^{\Diamond}$ refers to molar fractions and $j^{\Diamond}$ to diffusive fluxes at $x = 0$ and

$$v = \frac{\Omega}{M} \sum_{i=1}^{q+r} \int_0^h c_i \mu_i' \; \mathrm{d}x \tag{11}$$

for the prescribed chemical potentials μ_i as complicated functions of c; a prime symbol denotes a derivative with respect to x. The system (9) comes from the mass conservation law

$$\dot{c} - vc' + \Omega j' = 0 \tag{12}$$

with

$$Nj = -Bc' - Kc \; ;$$

another consequences of (12) are

$$(C^R - C^{R\times})/\tau - v(c^R - c^{\Diamond}) - \Omega j^{\Diamond} = 0 \tag{13}$$

and

$$(C^L - C^{L\times})/\tau - v(c^L - c^{\Diamond}) - \Omega j^{\Diamond} = 0 \tag{14}$$

where the upper indices ^{L} and ^{R} refer to the values at x^L and x^R, respectively. The iterative computational algorithm for any time step, suggested in [34], is based on the solution of the system (9) with B and K estimated from the preceding iterative step, but with respect to the unknown parameters $c^{\Diamond}$ and $j^{\Diamond}$; v is received by the numerical integration from (11), the results of numerical integration in (10) must be carefully incorporated into (9). The moving boundary conditions are needed for the determination of $c^{\Diamond}$ and $j^{\Diamond}$ (and consequently of c) from (13) and (14) in each iterative step a posteriori.

The numerical experiments (making use of the original MATLAB- and MAPLE-based software code) with a purely substitutional Fe-rich (q=3, r=0) Fe-Cr-Ni system (whose complete experimental description has been obtained from the Montanuniverität Leoben in Austria and from the Institute of Physics of Materials of the Academy of Sciences of the Czech Republic in Brno) for various fixed temperatures T between 1020 and 1080 K show that for steady-state simulation (neglecting $\dot{c}$ in (12) and the corresponding terms in all remaining relations) predicts some positive constant velocity v decreasing with T. However, the temperature T corresponding to $v \to 0$ is not quite the same as that received for the sharp interface (assuming $h \to 0$); this temperature has been validated indirectly by practical observations. The time-dependent simulation is moreover able to predict the characteristics of the whole process of phase transformation, including the sign changes of v and the possible convergence $v \to 0$ in time. The time distributions of c (at least after some sufficiently long time) are typically nearly constant from the rough view (connected with H), but they can be recognized as rather complicated functions of x in the fine scale (connected with h): this seems to be also the reason why no reference to such other simulation software can be found in the literature.

The above discussed numerical calculations generate reasonable results, but their interpretation using the two-scale (or other) homogenization approach is not available: we were not successful to identify some size parameter with the needed $\varepsilon \to 0$ and the derivation of some relatively simple limit form of our integro-differential problem cannot be expected. This may demonstrate certain limitations of the homogenization techniques, but also motivate their improvements and further development.

Acknowledgement. This research is supported by the Ministry of Education, Youth and Sports of the Czech Republic, No. MSM 0021630511, DT7.

References

[1] Allaire G. Homogenization and two-scale convergence, *SIAM J. Math. Anal.*, **23** (1992), 1482-1512.

[2] Arbogast T., Douglas J., Hornung V. Derivation of the double porosity model of single phase flow via homogenization theory, *SIAM J. Math. Anal.*, **21** (1990), 823-836.

[3] Babuška I. *Homogenization approach in engineering*, in *Lecture Notes in Economics and Mathematical Systems* (Berkmann M., Kunzi H. P., eds. – Springer, Berlin), 1975, 137-153.

[4] Bensoussan A., Lions J. L., Papanicolaou G. *Asymptotic Analysis for Periodic Structures*, North Holland, Amsterdam, 1978.

[5] Bouchité G., Fragalà I. Homogenization of thin structures by two-scale method with respect to measures, *SIAM J. Math. Anal.* **32** (2001), 1198-1226.

[6] Černý R., Pavlík Z. Homogenization techniques for determination of thermal conductivity of porous materials, *Proc. Thermophysics* (Kočovce, Slovak Rep.), STU Bratislava, 2007, 76-80.

[7] Cioranescu D., Donato P. *An Introduction to Homogenization*, Oxford University Press, Oxford, 2000.

[8] Dal Maso G. *An Introduction to* Γ*-Convergence*, Birkhäuser, Boston, 1993.

[9] Defranceschi A. *An Introduction to Homogenization and G-Convergence*, Int. Center Theor. Physics, Trieste, 1993.

[10] De Giorgi E. Some remarks on Γ-convergence and least square methods, in *Composite Media and Homogenization Theory* (Dal Maso G., Dell'Antonio G.F., eds.), Birkhäuser, Boston, 1991, 135-141.

[11] Efendiev Y., Hou T. Y. *Multiscale Finite Element Methods – Theory and Applications*, Springer, New York, 2008.

[12] Fish J. Multiscale computations: boom or bust, *IACM Expressions* **22** (2008), 4-7.

[13] Fragalà I., Mantegazza C. On some notions of tangent space to a measure, *Proc. Roy. Soc. Edinburgh* **129A** (1999), 331-342.

[14] Gawin D., Pesavento F., Schrefler B. A. Hygro-thermo-chemo-mechanical modelling of concrete at early ages and beyond, *Int. J. Numer. Meth. Engng.* **67** (2006), 299-363.

[15] Glowinski R., He J., Lozinski A., Rappaz J., Wagner J. Finite element approximation of multiscale elliptic problems using patches of elements, *Numer. Math.* **101** (2005), 663-688.

[16] Holmbom A., Homogenization of parabolic equations – an alternative approach and some corrector-type results, *Appl. Math.* **47** (1997), 321-343.

[17] Holmbom A., Silfver J., Svanstedt N., Wellander N. On two-scale convergence and related sequential compactness topics, *Appl. Math.* **51** (2006), 247-262.

[18] Jiao Y., Stilinger, F. H., Torquato, S. Modeling heterogenous materials via two-point correlation functions, *Phys. Rev.* **E 76** 031110 (2007), 1-15, and **E 77** 031135 (2008), 1-15.

[19] Kufner A., John O., Fučík S. *Function Spaces*, Academia, Prague, 1977.

[20] Mascarenhas M. L., Toader A.-M. Scale convergence in homogenization, *Numer. Funct. Anal. Opt.* **22** (2001), 127-158.

[21] Matache A.-M., Babuška I., Schwab Ch. Generalized p-FEM in Homogenization, *Num. Math.* **86** (2000), 319-375.

[22] Matache A.-M., Schwab Ch. Two-scale finite element method for homogenization problems, in *Seminar of Applied Mathematics*, Rep. No 99-18 (ETH-Zentrum, Zürich), 2001.

[23] Maz'ya V. G. *Prostranstva S. L. Soboleva*, Izdateľstvo Leningradskogo universiteta, Leningrad (St. Petersburg), 1985.

[24] Murat F., Tartar L. Calcul des variations et homogénéisation, *Publ. du Laboratoire d'Analyse Numérique*, No 84012 (Univ. Pierre et Marie Curie, Paris), 1978.

[25] Nechvátal L. Alternative approach to the two-scale convergence, *Appl. Math.* **49** (2004), 97-110.

[26] Nguetseng G. A general convergence result for a functional related to the theory of homogenization, *SIAM J. Math. Anal.* **20** (1989), 608-623.

[27] Nguetseng G. Homogenization structures and applications, *Z. Anal. Anwendungen* **22** (2003), 73-107, and **23** (2004), 482-508.

[28] Pavliotis G. A., Stuart A. M. *Multiscale Methods*, Springer, New York, 2008.

[29] Pedregal P. Multi-scale Young measures, *Transact. AMS* **358** (2006), 591-602.

[30] Sanchez-Palencia E. *Nonhomogenous Media and Vibration Theory*, Springer, Berlin, 1980.

[31] Svanstedt N. Multiscale stochastic homogenization of convection-diffusion equations, *Appl. Math.* **53** (2008), 143-155.

[32] Spagnolo S. Sulla convergenza di soluzioni di equazioni paraboliche ed ellitiche, *Ann. Scuola Normale Superiore Pisa*, No 22, 1968.

[33] Vala J. Modelling of diffusive and massive phase transformation, in *Composites with Micro- and Nano-Structure – Computational Modelling and Experiments* (Kompiš V., ed.), Springer, Berlin, 2008, 67-86.

[34] Vala, J. Scale bridging in diffusive phase transformation, *Proc. Algoritmy 2009* (Podbanské, Slovak Rep.), submitted.

[35] Vala J. The method of Rothe and two-scale convergence in nonlinear problems, *Appl. Math.* **48** (2003), 587-606.

[36] Vala J. Two-scale finite element techniques in engineering mechanics, *J. Mech. Engng.* **57** (2006), 127-140.

[37] Vala J. Two-scale limits in some nonlinear problems of engineering mechanics, *Math. Comput. Simul.* **61** (2003), 177-185.

[38] Vala J., Šťastník S. On the heat propagation in buildings, *Building Research J.* **52** (2004), 31-56.

[39] Wiener O., Die Theorie des Mischkörpers für das Feld der stationären Strömung, *Gesellschaft der Wissenschaften* **32**, 1912, 509-604.

Study on thermal properties of laminating films of photovoltaic cells

O. Zmeškal, P. Štefková, L. Hřebenová, R. Bařinka*

Institute of Physical and Applied Chemistry, Faculty of Chemistry, Brno University of Technology, Purkyňova 118, 61200 Brno, Czech Republic, Email: zmeskal@fch.vutbr.cz

Solartec s.r.o., Televizní 2618, 756 61 Rožnov pod Radhoštěm

Abstract

The paper reports a study on thermal properties of laminating films used for the production of photovoltaic cells modules. The main attention is devoted to absorptive (reflective) and emissive properties of various types of films used for the module encapsulation. The main aim of encapsulation is the protection of photovoltaic panel against environmental damage (humidity especially). However, the laminating films have also an influence on the electrical behavior of the whole panel due to various working temperatures of individual photovoltaic cells.

It is generally known that increasing the temperature of photovoltaic cell leads to a decrease of its conversion efficiency. Therefore, the application of laminating films with small absorption, high reflectivity, and good thermal conductivity and with high emissivity on the rear (not illuminated) side causes a decrease of working temperature of photovoltaic panel and thus an increase of produced power. This eventually leads to the shortening of investment recovery time.

Key words: photovoltaic cells, thermal properties of materials, transient pulse method, thermo vision

INTRODUCTION

The absorption of electromagnetic (thermal) radiation was studied with the use of thermocamera Fluke TI55 and by means of the transient pulse method that enables to find out thermal properties of bulk materials (specific heat, thermal diffusivity and thermal conductivity). Thermal properties of defined system of bulk material were measured with and without the application of a laminating film. The surface temperature distribution of the panel was simultaneously monitored by thermocamera Fluke TI 55 during measurements.

EXPERIMENTAL SETUP

Thermocamera measurement

The quantitative study on thermal properties of laminating films was preceded by a preliminary measurement of a photovoltaic panel composed of 8 photovoltaic cells. The individual cells were covered by various laminating films from the rear side (see Fig. 1).

These laminating films types consisted of uni-color ones (white - F03, grey - F04 and black F06) with varying surface finish (mat, glossy), transparent ones (F05, F08, F09) and bi-color ones (blue/white F07, black/white - F02). The black/white laminating film was not placed under any photovoltaic cell.

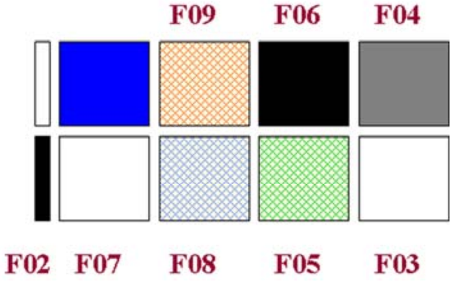

Fig. 1 Settlement of photovoltaic panel

The photovoltaic panel was oriented so that heat dissipation was enabled from the rear side (by conduction, convection and radiation). The steady temperature distribution on this panel after the irradiation by two 500 W bulbs from the distance of 1 m was monitored by the thermocamera Fluke TI 55 and is illustrated in Fig. 2.

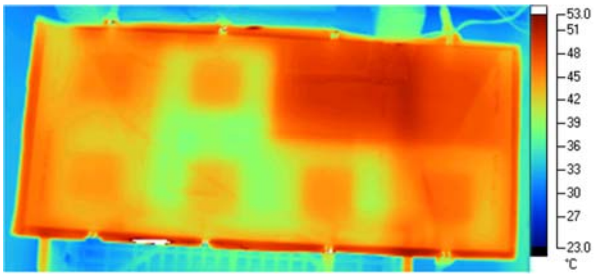

Fig. 2 Thermograph of photovoltaic panel consisting of cells encapsulated in various laminating films

The figure clearly depicts that the worst heat removal is from black and grey laminating film (F06, F04), whose temperature is approx. 50 °C. On the contrary, the best heat removal is from the transparent laminating films (F08, F09 and F05) whose temperature is approximately 35 °C.

Fig. 3 illustrates the situation when two photovoltaic cells were laminated by the same bi-colour laminating film in different orientation. On the left side, the film was placed so that its blue side (wb) is in touch with the photovoltaic cell and the white side is on the the surface. On the contrary, the laminating film orientation is reversed on the right white of the image (bw). It is evident that the temperature of the cell is higher in the second case because the emissivity of the white surface is bigger than the emissivity of the blue surface.

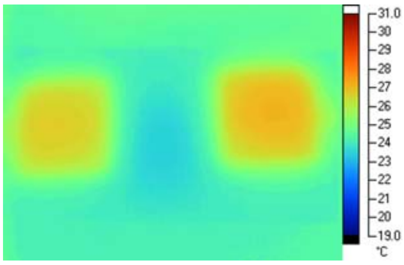

Fig. 3 Thermograph of two photovoltaic cells with different blue and white laminating film orientation (F07): left the white side is facoing out (wb), right vice versa (bw).

Pulse transient method measurement

The experiment setup for measurement by means of transient pulse method is illustrated in **Chyba! Nenalezen zdroj odkazů.** right. Heating caused by the irradiation of the sample (see Fig. 4 left) was simulated by surface thermal source, poly(methylmethacrylate) (PMMA) was used for heat removal from the laminating film (much like during previous experiment). Glass was replaced by PMMA from the frontal side where the temperatute was measured.

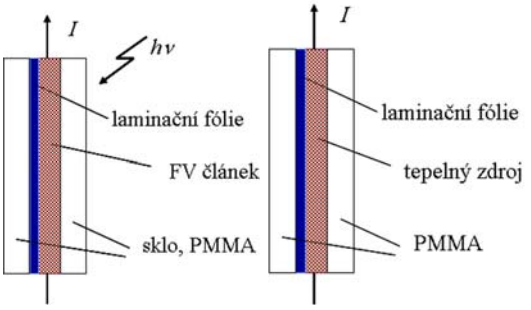

Fig. 4 Arrangement of photovoltaic cell and sample for transient pulse method measurement

The setup of the transient pulse method measurement is illustrated in Fig. 5, [1], [2]. Heating of surface thermal source is caused by defined current pulse. Measurement is usually conducted for various widths of pulses (t_0) and various powers $P = U I$. Temperature sampling is carried out by a NiCr-Ni thermocouple (for chosen experiments in combination with the thermocamera).

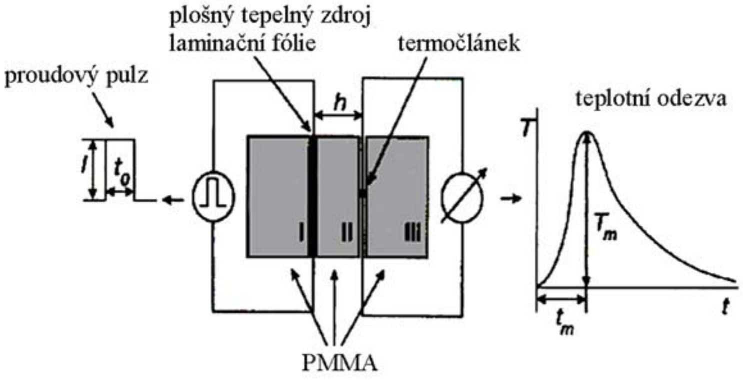

Fig. 5 Principle of measurement by means of pulse transient method

The aim of measurement was to compare thermal parameters of PMMA system without laminating films and with intermediate laminating films. It is possible to judge the suitability of laminating films for the application on photovoltaic panels from changes of thermal parameters (specific heat, thermal conductivity, and thermal diffusivity).

EXPERIMENTAL RESULTS

Measured response recorded by transient pulse method is illustrated in Fig. 6. It is evident from the figure that samples without use of laminating film (PMMA) have bigger maximum response temperature change than samples utilizing the laminating films.

There are negligible differences in the response temperature change of samples utilizing laminating film placed on one or both sides of heat source which is in and contradiction with thermographic record (Fig. 3).

By detailed analysis discussed later we found out that variations in responses really do exist.

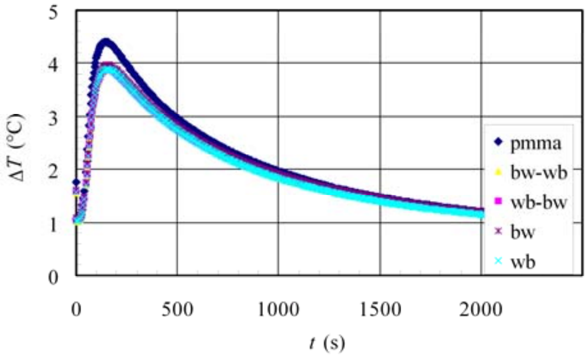

Fig. 6 Transient responses of studied samples: a) without laminating film (PMMA) b) with single blue and white laminating film (F07), see Fig. 4 right (bw, wb) and with two laminating films from both sides (wb-bw, bw-wb)

The dependence of thermal response ΔT on time t upon heat energy input $Q = U\,I\,t_0$ into the sample with thickness h (it equals to the distance of the thermocouple from the heat source) derived by means of the pulse transient method can bed describe by the relation

$$\Delta T = \frac{Q}{c_{\mathrm{p}}\rho\,(4\pi\,a\,t)^{(E-D)/2}} \cdot \exp\left(-\frac{h^2}{4a\,t}\right), \tag{1}$$

where a is thermal diffusivity, c_{p} specific heat and ρ is material density. Parameters D a E are determined by experimental setup: for planar heat source $D = 2$, for heat expanding in three – dimensional space is parameter $E = 3$, [3], [4] and [5]. Thermal conductivity can be determined from these parameters: $\lambda = c_{\mathrm{p}}\rho\,a$.

From the derivation of dependence of thermal response on the time

$$\frac{\partial \log \Delta T}{\partial \log t} = \left(\frac{D-E}{2} + \frac{h^2}{4at}\right) = 0 \tag{2}$$

it is possible to determine the thermal diffusivity of material being investigated

$$a = \frac{h^2}{2t_{\mathrm{m}} f_{\mathrm{a}}} = \frac{h^2}{2(E-D)t_{\mathrm{m}}}, \tag{3}$$

In this relation, the parameter f_{a} characterizes setup of experiment, deformation of heat field respectively. This coefficient is for ideal planar setup and heat transfer into the space ($E = 3$, $D = 2$) equal to one.

It is also possible to determine specific thermal capacity

$$c_{\mathrm{p}} = \frac{Q}{\rho\,\Delta T_{\mathrm{m}} h^{E-D}} \cdot \left(\frac{E-D}{2\pi \exp(1)}\right)^{(E-D)/2} \tag{4}$$

and thermal conductivity of material under investigation

$$\lambda = \frac{Q}{2(E-D)\Delta T_{\mathrm{m}} t_{\mathrm{m}} h^{E-D-2}} \cdot \left(\frac{E-D}{2\pi \exp(1)}\right)^{(E-D)/2} \tag{5}$$

from maximal value of change of temperature ΔT_{m}..

DISCUSSION

First, the parameters of the system were determined from the measurement of PMMA responses (Fig. 6), i.e. values of the thermal diffusivity, thermal conductivity and specific heat. Results obtained from the measurements of sample with average $R = 3$ cm and thickness h=6.0 mm correspond to values that are reported in literature: density of material under investigation (PMMA) is: $\rho = 1184$ kg.m^{-3}, thermal diffusivity $a = 1.12 \cdot 10^{-7}$ m^2.s^{-1}, specific heat $c_p = 1450$ J.kg^{-1}.K^{-1} and thermal conductivity $\lambda = 0.193$ W.m^{-1}.K^{-1}.
After inserting the laminating film from one (or both sides), the thermal properties of the system will be different because of different way of heat dissipation.
Maxima of responses will be shifted to lower (or higher values); maximal values will be lower (how it is evident from Fig. 6).
If we analyze these changed characteristics, we will obtain different values of thermal parameters than in the case of PMMA.
By comparing these values with values obtained for PMMA, it is possible to determine changes of heat conductivity and specific thermal capacity of the system. This is illustrated at following figures (Fig. 7 and Fig. 8)

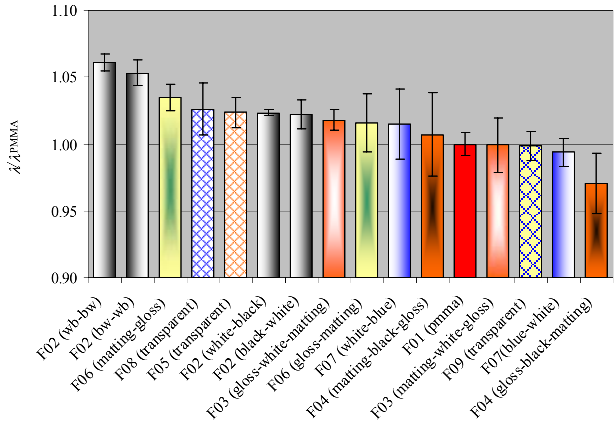

Fig. 7 Relative changes of thermal conducttivity of the system consisting of PMMA and laminating films in view of PMMA itself (F01)

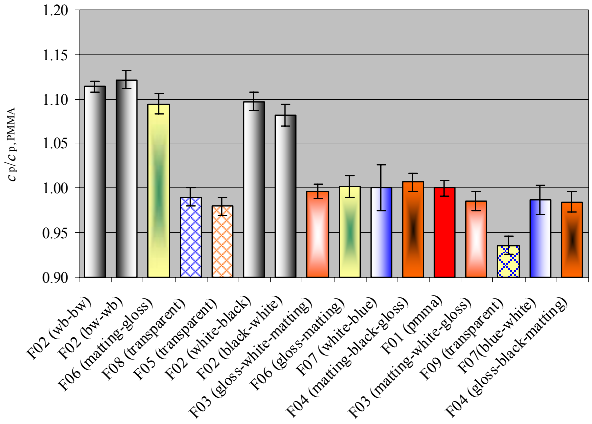

Fig. 8 Relative changes of specific thermal capacity of the system consisting of PMMA and laminating films in view of PMMA itself (F01)

As far as the thermal conductivity is concerned, suitable properties are demonstrated by samples placed left of the sample F01. After their application, these materials caused expansion of samples' thermal conductivity. From the specific heat viewpoint, suitable materials seem to those that caused its reduction.
The most suitable materials are transparent films F02 and F05. Another suitable adept for application to photovoltaic panels is also transparent film F07, which caused a prominent decrease of specific heat whereas the thermal conductivity did not change at all in comparison to PMMA.

CONCLUSIONS

Modified transient pulse method was applied for experimental data evaluation. This method describes general behavior of thermal properties of materials as fractal structures. Dependence of fractal parameter D characterizing non-homogeneous distribution of temperature in material (in E-dimensional space) depending on the distance from heat source and time was determined by using of space-time fractal theory.

Results of theoretical model were verified by measurements of real systems with encapsulated photovoltaic cells. Laminating films suitable both in terms of thermal conductivity (being bigger than conductivity of the system without laminating film - sample F01) and also in terms of specific heat (being smaller than the specific heat of the system without laminating film - sample F01). Transparent laminating films F05, F08, F09 have these properties, as illustrated in Fig. 7 and Fig. 8. Resulting knowledge will lead to optimization of photovoltaic modules construction with respect to heat dissipation in real conditions.

ACKNOWLEDGMENTS

This work was supported by project KAN401770651 from The Academy of Sciences of the Czech Republic and by grant FT-TA3/048 from the Ministry of Industry and Trade of the Czech Republic.

REFERENCES

[1] KUBIČÁR, L.: Pulse Method of Measuring Basic Thermophysical parameters (Bratislava and Elsevier Nederland, 1990) 344

[2] BOHÁČ, V., KUBIČÁR, L., VRETENÁR, V.: Methodology of parameter estimation of pulse transient method and the use of PMMA as standard reference material. In TEMPMEKO 2004, *9th International Symposium on Temperature and Thermal Measurements in Industry and Science* (Cavtat – Dubrovnik Croatia, 2004)

[3] ZMEŠKAL, O., ŠTEFKOVÁ, P., HŘEBENOVÁ, L., BAŘINKA, P.: Pulse Transient Method as a Tool for the Study of Thermal Properties of Solar Cell Laminating Films. In *18. European Conference on thermophysical properties*. 1. Pau, France, ECTP. 2008. p. 344 - 344.

[4] ŠTEFKOVÁ, P., ZMEŠKAL, O., CAPOUŠEK, R.: Study of Thermal Field in Composite Materials. In *Complexus Mundi*. WS. London, World Scientific. 2006. p. 217 - 224. ISBN 981-256-666-X.

[5] ŠTEFKOVÁ, P., ZMEŠKAL, O.: Study of Thermal Diffusivity in Heat-Insulating Materials. *Chemické listy*. 2005. 99(S). p. s624 (2 p.). ISSN 0009-2770.

DETERMINATION OF LENGTH CHANGES OF ALKALI ACTIVATED SLAG CONCRETE AT ELEVATED TEMPERATURES

Lucie Zuda, Robert Černý

Czech Technical University in Prague, Faculty of Civil Engineering, Department of Materials Engineering and Chemistry, Thákurova 7, 166 29 Prague 6, Czech Republic, email: lucie.zuda@fsv.cvut.cz, cernyr@fsv.cvut.cz

Abstract:

The linear thermal expansion coefficient of two alkali-activated slag concretes produced from ground granulated blast furnace slag in the temperature range up to 1000°C is measured in the paper. Experimental results show that from the point of view of volumetric changes, both investigated alkali-activated slag concretes exhibit satisfactory response to high-temperature exposure up to 1000°C.

Keywords:

Aluminosilicates, high temperatures, linear thermal expansion coefficient

INTRODUCTION

Alkali-activated slag concrete was intensively studied over the past two decades as a promising alternative to Portland-cement based composites. The unique combination of high strength, considerable fire resistance and good chemical resistance which are characteristic for this type of materials attracted many investigators active in materials science, chemical engineering and civil engineering.

Mechanical properties were the most frequently investigated parameters of alkali-activated slag concrete, similarly as in the case of Portland-cement composites. They were analyzed both in room-temperature conditions and after high-temperature exposure. Other parameters such as hydric properties, chloride diffusion or thermal properties were studied only rarely. Volumetric changes of alkali-activated aluminosilicates were studied mostly in hydration stage as their drying and autogenous shrinkage was always considered a serious threat. Length changes at elevated temperatures were studied for several types of geopolymers only and in all cases remarkable thermal shrinkage (up to 20%) was observed.

In this paper, the linear thermal expansion coefficient of two alkali-activated slag concretes produced from ground granulated blast furnace slag in the temperature range up to 1000°C is measured.

METHOD FOR DETERMINATION OF LINEAR THERMAL EXPANSION COEFFICIENT

Thermal expansion of solid materials in high-temperature range is measured by commercially produced dilatometers mostly. Various treatments are employed, for instance the methods based on variations of electric resistance, capacitance, inductance, or the interference methods. However, the applicability of many common methods which work with small specimen dimensions may be rather limited for building materials which are mostly nonhomogeneous. Therefore, the comparative method proposed by Toman et al. [1] which was used for various building materials in the past was employed for the measurements in this paper. As some modifications of the experimental setup were done to bring the original method up to date we will give a brief description of the method in what follows.

The measuring device for determining the linear thermal expansion of porous materials in the high temperature range is based on the application of a comparative technique (see Fig. 1). A bar sample of the studied material is put into a cylindrical, vertically oriented electric furnace. As it is technically difficult to perform length measurements directly in the furnace, a thin ceramic rod, which passes through the furnace cover, is fixed on the topside of the measured sample. The length changes can be determined outside the furnace in this way, for instance by a digital dial indicator, but on the other hand, the temperature field in the ceramic rod is very badly defined, and it is not possible to determine directly, which part of the total change of length is due to the measured sample and due to the ceramic rod.

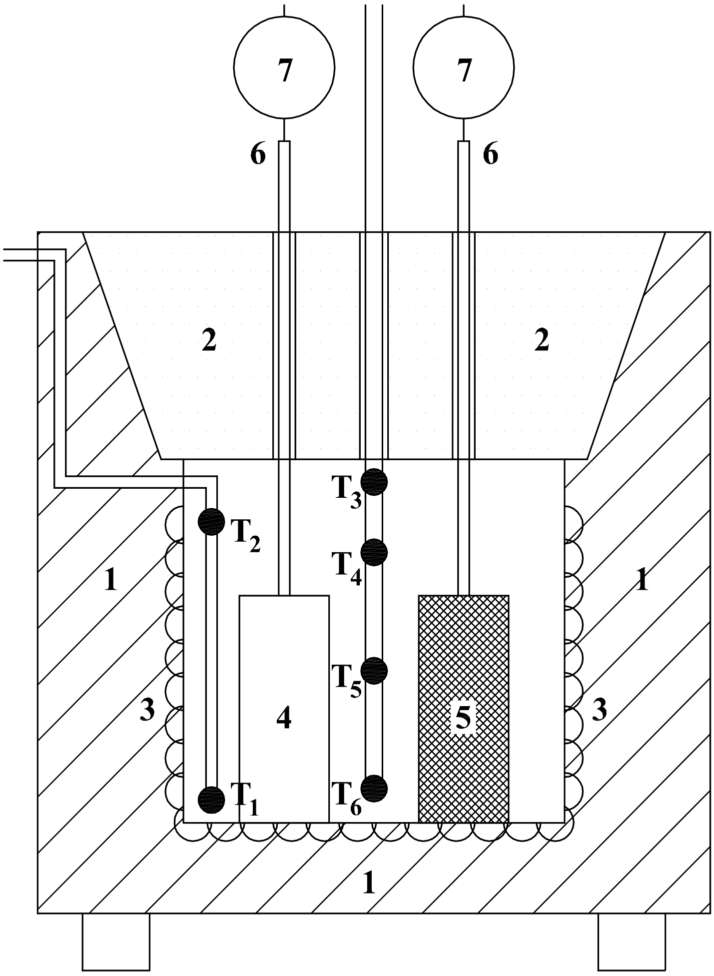

Figure 1 Scheme of the measuring device for determination of high temperature linear thermal expansion coefficient, 1 - furnace shell (thermal insulation), 2 - furnace cover, 3 - heating coil, 4 – standard, 5 - measured sample, 6 - ceramic rods, 7 – digital dial indicator, T_{1-6} – thermocouples

Therefore, the measurement is performed at the same time on the sample of a standard material (such as special steels where the $\alpha(T)$ function is known) which is put into the furnace together with the studied material and is provided with an identical ceramic rod passing through the over. The change of length of the ceramic rod can be determined in this way, and consequently also the length change of the measured sample.

It should be noted that temperature field is not constant in the whole volume of the furnace due to the differences of heat loss in the heated walls and in the cover. Therefore, temperature field in the furnace is measured by thermocouples, and an average value of temperature is considered in α calculations.

A practical measurement of the linear thermal expansion coefficient of a porous material with the device proposed in the previous section can be described as follows. The measured sample and the standard are put into the furnace, provided with contact ceramic rods, and the initial reading on the dial indicators is taken. Then, the electric heating regulation system is adjusted for the desired temperature T_i in the furnace, and the length changes are monitored. The data acquisition from the digital dial indicators is done on PC using specially developed software. After the steady state is achieved, i.e., no temperature changes in the furnace and no length changes of both measured sample and the standard are observed, the final readings of length changes are taken. The length change of the measured sample is calculated from the following formula:

$$\Delta l(T_i) = \Delta l_m(T_i) - \Delta l_s(T_i) + l_{o,s}\int_{T_o}^{Ti} \alpha_s(T)dT \tag{1}$$

where Δl_m, Δl_s are the final readings of total length changes of the studied material and of the standard including the length changes of the ceramic rods, respectively, $l_{o,s}$ is the initial length of the standard, and α_s is the known linear thermal expansion coefficient of the standard. The corresponding value of thermal strain can be expressed in the form:

$$\varepsilon(T_i) = \frac{\Delta l(T_i)}{l_{o,m}} \tag{2}$$

where $l_{o,m}$ is the initial length of the measured sample.

The measurements are then repeated with other chosen values of furnace temperature T_i, and the $\alpha(T)$ function of the measured material is determined using the definition relation

$$\alpha = \frac{d(l/l_o)}{dT} = \frac{d\varepsilon}{dT}\,. \tag{3}$$

MATERIALS AND SAMPLES

Two composite materials on the basis of alkali activated slag were investigated. They differed in the type of aggregates. The first aggregate type was quartz sand (this material will be denoted as NS in what follows), the second electrical porcelain (EP). Fine-ground granulated blast furnace slag of Czech origin (Kotouč Štramberk, Ltd.) was used for sample preparation. Its chemical composition is shown in Table 1, its granulometry in Table 2.

Table 1 Chemical composition of applied slag

SiO_2 [%]	Fe_2O_3 [%]	Al_2O_3 [%]	CaO [%]	MgO [%]	MnO [%]	Cl- [%]	Na_2O [%]	K_2O [%]	SO_3 [%]
38.6	0.52	7.22	38.77	12.90	0.50	0.06	0.21	0.38	0.36

Table 2 Slag granulometry

Sieve residue		Specific surface
0.045 mm [%]	0.09 mm [%]	$[cm^2/g]$
12.4	1.9	3920

As alkali activator, water glass solution (Na_2O . $xSiO_2$. yH_2O) was used. It was prepared using Portil-A dried sodium silicate (Na_2SiO_3) preparative (Cognis Iberia, s.l. Spain). The quartz sand aggregates were normalized according to ČSN EN 196-1 with the granulometry given in Table 3. Electrical porcelain was provided by P-D Refractories CZ, Velké Opatovice. Its porosity was 0.3%, water absorption at saturation 0.1%, bulk density 2350 kg/m^3. Chemical composition of the electrical porcelain is given in Table 4, its granulometry in Table 5.

Table 3 Sand granulometry

Sieve mesh [mm]	2	1.6	1.0	0.5	0.16	0.08
Total sieve residue (%)	0	7±5	33±5	67±5	87±5	99±1

Table 4 Chemical composition of electrical porcelain

SiO_2 [%]	Fe_2O_3 [%]	Al_2O_3 [%]	CaO [%]	MgO [%]	Na_2O [%]	K_2O [%]	TiO_2 [%]
48.6	0.8	45.4	0.3	0.2	1.0	2.9	0.7

Table 5 Electrical porcelain granulometry

Sieve mesh [mm]		4.00	2.50	1.00	0.50	0.25	0.125	0.090	0.063	0.045
Total sieve residue [%]	0-1 mm fraction	-	-	0.69	45.24	70.76	89.98	93.4	98.99	99.99
	1-3 mm fraction	-	4.12	78.33	99.57	99.94	99.94	99.95	98.98	100.00
	3-6 mm fraction	69.31	95.52	99.97	99.98	99.99	100.00	-	-	-

The composition of mixtures for sample preparation is presented in Tables 6a, b.

Table 6a Composition of the mixture with quartz sand aggregates for sample preparation

Sand [g]			Slag [g]	Alkali-activation silicate admixture [g]	Water [ml]
PG1	PG2	PG3			
450	450	450	450	90	190

Table 6b Composition of the mixture with electrical porcelain aggregates for sample preparation

Electrical porcelain [g]			Slag [g]	Alkali-activation silicate admixture [g]	Water [ml]
0-1 mm fraction	1-3 mm fraction	3-6 mm fraction			
450	450	450	450	90	190

The technology of sample preparation was as follows. First, the silicate preparative was mixed with water. The solution was then mixed in the homogenized slag-aggregate mixture. The final mixture was put into molds and vibrated. The specimens were demolded after 24 hours and then stored for additional 27 days in a water bath at laboratory temperature. The dimension of the specimens was 40 x 40 x 100 mm. Three specimens for each mixture were used for the measurement of linear thermal expansion coefficient.

EXPERIMENTAL RESULTS AND DISCUSSION

Fig. 2 shows the measured thermal strain of both studied materials as function of temperature up to 1000°C.

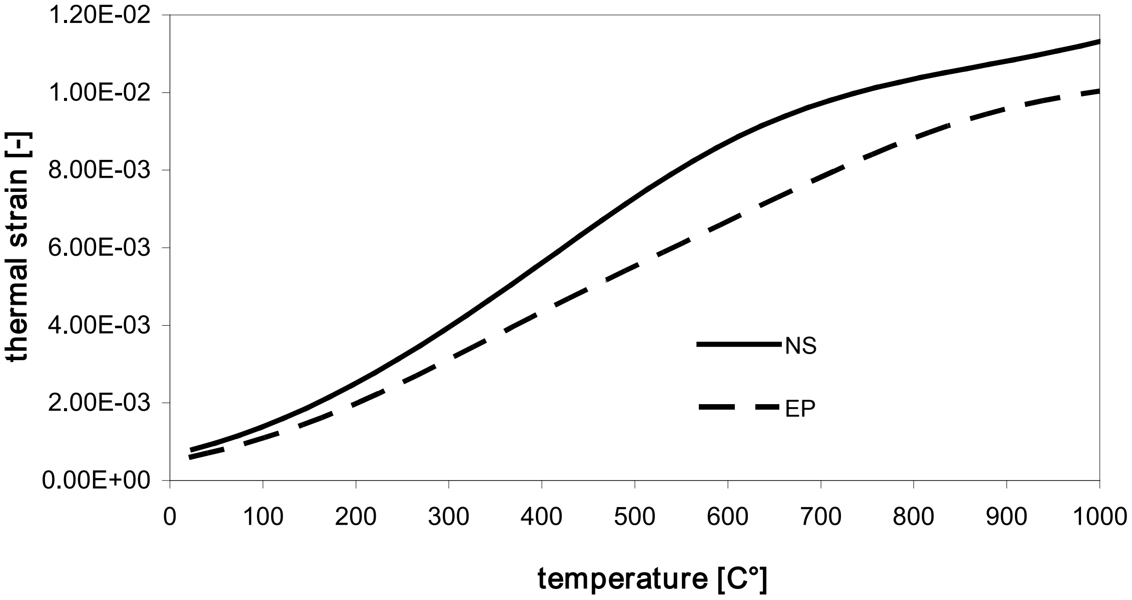

Figure 2 Thermal strain of analyzed materials as function of temperature

The $\varepsilon(T)$ functions of both materials were increasing in the whole temperature range so that no thermal shrinkage was observed up to 1000°C, contrary to the results obtained by several investigators for geopolymers [2-4]. This difference is apparently a consequence of the presence of aggregates in the alkali-activated aluminosilicate composites studied in this paper which caused thermal expansion mismatch in the material (the gel undergoes thermal shrinkage, the aggregates expand with increasing temperature); the materials analyzed in [2-4] were pastes. This statement can be supported by the investigations in [5] where for Portland cement mortar thermal expansion was observed in the whole studied temperature range of 20 to 500°C while cement paste underwent thermal shrinkage for temperatures higher than 150°C.

The linear thermal expansion coefficients calculated using the $\varepsilon(T)$ functions from Fig. 2 are presented in Fig. 3 which makes possible to analyze the effect of temperature increase on length changes of both studied aluminosilicates in more details. The $\alpha(T)$ functions were increasing in the lower-temperature range, for NS up to approximately 400°C, for EP to 300°C. Then the linear thermal expansion coefficient of NS began to decrease so that at 800°C it had similar value as at room temperature, and finally in the temperature range of 800°C to 1000°C it was almost constant. On the other hand, the $\alpha(T)$ function of EP was only slightly decreasing in the temperature range of 300°C to 700°C, and then it decreased faster so that at 1000°C it was similar as at room temperature.

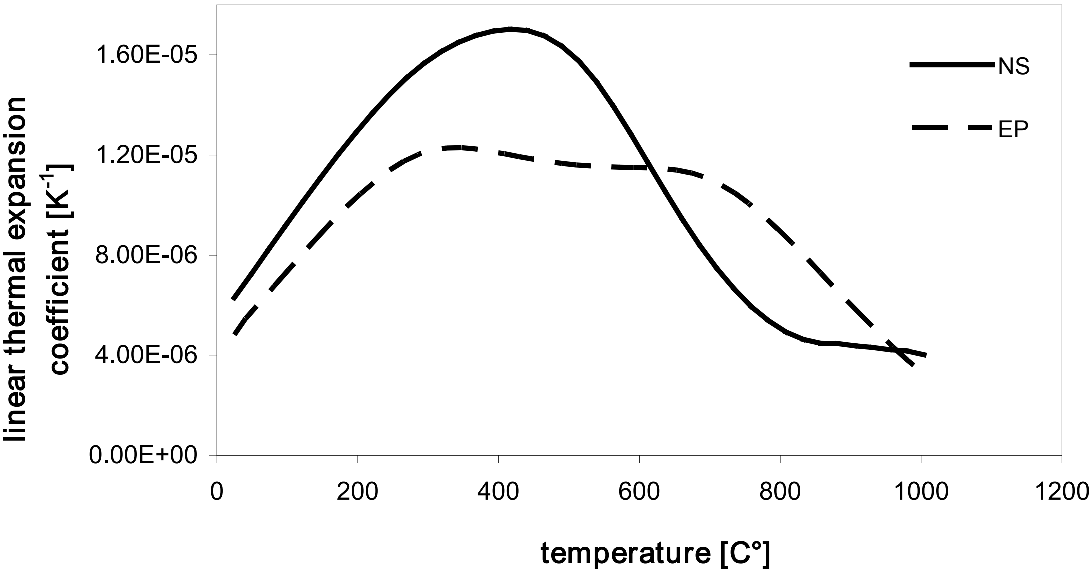

Figure 3 Linear thermal expansion coefficient of analyzed materials as function of temperature

The differences between the $\alpha(T)$ functions in Fig. 3 can be explained by the different behavior of the two materials used in the studied aluminosilicate composites as aggregates after their exposure to elevated temperatures. Electrical porcelain is characterized by low linear thermal expansion coefficient ($6\text{-}8 \cdot 10^{-6}$ K^{-1} in average) and no sudden volumetric changes in the temperature range up to 1000°C [6, 7]. Quartz, on the other hand, is subject of displacive phase transition from α (low) to β (high) modification at 573°C [8]. The different quartz forms differ also in their structural response to increasing temperatures. While the thermal expansion coefficient of α-quartz is positive ($18 \cdot 10^{-6}$ K^{-1} in average, calculated using the data in [8] and [9]), it was found that β-quartz does not exhibit any significant thermal expansion from 573°C up to 1000°C [8, 9] or possibly it even undergoes thermal shrinkage [10]. Thus, the electrical porcelain aggregates had clearly better prerequisites to compensate for the thermal shrinkage of aluminosilicate gel than quartz sand, in the temperature range of 573°C to 1000°C in particular. The more convenient thermomechanical behavior of the aluminosilicate composite with electrical porcelain aggregates was probably also the main reason for its much slower decrease of strength with increasing temperature (as compared with the analogous composite with quartz sand aggregates) observed in the measurements of compressive and bending strength in [11] and [12].

A comparison of results obtained for alkali-activated aluminosilicate composites in this paper with the thermal expansion properties of other types of cementitious composites can be done in a limited extent only as very few results were published until now. In [5], the total thermal strain of cement mortar at 500°C was approximately $9 \cdot 10^{-3.}$ This was 20% higher than for the aluminosilicate with quartz sand in this paper and almost 40% higher than for the material with electrical porcelain aggregates. The $\alpha(T)$ functions determined up to 1000°C for cement mortar in [1] and for high performance concrete in [13] were similar in shape to the aluminosilicate material with quartz sand but 20-50% higher in the whole temperature range. As lower thermal strain generally results in lower thermal stress, thus in lower risk of failure of a building element subjected to one-sided heating, the thermomechanical behavior of the aluminosilicates studied in this paper can be characterized as mostly better than of Portland cement based composites.

CONCLUSIONS

The experimental results obtained in this paper showed that among the two analyzed alkali-activated aluminosilicate composites with different aggregate type, the material with electrical porcelain aggregates was found a more convenient solution from the thermomechanical point of view than a similar material with quartz sand. This was a consequence of better high-temperature volumetric stability of electrical porcelain which is characterized by low linear thermal expansion coefficient and no sudden volumetric changes in the temperature range up to 1000°C while quartz is subject of displacive phase transition from α to β modification at 573°C and in addition, the different quartz forms differ also in their structural response to increasing temperatures.

Nevertheless, from the point of view of volumetric changes both investigated alkali-activated aluminosilicate composites exhibited satisfactory response to high-temperature exposure up to 1000°C. The linear thermal expansion coefficient of both studied materials was in the whole temperature range of 20-1000°C significantly lower as compared to Portland-cement based composites but no thermal shrinkage was observed. This makes good prerequisites for the applications in building industry where elevated temperatures may be expected, such as walls and floors adjacent to various heat machines, pipes or chemical process vessels, envelopes or linings of special vessels such as coal gasification vessel, nuclear safety related structures in nuclear power plants, tunnel or shaft walls and fire-protecting linings.

ACKNOWLEDGEMENT

This research has been supported by the Ministry of Education, Youth and Sports of Czech Republic, under grant No MSM: 6840770031.

REFERENCES

[1] Toman J, Koudelová P, Černý R., A measuring method for the determination of linear thermal expansion of porous materials at high temperatures. High Temperatures-High Pressures, vol. 31, 1999, pp. 595-600.

[2] Duxson P, Lukey GC, van Deventer JSJ, Thermal evolution of metakaolin geopolymers: Part 1 – Physical evolution. Journal of Non-Crystalline Solids, vol. 352, 2006, pp. 5541-5555.

[3] Duxson P, Lukey GC, van Deventer JSJ, Physical evolution of Na-geopolymer derived from metakaolin up to 1000 °C. Journal of Materials Science, vol. 42, 2007, pp. 3044-3054.

[4] Subaer, van Riessen A, Thermo-mechanical and microstructural characterisation of sodium-poly(sialate-siloxo) geopolymers. Journal of Materials Science, vol. 42, 2007, pp. 3117-3123.

[5] Fu YF, Wong YL, Poon CS, Tang CA, Lin P, Experimental study of micro/macro crack development and stress–strain relations of cement-based composite materials at elevated temperatures. Cement and Concrete Research, vol. 34, 2004, pp. 789-797.

[6] Amigo JM, Clausell JV, Esteve V, Delgado JM, Reventos MM, Ochando LE, Debaerdemaeker T, Marti F, X-ray powder diffraction phase analysis and thermomechanical properties of silica and alumina porcelains. Journal of the European Ceramic Society, vol. 24, 2004, pp. 75–81

[7] Kamseu E, Leonelli C, Boccaccini D, Non-contact dilatometry of hard and soft porcelain compositions. Journal of Thermal Analysis and Calorimetry, vol. 88, 2007, pp. 571-576.

[8] Carpenter MA, Salje EKH, Graeme-Barber A, Wruck B, Dove MT, Knight KS, Calibration of excess thermodynamic properties and elastic constant variations associated with the α → β phase transition in quartz. American Mineralogist, vol. 8, 1998, pp. 2–22.

[9] Lakshtanov DL, Sinogeikin SV, Bass JD, High-temperature phase transitions and elasticity of silica polymorphs. Physics and Chemistry of Minerals, vol. 34, 2007, pp. 11–22.

[10] Huang LP, Kieffer J, Structural origin of negative thermal expansion in high-temperature silica polymorphs. Physical Review Letters, vol. 95, 2005, paper 215901.

[11] Zuda L, Pavlík Z, Rovnaníková P, Bayer P Černý R, Properties of Alkali Activated Aluminosilicate Material after Thermal Load. International Journal of Thermophysics, vol. 27, 2006, pp.1250-1263.

[12] Zuda L, Bayer P, Rovnaník P, Černý R, Mechanical and Hydric Properties of Alkali-Activated Aluminosilicate Composite with Electrical Porcelain Aggregates. Cement and Concrete Composites, vol. 30, 2008, pp. 266-273.

[13] Toman J, Černý R, Thermal and Hygric Expansion of High Performance Concrete. Acta Polytechnica, vol.41, 2001, pp. 2-4.

LIST OF PARTICIPANTS

MSc. Muhammad Abid
Physikalisch Teschnische Bundesanstalt
Braunschweig, Germany
mabidmao@yahoo.com

MSc. Carlos Calvo Anibarro
Institute of Physics
Slovak Academy of Sciences
Bratislava, Slovakia
ccalvoanibarro@gmail.com

Prof. RNDr. Ivan Baník, PhD.
Faculty of Civil Engineering
Slovak University of Technology
Bratislava, Slovakia
ivan.banik@stuba.sk

Ing. Vlastimil Boháč, CSc.
Institute of Physics
Slovak Academy of Sciences
Bratislava, Slovakia
vlastimil.bohac@savba.sk

Mgr. Martin Brček
Faculty of Natural Sciences
Comenius University
Bratislava, Slovakia
martin.brcek@fns.uniba.sk

Prof. Ing. Robert Černý, DrSc.
Faculty of Civil Engineering
Czech Technical Univerzity
Prague, Czech Republic
cernyr@fsv.cvut.cz

Doc RNDr. František Čulík, PhD.
Faculty of Civil Engineering
Slovak University of Technology
Bratislava, Slovakia
fculik@atlas.sk

Doc. Ing. Peter Dieška, CSc.
Faculty of Electrical Engineering
and Informatics
Slovak University of Technology
Bratislava, Slovakia
peter.dieska@stuba.sk

Ing. Juma Haydary, PhD.
Faculty of Chemical and Food Technology
Slovak University of Technology
Bratislava, Slovakia
juma.haydary@stuba.sk

Ing. Martin Keppert, PhD.
Faculty of Civil Engineering
Czech Technical University
Prague, Czech Republic
martin.keppert@fsv.cvut.cz

Assoc. Prof. Piotr Koniorczyk,
PhD., DSc. Eng.
Military University of Technology
Warsaw, Poland
piotr.koniorczyk@wat.edu.pl

Prom. fyz. Oľga Koronthályová, CSc.
Institute of Construction and Architecture
Slovak Academy of Sciences
Bratislava, Slovakia
usarkoro@savba.sk

Ing. Ludovít Kubičár, DrSc.
Institute of Physics
Slovak Academy of Sciences
Bratislava, Slovakia
ludovit.kubicar@savba.sk

DI(FH) MSc. Daniel Lager
Austrian Research Centers
Seibersdorf, Austria
daniel.lager@arcs.ac.at

RNDr. Jozefa Lukovičová, PhD.
Faculty of Civil Engineering
Slovak University of Technology
Bratislava, Slovakia
jozefa.lukovicova@stuba.sk

Ing. Peter Matiašovský, CSc.
Institute of Construction and Architecture
Slovak Academy of Sciences
Bratislava, Slovakia
usarmat@savba.sk

Doc. RNDr. Igor Medveď, PhD.
Faculty of Natural Sciences
Constantine the Philosopher University
Nitra, Slovakia
imedved@ukf.sk

Ing. Peter Mihálka
Institute of Construction and Architecture
Slovak Academy of Sciences
Bratislava, Slovakia
usarmipe@savba.sk

Mgr. Ján Ondruška
Faculty of Natural Sciences
Constantine the Philosopher University
Nitra, Slovakia
jan.ondruska@ukf.sk

Assoc. Prof. Andrzej Panas, PhD., DSc. Eng.
Military University of Technology
Warsaw, Poland
andrzej.panas@wat.edu.pl

Ing. Zbyšek Pavlík, PhD.
Faculty of Civil Engineering
Czech Technical Univerzity
Prague, Czech Republic
pavlikz@fsv.cvut.cz

Mgr. Slávka Prváková, PhD.
Faculty of Civil Engineering
Slovak University of Technology
Bratislava, Slovakia
prvakova@yahoo.com

Doc. RNDr. Ing. Stanislav Šťastník, CSc.
Faculty of Civil Engineering
Brno University of Technology
Brno, Czech Republic
stastnik.s@fce.vutbr.cz

Prof. Mgr. Jan Toman, DrSc.
Faculty of Civil Engineering
Czech Technical Univerzity
Prague, Czech Republic
toman@fsv.cvut.cz

RNDr. Anton Trník, PhD.
Faculty of Natural Sciences
Constantine the Philosopher University
Nitra, Slovakia
atrnik@ukf.sk

Doc. Ing. Jiří Vala, CSc.
Faculty of Civil Engineering
Brno University of Technology
Brno, Czech Republic
vala.j@fce.vutbr.cz

Prof. Ing. Oldřich Zmeškal, CSc.
Faculty of Chemistry
Brno University of Technology
Brno, Czech Republic
zmeskal@fch.vutbr.cz

Assoc. Prof. Janusz Zmywaczyk, PhD., DSc. Eng.
Military University of Technology
Warsaw, Poland
janusz.zmywaczyk@wat.edu.pl